
International Conference on Numerical Optimisation Methods for Engineering Design

Proceedings of the
11th ASMO UK / ISSMO / NOED2016
conference

Institute of Advanced Studies
Technische Universität München
Munich, Germany
July 18th – 20th, 2016

Edited by:
Jens-Dominik Müller
Harvey Thompson
Fabian Duddeck
Vassili V. Toropov
Osvaldo M. Querin
Johann Sienz

International Conference on Numerical Optimisation Methods for Engineering Design



Proceedings of the 11th ASMO UK / ISSMO conference

Technische Universität München
Munich, Germany
July 18th – 20th, 2016

Edited by

Jens-Dominik Müller, Harvey Thompson, Fabian Duddeck
Vassili V. Toropov, Osvaldo M. Querin, Johann Sienz

Edited by:

Dr Jens-Dominik Müller, School of Engineering and Materials Science, Queen Mary University of London, Mile End Road, London, E1 4NS, UK, Tel: +44(0) 20 7882 5421, E-mail: j.mueller@qmul.ac.uk

Prof. Harvey M. Thompson, PhD, FHEA, FIMechE, Professor of Computational Fluid Dynamics School of Mechanical Engineering University of Leeds, Leeds, LS2 9JT, UK, Tel: +44(0)113 343 2136, E-mail: H.M.Thompson@leeds.ac.uk

Prof. Dr.-Ing. Fabian Duddeck, Technische Universität München (TUM), Aricsstrasse 21, D-80290 München, Germany, Tel: +49 (89) 289 28656, Email: duddeck@tum.de

Professor Vassili V. Toropov, Professor of Aerospace Engineering, Director of Centre for Simulation and Applied Mechanics Chair of Discipline Teaching Group Aero Engineering, Queen Mary University of London Mile End Road London E1 4NS, UK, Tel: +44 (0) 20 7882 6296, Email: v.v.toropov@qmul.ac.uk

Dr. Osvaldo M. Querin, School of Mechanical Engineering, The University of Leeds, Leeds LS2 9JT, UK Tel: +44 (0)113 343 2218, Fax: +44 (0)113 343 2150
E-mail: O.M.Querin@leeds.ac.uk

Professor Johann Sienz, School of Engineering, Swansea University, Swansea, SA2 8PP, Wales-UK, Tel: +44 (0)1792 295521, Fax : +44 (0)1792 295528
E-mail: J.Sienz@swansea.ac.uk

A copy of this publication has been deposited with the The British Library, Legal Deposit Office, Boston Spa, Wetherby, West Yorkshire, LS23 7BY, UK

First Edition, August 2017

ISBN: 978–085316–3480 (CD-ROM proceedings only)

Published by: ASMO-UK, University of Leeds, LS2 9JT, UK

Copyright © ASMO-UK and individual contributors, 2017. All rights reserved. No part of this publication may be produced, stored in a retrieval system, transmitted in any form or by any means electronic, mechanical, photocopying, recording or otherwise without either the prior written permission of the publisher or a license permitting restricted copying issued in the UK by the Copyright Agency and in the USA by The Copyright Clearance Center. No responsibility is accepted for the accuracy of the information contained in the text, illustrations or advertisements. The opinions expressed in the articles are not necessarily those of the Editors or of the publisher.

Association for Structural and Multidisciplinary Optimization in the UK (ASMO-UK)

Chairman:	Professor Vassili V. Toropov, Queen Mary University of London, UK
Secretary:	Dr. Osvaldo M. Querin, University of Leeds
Treasurer	Professor Johann Sienz, Swansea University
Past Chairman and EC member:	Professor Peter Bartholomew, QinetiQ, UK
Other Executive Committee (EC) members:	John J. Doherty, Faculty of Engineering & Physical Sciences, University of Surrey Professor Peter D. Gosling, University of Newcastle upon Tyne Professor Royston D Jones, Altair Engineering Ltd, UK Dr. Shahrokh Shahpar, Rolls-Royce, UK Professor Peter Bartholomew, QinetiQ, UK
Founding Chairman:	Professor Ernest Hinton (1946 - 1999)
Web Address:	http://www.asmo-uk.com/

International Society of Structural and Multidisciplinary Optimization (ISSMO)

President:	Professor Gengdong Cheng, Dalian University of Technology, China
Vice-Presidents:	Professor Pierre Duysinx, University of Liège, Belgium Professor Yoon Young Kim, Seoul National University, Korea
Secretary General:	Professor James K. Guest, Johns Hopkins University, USA
Treasurer	Professor Erik Lund, Aalborg University, Denmark
Past President	Professor Ole Sigmund, Technical University of Denmark, Denmark
Past Sec. General:	Professor Helder C. Rodrigues, Instituto Superior Técnico, Portugal
Other Executive Committee members:	Professor Wei Chen, Northwestern University, USA Professor Nam-Ho Kim, University of Florida, USA Dr. Ming Zhou, Altair Engineering, USA
Founding President and EC member:	Professor George I.N. Rozvany, Budapest University of Technology and Economics
Web Address:	http://www.issmo.net/

Organisation of the Conference

General Conference Secretary

Prof. Fabian Duddeck

Local Organising and Paper Committee

Dr Jens-Dominik Müller, Prof. Fabian Duddeck, Prof. Harvey Thompson, Daniel Baumgärtner, Anna Arsenyeva

Organising Committee

Dr. Osvaldo M. Querin, Prof. Vassili V. Toropov and Prof. Johann Sienz

Scientific Committee

Prof. Fabian Duddeck	(Technische Universität München, DE)
Dr Laurent Hascoët	(INRIA, Sophia Antipolis, FR)
Dr Rob Hewson	(Imperial College, London, UK)
Dr Marcus Meyer	(Rolls Royce, Dahlewitz, DE)
Dr Jens-Dominik Müller	(Queen Mary University of London, UK)
Prof. Uwe Naumann	(RWTH Aachen University, DE)
Dr Carsten Othmer	(Volkswagen, AG, Wolfsburg, DE)
Prof. Harvey Thompson	(University of Leeds, UK)
Prof. Vassili Toropov	(Queen Mary University of London, UK)
Prof. Tom Verstraete	(Queen Mary, University of London, UK)

Sponsor

We gratefully acknowledge the support of the following institution:



The AMEDEO Initial Training Network

The future development of environment-friendly aircraft complying with recent European directives and research objectives (e.g. ACARE 2020 Vision, ACARE Beyond 2020 Vision) will be based on a systematic, model-based process where Multidisciplinary Design Optimisation (MDO) will be a key enabling technology. This has been clearly stated in Flightpath 2050: Europe's Vision for Aviation. The goal of MDO is to coordinate the individual disciplines affecting the design (e.g. aerodynamics, structural mechanics, acoustics etc) toward a system design that is optimal as a whole, taking into account the key interactions between disciplines as well as competing objectives.

Over the last four years the AMEDEO (Aerospace Multidisciplinarity-Enabling Dsign Optimisation) Initial Training Network (<http://www.amedeo-itn.eu>) has brought together academic and industrial experts from across Europe, including leading universities, research organisations, multi-nationals and innovative SMEs, to develop innovative MDO methods that can be used by Europe's aerospace industry to design new generations of energy-efficient aircraft. We are delighted that the 11th ASMO-UK/ISSMO/NOED2016 conference is providing us with an excellent opportunity to showcase our research achievements and highlight the future research challenges for the wider optimisation community. The AMEDEO team are looking forward to many interesting discussions with optimisation colleagues to stimulate future research collaborations and transfer knowledge and expertise across the wide range of industry sectors represented at the conference.

Professor Harvey Thompson, University of Leeds, UK, Coordinator of AMEDEO.

The AboutFlow Initial Training Network

Adjoint-based methods have become the most interesting approach in CFD optimisation due to their low computational cost compared to other approaches. The development of adjoint solvers has seen significant research interest, and a number of EC projects on adjoint-based optimisation have been funded. In particular, partners of this proposal are members of the EC FP7 project FlowHead which has developed complete adjoint-based methods for steady-state flows in automotive design.

The project addressed integration of the currently available shape and topology modification approaches with the gradient-based optimisation approach, in particular development of interfaces to return the optimised shape into CAD for further design and analysis, an aspect that currently requires manual interpretation by an expert user.

Most industrial flows have small levels of instability, which leads to a lack of robustness and instability in the adjoint, such as trailing edge vortex shedding in turbo-machinery. Many industrial applications are also partly unsteady such as bluff body separation in cars or fully unsteady such as vertical-axis wind turbines.

In unsteady adjoints' 'checkpoints' of the flow solution at previous timesteps need to be recorded and algorithms for an effective balance between storage and recomputation need to be implemented. This involves significant memory and runtime overheads, efficient methods to overcome this are developed and implemented.

The methods developed in the project have been applied to realistic mid-size and large-scale industrial optimisation problems supplied by the industrial project partners ranging from turbo-machinery, to automotive to wind turbines.

About Flow is an Initial Training Network (ITN) funded by the European Commission running from November 2012 to October 2016. About Flow develops robust gradient-based optimisation methods using adjoint sensitivities for numerical optimisation of flows:

- Robust adjoint solvers with full second order accuracy and broad range of modelling capability
- Seamless integration of adjoint gradients into design chains
- Steady-state approaches with robust convergence, application of unsteady adjoints in industrial design

Dr Jens-Dominik Müller, Queen Mary, University of London, UK, Coordinator of AboutFlow

Page left intentionally blank

Contents

Editors	ii
Association for Structural and Multidisciplinary Optimization in the UK (ASMO-UK)	iii
International Society of Structural and Multidisciplinary Optimization (ISSMO)	iii
Organisation of the Conference	iv
Sponsor	v
The AMEDEO Initial Training Network	vi
The AboutFlow Initial Training Network	vii
Contents	viii
Author Index	x

Contributed Papers

Mohammed Aissa, Christopher Chahine, Anna Arsenyeva, Daniel Baumgärtner, Kai Uwe Bletzinger, Fabian Duddeck, Ipek Basdogan, Gokhan Serhat, Dmitri Bettebghor, Marco Bordogna, Gerald Carrier, Paul Lancelot, Andrea Viti, Roeland de Breuker, Kristofer Jovanov, Stefano Caloni, Gary Clayton, Shahrokh Shahpar, Sam Duckitt, Teun Weustink, Rob Hewson, Jonathan Ollar, Tim Surry, Julien Pohl, Harvey Thompson, Ralf Schlaps, Tom Verstraete and Vassili Toropov <i>Multidisciplinary Design Optimisation Research Contributions from the AMEDEO Marie Curie Initial Training Network</i>	1
Ruben Ansola, Alain Garaigordobil, Estrella Veguería and Osvaldo M. Querin <i>Sequential element rejection and admission method (SERA) for topology optimization using a constraint on Perimeter</i>	33
Anna L. Arsenyeva and Fabian Duddeck <i>Wingbox adaptive parametric modeling and its application to structural optimization</i>	40
Saeid Kazemzadeh Azad <i>Evaluating Sensitivity of Stochastic Search Techniques to Profile List Ordering in Discrete Sizing of Steel Frames</i>	46
Christopher Bach, Reda Jebari, Andrea Viti and Rob Hewson <i>A preliminary design method for optimizing composite forward-swept wings</i>	53
D. Baumgärtner, K.-U. Bletzinger, A. Vit and, A. Dumont <i>Node-based shape optimization in aircraft preliminary design</i>	62
Mariusz Bujny, Nikola Aulig, Markus Olhofer and Fabian Duddeck <i>Evolutionary Crashworthiness Topology Optimization of Thin-Walled Structures</i>	73
Christopher Chahine, Tom Verstraete and Li He <i>Multidisciplinary Design Optimization of Aero-Engine Fan Blades</i>	84
Kaspars Kalnins, Gints Jekabsons and Edgars Labans <i>Optimisation for scaling up of plywood sandwich panels with rigid PU foam-cores</i>	91
Paul Lancelot and Roeland De Breuker <i>Aeroelastic tailoring for gust load alleviation</i>	96

Julian Kajo Lüdeker and Benedikt Kriegesmann <i>Probabilistic Analysis of Topologically Optimized Structures Considering Geometric Imperfections</i>	108
David J. Munk, Gareth A. Vio, Timoleon Kipouros and Geoffrey T. Parks <i>Computational Design for Micro Fluidic Devices using a Tightly Coupled Lattice Boltzmann and Level Set Based Optimization Algorithm</i>	115
Jonathan Ollar, Royston Jones and Vassili Toropov <i>Incorporation of Bird Strike Requirements in MDO of an Aircraft Wing using Sub-space Metamodels</i>	130
Julien Pohl, Harvey M. Thompson, Vincenzo Fico and Gary A. Clayton <i>Turbine Stator Well Geometry Benefits - Method Validation and Design Optimisation</i>	143
Animesh Ranjan, Swami S Venkat, Romit Maulik and Flaviu Bogdan <i>Development of a ProcessWorkflow for Simulation of a Gas-Liquid Cyclone Separator with Uncertainty Quantification in an Open-Source Environment</i>	153
Gokhan Serhat and Ipek Basdogan <i>Effect of Aspect Ratio and Boundary Conditions on the Eigenfrequency Optimization of Composite Panels using Lamination Parameters</i>	160
A.Taftaf and L. Hascoët <i>Experiments on Checkpointing Adjoint MPI Programs</i>	169
Christos K. Vezyris, Evangelos M. Papoutsis-Kiachagias and Kyriakos C. Giannakoglou <i>Continuous Adjoint Method Using an Implicit, Block-Coupled Solver in OpenFOAM</i>	180

Author Index

A

Mohammed Aissa <i>Multidisciplinary Design Optimisation Research Contributions from the AMEDEO Marie Curie Initial Training Network</i>	1
Ruben Ansola <i>Sequential element rejection and admission method (SERA) for topology optimization using a constraint on Perimeter</i>	33
Anna L. Arsenyeva <i>Multidisciplinary Design Optimisation Research Contributions from the AMEDEO Marie Curie Initial Training Network</i>	1
<i>Wingbox adaptive parametric modeling and its application to structural optimization</i>	40
Nikola Aulig <i>Evolutionary Crashworthiness Topology Optimization of Thin-Walled Structures</i>	73

B

Christopher Bach <i>A preliminary design method for optimizing composite forward-swept wings</i>	53
Ipek Basdogan <i>Multidisciplinary Design Optimisation Research Contributions from the AMEDEO Marie Curie Initial Training Network</i>	1
<i>Effect of Aspect Ratio and Boundary Conditions on the Eigenfrequency Optimization of Composite Panels using Lamination Parameters</i>	160
Daniel Baumgärtner <i>Multidisciplinary Design Optimisation Research Contributions from the AMEDEO Marie Curie Initial Training Network</i>	1
<i>Node-based shape optimization in aircraft preliminary design</i>	62
Dmitri Bettebghor, <i>Multidisciplinary Design Optimisation Research Contributions from the AMEDEO Marie Curie Initial Training Network</i>	1
Kai Uwe Bletzinger <i>Multidisciplinary Design Optimisation Research Contributions from the AMEDEO Marie Curie Initial Training Network</i>	1
<i>Node-based shape optimization in aircraft preliminary design</i>	62
Flaviu Bogdan <i>Development of a ProcessWorkflow for Simulation of a Gas-Liquid Cyclone Separator with Uncertainty Quantification in an Open-Source Environment</i>	153
Marco Bordogna <i>Multidisciplinary Design Optimisation Research Contributions from the AMEDEO Marie Curie Initial Training Network</i>	1

Roeland de Breuker	
<i>Multidisciplinary Design Optimisation Research Contributions from the AMEDEO Marie Curie Initial Training Network</i>	1
<i>Aeroelastic tailoring for gust load alleviation</i>	96

Mariusz Bujny	
<i>Evolutionary Crashworthiness Topology Optimization of Thin-Walled Structures</i>	73

C

Stefano Caloni	
<i>Multidisciplinary Design Optimisation Research Contributions from the AMEDEO Marie Curie Initial Training Network</i>	1

Gerald Carrier	
<i>Multidisciplinary Design Optimisation Research Contributions from the AMEDEO Marie Curie Initial Training Network</i>	1

Christopher Chahine	
<i>Multidisciplinary Design Optimisation Research Contributions from the AMEDEO Marie Curie Initial Training Network</i>	1
<i>Multidisciplinary Design Optimization of Aero-Engine Fan Blades</i>	84

Gary Clayton	
<i>Multidisciplinary Design Optimisation Research Contributions from the AMEDEO Marie Curie Initial Training Network</i>	1
<i>Turbine Stator Well Geometry Benefits - Method Validation and Design Optimisation</i>	143

D

Fabian Duddeck	
<i>Multidisciplinary Design Optimisation Research Contributions from the AMEDEO Marie Curie Initial Training Network</i>	1
<i>Wingbox adaptive parametric modeling and its application to structural optimization</i>	40
<i>Evolutionary Crashworthiness Topology Optimization of Thin-Walled Structures</i>	73

Sam Duckitt	
<i>Multidisciplinary Design Optimisation Research Contributions from the AMEDEO Marie Curie Initial Training Network</i>	1

A. Dumont	
<i>Node-based shape optimization in aircraft preliminary design</i>	62

F

Vincenzo Fico	
<i>Turbine Stator Well Geometry Benefits - Method Validation and Design Optimisation</i>	143

G

Alain Garaigordobil	
<i>Sequential element rejection and admission method (SERA) for topology optimization using a constraint on Perimeter</i>	33

Kyriakos C. Giannakoglou	
<i>Continuous Adjoint Method Using an Implicit, Block-Coupled Solver in OpenFOAM</i>	180

H

L. Hascoët	
<i>Experiments on Checkpointing Adjoint MPI Programs</i>	169

Li He	
<i>Multidisciplinary Design Optimization of Aero-Engine Fan Blades</i>	84

Rob Hewson	
<i>Multidisciplinary Design Optimisation Research Contributions from the AMEDEO Marie Curie Initial Training Network</i>	1
<i>A preliminary design method for optimizing composite forward-swept wings</i>	53

J

Reda Jebari	
<i>A preliminary design method for optimizing composite forward-swept wings</i>	53

Gints Jekabsons	
<i>Optimisation for scaling up of plywood sandwich panels with rigid PU foam-cores</i>	91

Royston Jones	
<i>Incorporation of Bird Strike Requirements in MDO of an Aircraft Wing using Sub-space Metamodels</i>	130

Kristofer Jovanov	
<i>Multidisciplinary Design Optimisation Research Contributions from the AMEDEO Marie Curie Initial Training Network</i>	1

K

Kaspars Kalnins	
<i>Optimisation for scaling up of plywood sandwich panels with rigid PU foam-cores</i>	91

Saeid Kazemzadeh Azad	
<i>Evaluating Sensitivity of Stochastic Search Techniques to Profile List Ordering in Discrete Sizing of Steel Frames</i>	46

Timoleon Kipouros	
<i>Computational Design for Micro Fluidic Devices using a Tightly Coupled Lattice Boltzmann and Level Set Based Optimization Algorithm</i>	115

Benedikt Kriegesmann	
<i>Probabilistic Analysis of Topologically Optimized Structures Considering Geometric Imperfections</i>	108

L

Edgars Labans	
<i>Optimisation for scaling up of plywood sandwich panels with rigid PU foam-cores</i>	91
Paul Lancelot	
<i>Multidisciplinary Design Optimisation Research Contributions from the AMEDEO Marie Curie Initial Training Network</i>	1
<i>Aeroelastic tailoring for gust load alleviation</i>	96
Julian Kajo Lüdeker	
<i>Probabilistic Analysis of Topologically Optimized Structures Considering Geometric Imperfections</i>	108
M	
Romit Maulik	
<i>Development of a ProcessWorkflow for Simulation of a Gas-Liquid Cyclone Separator with Uncertainty Quantification in an Open-Source Environment</i>	153
David J. Munk	
<i>Computational Design for Micro Fluidic Devices using a Tightly Coupled Lattice Boltzmann and Level Set Based Optimization Algorithm</i>	115
O	
Markus Olhofer	
<i>Evolutionary Crashworthiness Topology Optimization of Thin-Walled Structures</i>	73
Jonathan Ollar	
<i>Multidisciplinary Design Optimisation Research Contributions from the AMEDEO Marie Curie Initial Training Network</i>	1
<i>Incorporation of Bird Strike Requirements in MDO of an Aircraft Wing using Sub-space Metamodels</i>	130
P	
Evangelos M. Papoutsis-Kiachagias	
<i>Continuous Adjoint Method Using an Implicit, Block-Coupled Solver in OpenFOAM</i>	180
Geoffrey T. Parks	
<i>Computational Design for Micro Fluidic Devices using a Tightly Coupled Lattice Boltzmann and Level Set Based Optimization Algorithm</i>	115
Julien Pohl	
<i>Multidisciplinary Design Optimisation Research Contributions from the AMEDEO Marie Curie Initial Training Network</i>	1
<i>Turbine Stator Well Geometry Benefits - Method Validation and Design Optimisation</i>	143
Q	
Osvaldo M. Querin	
<i>Sequential element rejection and admission method (SERA) for topology optimization using a constraint on Perimeter</i>	33

R

Animesh Ranjan

<i>Development of a ProcessWorkflow for Simulation of a Gas-Liquid Cyclone Separator with Uncertainty Quantification in an Open-Source Environment</i>	153
--	-----

S

Ralf Schlaps

<i>Multidisciplinary Design Optimisation Research Contributions from the AMEDEO Marie Curie Initial Training Network</i>	1
--	---

Gokhan Serhat

<i>Multidisciplinary Design Optimisation Research Contributions from the AMEDEO Marie Curie Initial Training Network</i>	1
<i>Effect of Aspect Ratio and Boundary Conditions on the Eigenfrequency Optimization of Composite Panels using Lamination Parameters</i>	160

Shahrokh Shahpar

<i>Multidisciplinary Design Optimisation Research Contributions from the AMEDEO Marie Curie Initial Training Network</i>	1
--	---

Tim Surry

<i>Multidisciplinary Design Optimisation Research Contributions from the AMEDEO Marie Curie Initial Training Network</i>	1
--	---

T

A.Taftaf

<i>Experiments on Checkpointing Adjoint MPI Programs</i>	169
--	-----

Harvey M. Thompson

<i>Multidisciplinary Design Optimisation Research Contributions from the AMEDEO Marie Curie Initial Training Network</i>	1
<i>Turbine Stator Well Geometry Benefits - Method Validation and Design Optimisation</i>	143

Vassili Toropov

<i>Multidisciplinary Design Optimisation Research Contributions from the AMEDEO Marie Curie Initial Training Network</i>	1
<i>Incorporation of Bird Strike Requirements in MDO of an Aircraft Wing using Sub-space Metamodels</i>	130

V

Estrella Veguería

<i>Sequential element rejection and admission method (SERA) for topology optimization using a constraint on Perimeter</i>	33
---	----

Swami S Venkat

<i>Development of a ProcessWorkflow for Simulation of a Gas-Liquid Cyclone Separator with Uncertainty Quantification in an Open-Source Environment</i>	153
--	-----

Tom Verstraete

<i>Multidisciplinary Design Optimisation Research Contributions from the AMEDEO Marie Curie Initial Training Network</i>	1
<i>Multidisciplinary Design Optimization of Aero-Engine Fan Blades</i>	84

Christos K. Vezyris	
<i>Continuous Adjoint Method Using an Implicit, Block-Coupled Solver in OpenFOAM</i>	180

Gareth A. Vio	
<i>Computational Design for Micro Fluidic Devices using a Tightly Coupled Lattice Boltzmann and Level Set Based Optimization Algorithm</i>	115

Andrea Viti	
<i>Multidisciplinary Design Optimisation Research Contributions from the AMEDEO Marie Curie Initial Training Network</i>	1
<i>A preliminary design method for optimizing composite forward-swept wings</i>	53
<i>Node-based shape optimization in aircraft preliminary design</i>	62

W

Teun Weustink,	
<i>Multidisciplinary Design Optimisation Research Contributions from the AMEDEO Marie Curie Initial Training Network</i>	1

Multidisciplinary Design Optimisation Research Contributions from the AMEDEO Marie Curie Initial Training Network

Mohammed Aissa and Christopher Chahine
Von Karman Institute for Fluid Dynamics, Brussels, Belgium

Anna Arsenyeva, Daniel Baumgärtner, Kai-Uwe Bletzinger and Fabian Duddeck
Technische Universität München, Germany

Ipek Basdogan and Gokhan Serhat
Koç University, Istanbul, Turkey

Dmitri Bettebghor, Marco Bordogna, Gerald Carrier, Paul Lancelot and Andrea Viti
ONERA, Paris, France

Roeland de Breuker and Kristofer Jovanov
Delft University of Technology, the Netherlands

Stefano Caloni, Gary Clayton and Shahrokh Shahpar
Rolls Royce PLC, Derby, UK

Sam Duckitt and Teun Weustink
ALE Ltd, Delft, Netherlands

Rob Hewson
Imperial College London, UK

Jonathan Ollar and Tim Surry
Altair Engineering, Royal Leamington Spa, UK

Julien Pohl and Harvey Thompson*
University of Leeds, Leeds, UK,

Ralf Schlaps, Tom Verstraete and Vassili Toropov,
Queen Mary, University of London, London

This paper reviews the key research activities and results produced during the AMEDEO (Aerospace Multidisciplinary-Enabling Design Optimisation) Marie Curie Initial Training Network (ITN). AMEDEO brought together optimisation researchers and practitioners from European universities, research organisations, multinationals and SMEs to develop innovative Multidisciplinary Design Optimisation (MDO) methods for the design of energy-efficient aircraft. A range of new results are presented in the areas of: 1) efficient High Performance Computing techniques for MDO, 2) efficient metamodel-based robust MDO frameworks, 3) the application of advanced MDO methods to aircraft engine design and 4) novel applications of MDO to the design of composite aeronautical structures. The future challenges that need to be overcome to embed MDO methods more effectively within commercial design cycles in the aerospace industry are also briefly discussed.

I. Introduction

Aviation is facing a critical challenge of meeting the growing demand for air travel while reducing significantly its impact on the environment. The future development of environment-friendly aircraft complying

* Corresponding author, H.M.Thompson@leeds.ac.uk

with recent European directives and research objectives (e.g. ACARE 2020 Vision [1]; ACARE Beyond 2020 Vision [2]) will be based on a systematic, model-based process where Multidisciplinary Design Optimisation (MDO) will be a key enabling technology. The recent EU document, *Flightpath 2050: Europe's Vision for Aviation* [3] predicts that by 2050 'multidisciplinary design and development tools are used routinely and co-operatively to support a high level of integrated system design'. The goal of MDO is to coordinate the individual disciplines affecting the design (e.g. aerodynamics, structural mechanics, acoustics, etc...) toward a system design that is optimal as a whole, taking into account the key interactions between disciplines as well as competing objectives. Unlike traditional sequential single discipline design optimisation approaches, MDO aims to avoid the generation of sub-optimal solutions due to poor balancing in the design process, which are too costly to remedy later in the design cycle.

Multidisciplinary analysis and optimisation methods were first used in the US to optimise complex aerospace systems and products [4] and are now a critical aerospace technology within Europe. Several MDO methodologies have been proposed, ranging from relatively straightforward (All-At-Once and Individual Discipline Feasible [5], Multiple-Discipline feasible [6]) to those aiming to partition large optimisation problems into a set of sub-problems where a coordination algorithm drives the sub-problem designs towards an optimal solution for the overall system. Promising decomposition methods include Bi-Level Integrated System Synthesis (BLISS) and its variants, Collaborative Optimisation and Analytical Target Cascading [7-9].

Since computational costs in MDO can be prohibitive, meta-models (also known as surrogate or response surface models) can reduce the computational effort. These replace the computationally expensive simulation model by an approximate one, which is then used in optimisation. Another challenging MDO problem, that is particularly relevant to energy efficient aerospace vehicles, arises in lightweight composite materials where the design variables describing the composite lay-up belong to discrete sets (integer number of plies, discrete set of ply orientations) where shape variables are continuous. Several requirements have to be satisfied, including ply continuity maximisation (also termed composite blending). Several bi-level strategies have been proposed [10] where the top level continuous optimisation is performed at the structure level by fast gradient-based techniques, and a stacking sequence optimisation at the local level is performed by evolutionary algorithms. It is also important to ensure that an aircraft performs consistently as desired [11], so that robust MDO frameworks are required. Some of the important approaches to such problems include metamodel-assisted stochastic optimisation and/or use of polynomial chaos expansions accompanied by advances in High Performance Computing [12]. The reader is referred for further details to the recent review of Martins & Lambe [13], which provides an introduction to MDO for non-specialists together with a description and classification of the most popular MDO architectures.

Over the last four years the AMEDEO (Aerospace Multidisciplinary-Enabling DEsign Optimisation) Initial Training Network (ITN) [14] has brought together optimisation researchers and practitioners from European universities, research organisations, multinationals and SMEs to create a unique cohort of highly trained early stage researchers to develop innovative MDO methods for the design of energy-efficient aircraft. This paper reviews briefly some of the important scientific achievements of the AMEDEO ITN over the last four years and reflects on the future challenges that need to overcome to embed MDO methods more effectively within commercial design cycles in the aerospace industry.

II. The AMEDEO Research Projects

The AMEDEO network includes four universities (Technische Universität München, Germany (TUM); Technische Universiteit Delft, Netherlands (TUD); Koç University, Turkey (KU), and the University of Leeds, UK, (UoL, the Coordinator of AMEDEO)), five technology-focussed companies operating in the aerospace industry (Rolls Royce PLC, Derby, UK (RR); Airbus, France; Altair, UK; ALE Ltd, Netherlands; SFE GmbH, Germany) and two research and technology organisations (ONERA, France; Von Karman Institute, Belgium (VKI)). The scientific work was organised into four broad Scientific Work Packages (SWPs), which are described briefly below. The research collaborations and Early Stage Researcher (ESR) working on each project are highlighted in brackets after the project title.

SWP1: New computational and parametrisation methods for large-scale MDO problems

This Scientific Work Package addresses the need to improve the computational efficiency of optimisation methods in order that the largest possible design space can be explored in feasible timescales.

Project 1: Efficient High Performance Computing Techniques for Multi-disciplinary Optimisation (ESR: Mohammed Aissa, VKI; RR)

MDO methods require highly efficient computational methods so that several solutions of the governing discipline equations (fluids, solids, heat transfer etc) can be obtained in feasible timescales. This project explored the potential of GPU (Graphical Processing Unit) techniques for large-scale MDO problems since the computational costs associated with CPU-based solvers for MDO methods are currently prohibitive and form a bottleneck in the optimisation process. At the start of the project, an automated optimisation framework called

CADO, using Computational Fluid Dynamics (CFD) and Computational Stress Analysis (CSM), already existed at VKI and proved to be very efficient in compressor and turbine optimisation. The CSM evaluation was very computationally efficient, whereas the CFD evaluation was much slower. This project aimed to exploit the power of GPUs to accelerate the CFD evaluations and thus to accelerate the entire CADO procedure.

During the first half of the project the CADO software was examined in detail, together with the performance of the existing CPU-based CFD solver. Two main problems were identified, the first being slow convergence for complex test cases such as compressor blade cascades and turbine cascades. This was due to the pressure interpolation on the mesh boundaries of the blade surfaces, required to represent flow in the viscous boundary layer. A higher order interpolation and multi-grid acceleration techniques were used to improve convergence. These changes allowed the number of iterations to be reduced by between a factor of 2 and a factor of 3.

The next step was to port the CPU-based Euler CFD solver to the GPU. The Euler solver was chosen as a less complex alternative to Navier-Stokes solvers which would still enable the performance of the GPU to be tested. The results of this work were published as a VKI Symposium paper in 2014 [15]. The GPU-based Euler solver was then extended to solve the Navier-Stokes equations. At this stage, the GPU code had a speed up of only 1x to 2x.

Following a secondment to the University of Leeds, and following consultations with a PhD student, Nic Delbosc, significant speed ups of up to 28x faster than the CPU-based solver was achieved by optimising the number of user threads (computation units) increasing the active portion of the GPU card [16]. Since the GPU provides a limited number of registers for memory storing the code has been adapted to use less memory and sometimes it was found that it was faster to re-compute some variables than to store them, as is usual for CPU programming. Further speed up was achieved by examining the data exchange with the CPU. This exchange was minimised by running all the solver routines on the GPU, even the less adapted ones like the update of the mesh block interfaces. The GPU interface update does not rely on data stored on the CPU but instead made use of a lookup table sorting the cell face connections throughout the faces that are created only once, at the beginning of the simulation. The final GPU code optimisation considered the use of multi-streaming that allows many GPU functions to be run simultaneously. For a multi-block mesh, the multi-streaming feature allows the computation of all the mesh blocks at the same time. Without multi-streaming all GPU functions run on a standard single stream in a serial way, one function after another. Further details of the GPU RANS solver are available in the parCFD conference paper given in May 2015 in Montreal [17].

The final part of the project focussed on improving the efficiency of the CADO multi-disciplinary optimisation framework. CADO's modular design means that the CFD solver can be changed easily. The GPU-based CFD solver was implemented within the CADO framework and then tested on a transonic compressor cascade, which achieved a 25% reduction in entropy generation 23-times faster than when the CPU-based solver is used within CADO. This work is described in greater detail in a conference paper at the ICNAAM conference in Greece in September 2015 [17].

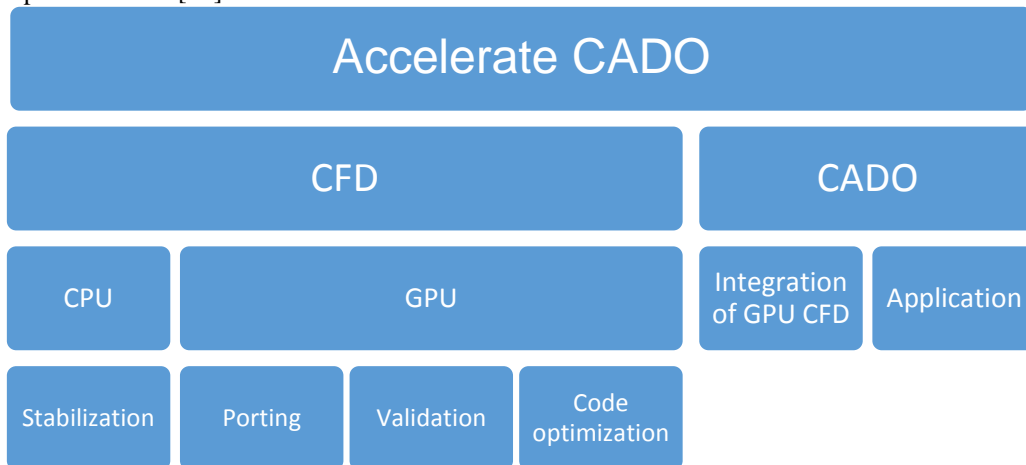


Figure 1.1: Chart of the strategy used to accelerate CADO showing tasks, subtasks and undertaken actions.

The application of the GPU-accelerated CFD codes for the aerodynamic performance evaluation of the annular stator geometry of the TurboLab Stator test case was reported at the 11th ASMO-UK/ISSMO/NOED2016 conference in Munich [17]. The TurboLab is a low Mach number compressor stator from the Technical University Berlin which is used to turn the inlet swirling flow into an axial outflow with a minimal total pressure loss. The stator was parametrized using common turbomachinery blade parameters such as chord length, chordwise blade metal angle distributions and thickness distributions on several spanwise blade sections. Lean and sweep are applied as three dimensional design features. The goal of the optimisation was to minimise the pressure loss and

improve the axial outflow. 21 design variables were used for the optimisation namely: 9 for the metal angle distribution for the camberline, 2 for the thickness distribution, 6 for lean and sweep and 4 for the hub contouring.

The core components of the optimisation system were the multi-objective Differential Evolution algorithm, a database, several metamodels and a high fidelity evaluation chain. The evaluation chain comprised a fully automatic geometry and CAD generation, an automatic meshing and a high-fidelity performance evaluation using CFD. CFD evaluation was carried out using two solvers: FIME™ (<http://www.numeca.com/product/fineturbo>) a commercial RANS solver from Numeca with explicit time stepping and an in-house CFD solver with GPU acceleration and implicit time-stepping. The GPU accelerated steady RANS solver followed a special discretization based on Finite Volumes and convective fluxes were calculated using a Roe upwind approximation while second order accuracy was achieved through the MUSCL approach. Viscous fluxes were approximated following a central discretization scheme and the source term contained a contribution from the Spalart-Allmaras (SA) one-equation turbulence model. Time integration was performed using a 3 stages implicit Runge-Kutta first order scheme. The commercial solver has a similar space discretization with a low Mach number preconditioning of the right hand side. The time integration differs also since FINE™ uses the explicit time stepping multistage Runge-Kutta scheme. For both solvers total quantities are imposed at the inlet along with the flow direction and the mass flow is imposed at the outlet. The total pressure loss is calculated in terms of the Loss = $(p_{01}-p_{02})/(p_{01}-p_1)$. The area averaged axial deviation is also provided.

The first objective of the optimisation was to reduce the total pressure loss and the second objective was to reduce the deviation of the outflow as the integral of the whirl angle squared. Optimisation was carried out around 3 operating points with whirl angles of -47, -42 and -37 degrees. The first operating point with the nominal whirl angle had a weight of 0.5 for the optimisation objectives while both other operating points each had a weight of 0.25. The constraints were of two types: CFD and manufacturing constraints. The CFD constraint concerned the mass flow of the full annulus, which had to be 9 kg/s with a tolerance of 0.1kg/s, and this was imposed as an outlet boundary condition. The manufacturing constraint took the form of a geometry check which fixed the number of blades, axial chord length and requirements on the blade thickness. The blade was required to be thick enough to have sufficient space for 2 cylinders of material fixed onto the hub and a shroud with a radius of 5mm and 20mm depth. The distance between the two holes was fixed at 60mm. Another constraint concerned the hub contouring for which the radius change was limited by -5mm and +10mm. This limit was introduced in the hub parametrisation restricting the vertical translation of the control points.

The objective space was populated with 198 CFD evaluations. All plotted designs satisfied both the aerodynamic and manufacturing constraints. Different points from the Pareto Front dominated the baseline designs. A trade-off had to be made for the selection of a design from the Pareto front but the design that was non-dominated by any other design achieved relatively small improvements of 0.07% and 6% in total pressure drop and outflow angle respectively.

Publications [15-23] were produced from this project.

Project 2: Multidisciplinary node-based shape optimisation for composite wing preliminary design (ESR: Daniel Baumgärtner, ALE; TUM, ONERA)

Designing a wing to reduce the fuel consumption of an aircraft implies reducing drag while increasing structural performance. The latter typically corresponds to a minimization of the structural weight which in modern aircraft gives rise to the use of lightweight composite components. Lightweight composite wing designs, however, are susceptible to dynamic aeroelastic phenomena (e.g. flutter) which significantly influence their drag characteristics. Therefore, to effectively minimize the fuel consumption, an optimal trade-off between structural and aerodynamic performance must be found. This can be accomplished by means of a multidisciplinary shape optimisation approach in general or an aeroelastic shape optimisation approach in particular.

This project focusses on development of a new, flexible shape optimisation method for aeroelastic optimisation in the early phase of wing design. The aim is to provide more design freedom and greater optimisation potential than existing formulations. It used a consistent node-based formulation in which the optimisation directly operates on the numerical model rather than using a restrictive parametrisation approach. The node-based approach used is the Vertex Morphing Method (WMM) originally developed at TUM. Computational aerodynamic shape optimisation has become a standard process in the preliminary design of an aircraft's external shape, and is driven by the need for a trade-off between exploring the design space with a minimum number of constraints so as not to restrict the range of potential improvements, while introducing as much design knowledge as possible to avoid costly modifications later in the design process. This project developed the WMM for wing preliminary design in particular and for aircraft preliminary design in general.

The project began by testing whether the WMM can optimise a coupled, multi-disciplinary problem. An efficient coupled adjoint sensitivity analysis was derived and tested on a flexible cylinder shell immersed in a laminar incompressible fluid flow, Figure 2.1. The goal was to optimise the shape of the cylinder such that it generates maximum lift while minimising the drag. This showed that the optimal shape for this problem is a modified 'cylinder' which in its deformed shape turns into an airfoil, Figure 2.2.

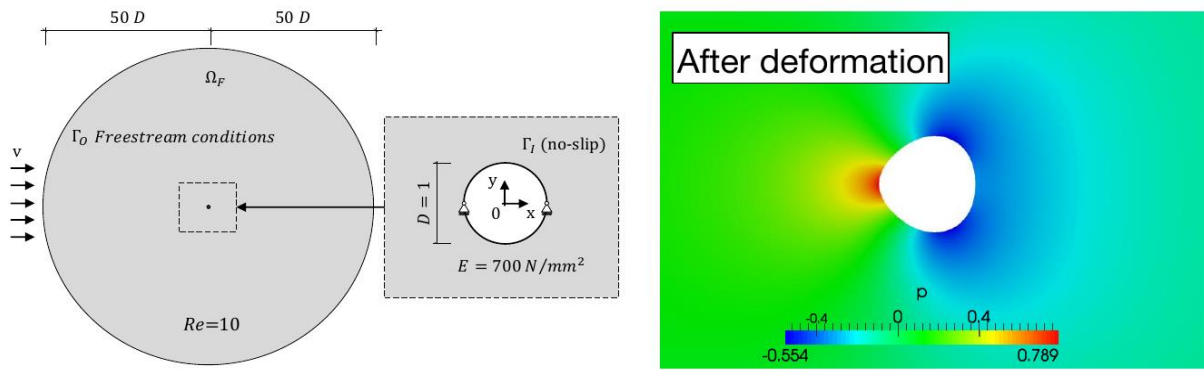


Figure 2.1: Node-based multidisciplinary shape optimisation– A generic test case

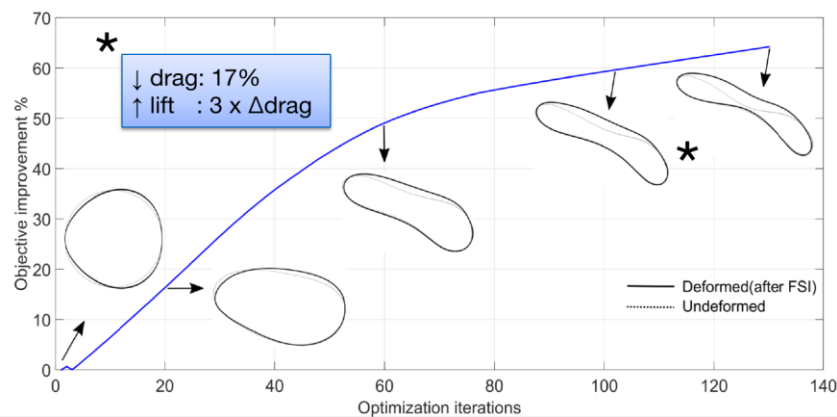


Figure 2.2: Shape evolution of flexible cylinder in laminar fluid flow during node-based multidisciplinary shape optimisation

This produced a new, more efficient and flexible but less accurate and more application dependent way of computing coupled sensitivities. It did, however, demonstrate that VMM showed good potential for both single disciplinary (aerodynamic) and multi-disciplinary (aeroelastic) problems.

The next stage was to apply the VMM to aircraft preliminary design. The first problem of interest was the aerodynamic shape optimization of a forward-swept wing aircraft. This required the development of a new algorithm for constrained optimisation and an extension of the surface sensitivity analysis. The new optimisation process was applied to find optimal shapes for the complete aircraft, including the wing, the fuselage and the attachment area of the wing to the fuselage. Generally, the optimal solutions represented 5-10% improvements compared to the previous state-of-the-art solutions. Figure 2.3 and Figure .4 show the design improvement for the wing and the inboard area around the wing attachment.

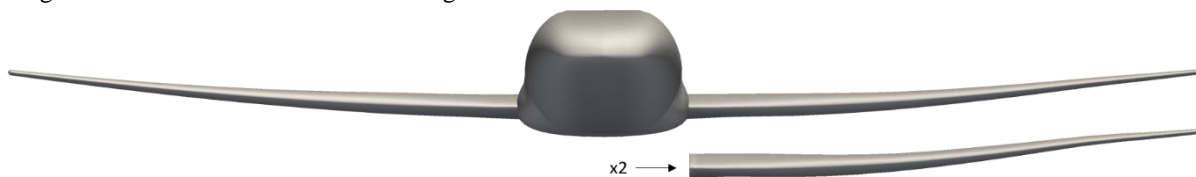


Figure 2.3: Comparison of baseline (left) and optimized (right) wing shape

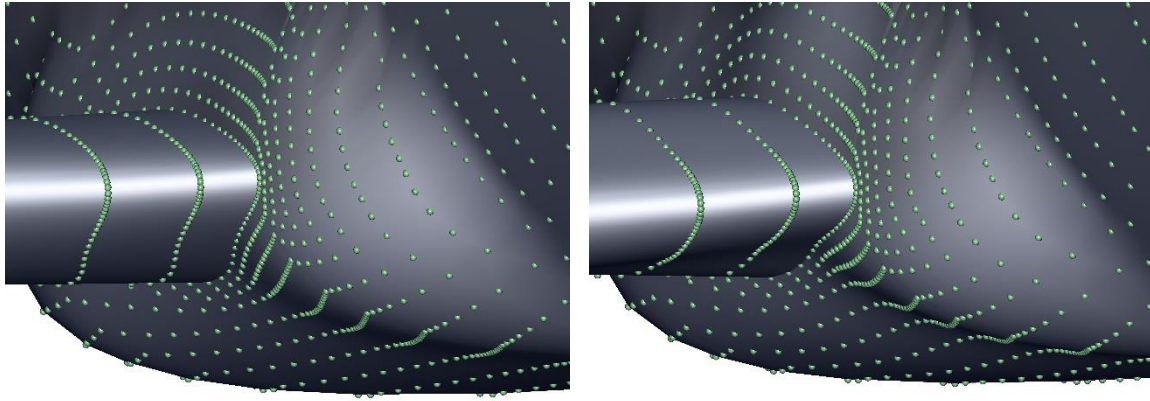


Figure 2.4: Inboard design before (left) and after optimization (right, design changes were scaled by x5). Points indicate surface nodes controlled during the optimization process.

Figure 2.5 shows the optimized surface pressure distribution. Significantly improved pressure gradients can be observed in particular inboard (reduced shocks). Overall, these results demonstrated that the VMM is a powerful alternative to traditional approaches in preliminary design.

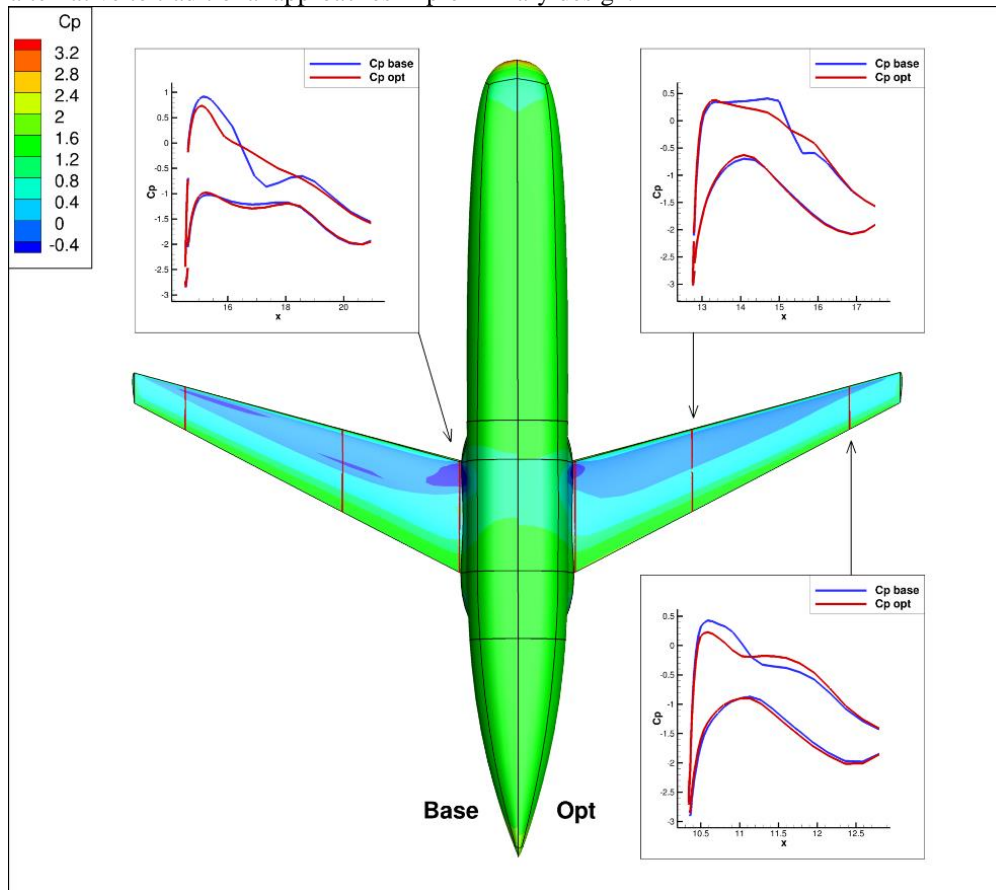


Figure 2.5: Pressure distribution at baseline (left) and optimized (right) design. Results correspond to some 21% improved drag at constant lift and constrained wing thickness.

In addition to being published in papers [24-27], all developments regarding the VMM were implemented in the open source multi-physics software, Kratos Multiphysics [28]. Any interested reader is able to test the process for their own applications.

The VMM-based optimisation method was then used to optimise the ONERA M6 benchmark wing at cruise conditions, where a flexible structure is considered. Correspondingly, the wing was modelled as a flexible shell whereas coupled sensitivities were neglected but a full fluid-structure interaction analysis was performed in every

optimisation step. The optimised wing finally performed roughly 30% better than the baseline design, see Figures 2.6 and 2.7.

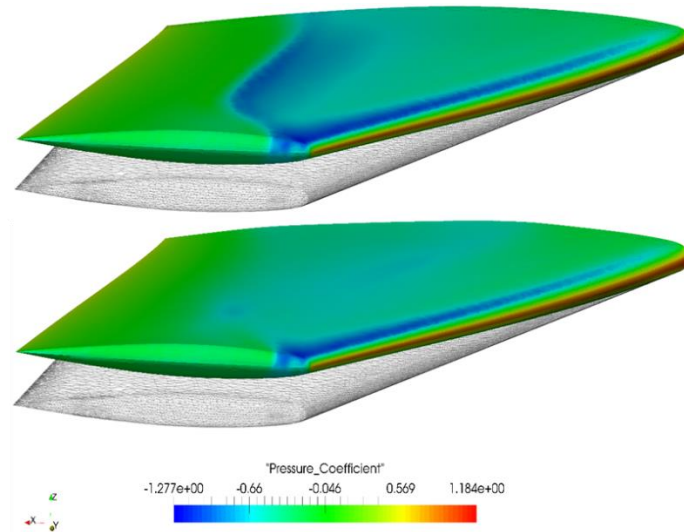


Figure 2.6: Initial (top) and optimized (bottom) pressure distribution at a flexible ONERA M6 wing. Black indicates the jig-shape. Results correspond to some 30% improved drag at constrained lift and thickness each in the deflected state.

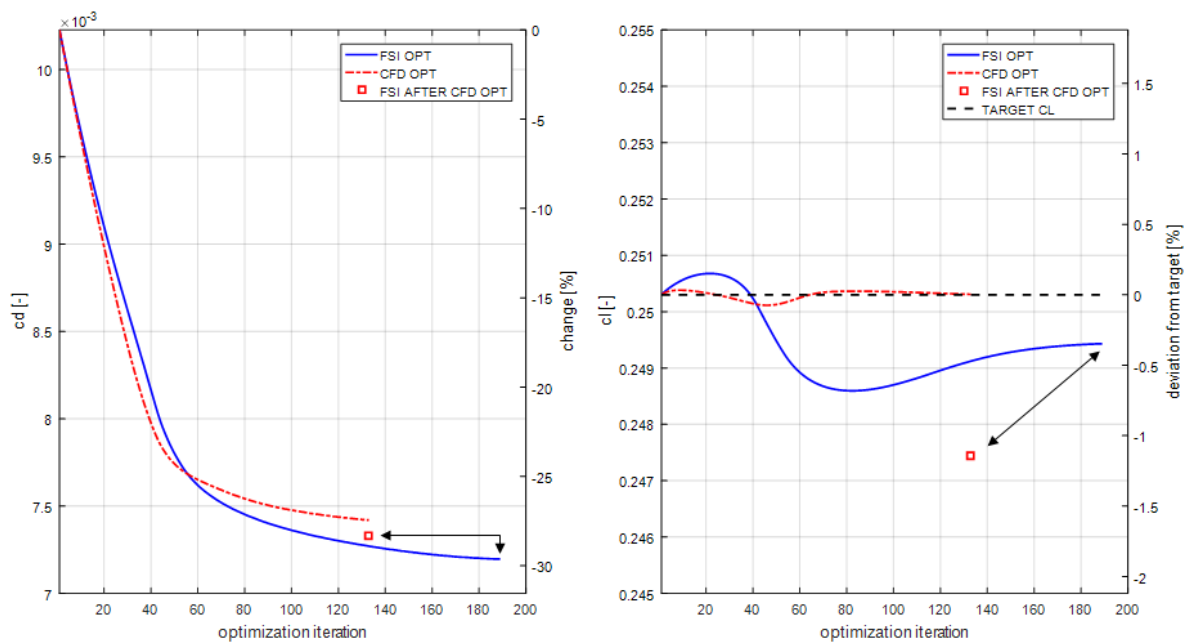


Figure 2.7: Comparison of a single disciplinary (CFD) and multidisciplinary (aeroelastic / FSI) node-based shape optimisation of the ONERA M6. Left diagram shows the drag coefficient as objective function and the right diagram shows the lift coefficient as constraint. Note that the FSI optimisation performs better in both cases.

In addition, the results demonstrated that this simplified aeroelastic optimisation without coupled sensitivities already outperforms a pure single disciplinary aerodynamic optimisation. Results regarding the node-based aeroelastic shape optimisation were published in [29]. This was the first published node-based aeroelastic (multidisciplinary) shape optimisation of a wing.

Project 3: A Unified Multidisciplinary Shape Optimisation Methodology for Composite Aircraft Structures (ESR: Anna Arsenyeva, TUM; ALE, TUD, SFE)

The general goal in aviation is that fuel efficiency should increase by 1.5% per year, and this target has stimulated lots of effort to reduce the weight of aircraft. This project focusses on the multidisciplinary optimisation

of composite aircraft structures, and the interplay between composite wing structural and aerodynamic optimisations. These consider shape and topology optimisation of the wing geometry and optimisation of the composite material structure. This means, for example, that the number of wing structure components (ribs, spars, etc.), as well as the number and orientation of the laminated composite layers can be changed during the optimisation, which leads to a mixed discrete-continuous design variables space. This requires special approaches to be employed for the optimisation.

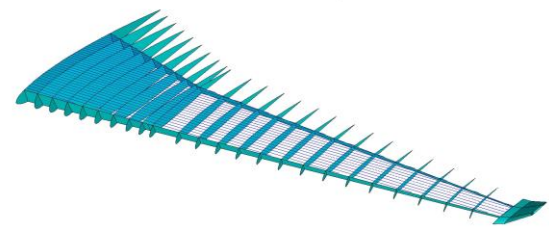
The initial objectives of the project were as follows:

- To create an adaptive wing box model for an arbitrary outer shell
- To develop an implicit geometry parameterisation for topology/shape optimisation of internal wing box components
- To include steered fibre composite materials optimisation into wing box design
- Optimisation of the developed parametric wing model

A flexible wingbox model which can be easily adapted to a given outer wing shell was developed with an implicit geometry parameterisation for the further subcomponent optimisations, easy automatic sub-modelling and load extraction for different wing box components. A steered-fibre composite materials optimisation for designing optimal composite wing box components was also developed.

The wing outer shell was created by using a set of NACA-type airfoils, which enable automatic changes of the global wing architecture by specific positioning of 2D airfoils in the 3D space. This project focussed on the internal structure optimisation, for the given wing outer shape. Parameters of the wing box such as number and location of ribs/spars/stringers, their shape and thickness, which may linearly vary along the length for skin and spars components are considered as the optimisation variables, see Figure 3.1.

Several types of loads are considered, including acceleration load, engine loads and aero loads. The aero loads can be calculated using ANSYS Fluent CFD or simplified XFOIL 2D code. The flow simulation is calculated for a fixed external shape and obtained pressure distribution is mapped automatically to existing structural model in ANSYS Mechanical. (Figure 3.2).



Possible shape of the stringers:

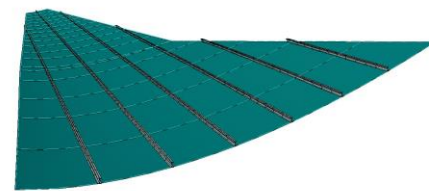


Figure 3.1: Ribs and spars definition (a), stringer components and its possible shape (b)

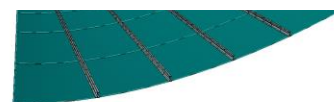


Figure 3.1: Ribs and spars definition (a), stringer components and its possible shape (b)

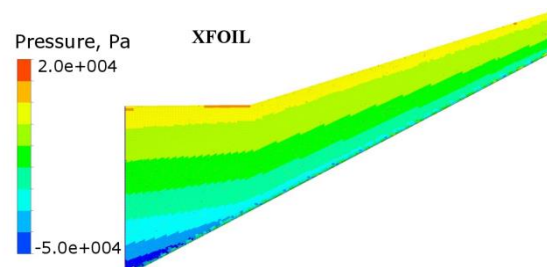
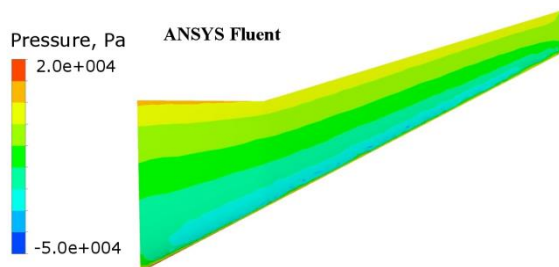


Figure 3.2: Pressure distribution for a wing obtained by ANSYS Fluent (left), XFOIL software (right).

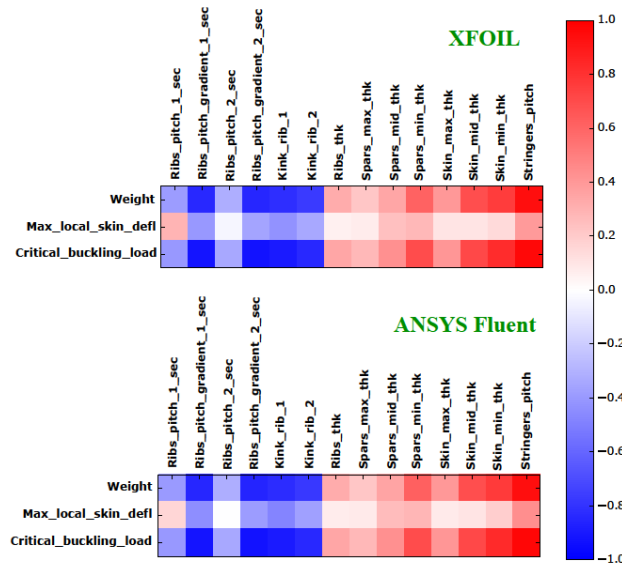


Figure 3.3: The resulting Spearman coefficient matrices: 300 designs

Spearman coefficient matrices for correlations between design parameters and resultants were obtained and good agreement with known wingbox design dependencies was achieved. Two numerical experiments, generated using Latin-Hypercube sampling within the coarse parameters, are performed for the models with XFOIL and ANSYS FLUENT. The resulting Spearman coefficient matrices for correlations between responses and the coarse design parameters are shown in Figure 3.3.

As can be seen XFOIL results give very similar correlations, compared to the results obtained for Fluent, meaning that it can at least capture general trends accurately. Considering that the XFOIL approach is much faster, compared to full CFD analysis, it can be used for the preliminary global optimization studies.

A two-stage approach for the wingbox parametrisation was used: at first, the spacing density of the ribs is described in each wing section as a linear function with two parameters. This helps to identify approximate ribs layout very fast (only 4 design parameters). At the second stage, the obtained rib positions can be varied, also allowing changing the rib angle individually, in order to refine to an optimal layout. The objective is to reduce the wing weight with constraints on maximum local skin deflection between each pair of ribs and also wing tip displacement, Figure 3.4.

For detailed optimisation of the ribs design, the special generic pattern model in the parametric space was created using the SFE CONCEPT software. Figure 3.5 shows an example of rib parametrisation and automatic connection to an external mesh. This pattern is capable of representing simplified topological optimal results for different ribs and can be automatically mapped to different rib shapes.

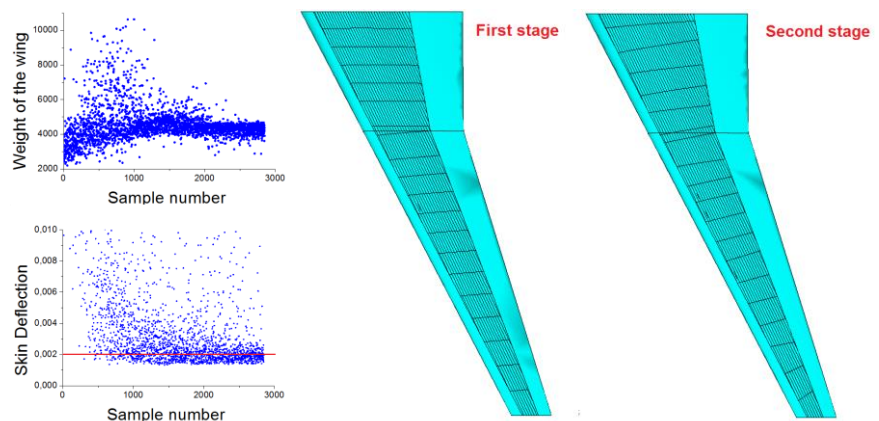


Figure 3.4. Convergence for skin deflection constraint (left), coarse model (middle) and refined optimization (right)

Another rib stiffeners parametrisation approach, well-suited for direct search methods (e.g. evolutionary algorithms), was proposed and implemented. It enabled topology-like shape optimisation to be performed, and to include various constraints within the optimisation (e.g. displacements, stresses, buckling, etc.), which is not possible in standard density-based topology optimisation. For similar optimisation tasks (stiffness maximization) this approach gives similar results to the topology optimisation, which was shown with various rib shape optimisations.

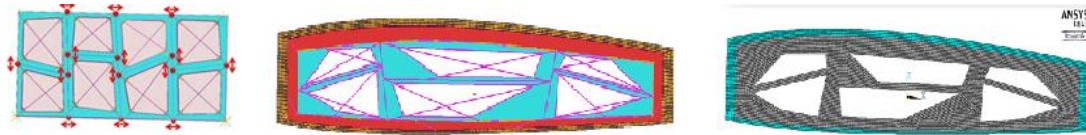


Figure 3.5: Generic parametric sub-model (left) SFE mapped geometry (middle) and mesh coupling with external mesh (right)

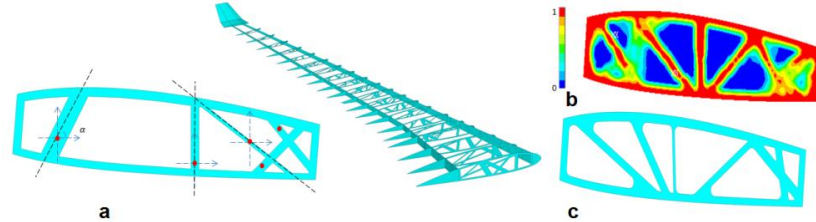


Figure 3.6: Example of Point-Angle-Width (a), Topology optimal result (b) and optimal result obtained by shape optimisation(c)

A new approach for fibre-steered composite optimisation was developed and evaluated. Here, the Maximum curvature constraint (MFCC) was added to the optimisation process and results were presented in a conference paper, where the method showed great capabilities of finding optimal fibre path. As an example, a 4-layer steered-fibre fuselage section with a window was optimised for higher buckling loads, see Figure 3.7.

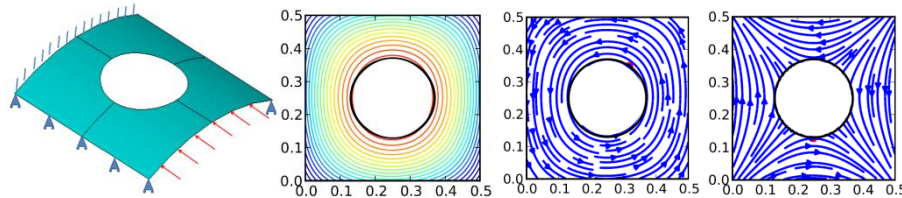


Figure 3.7: Problem example (left), optimal iso-lines obtained by 9 parameters (middle), optimal fibres placement for $[\pm\alpha]_s$ laminate with $MFCC = 10 \text{ m}^{-1}$ at each layer of laminate (right)

The method was applied successfully to fibre-steered rib optimisation. Results are compared with the topology optimisation in Figure 3.8.

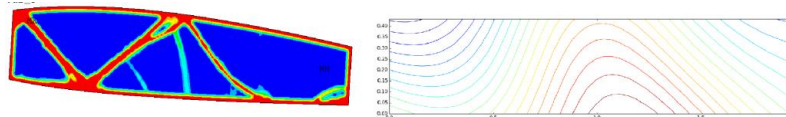


Figure 3.8: Results for two rib designs: topology optimisation (a), surface's iso-contour lines

Publications [30] and [31] resulted from this project. A journal paper on composite modelling and composite optimisation is now being prepared.

SWP2: Efficient metamodel-based robust MDO frameworks

Lightweight composite structures are making an increasingly important contribution to energy-efficient aircraft. This Scientific Work Package provides new approaches to complex composite optimisation problems where the design variables describing the composite lay-up belong to discrete sets (integer number of plies, discrete set of ply orientations) whereas shape variables are continuous.

Project 4: Cohesive Zone Modelling of Thermo-Mechanical Delamination Propagation and MDO in the framework of Isogeometric analysis (ESR: Sam Duckitt, ALE; TUD, TUM, RR)

A revised project description was accepted in February 2014; the new project aimed to model propagation of delamination in composite structures using Isogeometric Analysis (IGA), focussing on the optimal shape design of a composite fan blade subject to high velocity impact. It combines aspects of composite failure and isogeometric analysis within a complex MDO problem. The first objective was to link the SOPHY (SOFT+HYDRA+PADRAM) design system at Rolls Royce with LS-Dyna, as a means of including impact analysis and enable validation of the current design rules used at Rolls Royce for impact which could potentially lead to a lighter weight fan blade. The second objective was to utilize the benefits of IGA, directly comparing the results with those obtained from objective 1. IGA can not only provide increased accuracy with fewer degrees of freedom, it has the potential to dramatically reduce the time spent setting up a suitable computational mesh, which can account for up to 80% of the analysis time in industrial problems.

The majority of the first 2 years of the project were spent gaining experience with Isogeometric Analysis (IGA). A library of NURBS scripts were written in Matlab and used to implement a new parameterisation method within an isogeometric cohesive element for the simulation of composite failure. A NURBS model defined the blade surface into 4 separate surfaces: 1 each for the pressure and suction sides, and 1 each for the leading and trailing edges. This technique enables the user to define the number of control points of each surface as a means of controlling the number of elements in the 3D IGA model. After ensuring the surfaces have matching parametrisations, a separate routine was created to automatically insert interior control points to create a valid solid NURBS model suitable for IGA. This process has been automated to also include the generation of LS-Dyna input files so that it can be used in an optimisation framework.

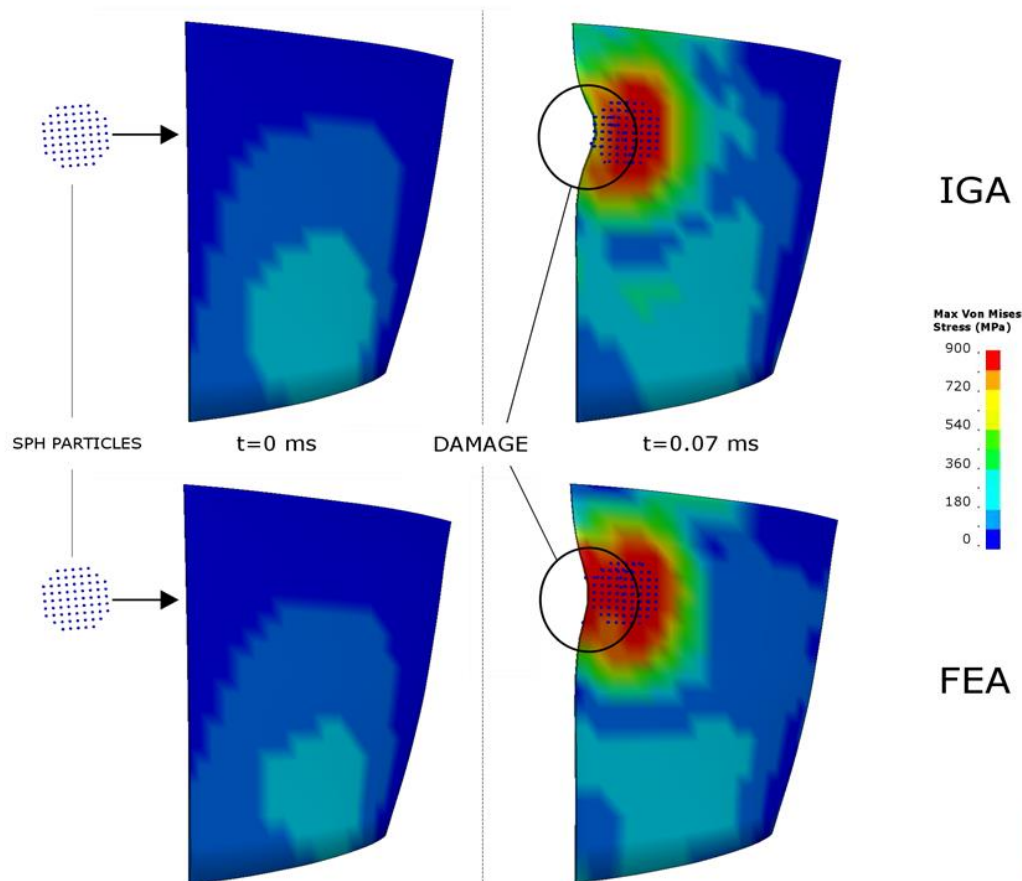


Figure 4.1: Maximum Von Mises Stress Plots for IGA (top) and FEA (bottom), (a) stress initialization before impact, (b) highest peak stresses after impact at $t=0.07$ ms.

An investigation was performed to validate the IGA approach against finite elements. Initial results were obtained for a centrifugally loaded blade before moving on to impact simulations achieved using the Smoothed Particle Hydrodynamics (SPH) method. Bird strike simulations were performed on the NASA rotor 37 geometry and this was the first time that solid NURBS elements had been used to simulate high velocity impact. The results were presented at the 2016 ASME Turbo Expo conference and a paper was included in the proceeding (GT2016-567464) [32]. Figure 4.1 shows a comparison between the maximum Von Mises stress distributions obtained from IGA and finite element bird strike simulations. The method is now being validated against experimental impact data which has become available at Rolls-Royce. It is planned to re-run this approach and validate against experimental data. With this addition there are plans to publish a subsequent journal paper on the subject.

A detailed investigation into the use of NURBS control points as design variables to facilitate an IGA centred approach to optimisation was also carried out. This resulted in a more efficient approach which can dramatically reduce the number of design variables. The concept is to use a smaller set of control points to approximate the true geometry. These control points are then perturbed during the optimisation which generates a displacement field. This displacement field can then be mapped onto the true geometry to create new designs with a much smaller set of design variables hence speeding up the optimisation. This approach was implemented successfully

for a simple 2D airfoil and a more complex 3D implementation on a stator blade surface. This approach is illustrated in Figure 4.2(a) for the simple 2D airfoil example.

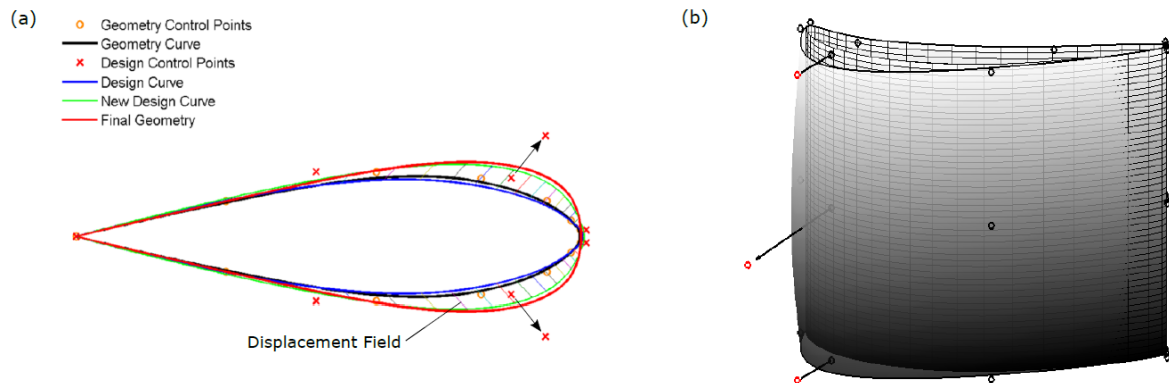


Figure 4.2: (a) 2D illustration of a B-spline parametrisation method and (b) perturbing a stator blade design by moving 3 control points (red).

The original airfoil geometry (black) is represented by 14 control points. This is then approximated by the blue curve which is defined with just 8 control points. Two of these ‘design’ control points are perturbed as indicated which generates the new green airfoil curve and an associated displacement field. This displacement field is then mapped and added to the original geometry which produces the final geometry (red). It can be seen that this is a far more efficient approach to generate new designs as opposed to using all of the original geometry control points as design variables.

Figure 4.2(b) demonstrates the 3D implementation on a stator blade surface and shows the design changes which can be achieved by moving 3 of the control points (red) close to the leading edge of the blade. This approach has now been implemented to work with the Rolls-Royce SOPHY system.

The final part of the revised project was to combine the new B-spline parametrisation method together with the IGA approach for impact analysis into an automated multi-disciplinary design optimisation framework. Work was also carried out to automate the generation of finite element models from PADRAM. A routine was written to automatically create LS-Dyna input files for solid finite element models. Having both IGA and finite element optimisation frameworks, the methods can be compared to see which is most efficient in terms of computational time. This project produced publications [32-34].

Project 5: Aeroelastic Tailoring of Composite Wings using Mixed Fidelity Modelling (ESR: Kristofer Jovanov, TUD; ONERA, ALE)

The overarching aim of this project was to combine multi-fidelity models for design of composite wings in order to reduce overall computation time. Industry standard low-fidelity models used in the conceptual design stages neglect important physical effects that typically emerge in the transonic flight regime. With the inception of high-fidelity models in the conceptual design stages an optimal design tailored for transonic flight will outperform the design generated by the use of low-fidelity models. This will improve the aerodynamic efficiency, reduce the overall weight and consequently reduce the fuel emissions.

Generating responses and gradients for aero-structural optimisation is very computationally intensive. This project investigated if it is possible to alleviate the computational burden for high-fidelity aero-structural analysis and sensitivity analysis in a gradient-based optimisation framework by introducing low-fidelity aerodynamic models for the aeroelastic responses. The idea is to minimise the number of high-fidelity function evaluations and consequently reduce the overall computing time.

The performance of several aerodynamic models has been investigated. Three levels of fidelity were established, the lowest being a Vortex Lattice Model (VLM), which solves a set of linear potential equations, the second a panel code PANAIR A352 solving similar linear equations but on an arbitrary 3D wing model, and the third, highest level of fidelity where the high fidelity Euler equations were solved using the open source CFD code SU² and the in-house Computational Fluid Dynamics tool from ONERA, elsA. The VLM code solves the linear potential flow equations and is thus limited to the subsonic flow regime. Shock-induced flow in the transonic regime was modelled by the solution of the Euler equations. The vortex lattice code was modified to enable an explicit formulation of the aerodynamic stiffness matrix, which were then used in the solution of the nonlinear aeroelastic problems for their efficient convergence abilities. The structural governing equations are solved using the finite element method (FEM) and the wing is discretized by a combination of shell, shear and bar elements

with multipoint constraint elements, see Figure 5.1.



Figure 5.1: Structured CFD model (left) and a structural Nastran-based model (right) of an ONERA M6 wing. Courtesy of ONERA.

Several techniques for solving the nonlinear aeroelastic equations together have been investigated. A nonlinear block Gauss-Seidel (NLBGS) method was implemented and augmented with a successive over-relaxation (SOR) scheme. The performance of the NLBGS method was enhanced by replacing the stationary relaxation factor with a dynamic relaxation factor, i.e. a relaxation factor that is updated for each iteration. This project used Aitken's delta method, which required only the displacement increments of previous iterations to update the relaxation factor.

The NLBGS scheme is one of the most popular methods for solving the high-fidelity steady-state aeroelastic problem. A major reason for this is its ability to preserve software modularity, i.e. it allows for established single-disciplinary solvers to be used in order to solve the coupled aeroelastic problem, however its performance is highly dependent on the value of the relaxation factor and has even been shown to diverge for problems with a strong fluid-structure coupling.

To further increase the convergence performance of the aeroelastic solver, Newton schemes were considered. These have second-order convergence rates and require inter-disciplinary gradient terms to form the aeroelastic Jacobian. These terms are not easy to acquire and can be prohibitively expensive for high-fidelity models. A multi-fidelity Newton (or quasi-Newton) scheme was therefore implemented where the low-fidelity aerodynamic model is used to form the interdisciplinary gradient terms. This methodology significantly increased the performance of the Newton schemes.

As mentioned above, the aeroelastic analysis is not sufficient for a gradient-based optimisation framework. Sensitivities need to be evaluated for the gradient-based optimizer to work properly. The methodology of computing gradients is analogous to the solution procedure of the static aeroelastic problem. The implementation costs are therefore minimal. A coupled link is established between the aerodynamic gradients in elsA and the structural gradients in Nastran. The sensitivities are then coupled using Matlab to solve the aero-structural sensitivity equations. Again, low-fidelity gradients from the VLM code are used to accelerate the solution of the high-fidelity sensitivity equations.

The goal of this project is to reduce the computational effort of high-fidelity aero-structural optimisation and make it an affordable instrument in the conceptual design stages. Industry standard low-fidelity models used in the conceptual design stages neglect important physical effects that typically emerge in the transonic flight regime. With the inception of high-fidelity models in the conceptual design stages an optimal design tailored for transonic flight will outperform the design generated by the use of low-fidelity models. This will improve the aerodynamic efficiency, reduce the overall weight and consequently reduce the fuel emissions.

At the end of this project, weight reduction optimisation was performed on a simplistic ONERA M6 wing model, where the objective was to reduce the weight during trimmed flight while not violating stress constraints. The design variables were the thicknesses of the structural members. This provides the groundwork for a later optimisation on a more realistic case, such as the NASA Common Research Model (CRM). This project produced publications [35-38].

Project 6: Conceptual Multidisciplinary Aircraft Design using Aero-Structural Adjoint-based Method (ESR: A. Viti, ONERA; Airbus, ICL)

Airlines and aircraft manufacturers face the key challenge of keeping fuel consumption down, while achieving ever better performance. Fuel consumption can be reduced through improvements in engine efficiency, aerodynamic performance, lightweight materials, etc. however these cannot be considered in isolation. This project addresses one of the most important trade-offs: aerodynamic vs structural performance in the preliminary design phase and develops an adjoint-based optimisation method which can identify the best aero-structural trade-off for new aircraft configurations.

A forward swept wing (FSW) has been analysed in detail. The geometry was generated by using an airfoil for the wing-fuselage interaction and the Euler equations were solved for the flow analyses, using an in-house ONERA code. A structural analysis code was also developed in order to determine the stresses on the internal structure wing elements. These were then coupled successfully into a fluid-structure coupled analysis which was tested for shock-free and fully-shocked cruise conditions. A comprehensive investigation on the coupling was carried out by analysing the effect of all the different parameters that play a role in the interaction analysis. A shock-free and a fully shocked cruise condition have been taken into consideration and a range of parametrisations were tested in order to provide the fastest and most reliable optimisation for the two cruise conditions. This clearly demonstrated the need for aero-elastic coupling, which is much more important for FSWs compared to classical wings.

The wing-body geometry was then generated and a comparison between an isolated wing case and a wing-body configuration performed. This demonstrated the benefits of having a full wing-body configuration even in preliminary design. In parallel, the in-house ONERA code InAirSsi was developed to handle the unconventional FSW configuration and the structure of the wing was then optimized for a typical certification load. The project then focussed on the wing-body configuration, on which substantial progress was made. The main achievements with the wing-body configuration were:

Aerodynamic and aero-elastic optimisation comparison for the wing-body configuration. A rigid aerodynamic optimisation of the flight shape is not consistent since this would mean that whenever the load changes during the optimisation, the structure is not updated to achieve aero-elastic equilibrium. This inconsistency would be particularly serious for a Forward Swept Architecture, although it is less important for a classical wing, see Figure 6.1.

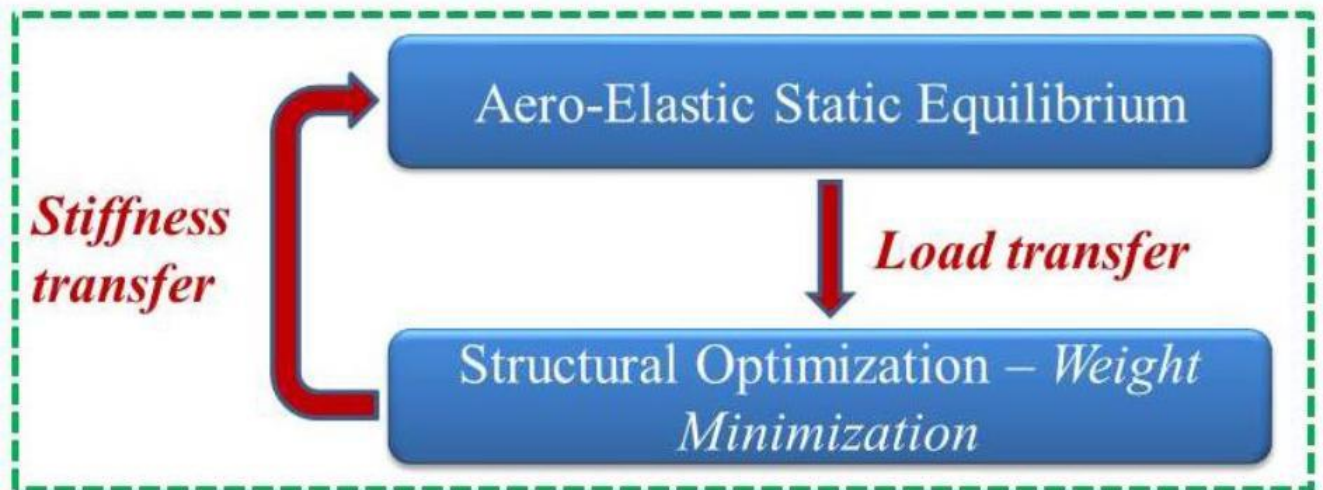


Figure 6.1: Structural optimisation at the aero-elastic equilibrium.

Development of consistent structural optimisation for the wing structure. Once the structural optimisation has been validated, a procedure for consistent structural optimisation was developed. The aerodynamic wing load was computed over time during the structural optimisation in order to have a load consistent with the new structural stiffness and wing deformation. This resulted in an iterative procedure that converges successfully to an optimized weight of the wing structure.

Mesh deformation procedure to handle wing planform change. A mesh deformation procedure to handle wing planform deformation has been developed. Starting from an in-house ONERA mesh deformation code, a procedure for global wing parameter mesh deformation was developed that is very useful for computing the sensitivity analysis of the configuration with respect to global wing shape parameters.

Sensitivity analysis for OAD top level optimisation. A procedure to compute the sensitivity of aerodynamic and structural wing characteristics with respect to top level global parameters that define the wing planform has been developed. Comparison between finite difference and adjoint method techniques for sensitivity analysis has been performed, the results of which have been used to improve the performance of the finite difference approach.

Collaborations with Airbus for OAD top level optimisation procedure. During a secondment in Airbus an Overall Aircraft Design procedure has been put in place. This has been completely developed and tested on conventional

and unconventional aircraft architectures. The analysis was presented during the AIAA Aviation conference in Washington, June 2016 [39]. The procedure is summarised in Figure 6.2.

Multidisciplinary Optimization

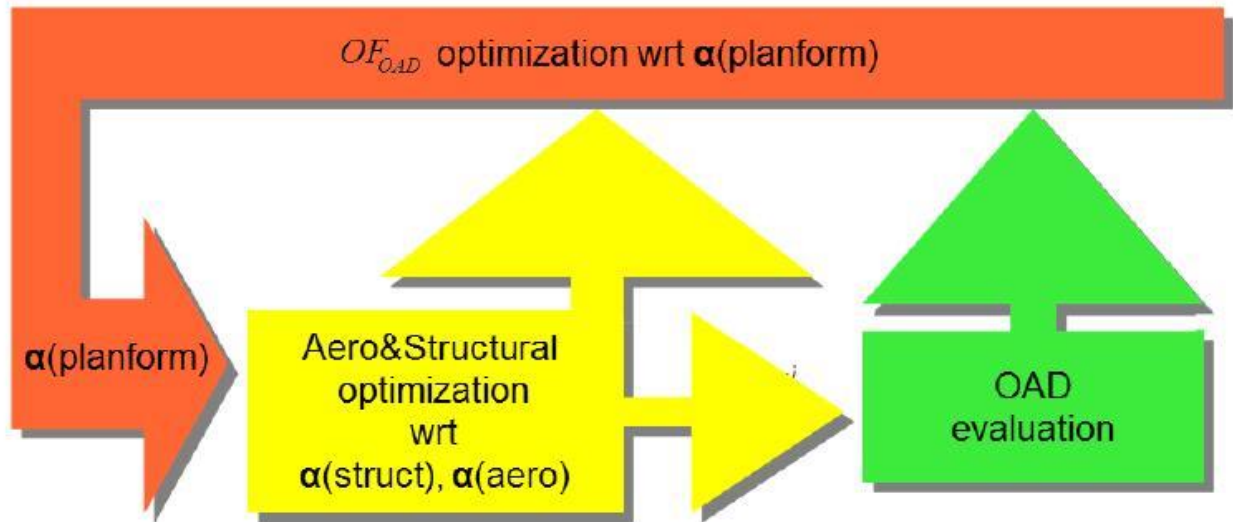


Figure 6.2: Overall Aircraft Design top level optimisation on top of the aero-elastic and structural ones; $\alpha(\text{struct})$ and $\alpha(\text{aero})$ are the structural and aerodynamic variables respectively.

An investigation into parametrisation techniques for shape optimisation. Working with ESR2 in ONERA during a 3 months secondment, ESR2 and ESR6 collaborated to investigate parametrisation techniques for preliminary shape optimisation. The results of this were presented during the AIAA Aviation conference in Washington, June 2016 [41].

The project resulted in publications [39-42].

SWP3: Application of advanced MDO methods to aircraft engine design.

Highly energy-efficient aero engines will form an important component of any energy-efficient aircraft. This Scientific Work Package develops new MDO methods for important aspects of aero engine design affecting their overall fuel consumption including, cooling, fan and compressor geometries and materials, and high pressure turbines.

Project 7: Turbine Stator Well Heat Transfer and Design Optimisation using Numerical Methods (ESR: Julien Pohl, UoL; RR, VKI)

The requirement for ever more efficient gas turbine engines is leading to increased gas path temperatures, creating increasingly hostile environmental conditions for the adjacent turbomachinery and support structures. Cooling air systems are designed to protect vulnerable components from the hot gas that would otherwise be entrained into the cavities communicating with the gas path through the inevitable gaps between rotating and static parts. These cooling flows are bled from the compressor stages and reduce the engine efficiency, as they can represent around 20% of the total main gas path flow. The aim of this project was therefore to minimise the air cooling flows to levels consistent with maintaining the optimum component lives and the mechanical integrity of the engine. The project was carried out in three main steps to develop an automated MDO method. In the first step, a coupled method between a Computational Fluid Dynamics (CFD) solver and a Finite Element (FE) solver is validated against experimental data obtained on the MAGPI project [43]. The second step consisted of a flexible parametrisation of the cavity geometry, which is necessary for the third and final step, the application of a suitable optimisation technique to optimise the shape of the cavity.

The predictions are validated against the experimental data generated during the MAGPI project. In the latter project a two-stage turbine test rig was constructed with instrumentation for air and metal temperature measurements, as well as pressure taps, both in the main gas path and the adjacent cavity (turbine stator well). Two CFD solvers have been used: HYDRA (Rolls-Royce in-house) and ANSYS FLUENT (commercial). These CFD solutions have been coupled to the in-house FE solver SC03, which calculates the conjugate heat transfer

thermal boundary conditions necessary to obtain the turbine assembly metal temperatures. The baseline and modified FE models are shown in Fig. 7.1.

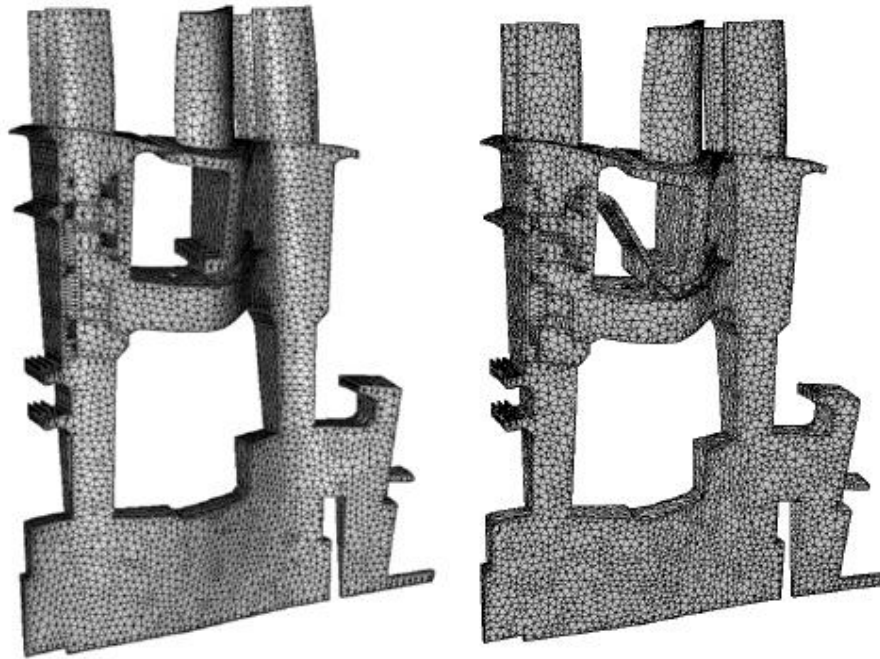


Figure 7.1: baseline FE model (left) and deflector FE model (right).

The CFD setup for the standard geometry is shown in Figure 7.2, where the main annulus and the cavity are meshed in a structured way and the stationary and rotating parts are connected by mixing planes for steady runs and by sliding planes for unsteady simulations. A second test case was also modelled for validation purposes. This contains an additional deflector plate inside the upstream cavity, which is attached to the stator foot. The additional deflector plate turns the cooling flow towards the rotor disc after entering the cavity, resulting in improved cooling. For this case, the main gas path has the same mesh as for the first test case, but the cavity is meshed separately: first in ICEM (structured mesh) and secondly in HYDRA (unstructured mesh). These meshes are then merged to the structured mesh of the main annulus, either non-conformally (with ICEM) or conformally (with HYDRA).

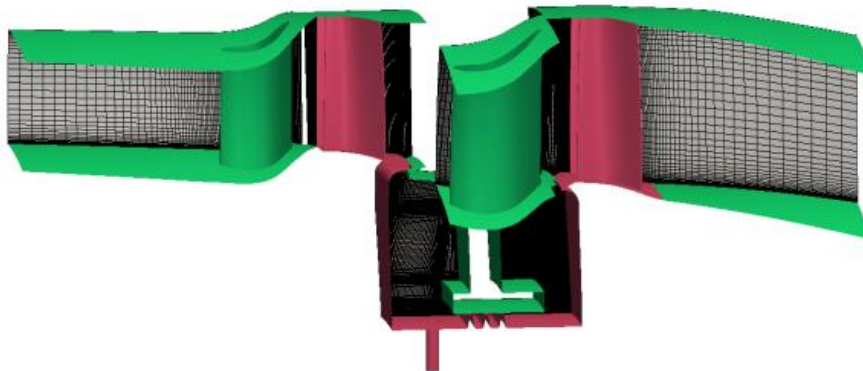


Figure 7.2: CFD model of the two-stage MAGPI test rig

Schematic illustrations of the turbine cavity flows for both test cases are given in Figure 7.3. In the standard geometry (left), cooling air is introduced into the rotor stator well cavity through a drive arm or disc spacer hole. Inside the cavity, a complex flow field is generated, including a core flow and a disc entrainment flow, induced by the rotating part of the turbine. The rim seal flow mixes the hot gas and cooling air, which has a significant effect on the temperature inside the cavity. In the deflector plate geometry, the cooling air does not penetrate the cavity to form a core flow, but instead impinges on the deflector plate and is turned towards the rotor disc, by forming a complex 3D vortex flow structure. The cooling air which reaches the disc is then entrained radially outwards by the rotating part of the turbine.

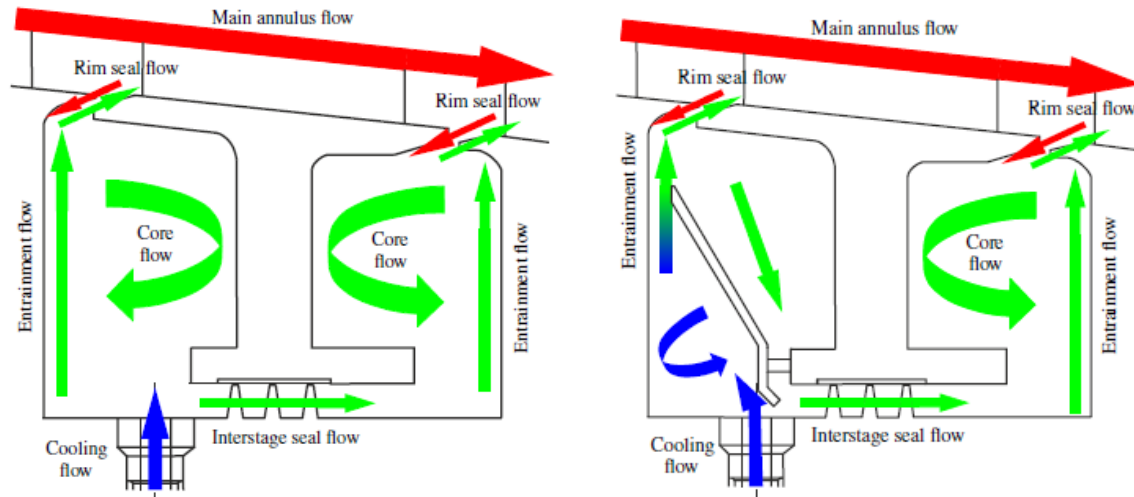


Figure 7.3: Turbine Stator well flow structure for standard geometry (left), with inserted deflector (right).

Earlier analyses showed good agreement between the CFD-FE temperature predictions and the experimental measurements along the cavity walls, for some flow conditions using the benchmark geometry without a deflector plate. In the rim seal region, however, larger discrepancies were observed. Further investigation showed that the thermal growth of the stator foot, (pulled radially outwards by the casing), is higher than the combined effects of the centrifugal forces and thermal loads induced in the rotor. This results in an increase of the inter-stage seal clearance by roughly one third. This increase in seal size has an effect on the flow field inside the cavity and also on hot gas ingestion from the main annulus, which explains why the experimental temperatures in the rim region are higher than predicted. In order to improve the temperature predictions, the geometry has been modified to account for the larger seal clearances. The modified geometry was then re-meshed and the new CFD results obtained. The resultant non-dimensional temperature predictions around the stator cavity wall are shown in Figure 7.4, where measurement points 14 and 24 are thermocouple positions near the up- and downstream rim, respectively.

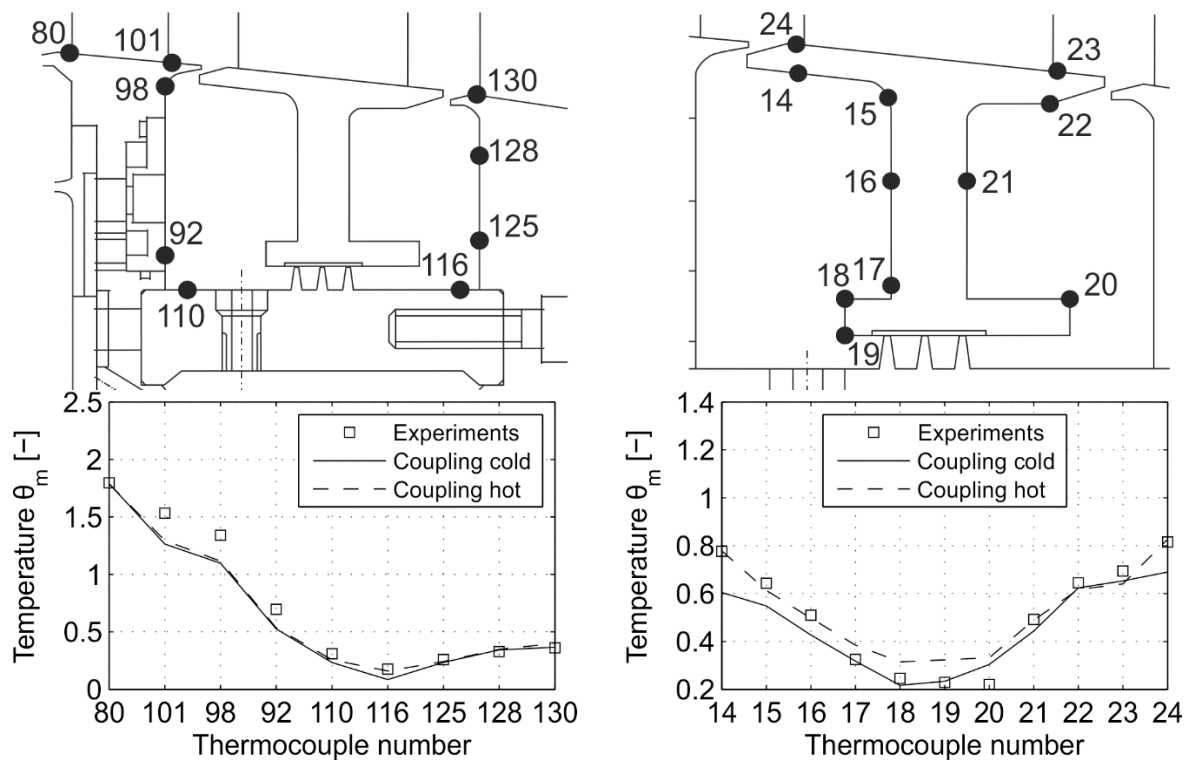


Figure 7.4: Rotor (left) and stator (right) disc.

The validation of the deflector plate geometry showed similar results. Both the cold and hot running clearances were modelled, in order to conduct a coupled FE-CFD simulation. Although the cold running model gave encouraging results, the hot running clearance improved the predictions significantly.

A flexible design parametrisation of the deflector plate has been developed (see Figure 7.5) in order to optimise the deflector geometry for rotor disc cooling. In total seven geometrical design variables were defined (Figure 7.5 (b)) plus one constraint ($\theta_{disc,ad}$). The objective function to be minimised was the mass flow rate of cooling air without penalising the constraint.

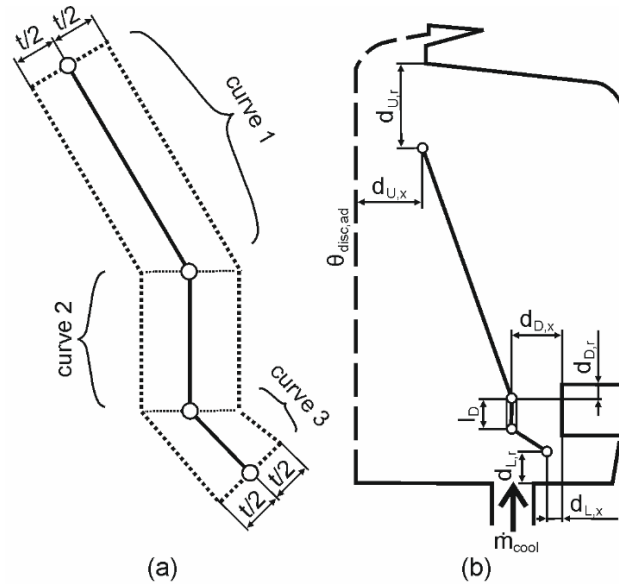


Figure 7.5: (a) parametrisation of the deflector plate and (b) its position inside the cavity.

The parametrised geometry is optimised using a meta-model assisted approach based on regressing Kriging in order to identify the optimum position and orientation of the deflector plate inside the cavity. The temperature distributions of the baseline and optimised deflector geometry cases are given in Figure 7.6. The optimised deflector plate geometry enabled the cooling air mass flow rate to be reduced by 70% compared to the baseline geometry without a deflector, while meeting critical cooling requirements.

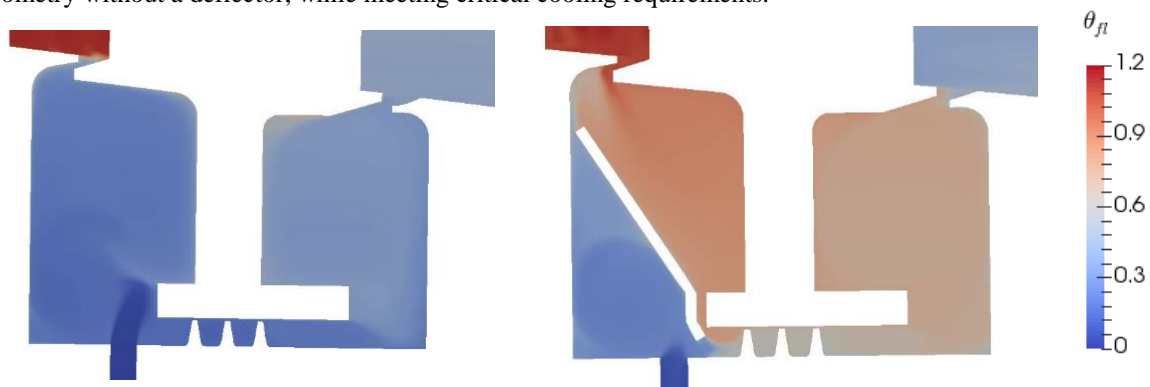


Figure 7.6 Temperature distribution in the baseline (left) and optimised deflector plate geometry (right).

The outcome of the optimisation was validated using the coupled CFD-FE methodology. This project produced publications [44-48].

Project 8: Novel 3D Shapes for MDO of Fans and Compressors (ESR: Ralf Schlaps, QMUL, RR)

Modern aero-engines are developed to reduce the specific fuel consumption to achieve the aim of reducing their global CO₂ emissions. The component efficiencies of components such as fans, compressors, turbines or combustors, therefore, need to be continuously increased. This becomes increasingly difficult since the component efficiencies are getting closer and closer to the physical limits. For instance, the efficiencies of compressor stages are already typically above 90%. Getting closer to 100% means minimising viscous effects without compromising the compressor performance at other engine speeds since an aero engine needs to operate efficiently at a wide

range of operating conditions such as idle during approach and taxiing, and maximum thrust during take-off or cruise. Additionally, fan and compressor rotors are subjected to high mechanical demands since they need to resist high centrifugal forces as well as foreign object impact such as bird strike, ice impact or impact from debris.

In order to meet the structural requirements, the range of designs that can be considered in current design processes are somewhat limited, which usually hinders the goal of maximising the aerodynamic performance. A trade off must be found which satisfies the stability and efficiency requirements. Multidisciplinary Design Optimisation, where both the aerodynamic and structural aspects are considered simultaneously, has the potential to overcome the limitations of current design processes.

The goal of this project was to establish a multidisciplinary optimisation strategy enabling novel 3D aerofoil shapes for fans and compressors. These novel aerofoil shapes should meet all the requirements in terms of flow stability, structural stability, resistance against foreign object impacts, manufacturability and efficiency in order to reduce the fuel consumption of the aircraft. Furthermore, by improving these features aircraft would be safer, more environmental-friendly, quieter and more economical.

A number of essential steps were defined to achieve the goal of developing an automated multi-disciplinary optimisation process for compressor design. The first step included the development and validation of the methods in each discipline. In the second step the optimisation process was designed by choosing an appropriate parametrisation and selecting the optimisation technique suitable for the multi-disciplinary optimisation. In the third step, the optimisation process was applied to a compressor rotor to optimise its shape.

The validation of the Rolls-Royce in-house CFD code was carried out using the test data of a 4 stage high pressure compressor research rig. This is necessary since 3D design optimisation relies heavily on the predictions of Computational Fluid Dynamics (CFD) analyses, which must be reliable and accurate. The CFD validation work demonstrated that CFD was able to predict trends correctly, enabling designers to find tangible design improvements.

Furthermore, a parametrisation defining the compressor aerofoil was developed and two different optimisation processes were established. The first optimisation process uses a trust-based, automatic metamodeling method (known as MAM) and the other one used the Kriging (Gaussian Process Regression) technique. Both design processes have been tested, and they were both able to find significant design improvements. These successful optimisations demonstrated that the chosen parametrisation was appropriate for the compressor optimisations.

In addition, a framework to model impact of ice slabs onto compressor components has been developed, Figure 8.1. The consideration of FOD (foreign object damage) in the early design stage is a novel feature of this research.

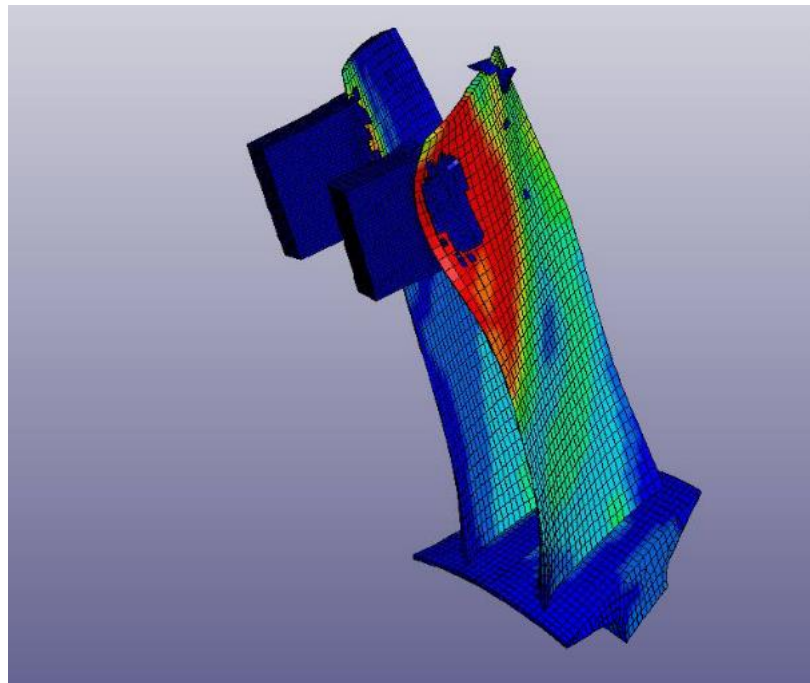


Figure 8.1: Ice impact model with two impacting ice slabs onto two disks.

It allows designers to take account of the requirements for impact-worthiness earlier in the design process, thereby reducing the risk of costly redesigns in a later design phase. This feature was also considered to provide the greatest benefit to the multi-disciplinary design process since it widens the design space for the optimiser.

The design processes developed during this project have a high potential to reduce costs, enhance efficiency and generally improve future designs. The final optimisation run showed that the compressor rotor can be further improved in terms of impact-worthiness and aerodynamic efficiency, even though the rotor had already been optimised by experienced designers, see Figure 8.2.

The project resulted in publications [49-51].

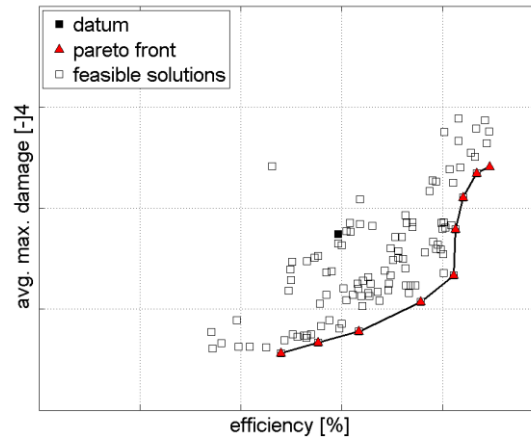


Figure 8.2: Pareto front showing possible trade-offs between efficiency and maximal damage.

Project 9: Multidisciplinary Design Optimisation of Aero-Engine Fan Blades (ESR: Christopher Chahine, VKI, RR, KU, University of Oxford)

Fan blades are central components of a modern aero-engine, are readily visible to the naked eye at the front face of an installed engine and produce more than 80% of total thrust for today's engines. This percentage can be expected to increase further for future high and ultra-high bypass ratio aero-engines.

Designing fan blades is a demanding task. Design considerations need to be driven by several disciplines including aerodynamics, structural mechanics, manufacturing and cost. In today's industrial design practice, blades are designed by a number of different departments, whereas each department is specialised in one particular discipline. The blade design progresses iteratively between the departments until a solution is found that satisfies all disciplinary requirements. This process, however, is very time and cost intensive. Moreover, it decouples the disciplines involved in the design process, which makes it difficult to reveal interactions between them. In view of the challenges that lie ahead of the aircraft industry in terms of the required reduction of fuel burn and exhaust emissions, increasing demands on reliability and increased competition, new, innovative design methods are required. These will need to be able to take full account of disciplinary interactions during the design process. Such methods are the subject of Multidisciplinary Design Optimisation (MDO). The goal of this project was the further development and application of these methods for the design of modern aero-engine fan blades.

A blade design resulting from a recent Multidisciplinary Design Optimisation study in this project is shown in Fig. 9.1. A CAD model of the blade is shown which is directly exported from the optimisation system, allowing the blade to be manufactured or, as shown, visualised in any standard CAD package.



Figure 9.1: Rendered CAD model of optimised fan blade

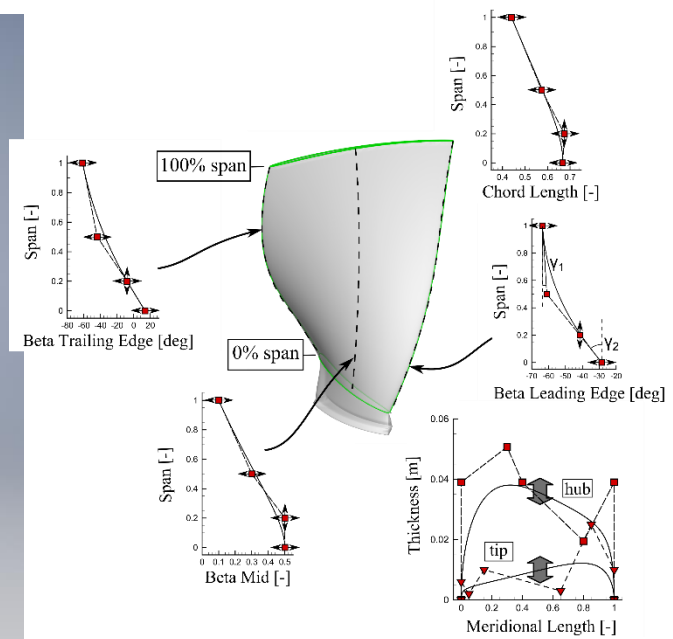


Figure 9.2: Fan blade parametrisation

The first part of the project aimed to establish a MDO framework for metallic aero-engine fan blades. A fan blade shape parametrisation based on parametric Bezier and B-Spline curves was developed allowing all design features of a modern fan blade, including three dimensional features like lean and sweep, to be represented, see Figure 9.2. Further, a comprehensive fully automated high-fidelity evaluation chain was established, consisting of the generation of the blade geometry and the associated fluid and solid domains, structured and unstructured meshing, as well as performance evaluations by Computational Fluid Dynamics (CFD) and Computational Structural Mechanics (CSM). An example of a resulting solid and fluid mesh is shown in Fig. 9.3. The evaluation chain was coupled to an Evolutionary Algorithm and accelerated by a Kriging metamodel. The successful application of the optimisation method was shown in a number of conference and symposium papers, including a paper that was presented at the 11th World Congress on Structural and Multidisciplinary Optimisation in Sydney, Australia [52].

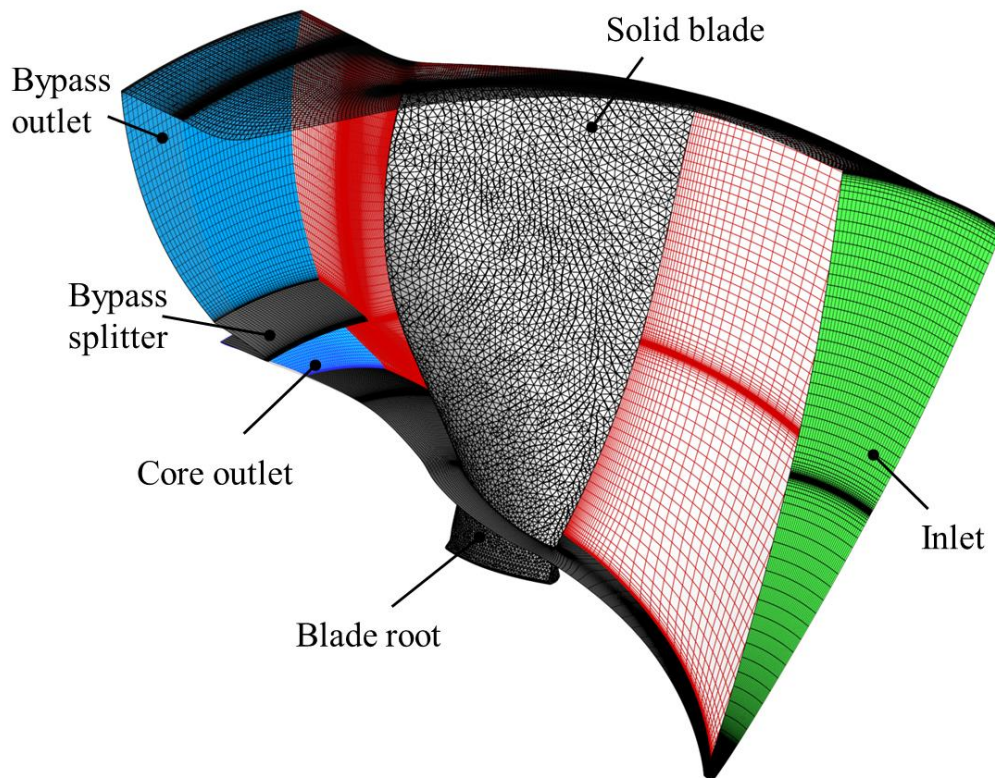


Figure 9.3: Meshed solid and fluid domain of the fan blade

Increased engine efficiency and an associated reduction in fuel consumption are currently the main targets in the development of new engines. To this end, jet engine manufacturers seek to increase the bypass ratio, which results in increased fan diameters. The weight of the fan blades and the fan section structure (disk, casing, outlet guide vanes and struts) are posing a limit on the potential efficiency gain associated with a larger bypass ratio, as improved aerodynamics is countered by the increase in engine weight. If the weight of the fan section can be decreased, engines with larger bypass ratios and in turn lower fuel burn can be realised. Lightweight materials are a key requirement for this purpose.

Composite materials like Carbon-Fibre Reinforced-Plastics (CFRP) offer increased specific stiffness and strength compared to metallic alloys and therefore are attractive replacement materials for engine components. The first high bypass ratio aero-engine fan blades made of CFRP entered service in 1995. Since then, manufacturing techniques and design methods have advanced considerably, allowing blades to become thinner and lighter. This development introduces a number of challenges for design optimisation, including an increasing impact of aeroelastic effects on overall fan performance and a substantial increase in the complexity of the design problem. Both of these aspects were addressed in this project.

Aeroelasticity becomes an important consideration for composite fan blades due to lower mass densities and reduced out-of-plane stiffness compared to metallic blades. The correct prediction of the static aeroelastic equilibrium at different operating points, i.e. the determination of the correct running shape of the blade under centrifugal and aerodynamic loads, is an important requirement for accurate off-design performance analyses since the transonic flow field that spans much of the fluid domain has a dominant impact on overall performance and is sensitive to small changes in geometry. The impact of the aeroelastic blade deformation on fan performance has been reported in the open literature for titanium blades but is less well known for composite ones. Bigger deformations than are typical for titanium blades are to be expected which introduce various modelling challenges. Unlike traditional methods that are based on the deformation of the fluid mesh, the method followed here is based on a deformation of the CAD model and a re-meshing of the resulting fluid domain. This has several advantages, with the most important ones being: 1) re-meshing of the fluid domain retains high quality grids even in highly deformed regions of the domain which typically tend to produce highly skewed cells (e.g. in the tip clearance at high levels of untwist 2) a CAD model of the deformed blade is available. The method was implemented for titanium blades and allowed an assessment of the impact of the aeroelastic deformation on the aerodynamic design and off-design performance. This enabled the error that is introduced when excluding aeroelastic deformations from the design process to be quantified.

The second aeroelastic effect considered in this work was blade flutter. Flutter is a self-excited aeroelastic instability, which, if not properly damped, can rapidly lead to a failure of the component. Fan blades of large aero-

engines are particularly prone to flutter. It is therefore important to take it into account in the design process. Flutter has been the subject of a large body of research in the past few decades. However, for some variants of flutter the underlying physical mechanisms are still not well understood. Hence, accurate flutter modelling and its prediction using computational tools is a demanding task. Various techniques have been proposed and are in use today by industry and academia which vary in the degree of coupling between structural and aerodynamic modelling. Their range of validity therefore equally depends on the degree of aeroelastic coupling present in the system. At the beginning of this project there was no clear indication in the literature on which methods would be the most suitable for the application to large composite fan blades in terms of validity and computational efficiency. Hence, this project also considered whether the most commonly applied technique today, i.e. the so-called energy method, could be applied to composite fan blades in order to produce sufficiently accurate results. Work in this direction was initiated and first results were published at the 14th International Symposium on Unsteady Aerodynamics, Aeroacoustics & Aeroelasticity of Turbomachines (ISUAAAT14) in Stockholm, Sweden [53]. The results indicated the existence of considerable aeroelastic coupling in the system.

Composite materials add an entirely new dimension to the design problem. Whereas with metallic materials, material properties are known at the outset of the design stage, the properties of a composite material are subject to design. The material design fundamentally impacts the stiffness of the blade which has important consequences for several performance parameters including structural performance like strength and natural frequencies, but also the static and dynamic aeroelastic response which in turn impacts aerodynamic performance. Design variables of a composite laminate include the choice of constituent materials, fibre orientations, ply stacking sequences and ply thicknesses. By locally adapting the design variables, the material can be tailored for improved fan blade performance. This, however, comes at the cost of an extensive expansion of the design space.

To circumvent some of this complexity, it is common practise to design composite components using a ply stacking sequence with a specific fibre orientation pattern which results in globally isotropic in-plane properties. These so-called quasi-isotropic laminates considerably facilitate design, analysis and manufacturing. They allow to design components with reduced mass compared to metals, but neglect the potential of optimally adapting the material for the application at hand. Particularly for applications where weight is of critical concern, like in the aerospace industry, there is a considerable interest in using the material more efficiently.

Fan blades present a particularly demanding application because of the inherent multidisciplinary nature of the design problem. Besides the fact that the material design affects overall blade performance as described above, it also determines the best possible blade shape. The same is true in the other direction, as the blade shape predetermines the best possible material distribution. Hence, in order to generate an optimal blade design, shape and material parameters should be treated in unison in the design process.

The final goal in this work was therefore the introduction of composite material optimisation into the already established shape optimisation framework, enabling for the first time a multidisciplinary fan blade optimisation with a concurrent consideration of blade shape and material parameters. A key challenge for the completion of this task was met with the development of a composite material parametrisation method that enables the material to be characterised with a small number of continuous design variables while maintaining the most influential parameters for the blade design. The implementation of this method is almost finalised and details of the method are planned to be published after testing and validation have been completed.

The publications [52-54] resulted from this project. ESR9 also won the ‘Best Presentation Award’ for his talk at the ‘10th ASMO-UK/ISSMO Conference on Engineering Design Optimisation’.

Project 10: Multidisciplinary design optimisation of winglet and squealer for high pressure turbine applications (ESR: Stefano Caloni, RR, QMUL, UoL)

The design of a turbine blade is a complex task involving several disciplines with competing requirements. The use of shroudless high pressure turbines emphasises the importance of these competing disciplines. On the one hand the component has to be as aerodynamically efficient as possible whilst on the other hand it has to satisfy given temperature requirements that limit the ability to achieve very efficient tip designs.

Currently, such components are designed jointly by several departments addressing one discipline at the time. Usually the design is achieved in a sequential work-flow where the outcome of a department becomes the input for the next. If the requirements are not met, the current design is revised and iterated in the design chain. The design process iterates between departments till the final design is obtained or the project runs out of time. Therefore, through experience, a set of design rules are used to guide the design process avoiding the need of additional iterations between departments. However, this reduces the likelihood of achieving a true global optimum design during the design process. This project aimed to develop more effective design processes for improving the performance of turbine blades. Multi-disciplinary techniques were used to analyse the component from different perspectives simultaneously and Multidisciplinary Design Optimisation techniques used to carry out a detailed exploration of the design space, to identify new, high performance designs.

At the beginning of the project, the research focussed on three main configurations, those with flat tips, winglets and squealers and shapes with combinations of winglet and squealer shapes. A multi-disciplinary analysis

methodology for turbine blade design was developed during the project. Initially, a simple single discipline analysis was used and subsequently the complexity of the system was increased by adding other disciplines. Every time a new discipline was involved the design space was modified accordingly. An automatic work flow was progressively updated to handle the different disciplines and different tools required.

At the start of the project, the geometry of the tip was parametrised and the parametrisation was then used by the different analyses; a single geometry definition shared between disciplines was found to simplify the process of exchanging information between simulations. The aerodynamic performance was analysed first by using Computational Fluid Dynamics (CFD) to predict the flow behaviour. Key performance attributes were determined and automatically extracted for different designs, together with preliminary information about the cooling requirements. Experimental data has been provided by the Rolls Royce Osney Lab, University Technical Centre, to validate the simulations and good agreement between the numerical simulations and experimental results was achieved. This agreement provided confidence that the simulations can be used within a meaningful optimisation analysis.

Optimisation techniques were then used to increase the aerodynamic efficiency of the component whilst reducing the cooling requirements. The optimisation was successful and demonstrated the trade-off between cooling requirements and efficiency. A number of interesting configurations were found and analysed, the results of which were presented at the European Turbomachinery Conference (2015) held in Madrid [55]. Following this optimisation, the fidelity of the model was increased. The internal cooling passages and the cooling holes near the tip area were fully modelled by using an internal parametrisation in conjunction with scripts for generating the geometry. In order to comply with the requirements for an automatic design optimisation, this geometry generation was fully automated.

The performance analysis considered not only the flow behaviour around the aerofoil but also the temperature distribution achieved inside the blade due to the cooling. This was achieved using three steps, the first involving the setup of a Finite Element (FE) model for solving the solid domain, the second the implementation of interpolation techniques for exchanging information between the two disciplines, then finally the development of coupling techniques. During a secondment at the Von Karman Institute in Brussels, the coupling techniques were further developed and tested successfully. The performance of the coupled techniques was compared with those of an uncoupled analysis and the results were presented at the ASME TurboExpo 2015 conference held in Montreal [56].

Further development of the coupled analysis was accomplished successfully. The Rolls Royce CFD solver was modified to enable conjugate analyses of the turbine blade using a single solver. This was found to significantly reduce the computational time and increase the quality of the results by avoiding the numerical noise caused by FE-CFD interpolations. The CFD conjugate solver was validated and new boundary conditions successfully implemented. The conjugate method was then applied to different squealer tip configurations (one closed and three opened). An opened squealer was found to show particular promise and was identified as being worthy of further investigation. These results were positively received by the audience during the ASME TurboExpo 2016 conference in Seoul where the findings were presented [57].

Finally, stress considerations were included in the design optimisation. The optimisation focused on the geometries that had showed most promise in previous studies. The analysis involved conjugate CFD simulations for understanding the aerodynamic performance, the behaviour of the cooling system and thermal effects on the blade. Moreover, a FE analysis was conducted to understand the stress state imposed to the blade. A multi-objective optimiser (MAM) recently developed at QMUL was used in the optimisation, which used surrogate models to increase the performance of the tip addressing both the fluid and solid performance simultaneously. A journal article on the optimisation work is currently being prepared [58].

Publications [55-60] have arisen from this project.

SWP4: Novel applications of MDO to the design of composite aeronautical structures.

Lightweight composites are now widespread in aircraft design and will be vital in enabling the industry to meet ever increasing targets for aircraft efficiency and sustainability. This Scientific Work Package develops novel MDO methods that can address key challenges in modelling composite damage, crashworthiness and acoustic performance and exploring the potential of forward swept composite wings.

Project 11: Incorporation of Bird Strike Requirements in MDO of an Aircraft Wing using Sub-Space Metamodels (ESR: Jonathan Ollar, Altair; QMUL, UoL)

This project aimed to transfer existing knowledge about crashworthiness optimisation from the automotive sector to the aerospace sector. In the automotive industry crashworthiness requirements often require analysis time measured in days rather than hours and results that are noisy and need to be filtered before assessment. This project explored techniques for handling the disparity in execution time between static and crashworthiness analyses.

An optimisation architecture, the Multi-Point Approximation Method (MAM) was identified as a suitable starting point for the project. The architecture was initially extended to handle MDO more efficiently by introducing the concept of disciplines within the optimiser. This allows for separate attributes (e.g. number of points per iteration, whether gradients should be used, etc.) to be handled for each discipline individually. Following this, a method was developed within the project, the sub-space approximation method, which takes advantage of any disparities in design variable dependence between the disciplines and reduces the computational budget needed to solve the optimisation problem.

To overcome identified limitations in terms of variable dependence, which can spoil the optimisation process as a whole, resulting in constraint violations in the final solution, the sub-space approximation method was extended into two, more robust methods. The first method is less sensitive to erroneous assumptions by adaptively accounting for incorrect assumptions by updating the values of eliminated variables in each iteration of a trust region-based optimisation process. The second method is a fully automatic approach, without any need for assumptions to be made, which makes use of a variable screening approach. In each iteration of a trust-region based optimisation, the previously evaluated designs are used to determine the dimensionality of the response produced by each model, and eliminate insignificant variables. Both methods have been tested on analytical examples and on simple finite element models successfully.

Furthermore, the pool of available approximation methods in the MAM was extended to include Kriging and gradient-enhanced Kriging, a method which is computationally expensive for large problems, especially when enhanced by design sensitivities. This led to a novel method being developed in collaboration with Swansea University, for reducing the computational budget needed.

The final part of the project was dedicated for testing of the developed MDO framework on an aircraft example. A wing model was devised and an optimisation was carried out considering both static stiffness of the wing as well as bird strike at several locations along the leading edge. The wing structure was a 3m long aluminium structure with a root chord of 830mm and a tip chord of 670mm. It had two longitudinal spars and 11 ribs as shown in Figure 11.1: the complete structure is shown on the left and the internal structure on the right. The material is precipitation-hardened aluminium (6061-T6).

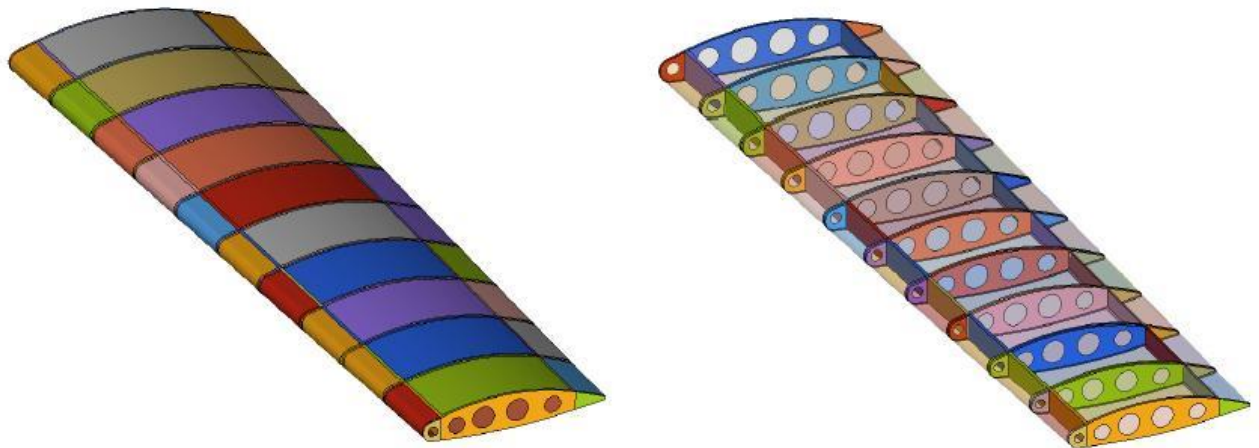


Figure 11.1: The wing model: complete structure (left) and internal structure (right).

The objective of the optimisation was to minimise the weight of the structure subject to meeting the structural requirements. The design variables were the thicknesses of the 100 components. The starting thickness for all components was 3mm with a lower bound of 2mm and upper bound of 5mm. The leftmost rib was not designable as in this study it was constrained by boundary conditions. The final thickness distribution is shown in Figure 11.2. None of the panels have gone to the upper thickness of 5mm, but some are lower than 2mm. Many of the ribs have resulting thicknesses which are in the thinner part of the thickness range. This may be due to the very simplistic set of static requirements for the optimisation. All leading edge skins have high thickness whilst leading edge ribs are thinner. This is probably because the leading edge skin is more likely to rupture if the leading edge rib is less compliant.

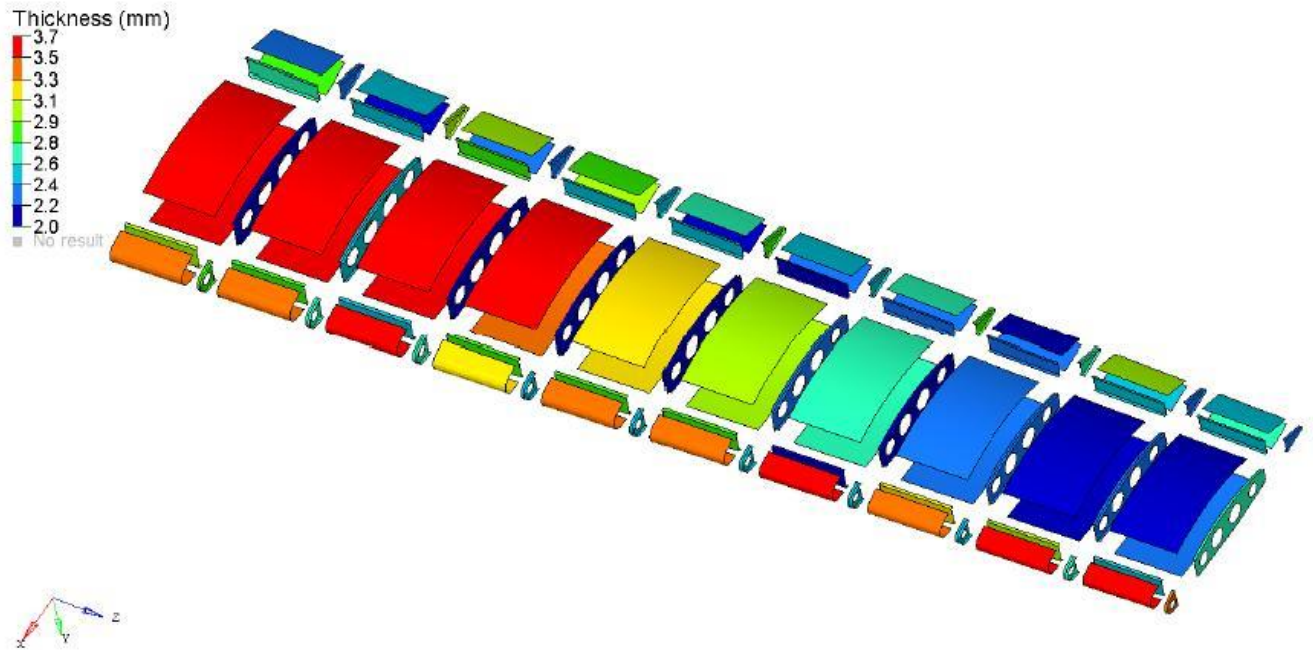


Figure 11.2: Final thickness for each of the considered components.

It was shown that by using the sub-space approximations proposed as part of the newly developed MDO framework, the computational effort needed to solve the optimisation problem was far lower than what would otherwise be possible. The optimisation finished in 8 iterations having evaluated 139 stiffness simulations and 1276 bird strike simulations in total, less than would have been required per iteration had sub-space metamodels not been used. The final result is a mass saving of 4.7% and a reduction of all previously violated constraints to less than 1%.

Publications [61-67] resulted from this project.

Project 12: Multi-disciplinary Analysis and Optimisation of Composite Forward Swept Wings (ONERA,TUD, Altair)

Due to recruitment difficulties, this project was split into two complementary projects. The first project was carried out by ESR12a, Marco Tito Bordogna, and aimed to develop a new strategy for composites tailoring which can account for aeroelastic phenomena.

An important aspect of the strategy was that it included high-fidelity CFD-CSM loads computation and their associated sensitivities with respect to the design parameters. A detailed comparison between two different composite parametrisation methods (lamination parameters and polar invariants) for a composite forward swept wing was performed. This demonstrated that both methods are capable of modelling composites in a continuous fashion; this makes them suitable for composite optimisation. For both methods the feasible design space was introduced according to the latest literature and their spaces have been explored with respect to manufacturable stacking sequence. The goal of the comparison was to find the most suitable method for optimising a real case aerospace structure. Buckling, strength, manufacturing and aeroelastic constraints were all taken into account in the comparison. The comparison concluded that lamination parameter approach is the most suitable for the optimisation of an aerospace composite structure.

The strategy was applied to the test case of a composite forward swept wing short-range civil aircraft to evaluate whether or not the use of unconventional laminates improves the overall structural weight. In collaboration with ESR12b, blending constraints to be implemented during gradient based structural optimisation were derived and applied. The outcome of the cooperation was a paper in the Journal of Composite Structures [68]. The focus then moved to identifying the recommended fidelity level to be used in the wing optimisation strategy. A backward swept wing model ("Acquill wing model") was used to set up a preliminary optimisation via MSC Nastran SOL 200, see Figure 12.1.

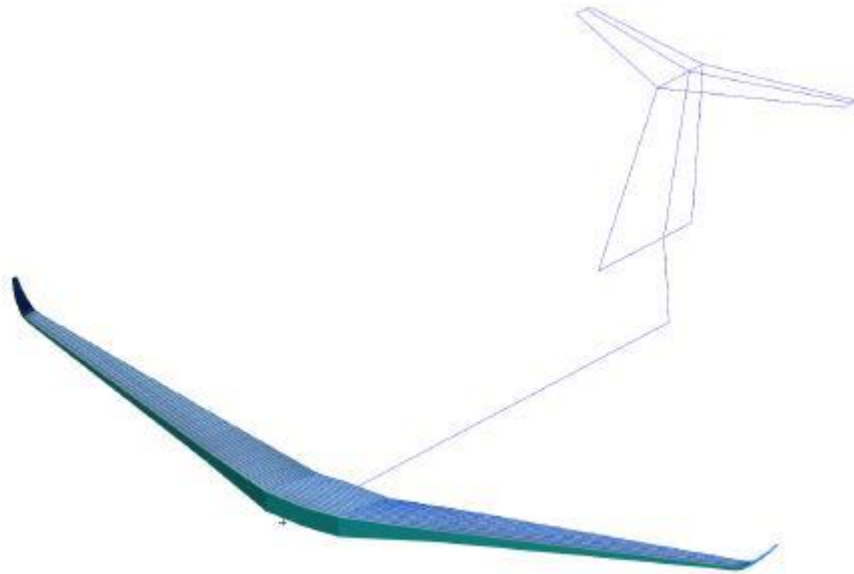


Figure 12.1: Aircraft wing model used in the optimisation.

The goal was to start treating large scale structural optimisation with important constraints on buckling, strength, aeroelasticity, manufacturing and perhaps winglet efficiency. This work is currently ongoing. It will create the basis for performing a fidelity level analysis where DLM loads will be compared those generated from the ONERA elsA/AEL module. The optimisation was carried out with MSC Nastran SOL 200 demonstrating that the constraints can be implemented using commercial optimisation software. This project produced publication [68].

Project 12a was supplemented by project 12b, carried out by Paul Lancelot, entitled **Investigation of stacking sequence parametrisation options for aeroelastic tailoring**. This project investigated the different methods available for composite structure optimisation under aeroelastic loads.

The use of composite materials to build large structures is one of the main challenges facing the aircraft industry. While in general they offer improved mechanical performance with higher strength and lower weight compared to their more conventional aluminium counterparts, they are more difficult to design due to the increased number of design variables that need to be correctly chosen. These methods are based on different types of parametrisation for the stacking sequence, like for instance the lamination parameters or the polar form. Several ways of optimizing these parameters for given constraints were compared and a number of techniques for retrieving a feasible stacking sequence from the optimal set of parameters, taking into account the blending and manufacturing constraints, were analysed.

Whilst most simulations used lamination parameters to formulate the stiffness properties of the laminates, the performance of polar invariants were also considered. On this type of problem, both lamination parameters and polar invariants were found to give similar outputs. A simplified version of NASA's Common Research Model (CRM) wingbox was used as a test case for strength optimisation under gust loads. Gust load computations require nonlinear dynamic solutions for which NASTRAN cannot compute derivatives for the gradient-based optimisation. This issue was overcome by implementing the equivalent static load technique using Matlab. A number of different strategies to ensure that the optimisation performs optimally for both thickness and stiffness were considered. Results showed a good improvement in term of weight between the quasi-isotropic solution (black aluminium) and the anisotropic solution.

This project collaborated with ESR12a on the definition of blending constraints. Blending is one of the most important manufacturing issues for variable stiffness composites. When the structure which has to be optimised is composed of several panels, it requires ply continuity throughout the structure. In the continuous optimisation level, this requirement is usually not applied since the stacking sequence is unknown. However this leads to a gap in terms of performance between the continuous optimum solution and the retrieved feasible stacking sequence (using a genetic algorithm optimisation procedure). Defining maximum allowable gradients between panels during the continuous optimisation allows a reduction of this gap, and aids the stacking sequence retrieval algorithm. This innovative method was successfully applied on the classical 18 panels horseshoe problem, and to a gust load benchmark problem. The latter considered a transport aircraft wing that can freely move in plunge and was hit by a *1-cosine gust*. The objective function is the structural mass and only the strength constraints were applied. The loads are extracted from NASTRAN Solution and the optimisation performed within Nastran Solution 200. A matlab script was used for the data transfer between the two solvers. Thicknesses of several panels

over the wing box are used as design variables, and the convergence was reached after 25 iterations, providing a significant reduction in mass and root bending moment, see Figure 12.2.

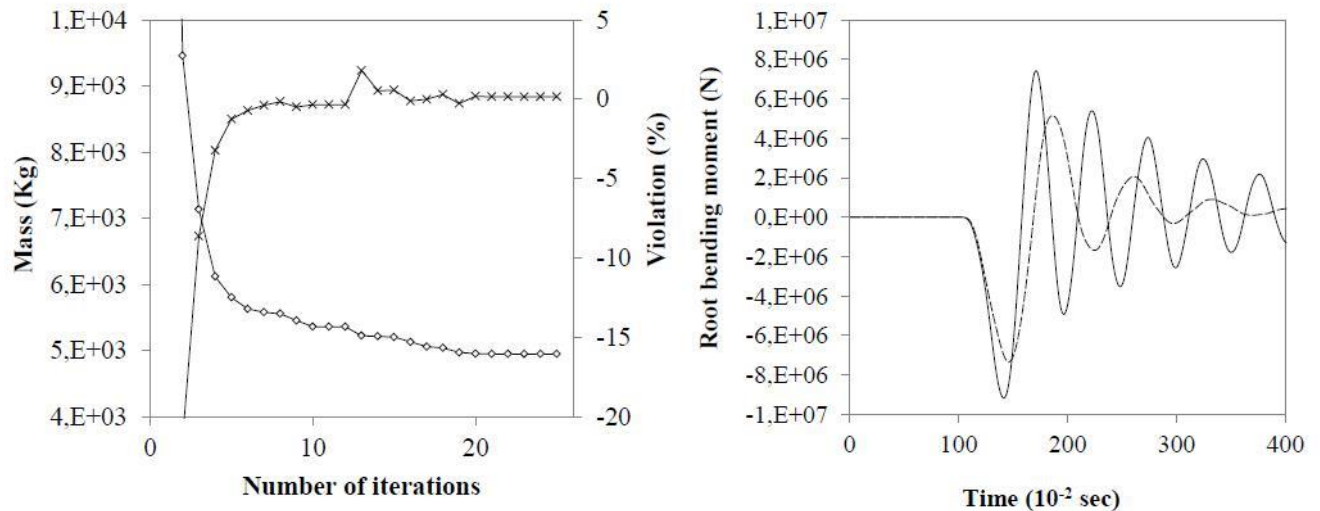


Figure 12.2: Optimisation results of a wing hit by a 1-cos gust.

Finally, the well-known problem of non-continuity of flutter and divergence inside the lamination parameters design space, which makes gradient-based optimisation difficult, was considered. This project considered a two-step strategy to reduce the number of design variables in aeroelastic tailoring problems, combining the lamination parameters (or polar invariants) with the kick angle definition. This showed promising results for future application.

This project produced publications [68] and [69].

Project 13: MDO of composite fuselage structure with vibro-acoustic requirements (ESR: Gokhan Serhat, KU,TUD, Altair,UoL)

This project aimed to provide a methodology for the early design stages of the development of modern composite fuselages to satisfy the competing objectives of high strength, low weight and low inner cabin sound pressure level.

During the optimisation of the fuselage section with respect to structural and acoustic requirements, a large range of different designs have to be generated and evaluated. In order to automatize the entire optimisation process an Automatic Optimisation Engine (AOE) was developed. This links together all of the numerical tools and automates each different task. In order to have a modular structure, the facilities of AOE were grouped under several subroutines. For each subroutine the user is allowed to choose between available options or specify the values of the parameters. The working principle of AOE is presented in Figure 13.1.

Automatic Optimization Engine (AOE)

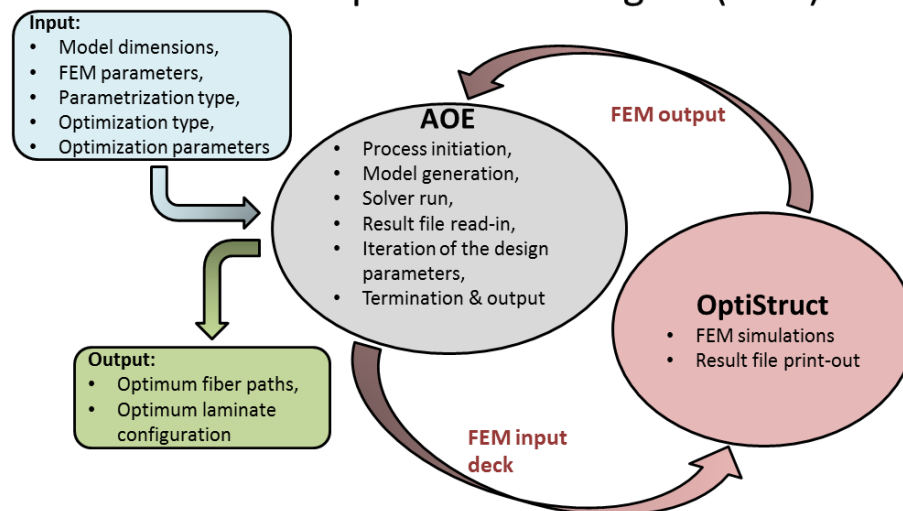


Figure 13.1: A schematic diagram showing the working principle of AOE.

Since Multi-disciplinary design of complex products using MDO requires rapid generation of computational models for multiple disciplines, an automatic Model Generator that generates mechanical, acoustical models for subsequent FE analyses has been built. Figure 13.2 shows a sample finite element model of the fuselage section and an acoustic cavity.

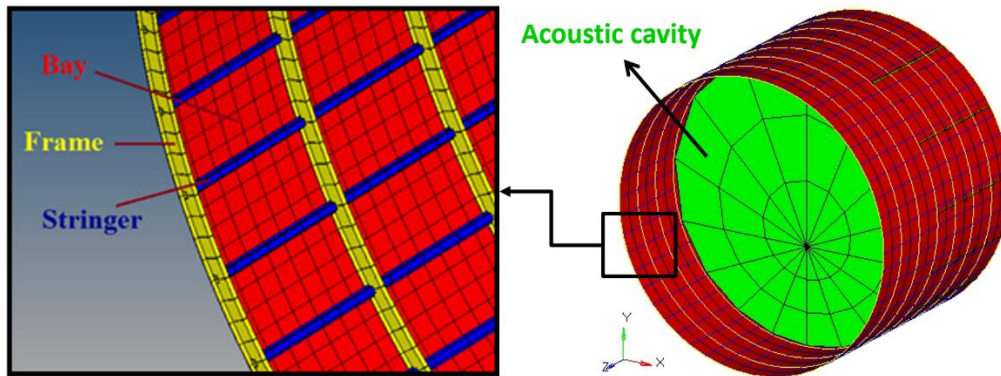


Figure 13.2: Sample finite element model of the fuselage section and acoustic cavity generated by Model Generator module.

An optimizer module is used to carry out a laminate optimisation process. It contains optimisation algorithms including Full-Factorial DoE, 0th Order (Derivative-Free) Local Search and 1st-order Gradient-Based Local Search. Low frequency sound transmission properties of the shell structures can be altered by varying the stiffness properties. Numerical simulations were carried out to observe the effects of fibre orientations and laminate stacking sequence on the sound absorption capabilities as well as structural strength. This favoured the development of different parametrisation approaches for the vibro-acoustic analysis of a fuselage made of composite laminates. Three different parametrisation approaches were developed based on panel, bay-based fuselage and continuous fuselage optimisation.

The most important functions of an aircraft fuselage are to enclose the passenger cabin, hold the aircraft structure together and withstand forces and bending moments to ensure flight safety. It is also necessary to ensure adequate vibro-acoustic performance in order to provide the passengers with a comfortable environment. Therefore, a multi-objective optimisation study is required. Figure 13.3 depicts the response surfaces and optimum points for maximum longitudinal stiffness and maximum panel natural frequency which are mechanical and vibro-acoustic performance metrics, respectively. The lower axes of the diagrams stand for the lamination parameters V_1 and V_3 which are the design variables while vertical axes are the responses.

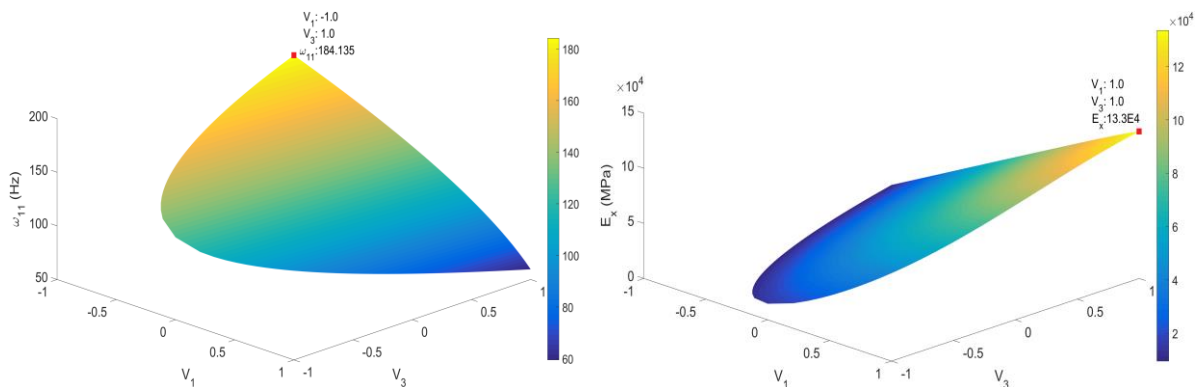


Figure 13.3: The response surfaces and optimum points for maximum panel natural frequency (left) and maximum longitudinal stiffness (right).

A comparison of preliminary design methodologies for the optimisation of stiffened, fibre-reinforced composite fuselages for vibro-acoustic requirements was carried out. The effect of fuselage stiffness properties on the vibro-acoustic performance was investigated using two different approaches. The first method only considered the structural model in order to explore the effect of design variables on fuselage vibrations. The simplified estimation of the acoustic behaviour without considering fluid-structure interaction brings certain advantages such as reduced modelling effort and computational complexity. The second method utilized coupled vibro-acoustic simulations and provided more accurate results at the expense of increased computational cost. The

vibro-acoustic performance metrics used in the research included: maximum panel fundamental frequency, minimum equivalent radiated power (ERP) from the panels or fuselage section, and the minimum average sound pressure level (SPL) in the acoustic cavity.

For ERP calculations, bay panel and fuselage section models were used, whereas for the SPL calculations the fuselage section model with acoustic cavity was used. The structures were excited by uniform outer harmonic pressure which is a simple representation of turbulent boundary layer noise outside the aircraft. Both ERP and SPL are averaged in the excitation frequency range: 1-250 Hz. The values of the design variables at minima and maxima have been observed to be similar for the bay ERP, fuselage section ERP and SPL. However, the general trend of fuselage section ERP has been found to be considerably closer to the SPL than the bay ERP and its overall accuracy is therefore superior. This is very important in multi-objective optimisation, as the optimum might be located in the middle regions of the design space.

In order to quantify the total conformity of the two different metrics, the error was defined by: $|\{\overline{SPL}\} - \{\overline{ERP}\}|$. The optimisations have shown the ERP to be a useful performance metric in early-stage vibro-acoustic design optimisation.

The project produced publications [70-72].

III. Conclusions

Collectively, the AMEDEO research projects have developed new and/or improved MDO methods for a number of strategically-important aspects of aerospace design. For example, ESR2's development of a powerful new node-based shape optimisation method, which has been adopted by ONERA and its wider dissemination throughout industry has been facilitated by its implementation into the well-established open-source Multiphysics framework KRATOS Multiphysics. The methodology and corresponding source tools are now publicly available so anyone from industry or academia may use the tools to perform node-based single and multi-disciplinary shape optimisation with their own designs.

Other examples include the new advanced MDO method for preliminary aircraft design (developed by ESR 6) which enables Direct Operative Costs to be modelled accurately in the early stages of aircraft design, the MDO methodologies of ESRs 7, 8 and 10 for improving aero-engine design and ESR 11's powerful new sub-space optimisation method for crash and safety investigations. These outcomes and those from the other projects are already providing important benefits for key EU aerospace manufacturing and supply chain companies.

However, although the improvements in automated design optimisation processes achieved in AMEDEO are indeed substantial it is important to recognise that, as identified recently by Shahpar [73], the impact of MDO anticipated in ACARE 2020 Vision [1] and ACARE Beyond Vision 2020 [2] will depend on overcoming deeply entrenched human factors and organisational issues. It is therefore likely that the greatest long-term impact of AMEDEO on the wider adoption of MDO throughout the aerospace industry will be through the future careers and achievements of its highly-trained ESRs.

Acknowledgements

The financial support for AMEDEO through EU grant reference 316394 is gratefully acknowledged.

References

1. European Aeronautics: A vision for 2020. Meeting society's needs and winning global leadership. *Advisory Council for Aeronautics Research in Europe (ACARE)*, <http://www.acare4europe.com>, (2001).
2. Aeronautics and Air Transport: Beyond Vision 2020 (Towards 2050). Background Document. *Advisory Council for Aeronautics Research in Europe (ACARE)*, <http://www.acare4europe.com>, (2010).
3. Flightpath 2050. Europe's vision for aviation. Report of the high level group on aviation research. European Commission, http://ec.europa.eu/transport/air/hlg_aviation_aeronautics_en.htm, (2011).
4. J. Sobieszcanski-Sobieski, R.T. Haftka. Multidisciplinary aerospace design optimization: survey of recent developments, *Struct. Opt.*, **14**, 1-23, (1997).
5. E.J. Cramer, P.D. Frank, G.R. Shubin, J.E. Dennis and R.M. Lewis. On alternative problem formulation for multidisciplinary optimization. *Proc. 4th AIAA/USAF/NASA/OAI Symp. on Multidisciplinary Analysis and Optimization*, Cleveland, OH, AIAA 92-4752 (1992).
6. S. Kodiyalam and J. Sobieszcanski-Sobieski. Multidisciplinary design optimization: some formal methods, framework requirements and application to vehicle design. *Int. J. Vehicle Design*, **25**, 3-32 (2001).
7. R.D. Braun, P. Gage, I.M. Kroo, I. Sobieski. Implementation and performance issues in CO. *Proc. 6th AIAA Symp. MDAO*, Bellevue, WA, (1996).
8. H.M. Kim, D.G. Rideout, P.Y. Papalambros, J.L. Stein. ATC in automotive vehicle design, *J. Mech. Des.*, **125**, 481-489, (2003).
9. S. Tosserams. Distributed Optimization for System Design – an augmented Lagrangian coordination approach, *PhD thesis*, University of Eindhoven, (2008).
10. D. Liu, V.V. Toropov, O.M. Querin and D.C. Barton. Bilevel optimization of blended composite wing panels. *AIAA Journal of Aircraft*, **125**-1, 107-118 (2011).
11. P.N. Koch, R.-J. Yang and L. Gu. Design for six sigma through robust optimization. *Structural and Multidisciplinary Optimization*, **26** (2004), 235-248.

12. D. M. Frangopol, K. Maute. Life-cycle reliability-based optimization of civil and aerospace structures (Review article), *Computers and Structures*, 81 (2003) 397–410.
13. J.R.R.A. Martins, A.B. Lambe. Multidisciplinary Design Optimisation: A Survey of Architectures. *AIAA Journal*, 51(9), 2049-2075, 2013.
14. AMEDEO ITN (EU FP7-PEOPLE-2012-ITN, project no. 316394). <http://www.amedeo-itn.eu/>
15. Aissa, M.H.; Verstraete, T. (2014) "Efficient high Performance Computing Techniques for Multi-disciplinary Optimisation", 5th Symposium of VKI PhD research, March 10-12th 2014, von Karman Institute for Fluid Dynamics, Rhode-Saint-Genese, Belgium.
16. Aissa, M.H., Verstraete, T. and Cornelis, V. "Aerodynamic optimization of supersonic compressor cascade using differential evolution on GPU." *INTERNATIONAL CONFERENCE OF NUMERICAL ANALYSIS AND APPLIED MATHEMATICS 2015 (ICNAAM 2015)*. Vol. 1738. No. 1. AIP Publishing, 2016.
17. Aissa, M.H., Verstraete, T. and Vuik, V. (2016). "A GPU-Accelerated Steady CFD Solver for Turbomachinery Optimization" 28th International Conference on Parallel Computational Fluid Dynamics (ParCFD 2016), May 9-12st 2016, Kobe, Japan (extended abstract).
18. Aissa, M.H., Chahine, C. and Verstraete, T. (2016). "Surrogate-Model Assisted Evolutionary Optimization of an Axial Compressor Stator" 11th ASMO UK/ISSMO/NOED2016: International Conference on Numerical Optimisation Methods for Engineering Design, July 18th-20th 2016, Munich Germany. (extended abstract).
19. Aissa, M.H. , Mueller, L., Verstraete, T. and Vuik, C. (2016). "Acceleration of Turbomachinery Steady Simulations on GPU" Euro-Par 2016 WS, 22nd International European Conference on Parallel and Distributed Computing, 22th-26th of August, Grenoble France (in publication: Lecture Notes in Computer Science)
20. Aissa, M.H., Verstraete, T. and Vuik, C. (2016). "How GPU Computational Power Can Alter the Established Comparison of Explicit to Implicit CFD Simulations?" abstract at 5th European Seminar on Computing June 5 - 10, 2016 Pilsen, Czech Republic (abstract).
21. Aissa, M.H. (2015) "A GPU-Accelerated Navier-Stokes Solver for Multidisciplinary Design Optimization". 27th International Conference on Parallel Computational Fluid Dynamics (ParCFD 2015), May 17-21st 2015, Montreal, Canada (extended abstract).
22. Aissa, M.H. (2015) "A GPU-accelerated Navier-Stokes solver for steady turbomachinery simulations". 6th VKI PhD symposium, March 11-13th 2015, von Karman Institute for Fluid Dynamics, Rhode-Saint-Genèse, Belgium.
23. Aissa, M.H.; Verstraete, T.; Vuik, C. (2014) "Use of modern GPUs in Design Optimization", 10th ASMO-UK/ISSMO conference on Engineering Design Optimization, June 30th - July 1st 2014, Delft University of Technology, Delft, The Netherlands.
24. Najian Asl, R.; Baumgärtner, D.; Bletzinger, K.-U. (2015) "Towards shape optimization of steady-state fluid-structure interaction problems using vertex morphing". 16th AIAA ISSMO Multidisciplinary Analysis and Optimization Conference, June 22-26th 2015, Dallas USA. doi: 10.2514/6.2015-3356.
25. Baumgärtner, D.; Najian, R.; Bletzinger, K.-U. (2015) "Potential and difficulties of node-based shape optimization taking into account fluid-structure interaction". 3rd ECCOMAS Young Investigators Conference, July 20-23rd 2015, Aachen Germany. (Abstract)
26. Baumgärtner, D.; Wolf, J.; Rossi, R.; Wüchner, R.; Dadvand, P. (2015) Contribution to the Fluid-Structure Interaction Analysis of Ultra-Lightweight Structures using an Embedded Approach. CIMNE Monograph (ISBN: 978-84-943307-6-6)
27. Baumgärtner, D.; Viti, A.; Dumont, A.; Carrier, G.; Bletzinger, K.-U. (2016) "Comparison and combination of experience-based parametrization with Vertex Morphing in aerodynamic shape optimization of a forward-swept wing aircraft". 17th AIAA/ISSMO Multidisciplinary Analysis and Optimization Conference, June 13-17th 2016, Washington D.C. USA. doi:10.2514/6.2016-3368. <http://kratos-wiki.cimne.upc.edu>.
29. Baumgärtner, D.; Bletzinger, K.-U.; Viti, A.; Dumont, A. (2016) Node-based shape optimization in aircraft preliminary design. 11th ASMO UK/ISSMO/NOED2016: International Conference on Numerical Optimisation Methods for Engineering Design, Munich, Germany.
30. A.L. Arsenyeva, F. Duddeck, Optimization of fiber-steered composites by using Iso-contour method with maximum curvature constraint, ECCM17, Munich, Germany, July 2016.
31. A. Arsenyeva, F. Duddeck, "Efficient and adaptive parametric modeling for shape optimization of a wingbox", In: 3rd ECCOMAS Young Investigators Conference, Aachen, Germany, 2015.
32. Duckitt, S. J.; Shahpar, S.; Bisagni, C. (2016) "Parametric Bird Strike Study of a Transonic Rotor Using Isogeometric Analysis", Proceedings of ASME Turbo Expo, GT2016-567464, June 13-17th, 2016, Seoul, South Korea.
33. Duckitt, S. J.; Guo, Y.; Ruess, M. (2014) "Isogeometric modelling of composite delamination", Proceedings of NSCM-27: the 27th Nordic Seminar on Computational Mechanics, October 22-24th, 2014, Stockholm, Sweden. (TRITA-MEK Technical Report 2014:24, KTH Mechanics, Stockholm, Sweden, 2014).
34. Duckitt, S. J.; Shahpar, S.; Bisagni, C.; (2016) "Multiobjective Optimisation of a Compressor Stator using a 3D B-Spline Parameterisation", Proceedings of 11th ASMO UK / ISSMO / NOED2016: International Conference on Numerical Optimisation Methods for Engineering Design, July 15-18th, 2016, Munich, Germany.
35. Jovanov K.; De Breuker, R.; Abdalla, M.M.; Blondeau, C. (2016) "Multi-fidelity aeroelastic analysis and sensitivity analysis for gradient-based structural optimization", 11th ASMO UK/ISSMO/NOED2016, July 18 – 20th 2016, München, Germany.
36. Jovanov K.; De Breuker, R.; Abdalla, M.M.; Blondeau, C. (2016) "A Linear Aerodynamics-based Preconditioner for High-Fidelity Aeroelastic Analysis and Sensitivity Analysis". 17th AIAA/ISSMO Multidisciplinary Analysis and Optimization Conference, AIAA Aviation 2016, June 13 – 17th 2016, Washington, USA.
37. Jovanov K.; De Breuker, R. (2015) "Accelerated Convergence of High-Fidelity Aeroelasticity Using Low-Fidelity Aerodynamics". International Forum on Aeroelasticity and Structural Dynamics June 28th - July 2nd 2015, Saint Petersburg, Russia.
38. Jovanov, K.; De Breuker, R.; Abdalla, M.M. (2015) "Accelerated convergence of static aeroelasticity using low-fidelity aerodynamics", 56th AIAA/ASCE/AHS/ASC Structures, Structural Dynamics, and Materials Conference, SCITECH 2015, January 5 - 9th 2015, Kissimmee, Florida.
39. Viti A., Druot T., Dumont A. (2016) "Aero-structural approach coupled with direct operative cost optimization for new aircraft concept in preliminary design", AIAA/ISSMO-MOA conference, June 2016, Washington.
40. Viti A., Dumont A., Carrier G., Hewson R. (2015) "Innovative Aero-Structural Design Process for a Forward-Swept Wing in Preliminary Design", 3AF 50th International Applied Aerodynamics Conference, March 2015, Toulouse.
41. Baumgaertner D., Viti A. (2016) "Comparison and combination of experience-based parameterization with vertex-morphing in aerodynamic shape optimization of a forward-swept wing aircraft", AIAA/ISSMO-MOA conference, June 2016, Washington.
42. Bach C., Jebari R., Viti A., Hewson R. (2016) "Composite stacking sequence optimization for aeroelastically tailored forward-swept wings", Structural and Multidisciplinary Optimization, Springer Edition, pp. 1-15.

43. MAGPI. 'Main Annulus Gas Path Interaction – Specific Targeted Research Project'. EU contract no. 30874, 2006.
44. J. Pohl, H.M. Thompson, R.C. Schlaps, S. Shahpar, V. Fico, G.A. Clayton, 'Innovative turbine stator well design using a kriging assisted optimization method' to appear in *Journal of Engineering for Gas Turbines and Power*, 2017.
45. J. Pohl, H. Thompson, A. Guijarro Valencia, G. Lopez Juste, V. Fico, G. A. Clayton, 'Structural Deflection's Impact in Turbine Stator Well Heat Transfer', *Journal of Engineering for Gas Turbines and Power*, **139**, 041901-1, 2017.
46. Pohl, J.; Thompson, H.; Schlaps, R.; Shahpar, S.; Fico, V.; Clayton, G. (2016) "Innovative Turbine Stator Well Design Using Design Optimisation" 16th International Symposium on Transport Phenomena and Dynamics of Rotating Machinery (ISROMAC 2016), April 10-16th 2016, Honolulu, Hawaii
47. Pohl, J.; Fico, V.; Dixon, J. (2015) "Turbine Stator Well Cooling - Improved Geometry Benefits" Proceedings of ASME Turbo Expo 2015: Turbine Technical Conference and Exposition, June 15-19th 2015, GT2015-42658, Montreal, Canada.
48. Pohl, J, Thompson, H.M., Fico, V., Clayton, G.A. (2016), Turbine stator well geometry benefits – method validation and design optimisation. 11th ASMO UK/ISSMO/NOED2016: International Conference on Numerical Optimisation Methods for Engineering Design, Munich, Germany.
49. Schlaps, R.; Shahpar, S.; Toropov, V.V. (2015) "Multi-fidelity optimisation of compressors". 3rd ECCOMAS Young Investigators Conference, July 20-23rd 2015, Aachen Germany.
50. Schlaps, R. C.; Shahpar, S.; Guemmer, V. (2014): "Automatic Three-Dimensional Optimisation of a Modern Tandem Compressor Vane", In Proceedings of the ASME Turbo Expo 2014, GT2014-26762, 16th-20th June 2014, Duesseldorf, Germany
51. Pohl, J.; Thompson, H.; Schlaps, R.; Shahpar, S.; Fico, V.; Clayton, G. (2016) "Innovative Turbine Stator Well Design Using Design Optimisation" 16th International Symposium on Transport Phenomena and Dynamics of Rotating Machinery (ISROMAC 2016), April 10-16th 2016, Honolulu, Hawaii
52. Chahine, C. Verstraete, T., He, L.: "Multidisciplinary Design Optimization of an Aero-Engine Fan Blade with Consideration of Bypass and Core Performance", June 8th-12th 2015, Sydney, Australia.
53. Chahine, C., Verstraete, T., He, L.: "On the Validity of Decoupled Flutter Prediction Methods for Composite Fan Blades", 14th International Symposium on Unsteady Aerodynamics, Aeroacoustics and Aeroelasticity of Turbomachines, September 7th-11th 2015, Stockholm, Sweden.
54. Chahine, C., Verstraete, T., He, L.: "Multidisciplinary Optimization of Aero-Engine Fan Blades", 6th Symposium of VKI PhD research, March 11th-13th 2015, Von Karman Institute for Fluid Dynamics, Rhode-Saint-Genese, Belgium.
55. Caloni, S.; Shahpar, S.; Coull, J. D. (2015) "Numerical investigations of different tip designs for shroudless turbine blades", 11th European Turbomachinery Conference, ETC11, March 23-27th 2015, Madrid, Spain.
56. Caloni, S.; Shahpar, S. (2015) "Investigation into coupling techniques for a high pressure turbine blade tip" ASME Turbo Expo 2015, June 15-17th 2015, Montreal, Canada.
57. Caloni, S., Shahpar, S. (2016) "Multi-Disciplinary Analyses for the Design of a High Pressure Turbine Blade Tip" ASME Turbo Expo 2016, June 13-17th 2016, Seoul, South Korea
58. Caloni, S.; Shahpar, S.; Coull, J. D. (2016) "Numerical investigations of different tip designs for shroudless turbine blades" IMechE part A "Journal of Power and Energy" (accepted for publication, the publisher is finalising the article).
59. Caloni, S., Shahpar, S. (2016) "Multi-Disciplinary Analyses for the Design of a High Pressure Turbine Blade Tip" ASME Journal of Turbomachinery (submitted).
60. Caloni, S., Shahpar, S., Kovoloev, Y., Toropov, V. (2016) "Multi-Disciplinary Optimisation of the shroudless turbine tip" under preparation, 2017.
61. Ollar, J., Toropov, V., and Jones, R. (2016) Sub-space approximations for MDO problems with disparate disciplinary variable dependence. Structural and multidisciplinary Optimization, DOI: 10.1007/s00158-016-1496-0.
62. Ollar, J., Mortished, C., Jones, R., Siens, Johann., Toropov, V. (2016) Gradient based hyper-parameter optimisation for well conditioned kriging metamodels. Submitted to structural and multidisciplinary optimization.
63. Schlaps, R., Ollar, J., Shahpar, S., and Toropov, V. (2016) Multi-disciplinary optimization of compressor rotor subjected to ice impact. 11th ASMO-UK/ISSMO International Conference on Engineering Design Optimisation, Munich, Germany, July 18-20, 2016.
64. Ollar, J., Jones, R., and Toropov, V. (2016) Incorporation of bird strike requirements in MDO of an aircraft wing using subspace approximations. 11th ASMOUK / ISSMO International Conference on Engineering Design Optimisation, Munich, Germany, July 18-20, 2016.
65. Mortished C, Ollar, J., Jones R, Benzie P, Toropov V, Siens J (2016) Aircraft wing optimisation based on computationally efficient gradient-enhanced kriging. 57th AIAA/ASCE/AHS/ASC Structures, Structural Dynamics, and Materials Conference, Kissimmee, FL, USA, January 4-8, 2016
66. Ollar, J., Toropov V, Jones R (2015) Adaptive sub-space approximations in trust regions for large scale MDO problems. 56th AIAA/ASCE/AHS/ASC Structures, Structural Dynamics, and Materials Conference, FL, USA, January 5-9, 2015.
67. Ollar, J., Toropov V, Jones R (2014) Mid-range approximations in sub-spaces for MDO problems with disparate discipline attributes. 15th AIAA/ISSMO Multidisciplinary Analysis and Optimization Conference, GA, USA, June 16-20, 2014.
68. Terence Macquart, Marco T. Bordogna, Paul Lancelot, Roeland De Breuker (2015) Derivation and application of blending constraints in lamination parameter space for composite optimisation. Composite Structures, Volume 135, January 2016, Pages 224–235.
69. Lancelot, P.M.G.J., de Breuker, R. (2016). Aeroelastic tailoring for gust load alleviation. Proceedings of the 11th ASMO UK / ISSMO / NOED2016 Conference on Numerical Optimisation Methods for Engineering Design, July 18-20th 2016, Munich, Germany
70. Serhat, G., Faria, T.G., and Basdogan, I. "Multi-Objective Optimization of Stiffened, Fiber-Reinforced Composite Fuselages for Mechanical and Vibro-Acoustic Requirements," 17th AIAA/ISSMO Multidisciplinary Analysis and Optimization Conference, (AIAA 2016-3509), Washington, D.C., 2016.
71. Serhat, G., and Basdogan, I. "Effect of Several Modelling Techniques and Parameters on the Optimization of Composite Laminates for Vibro-Acoustic Requirements," 11th ASMO UK/ISSMO/NOED2016: International Conference on Numerical Optimisation Methods for Engineering Design, Munich, Germany, 2016.
72. Serhat, G., and Basdogan, I. "Comparison of vibro-acoustic performance metrics in the design and optimization of stiffened composite fuselages," 45th International Congress and Exposition on Noise.
73. S. Shahpar (2011). Challenges to overcome for routine usage of automatic optimisation in the propulsion industry, The Aeronautical Journal, 115, paper no. 3637.

Sequential element rejection and admission method (SERA) for topology optimization using a constraint on Perimeter

Ruben Ansola, Alain Garaigordobil, Estrella Veguería

*Mechanical Engineering Department, School of Engineering, University of The Basque Country (UPVEHU),
Alda. Urquijo, s/n, 48013 Bilbao, Spain*

Osvaldo M. Querin

School of Mechanical Engineering, University of Leeds, Leeds LS2 9JT, UK.

Abstract

This paper presents an implementation of the perimeter constraint for topology optimization of elastic structures using the Sequential Element Rejection and Admission Method (SERA). The perimeter constraint allows the designer to control the number of holes in the optimal design and to establish their characteristic length scale. This work shows an improved SERA methodology incorporating a strategy to efficiently control the optimization process satisfying a constraint on structural perimeter. Some benchmark examples are shown to demonstrate the efficiency and capacities of the algorithm.

Keywords Topology optimization · SERA method · Perimeter constraint

1. Introduction

Topology optimization is a computational approach that optimizes material distribution within a fixed design domain and for a given set of loads and boundary conditions such that the resulting layout meets a prescribed set of the design requirements. It is an expanding research field of computational mechanics which has been growing very rapidly and has attracted the interest of numerous applied mathematicians and engineering designers, becoming extremely popular in the last years. Topology optimization has interesting applications in mechanics, multiphysics and micro- and nanotechnologies, allowing for efficient designs with minimal preconceived decisions. Because of the complexity and intricacy of the solutions obtained, topology optimization was often constrained to research and theoretical studies. Recently, additive manufacturing has opened the possibility to overcome limits currently imposed by conventional manufacturing techniques, filling the gap between topology optimization academic research and industrial application priorities, and positioning itself as the missing link towards a fully integrated optimum structural design.

Since the landmark paper of Bendsoe and Kikuchi [1], where a so called microstructure or homogeneization based approach was used, numerical methods for topology optimization have been investigated extensively. At present the most popular topology optimization method is the SIMP method, which stands for “Solid Isotropic Material with Penalization”, proposed in the late eighties by Bendsoe [2]. A well known problem associated with topology optimization is that the optimal solution depends on the discretization level, as observed in many applications based on the finite element method. In order to ensure existence of solutions to the topology optimization problem, some sort of restriction on the resulting design must be introduced, combining the power law approach with, e.g., a perimeter constraint [3]. During last years, Level Set Methods have emerged as an attractive and promising alternative to perform structural shape and topology optimization, inspired in the work on topological derivatives by Sokolowski and Zochowski and the paper by Sethian and Wiegman [4]. Apart from above mentioned approaches, a number of heuristic or intuition based approaches have effectively addressed a variety of size, shape and topology optimization problems. An important branch of these approaches for topology optimization is the evolutionary structural optimization approach (ESO) by Xie and Steven [5]. The initial concept was that by systematically removing

inefficient material (elements with the lowest strain energy density), the structure evolves towards an optimum. Its application in topology optimization of continuum media is quite extensive, see e.g., [5]. Although initially solely based on intuition, this basic idea has developed from simple hard-kill strategies to more efficient soft-kill bidirectional schemes (BESO), which allow efficient materials to be added in addition to the inefficient ones being removed [6]. The newer BESO method has demonstrated its strength in solving a variety of topology optimization problems, but as it is presently defined, it uses a power law (SIMP) parametrization strategy and standard filtering techniques similar to those used in the density approach in order to stabilize results, so it could be categorized as a discrete update version of the standard SIMP scheme. Rozvany and Querin [7] proposed some improvements of this method under the term SERA (Sequential Element Rejection and Admission), where a “virtual material” was introduced, without the use of any intermediate densities or power law interpolations. Additionally, two separate criteria are considered in the topology optimization process by SERA method, where the sensitivity numbers of real and virtual material present in the domain are sorted out separately. These ideas were developed for fully stressed design and extended to most of the classical problems in structural topology optimization and compliant mechanisms design [8,9].

This novel perimeter control algorithm works with the two separate lists/criteria proposed in the SERA method and analyzes the effect in this constraint when an element is removed or added through the optimization process, since it has different effects on the structural perimeter depending on its current connections with the neighboring elements. The classical algorithm based on a continuous approximation of the perimeter is substituted here by a discrete implementation of the algorithm, without the use of any intermediate densities or power law interpolations necessity. Preliminary results show the capacity of SERA method in combination with perimeter control and are demonstrated through different numerical examples.

2. SERA method + perimeter constraint

The perimeter of a mechanical element Ω^{mat} is defined as the sum of the lengths/areas of all inner and outer boundaries [10]. The final value of the perimeter will therefore depend on the mesh refinement level; however, the aim of this algorithm is to control the perimeter, whose value is only used as a reference.

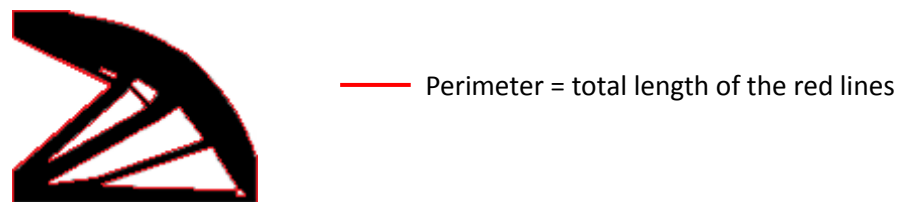


Figure 1: Physical representation of the perimeter of a mechanical element Ω^{mat}

For this sake, the first step should be then to classify elements according to their material status and the effect over the perimeter when their material status switches. According to the work by Yang et al [11] the elements can be classified in five different groups named E4, E3, E2, E1 and E0 and the type of elements for each of the groups are the one represented in figure 2.


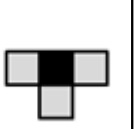
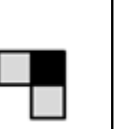

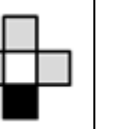
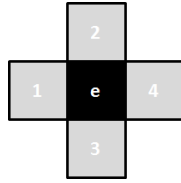
					
ΔP_{real}	4	2	0	-2	-4
ΔP_{void}	-4	-2	0	2	4

Figure 2: Type of element

According to the table above, if an element from group E4 switches its material status, the change on the perimeter is ± 4 , depending on if the element changes from real to void or vice versa. If the E4 element becomes real, the amount of free edges lowers in 4 and if it switches from real to void the number of free edges increases in 4. This same analysis can be done for every of the groups. E2 is the special group, and even if an element changes the material status, the perimeter does not suffer any change as the number of free edges remains equal.

Generally SERA method starts from a fully filled or a fully void domain, therefore at the first iteration every element belongs to group E0 and the value of the initial perimeters are 0 for the fully void domain and $2 \cdot (\text{elements in X} + \text{elements in Y})$ for the fully filled domain. It is recommended to use a fully void starting domain when the objective perimeter is below the perimeter of the fully filled domain ($P_{O_{fullyfixed}} > P_{obj}$). The sensitivities towards the elemental density of the perimeter is represented by the next equation,



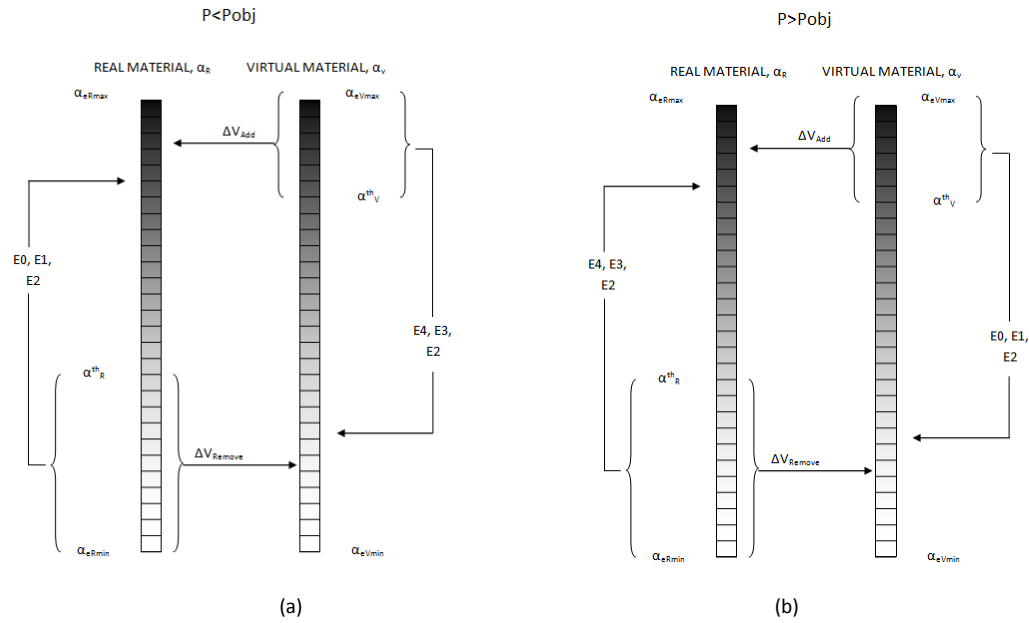
$$\delta S = (-1)^{p_e} \cdot (4 - 2 \cdot (\rho_1 + \rho_2 + \rho_3 + \rho_4)) \quad (2.1)$$

Figure 3: Element density reference name

Where p_e is the density of the actual element and ρ_1, ρ_2, ρ_3 and ρ_4 are the densities of the 4 surrounding elements.

Once the elements are classified, we must consider their position on the two lists in order to control their removal or addition. In this point, the designer can face two situations, first $P(i) < P_{obj}$, where the objective perimeter is greater than the current perimeter of the structure; and $P(i) > P_{obj}$, where the current perimeter overcomes the objective value. Whatever situation is faced one must ensure that the objective perimeter is met so it must be ensured that not only the appropriate elements are removed, but also that those that will be added are appropriate too. For this reason, we should analyze the location of those elements in the lists and ensure that non desired elements are not added/removed.

In case of the situation where $P < P_{obj}$ that the perimeter must be increased, analyzing the figure 2, we can conclude that elements to be removed belong to groups E₄, E₃ & E₂ and elements to be added belong to groups E₀, E₁ & E₂. On the contrary, if $P > P_{obj}$ where the perimeter must be reduced, elements to be removed should belong to groups E₀, E₁ & E₂ and elements to be added should belong to groups E₄, E₃ & E₂. Figure 4 shows how the lists are transformed when these changes are introduced.


 Figure 4: Two list procedure with element transportation. (a) $P < P_{obj}$, (b) $P > P_{obj}$

For $P < P_{obj}$, in the real material list, the elements that belong to groups E0, E1 and E2 are moved to the side above the sensitivity threshold value so that they are maintained real and only elements belonging to groups E4 and E3 are kept in the removing area. In the same case but for the void material list, the same process is followed for locating elements belonging to groups E4, E3 and E2 in the non-adding area, below the threshold value. For $P > P_{obj}$ the methodology is equal but with the opposite purpose.

The element relocation is done by manipulating the sensitivity numbers of the affected elements. For the real material lists, the sensitivity of the elements that are relocated is changed to $\alpha_e = \alpha_{Rmax}$, and for the list of void elements, the sensitivity of those to be relocated is changed by $\alpha_e = \alpha_{Vmin}$. This process allows controlling the elements to be removed/added enhancing the perimeter controlling process.

In order to ensure that checkerboard patterns are avoided, we are not going to include elements that belong to the group E2 in the relocating process and they will keep their original sensitivity number. For low objective perimeter values this issue is negligible but when greater perimeter values are used and the checkerboard is more likely to appear, maintaining the original sensitivity number in elements from group E2 reduces the possibility that two elements are connected by just one point and checkerboards are avoided.

Once the elements are moved inside the lists, the next step is the addition and removal process. This process is carried out in the same way than for the ordinary SERA method, see Alonso et al [8].

Next section will show the results of some benchmark examples with the perimeter and volume constrained SERA method.

3. Examples

The goal of these examples is to demonstrate the effectiveness of this code in different geometries and load cases. For each of the examples four different optimizations are posed. The first optimization is a standard compliance minimization problem that seeks to obtain a reference geometry that is compared with the results obtained with the proposed code. The strategy with the perimeter is to pose three different values, one lower than the optimum, one close to it and one greater than it.

As it was previously explained, topology optimization problems need from a restriction in order to ensure existence of solutions. Generally when a perimeter constraint is used the goal is to stablish an upper limit

for the perimeter and the restriction is used in replacement of the filter. In this paper however, we seek a total freedom of the perimeter control and in cases where a high perimeter value is sought, we recommend introducing a small filtering radius in order to avoid possible mesh defects.

3.1. Cantilever beam (I)

A cantilever beam is posed in this example with a force of value $F=1\text{N}$ applied on the left edge's middle node. The beam is discretized with 90×60 elements and the volume fraction is 0.5 for all the cases. The values of the typical parameters are: progression ratio (PR)= 0.03, smoothing ration (SR)= 1.3, material redistribution fraction (β)= 0.0025, filter radius (r_{min})= 2.

Figure 4 shows the results for every of the optimizations. Also, it represents the optimized structure and the obtained perimeter value for the compliance minimization problem. This perimeter value is used as a reference value and for the next optimizations different values for that parameter are used, one below the reference value, one similar to it and one greater value.

For the lower value of the perimeter the number of needed iterations is greater than the nominal while for the other values the number of iterations remains quite the same. It is also appreciable the accurateness that the objective perimeter value and the objective volume fraction are approximated with, with errors of 4.45%, 0.4% and 0.93% for the perimeter value respectively. The number of member increases significantly with the greater values of the objective perimeter, which demonstrates the capacity of the code to control the complexity of the structure.



Iteration: 41
Volume fraction: 0.508
Obj. function: 16.021174
Perimeter: 994.000000




Pobj = 270	Pobj = 1000	Pobj = 1500
		
Iteration: 149 Volume fraction: 0.509 Obj. Function: 33.988678 Perimeter: 282.0	Iteration: 40 Volume fraction: 0.506 Obj. Function: 15.978823 Perimeter: 996.0	Iteration: 39 Volume fraction: 0.508 Obj. Function: 16.256312 Perimeter: 1486.0

Figure 5: Problem statement and results of cantilever beam (I) for perimeter values of 270, 1000 and 1500

3.2. Cantilever beam (II)

This time, the same cantilever beam is posed but with a force of $F=1\text{N}$ is applied on the lower right corner.. The beam is discretized with 90×60 elements and the volume fraction is 0.5 for all the cases. The values of the typical parameters are those used in the previous example, except for the filter radius that this time has a value of $r_{min}=1.1$.



Iteration: 75
Volume fraction: 0.508
Obj. function: 16.296981
Perimeter: 1158.000000




Pobj = 900	Pobj = 1200	Pobj = 1500
		
Iteration: 146 Volume fraction: 0.501 Obj. Function: 16.763516 Perimeter: 872.0	Iteration: 33 Volume fraction: 0.505 Obj. Function: 16.565073 Perimeter: 1178.0	Iteration: 45 Volume fraction: 0.507 Obj. Function: 16.517984 Perimeter: 1450.0

Figure 6: Problem statement and results of cantilever beam (II) for perimeter values of 900, 1200 and 1500

From the results of this examples we can extrapolate the same conclusions than from the previous and this time, the errors obtained in the approximation of the objective perimeter value are 3.11%, 1.83% and 3.33%.

3.3. Bridge structure

This time a bridge structure is optimized following the same scheme used in the previous examples. Once again the results show the same characteristics been this time the errors approaching the perimeter of 0%, 0% and 0.4%.



Iteration: 41
Volume fraction: 0.507
Obj. function: 7.078364
Perimeter: 1342.000000




Pobj = 500	Pobj = 1200	Pobj = 1500
		
Iteration: 104 Volume fraction: 0.509 Obj. Function: 8.655480 Perimeter: 500.0	Iteration: 44 Volume fraction: 0.507 Obj. Function: 7.080515 Perimeter: 1200.0	Iteration: 33 Volume fraction: 0.506 Obj. Function: 7.116379 Perimeter: 1494.0

Figure 7: Problem statement and results of a bridge structure for perimeter values of 500, 1200 and 1500

4. Conclusions

The results obtained with the proposed code are representative of the accurateness of the algorithm used and enable the designer not only to control the complexity of the structure and the amount of members, but also to control the smoothness of the geometry. The perimeter is a very effective property in the control of the number of members formed in the final geometry and this fact forms the basis for further research on the control of the complexity.

5. Acknowledgments

This work was supported by The European Regional Development Fund (ERDF-FEDER) and the Ministry of Education and Science in Spain through the project DPI2015-64863-R

6. References

- [1]Bensoe M.P., Kikuchi N., "Generating optimal topologies in structural design using a homogeneization method", *Comput Methods Appl MEch Eng* Vol. 71, pp. 197-224, 1988.
- [2]Bensoe M.P., "Optimal shape design as a material distribution problem", *Struct Optim* Vol. 1, pp. 193-202, 1989.
- [3]Haber R.B., Bensoe M.P., Jog C.S., "A new approach to variable topology shape design using constraint on the perimeter", *Struct Optim* Vol. 11, pp. 1-12, 1996.
- [4]Sethian J.A., Wiegman A., "Structural boundary design via level set and immersed interface methods", *J Comp Phys* Vol. 163, pp. 89-528, 2000.
- [5]Xie Y.M., Steven G.P., "Evolutionary structural optimization", Berlin, Heidelberg, New York: Springer-Verlag, 1997.
- [6]Querín, O.M., Evolutionary structural optimization: stress based formulation and implementation. Ph.D. Thesis, Department of Aeronautical Engineering, University of Sydney, Australia, 1997.
- [7]Rozvany G.I.N, Querín O, "Sequential element rejections and admissions (SERA) method: applications to multiconstraint problems", *Proceedings of the 10th AIAA/ISSMO Multidisc. Anal. Optim. Conference*, Albany, NY, Aug.-Sept. 2004.
- [8]Alonso C., Querín O.M., Ansola R., "A Sequential Element Rejection and Admission (SERA) method for compliant mechanisms design", *Struct Optim* Vol. 47, pp. 795-807, 2013.
- [9] Alonso C., Ansola R., Querín O.M., "Topology synthesis of multi-material compliant mechanisms with a Sequential Element Rejection and Admission method", *Finite Elem Anal Des* Vol. 85, 11-19, 2014.
- [10] Bendsoe M.P., Sigmund O. "Topology Optimization: Theory, Methods and Applications." Springer-Verlag Berlin Heidelberg, 2003-2004.
- [11]X.Y. Yang, Y.M. Xie, J.S. Liu, G.T. Parks and P.J. Clarkson. "Perimeter control in the bidirectional evolutionary optimization method", *Struct Multidisc Optim* Vol. 24, 430-440, Springer-Verlag, 2003.

Wingbox adaptive parametric modeling and its application to structural optimization

Anna L. Arsenyeva* and Fabian Duddeck†

Chair of Computational Mechanics, Technische Universität München (TUM), Munich, 80333, Germany

The research presented in this paper is focused on the development of an adaptive geometric model for the wingbox for structural optimization. The external wing shape is defined here with a set of parameterized NACA airfoils although the wingbox components can adapt to any closed wing skin surface. The implemented parametric model allows easy variation of different internal structural components of the wingbox, e.g. number and location of ribs/spars/stringers, their shape, thicknesses etc. The flexibility of the model allows the use of numerical optimization for automatized design improvement, considering structural design goals. To illustrate the potential of the parametric modeling, an efficient two-level optimization process is proposed, aimed to find the optimal global layout of the wingbox at the first level, and to refine subcomponents design (e.g. ribs) at the second level.

Nomenclature

EA = Evolutionary algorithm
COBYLA = Constrained optimization by linear approximation

I. Introduction

In order to achieve economic feasibility, fuel efficiency and cost reductions [1], careful optimization of each aircraft component is one of the main goals in the aerospace industry. In particular, weight reduction is important for structural components.

Wing optimization has gained high attention in the recent engineering optimization literature. A large number of papers focus on the optimization of the external aerodynamic wing shape, e.g. [2-4], often without consideration of the internal structure or with simplified optimization of internal structure based on sizing [4,5]. Additional popular areas are optimization of composite wingbox components [6] and wingbox topology optimization [7,8]. Development of generic wing models for preliminary design [9-12] is another important goal for efficient aircraft design process. Only a few papers address complex wingbox layout/shape optimization. For example, an optimization procedure where structural components can be added or removed automatically is proposed in [9]. Three-dimensional topology optimization is employed in [10,11] for finding general indications about placement and shape of wingbox internal components.

High computational costs of refined multi-disciplinary simulations, including aerodynamics, structural analysis and dynamic analysis, often result in infeasible optimization time. Due to this, fast parametric models need to be used at the preliminary design stages in order to find promising designs within a realistic time, while providing sufficient accuracy. Hence, this paper presents a flexible and fast parameterized wingbox model to find the optimal design of internal components. Additionally, a two-level optimization approach is proposed, including global wingbox layout optimization and sub-components shape optimization. Special stiffener-based parameterization for the ribs shape optimization, as well as an automatic sub-modeling and load extraction procedure for different wing box components, were implemented within this work.

* Research assistant, anna.arsenyeva@tum.de.

† Professor for Computational Mechanics, duddeck@tum.de.

II. Modeling of wing and wingbox

The outer wing shape is defined here by a set of NACA-type 2D airfoils and global wing parameters, such as sweep angle, dihedral angle, twist and length of the wing. The wing dimensions are taken from the A320 [13,14]; main dimensions for each section are given in Table 1. All airfoil parameters can be considered as design variables for optimization. Nevertheless, in the current work we focus only on internal structure optimization for a given wing outer shape. The approach can be transferred to arbitrary closed wing skin surfaces.

	Root section	Middle section	Tip section
Chord length	6 m	3.7 m	1.5 m
Profile thickness	NACA 2415	-	NACA 2410
Dihedral angle			-
Sweep angle			
Wingspan	34.1 m		

Table 1: Airbus A320 wing dimensions [13, 14]

Different parameters of the internal wing structures can be defined. The number and location of ribs/spars/stringers, their shape and thickness, which may vary linearly along the length for skin and spars components [15], can be considered. In this work, geometry and finite element (FE) models of the wing are generated using a combination of Python and ANSYS APDL scripting, which enables a flexible parameterization. In Figure 1, examples of the internal components of the wing model, which are used in the current optimization setup, are shown.

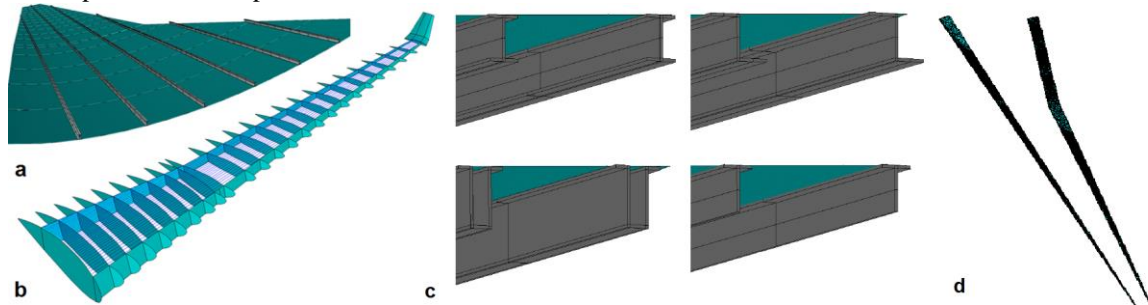


Figure 1. Wing skin with the stringers (a); Front / rear / middle ribs, spars and stringers definition for two sectioned wing with winglet (b); Different types of stringers cross sections (c); Tapered thicknesses changing for spars components (d)

Several types of loads are considered here, including static loads related to the weight of engines and aerodynamic forces. The aerodynamic loads were taken here from a simplified approach via XFOIL, see <http://web.mit.edu/drela/Public/web/xfoil/>, to allow method development without high computational costs. If more accurate data is needed, full 3D CFD can be integrated into the approaches easily (e.g. by ANSYS Fluent, <http://www.ansys.com/Products/Fluids/ANSYS-Fluent>, Figure 2 shows an exemplary comparison of pressure distributions from both approaches). Because this work is focused on interior structures, the outer shape is not modified. Hence, the aerodynamic pressures can be computed once and then used for all simulations in the optimization. The computed pressure distribution is mapped automatically to all structural models.

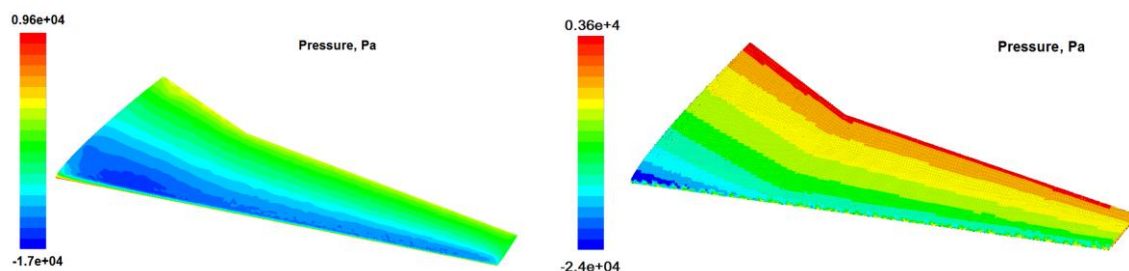


Figure 2. Pressure distribution for a wing (left: via ANSYS Fluent, right: via XFOIL)

A two-level optimization process is proposed as shown in Figure 3. The first level involves optimization of the "global" parameters of wingbox such as number, position and approximate thicknesses for various components. The objective here is to reduce the mass, while satisfying local skin deflection and buckling constraints. The second level includes optimization of the wingbox subcomponents (ribs, spars, etc.) for fixed global layout of the wingbox, obtained in the first level. Subcomponent optimization can include different approaches such as the steered fiber composite optimization for the wing skin [16], topology and shape optimization of ribs [15], etc.

At the beginning, the optimal number and positions of the ribs are determined. To reduce the number of wingbox parameters and consequently the computational effort for optimization, two different parameterization levels are introduced. At the first stage, a coarse parameterization is used, where the rib spacing for each section is defined using the pitch parameter, which can vary linearly within every section (see Figure 4). Thus, two parameters define rib positions for each section (pitch and pitch gradient), resulting in total 4 parameters. This setup allows using a global Evolutionary Strategy (ES) to find a good initial design, which is feasible w.r.t. local skin deflection and buckling constraints. At the second stage, a finer parameterization is applied, where the position and angle of each rib is varied individually in the vicinity of the previously obtained solution by moving the rib's start and end points along the spars. At this optimization process local optimization methods (e.g. gradient-based methods, COBYLA [17]) are used to obtain a refined design.

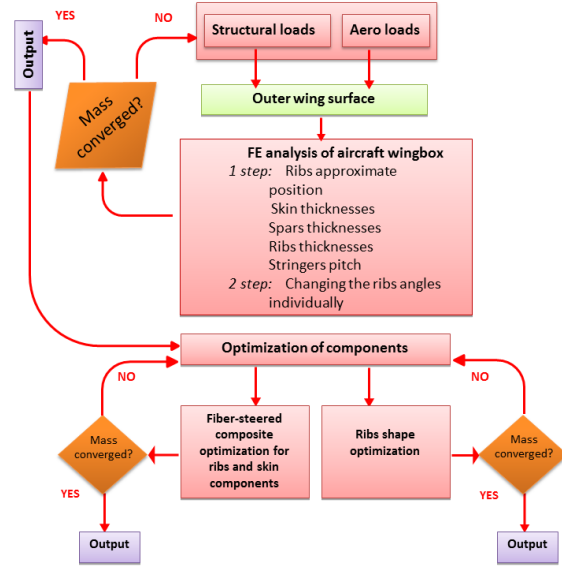


Figure 3. Workflow for component optimization

III. Sensitivity analysis

The impact of the first-level design variables (in total 14 parameters) on the structural responses, such as weight, maximum local skin deflection between each pair of ribs and maximum critical buckling load, is determined for the two different methods discussed above to compute aerodynamic loads. Two design-of-experiments schemes using Latin-Hypercube sampling are performed with aerodynamic loads from XFOIL and Fluent. The Spearman correlation matrices between responses and the first level design parameters are shown in Figure 4. It can be noted, that spar and shell thicknesses and ribs pitch have higher impact on weight and critical buckling. For the local skin deflections, the number and positions of ribs are very important. Hence, ribs are responsible for maintaining the aerodynamic shape. The XFOIL results give very similar correlations compared to the Fluent results, i.e., the simpler approach can at least capture general trends accurately. Because the XFOIL approach is much faster it is used for the preliminary global optimization studies presented in this study.

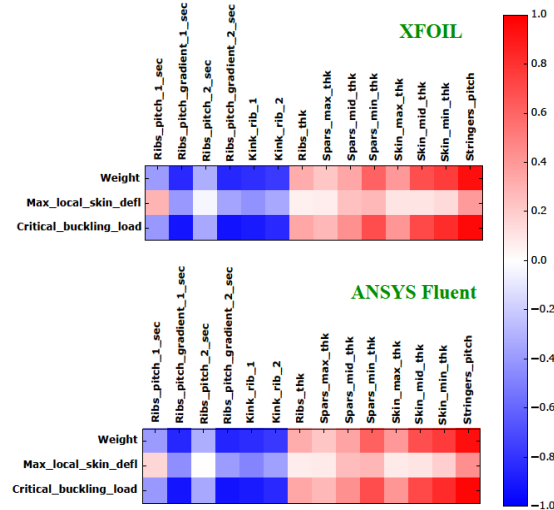


Figure 4. Spearman correlation (300 designs)

IV. Optimization of ribs number and their positions

At the first stage, the rib spacing for each section is defined using the pitch parameter, which can vary linearly within the section (see Figure 5). Besides that, individual parameters for the ribs at the wingbox kink, spars/ribs/skin thicknesses and stringer pitch are considered. In total 14 parameters are used here. The main objective of this optimization was minimization of total wing weight. Critical buckling of the wing and local deflection of the skin panels between the ribs are used as constraints. At the second stage, the position and angle of each rib is varied individually by moving the rib's start and end points, starting from the previously obtained solution.

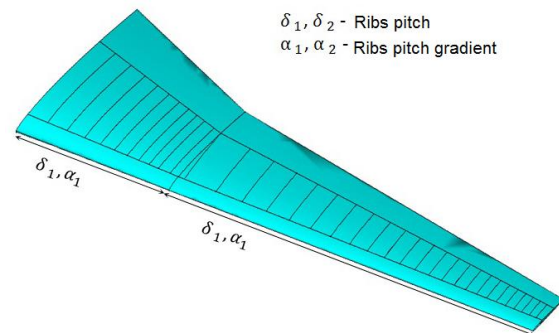


Figure 5. Parameters for finding ribs preliminary number and position

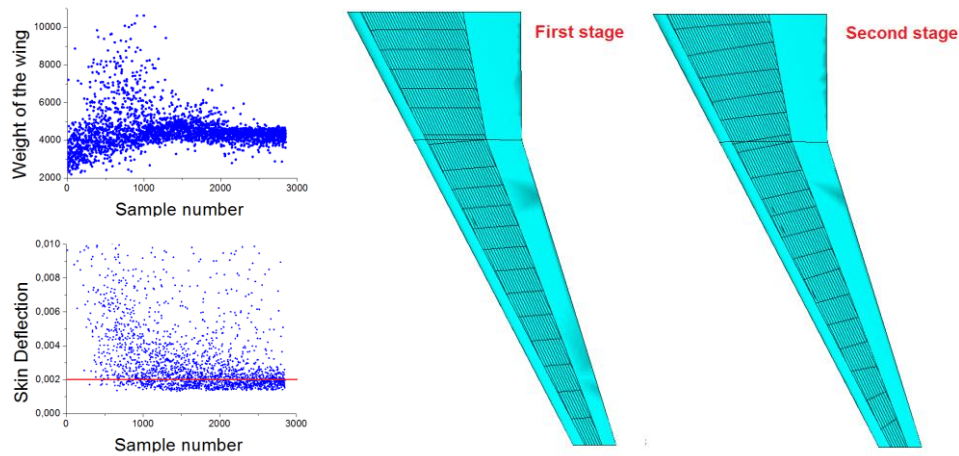


Figure 6. Convergence for the skin deflection constraint; left: first level (ES) result, right: second level (COBYLA) result

In Figure 6 (right), exemplary optimal results obtained using the proposed two-step approach are shown. After the first stage, the best feasible design (see Figure 6 left) obtained via an ES strategy [17] has the overall mass of 3342 kg and for COBYLA 3364 kg. The refinement step further reduces the mass to 3241 kg (see Figure 6 right). This brings a final weight reduction of 6.9%, compared to the initial 3480 kg, with all constraints being fulfilled. Table 2 provides a short summary of the optimization results.

	Approximate ribs position (ES)	Approximate ribs position (COBYLA)	Individual ribs position (COBYLA)
Number of FEA	2850	107	255
Wing weight reduction	-4 %	-3.3 %	-6.9 %
Skin Deflection (constraint)	1.99 mm	2 mm	2 mm
Buckling (constraint)	0.98	0.87	0.98

Table 2: Optimization results for weight reduction

V. Rib stiffeners topology like shape optimization

For a detailed optimization of the rib design, a topology-like optimization of stiffeners' location and size is considered. The main idea is to modify the ribs "topology" by a set of varying stiffeners. Each stiffener is defined using four parameters: x -, y - coordinates of reference point, turning angle and the width of the stiffener (Figure 7). The rectangular areas, modeling the stiffeners, are created over the rib 2D region and cut by the rib outer contour. After that, all these areas are merged together to form a new rib shape. This allows some stiffeners to merge together, thus the number of stiffeners may vary during the optimization, up to a predefined maximum.

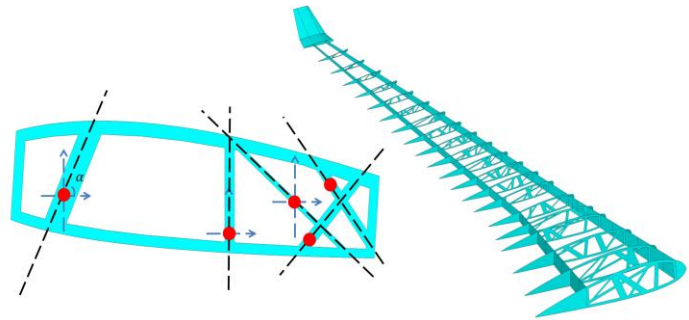


Figure 7. Example of Point-Angle-Width parameterization: Ribs topology definition (left), example of ribs topology in the global wing model (not optimal) (right)

The corners of the "holes" are rounded automatically with fillets between any two corner lines. This approach allows to perform topology-like shape optimization while including various constraints (e.g. displacements, stresses, buckling, etc.), which is not possible in standard density-based topology optimization. At the same time, for similar optimization tasks (stiffness maximization), this approach gives similar results to the topology optimization; an exemplary result from this rib shape optimization is shown in Figure 8 (right). The objective for shape optimization is to minimize an average displacement for top and bottom sides of ribs, while for topology optimization, maximizing stiffness is taken. A weight reduction of at least 64% from a full rib is required here for both methods. The proposed stiffeners placement method and the standard topology optimization show very similar optimal rib topology.

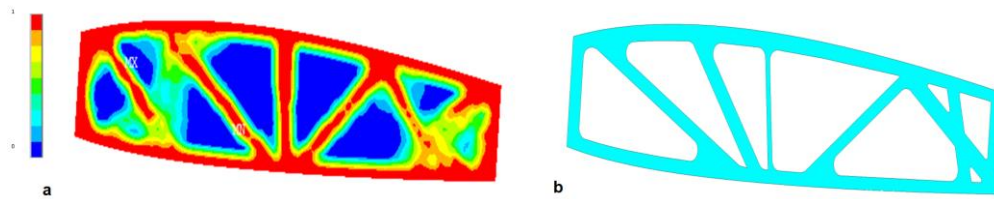


Figure 8. Left: Optimal result by standard topology optimization (a) and right: optimal result obtained by the proposed shape optimization (b)

VI. Conclusion and outlook

An approach for shape optimization of the wing box combining the global level optimization of the full wing box parametric model and the local level optimization of single components is proposed and tested. For subcomponents, specifically ribs, a parameterization is proposed for topology-like shape optimization of stiffeners location and size. The obtained results show comparable structures for both approaches, for the proposed stiffeners placement method and standard topology optimization. In future research, shape optimization for all ribs will be performed and the global model for the further shape optimization will be updated to realize an iteration loop.

Acknowledgments

The support of the Aerospace Multidisciplinary Enabling Design Optimisation project (AMEDEO), Marie Curie Actions – Research Fellowship Programme, Seventh Framework Programme (European Framework FP7, Project No. 316394), is acknowledged.

References

- [1] N.N. Reducing emissions from aviation through carbon-neutral growth from 2020; working paper developed for the 38th ICAO Assembly, 2013, www.iata.org/policy/environment/Documents/atag-paper-on-cng2020-july2013.pdf.
- [2] J.J. Reuther, A. Jameson, J.J. Alonso, M.J. Rimlinger and D. Saunders, Constrained Multipoint Aerodynamic Shape Optimization Using an Adjoint Formulation and Parallel Computers, Part 1, *Journal of Aircraft* **36**(1): 51-60, 1999.
- [3] C.A. Mader, J.R.R.A. Martins, Stability-Constrained Aerodynamic Shape Optimization of Flying Wings, *Journal of Aircraft* **50**(5): 1431-1449, 2013.
- [4] G.K.W. Kenway, J.R.R.A. Martins, G.J. Kennedy. Aerostructural optimization of the Common Research Model configuration. In: 15th AIAA/ISSMO Multidisciplinary Analysis and Optimization Conference, Atlanta, GA, USA, 2014.
- [5] G.K.W. Kenway, J.R.R.A. Martins, Multi-Point High-Fidelity Aerostructural Optimization of a Transport Aircraft Configuration, *Journal of Aircraft* **51**(1):144-160, 2014.
- [6] J.K.S. Dillinger, M.M. Abdalla, T. Klimmek, Z. Gurdal. Static Aeroelastic Stiffness Optimization and Investigation of Forward Swept Composite Wings. In: 10th World Congress on Structural and Multidisciplinary Optimization, Orlando, FL, USA, 2013.
- [7] B.K. Stanford, P.D. Dunning. Optimal Topology of Aircraft Rib and Spar Structures under Aeroelastic Loads. 10th AIAA Multidisciplinary Design Optimization Conference, Maryland, USA, 2014.
- [8] L. Krog, A. Tucker, G. Rollema. Application of Topology, Sizing and Shape Optimization Methods to Optimal Design of Aircraft Components, Altair Engineering, 2011.
- [9] W. Wang, S. Guo, W. Yang. Simultaneous Partial Topology and Size Optimization of a Wing Structure Using Ant Colony and Gradient Based Methods. *Engineering Optimization* **43**: 433-446, 2011.
- [10] D. Locatelli, R. Haftka. Topology Optimization of Transport Wing Internal Structure. *Journal of Aircraft* **33**: 232-233, 1996.
- [11] V. Balabanov, S. Mulani, R. Kapania. Wing-Box Weight Optimization Using Curvilinear Spars and Ribs (SpaRibs). *Journal of Aircraft* **48**: 1671-1684, 2011.
- [12] F. Dorbath. A FlexibleWing Modeling and Physical Mass Estimation System for Early Aircraft Design Stages, PhD thesis, Technische Universität Hamburg-Harburg, Germany, 2014.
- [13] A320: Aircraft Characteristics Airport and Maintenance Planning, AIRBUS S.A.S. Customer Services Technical Data Support and Services, France, Revision No. 29 - May 01/2015.
- [14] K. Hünecke, Die Technik des modernen Verkehrsflugzeuges, Motorbuch Verlag, Germany, 2008.

- [15] A. Arsenyeva, F. Duddeck, Efficient and adaptive parametric modeling for shape optimization of a wingbox, In: 3rd ECCOMAS Young Investigators Conference, Aachen, Germany, 2015.
- [16] S.H. Hesse, A. Arsenyeva, D.H.-J.A. Lukaszewicz, F. Duddeck, A Parameterized Surface Method to Determine Optimal Variable Stiffness Layup by Global Search, In: 20th International Conference on Composite Materials, Copenhagen, Denmark, 2015.
- [17] B. M. Adams, K. R. Dalbey, M. S. Eldred and L. P. Swiler, DAKOTA, a multilevel parallel object-oriented framework for design optimization, parameter estimation, uncertainty quantification, and sensitivity analysis, Version 5.2 Reference Manual, Sandia National Laboratories Albuquerque, New Mexico, 2011.

Evaluating Sensitivity of Stochastic Search Techniques to Profile List Ordering in Discrete Sizing of Steel Frames

Saeid Kazemzadeh Azad*

Atilim University, Department of Civil Engineering, Ankara, Turkey

In practical design of steel frame structures mostly the structural members are selected from a list of available sections resulting in a discrete optimization problem. In recent decades, considerable research work has been devoted to development of efficient algorithms for tackling discrete sizing optimization problems of steel structures. In spite of the large number of developed algorithms, only a few studies address non-algorithmic issues, such as profile list ordering, affecting the general performance of the algorithms in the course of optimization. This study is an attempt to investigate the effect of the order of sections in a profile list on general performance of stochastic search algorithms or the so called metaheuristics. To this end, sensitivity of recently proposed metaheuristic algorithms to different profile lists is investigated through practical sizing optimization of a real size steel frame structure according to AISC-LRFD specification. The numerical results reveal the effect of profile list ordering on optimality of final solutions as well as convergence rate of the investigated algorithms.

Nomenclature

AISC	= American Institute of Steel Construction
LRFD	= Load and Resistance Factor Design
\mathbf{I}	= vector of integer values
W	= weight of the structure
A_i	= cross sectional area for member group i
ρ_i	= unit weight of the steel section selected for member group i
L_j	= length of member j
N_m	= total number of structural members
N_d	= number of design groups
N_t	= total number of members in a design group
IEL	= element number
NEL	= total number of elements
ϕ	= resistance factor
C_{IEL}^i	= axial and flexural strength design constraint
C_{IEL}^v	= shear strength design constraint
C_D^l	= maximum lateral displacement design constraint
C_F^d	= interstory drift design constraint
F_x	= induced lateral seismic force at level x
h_n	= height of the building
T	= period of the structure
E	= modulus of elasticity
F_y	= yield stress
V	= seismic base shear
W_s	= total dead load of the building
CG_i	= column group i
B_i	= beam group i
BR_i	= bracing group i
ASCE	= American Society of Civil Engineers

Saeid Kazemzadeh Azad: saeid.azad@atilim.edu.tr

*Assistant Professor, Atilim University, Department of Civil Engineering, Ankara, Turkey.

I. Introduction

In the recent years numerous research studies have been conducted on proposing new strategies for automated design optimization of structural systems. Specifically, in case of steel frame structures the current academic trend is towards developing novel algorithms based on sophisticated stochastic search techniques or the so called metaheuristics¹. The popularity of stochastic search techniques such as simulated annealing², genetic algorithm^{3,4}, evolution strategies⁵, particle swarm optimization⁶, and ant colony optimization⁷, can be attributed to their capability of locating promising solutions for complicated structural optimization problems, as well as their independency to derivatives of objective functions. Moreover, metaheuristics are able to handle both discrete and continuous design variables and can be employed for solving a wide range of engineering optimization problems. In general, both trajectory and population based metaheuristic approaches aim to find the global optimum in the solution space through random moves. The key difference between the algorithms lies in the way that each algorithm suggests the next move in the solution space. In order to decide on a reliable search direction in the solution space researchers investigate different strategies and approaches. So far, these attempts have resulted in development of numerous efficient structural optimization methodologies. Although it is of a great importance to study and enhance the performance of optimization techniques by developing new search strategies, investigating non-algorithmic issues affecting the general performance of algorithms could be fruitful as well.

Basically, design optimization of a steel frame structure is an attempt to find the best combination of design variables that results in a minimum weight or cost design. Meanwhile, for practical applications the final design should satisfy a set of design constraints imposed based on a standard design code. Generally, optimal design of skeletal structures can be divided into three main categories as sizing, shape, and topology optimization. In sizing optimization the cross sectional areas of members are considered as design variables of the optimization problem. Sizing optimization can be divided into two subcategories in terms of the nature of the considered design variables: continuous and discrete. In continuous sizing optimization any positive value can be assigned to cross sectional areas of structural elements. However, this is not the common case in practical applications where structural members should be selected from a predetermined profile list. The latter is referred to as discrete sizing optimization. In shape optimization, the optimal nodal coordinates are sought. Due to practical aspects this type of design optimization is mostly considered in optimum design of truss structures rather than steel frames. In both the aforementioned optimization categories topology of a structure is assumed to be fixed. However, it is sometimes more expedient to search for the optimum topology of a structure which requires considering the presence or absence of structural components. This study covers discrete sizing optimization of steel frames which is the most common case in practical applications.

As noted before, in optimum sizing of steel frame structures the structural members are to be selected from a predetermined list of available profiles resulting in a discrete optimization problem. In the present study it is attempted to investigate the effect of the order of sections in a profile list on general performance of stochastic search algorithms. For this purpose, sensitivity of recently proposed metaheuristic algorithms to profile list ordering is investigated through discrete sizing optimization of real size steel frame structures according to AISC-LRFD⁸ specification. The numerical results indicate the effect of profile list ordering on solution quality and convergence rate of the investigated algorithms. The remaining parts of this paper are organized as follows. The second section briefly describes the optimum design problem of steel frames. In the third section the design optimization instances are investigated. The conclusion of the study is provided in the last section.

II. Discrete sizing of steel frame structures

Typically, in real world applications the steel frame members are selected from a set of available profiles resulting in a sizing optimization problem with discrete variables. For a steel frame composed of N_m members grouped into N_d design groups, the optimum sizing problem according to AISC-LRFD⁸ can be formulated as follows. Here, the objective of optimization is to find a vector of integer values \mathbf{I} (Eq. (1)) representing the sequence numbers of steel sections assigned to N_d member groups

$$\mathbf{I}^T = [I_1, I_2, \dots, I_{N_d}] \quad (1)$$

to minimize the weight, W , of the structure

$$W = \sum_{i=1}^{N_d} \rho_i A_i \sum_{j=1}^{N_i} L_j \quad (2)$$

Where A_i and ρ_i are the cross sectional area and unit weight of the steel section selected for member group i , respectively, N_i is the total number of members in group i , and L_j is the length of the member j which belongs to group i . Here, the optimization problem should be solved under several design constraints, including strength

and serviceability requirements. According to AISC-LRFD⁸ code, the following constraints must be satisfied for the strength requirements.

$$C_{IEL}^i = \left[\frac{P_{uJ}}{\phi P_n} \right]_{IEL} + \frac{8}{9} \left(\frac{M_{uxJ}}{\phi_b M_{nx}} + \frac{M_{uyJ}}{\phi_b M_{ny}} \right)_{IEL} - 1 \leq 0 \quad \text{for} \quad \left[\frac{P_{uJ}}{\phi P_n} \right]_{IEL} \geq 0.2 \quad (3)$$

$$C_{IEL}^i = \left[\frac{P_{uJ}}{2\phi P_n} \right]_{IEL} + \left(\frac{M_{uxJ}}{\phi_b M_{nx}} + \frac{M_{uyJ}}{\phi_b M_{ny}} \right)_{IEL} - 1 \leq 0 \quad \text{for} \quad \left[\frac{P_{uJ}}{\phi P_n} \right]_{IEL} < 0.2 \quad (4)$$

$$C_{IEL}^v = \left[\frac{V_{uJ}}{\phi_v V_n} \right]_{IEL} - 1 \leq 0 \quad (5)$$

In Eqs. (3) to (5), $IEL=1, 2, \dots, NEL$ is the element number, NEL is the total number of elements, $J=1, 2, \dots, N$ is the load combination number and N is the total number of design load combinations. P_{uJ} is the required axial (tensile or compressive) strength, under J -th design load combination. M_{uxJ} and M_{uyJ} are the required flexural strengths for bending about x and y , under the J -th design load combination, respectively; where subscripts x and y are the relating symbols for strong and weak axes bending, respectively. On the other hand, P_n , M_{nx} and M_{ny} are the nominal axial (tensile or compressive) and flexural (for bending about x and y axes) strengths of the IEL -th member under consideration. ϕ is the resistance factor for axial strength, which is 0.85 for compression and 0.9 for tension (based on yielding in the gross section) and ϕ_b is the resistance factor for flexure, which is equal to 0.9. Here, Eq. (5) is used for checking members' shear capacity wherein V_{uJ} is the required shear strength under J -th load combination and V_n is the nominal shear strength of the IEL -th member under consideration. In order to calculate the design shear strength the nominal shear strength is multiplied by a resistance factor ϕ_v of 0.9.

Besides the strength requirements, the serviceability criteria should be considered in the optimum design process. The serviceability constraints considered in this study are as follows:

$$C_D^t = \frac{\Delta_{MaxJ}}{\Delta_{Max}^a} - 1 \leq 0 \quad (6)$$

$$C_F^d = \frac{[\delta_J]_F}{[\delta^a]_F} - 1 \leq 0 \quad (7)$$

Eq. (6) compares the maximum lateral displacement of the structure in the D -th direction ($D=1, \dots, ND$) under J -th load combination Δ_{MaxJ} with the maximum allowable lateral displacement Δ_{Max}^a . Similarly, Eq. (7) checks the interstory drift of the F -th story ($F=1, 2, \dots, NF$) under the J -th load combination $[\delta_J]_F$ against the related permitted value $[\delta^a]_F$; here NF is the total number of stories. Further details related to optimization problem formulation and design constraints can be found in Kazemzadeh Azad et al.⁹

III. Numerical experiments

This section covers evaluation of the effect of profile list ordering on general performance of three contemporary metaheuristic algorithms, namely big bang-big crunch algorithm (BB-BC)^{10,11,12}, and its two enhanced variants i.e. modified (MBB-BC)¹¹ and exponential big bang-big crunch algorithms (EBB-BC)¹². These algorithms are selected based on their promising performances documented in the literature particularly in frame optimization problems. Here, a wide-flange profile list composed of 268 ready sections⁸ is used to size the structural members. In order to investigate the profile list ordering effect, first the optimization process is carried out using a set of ready sections ordered based on cross sectional area values. Next, the profiles are reordered randomly in the list and the new profile list is used for design optimization. The results obtained using each metaheuristic algorithm are compared for both the ordered and unordered profile lists.

A. 135-member steel frame

The design instance considered here is a 3-story steel frame⁹ shown in Fig. 1, consisting of 135 members including 66 beam, 45 column and 24 bracing elements. The stability of the frame is provided through moment-resisting connections and inverted V-type bracing systems along the x direction. For fabrication requirements the 135 members of the frame are collected under 10 member groups. In this example the columns are grouped into four sizing variables in a plan level as corner, inner, side x - z and side y - z columns, and they are assumed to

have the same cross-section over the three stories of the frame. On the other hand, all the beams in each story are grouped into one sizing variable, resulting in three beam-sizing design variables for the frame. Similarly, all the bracings in each story are grouped into one sizing variable, resulting in three bracing-sizing design variables for the frame. The material properties of steel are taken as follows: modulus of elasticity (E) = 200 GPa, yield stress (F_y) = 248.2 MPa, and unit weight of the steel (ρ) = 7.85 ton/m³.

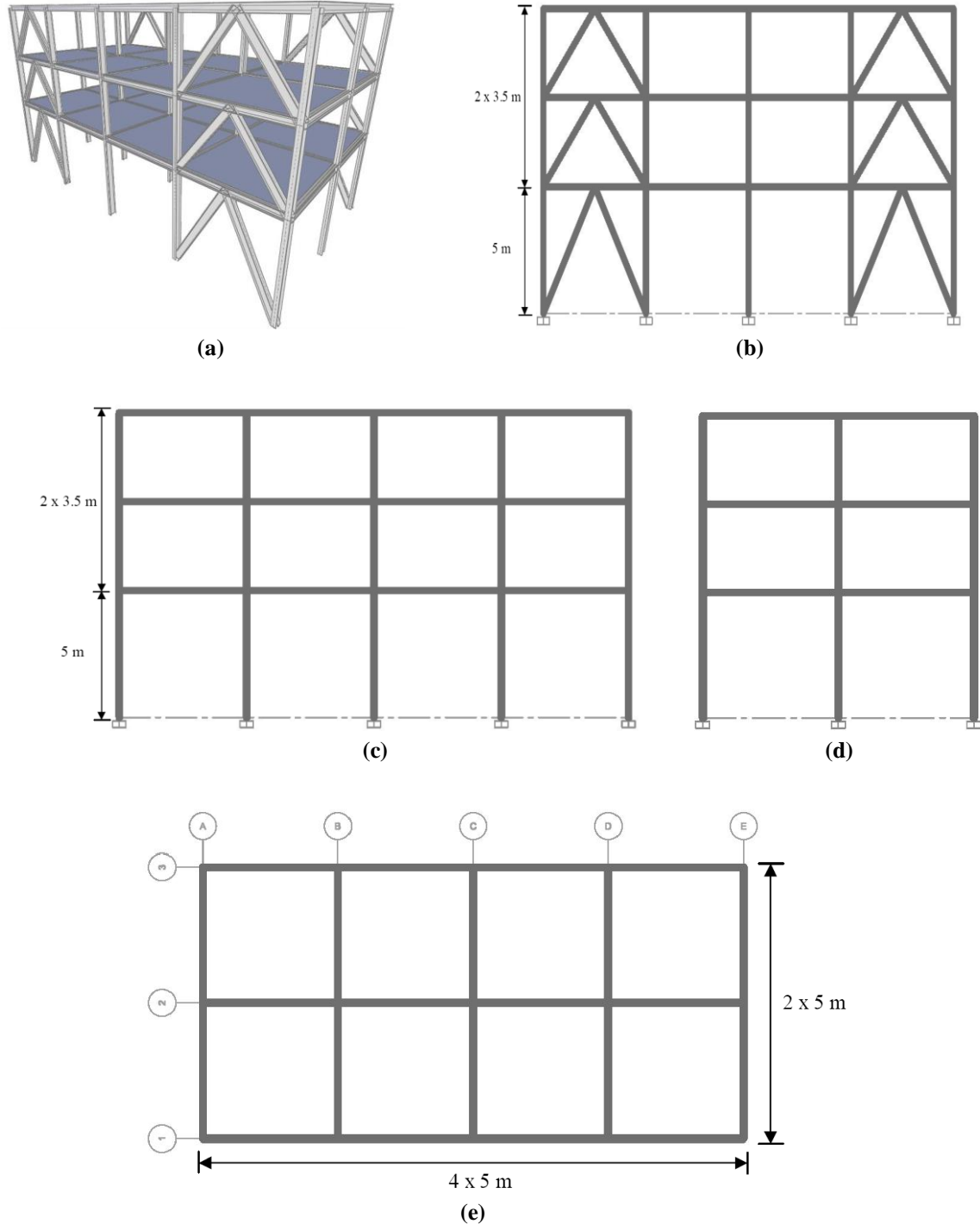


Figure 1: 135-member steel frame, (a) 3-D view (b) side view of frames 1 and 3 (c) side view of frame 2 (d) side view of frames A, B, C, D, and E (e) plan view

For design purpose, the steel frame is subjected to the following 10 load combinations in accordance with ASCE 7-98¹³: (1) $1.4D$, (2) $1.2D + 1.6L$, (3) $1.2D + 1.0E_x + 0.5L$, (4) $1.2D + 1.0E_{ex} + 0.5L$, (5) $1.2D + 1.0E_y + 0.5L$, (6) $1.2D + 1.0E_{ey} + 0.5L$, (7) $0.9D + 1.0E_x$, (8) $0.9D + 1.0E_{ex}$, (9) $0.9D + 1.0E_y$, (10) $0.9D + 1.0E_{ey}$, where D and L denote the dead and live loads, respectively; E_x and E_y are the earthquake loads applied to the center of

mass in x and y directions, respectively; and E_{ex} and E_{ey} are the earthquake loads applied considering the effect of accidental eccentricity of the center of mass in x and y directions, respectively. Based on ASCE 7-98 the amount of eccentricity is set to 5% of the dimension of the structure perpendicular to the direction of the applied earthquake load. The live loads acting on the floor and roof beams are 12 and 7 kN/m, respectively. The dead loads consist of the self-weight of the structure in addition to the uniformly distributed loads of 20 and 15 kN/m applied on floor and roof beams, respectively. The earthquake loads, are computed based on the equivalent lateral force procedure outlined in ASCE 7-98¹³. Here, the resulting seismic base shear (V) is taken as $V = 0.15W_s$ where W_s is the total dead load of the building. The calculated base shear is distributed to each floor using the following equation:

$$F_x = \frac{w_x h_x^k V}{\sum_{i=1}^n w_i h_i^k} \quad (8)$$

where F_x is the induced lateral seismic force at level x ; w is portion of the total gravity load assigned to the related level (i.e. level i or x); and h is the height from base to the related level. The parameter k is determined based on the structure period. It is equal to 1 for structures with a period of 0.5 sec or less; and 2 for structures with a period of 2.5 sec or more. For structures with a period in range of 0.5 to 2.5 sec, k is calculated through linear interpolation¹³. It is worth mentioning that the period of the structure is calculated using the following equation given in ASCE 7-98¹³.

$$T = C_T h_n^{3/4} \quad (9)$$

where C_T is taken as 0.0853 and h_n is the height of the building; namely 12 m for this example. Therefore, the period of the structure, T , is 0.55 sec. Based on the period obtained the value of parameter k in Eq. (8) is taken as 1.025 for this design example.

The beam elements are continuously braced along their lengths by the floor system; and columns and bracings are assumed to be unbraced along their lengths. The effective length factor, K , is taken as 1 for all beams and bracings. The K factor is conservatively taken as 1.0 for buckling of columns about their minor (weak) direction, since the frame is assumed to be non-swaying in that direction owing to inverted V-type bracing systems. However, for buckling of columns about their major direction the K factor is calculated⁹.

For the 3-story steel frame instance, the maximum lateral displacement of the top story is limited to 0.03 m and the upper limit of interstory drift is taken as $h/400$, where h is the story height. The interstory drifts are calculated based on the displacement of center of mass of each story. The maximum lateral displacement of the top story is calculated with respect to the maximum displacements of the ends of the structure. Here, horizontal displacements of all joints of each story are constrained to each other based on a rigid diaphragm assumption. Further details related to this test example can be found in Kazemzadeh Azad et al.⁹.

Groups	BB-BC		MBB-BC		EBB-BC	
	Case (I)	Case (II)	Case (I)	Case (II)	Case (I)	Case (II)
CG_1	W8X24	W21X57	W16X45	W12X40	W14X34	W16X36
CG_2	W30X90	W14X68	W14X48	W10X45	W21X62	W16X67
CG_3	W21X62	W18X60	W24X68	W24X76	W12X40	W14X74
CG_4	W21X68	W36X135	W30X90	W33X141	W30X108	W44X262
B_1	W21X68	W24X62	W18X40	W16X45	W24X55	W12X22
B_2	W18X40	W14X43	W21X50	W24X55	W16X26	W16X31
B_3	W14X22	W12X30	W12X16	W12X22	W16X26	W16X26
BR_1	W18X60	W18X46	W8X28	W8X31	W8X24	W10X33
BR_2	W6X20	W21X62	W6X15	W6X15	W6X15	W6X15
BR_3	W21X50	W14X53	W6X15	W8X31	W4X13	W14X22
Weight (ton)	46.12	47.97	36.43	42.50	36.94	43.56

Table 1: Comparison of designs obtained for 135-member steel frame in two cases

In order to evaluate the profile list ordering effect, optimum design of the 3-story steel frame is performed using BB-BC, MBB-BC, and EBB-BC algorithms in two different cases. In case (I), for each algorithm the sizing optimization is performed using a set of ready sections ordered based on cross sectional area values. In case (II), the profiles are reordered randomly in the list and the new profile list is employed for design optimization. All the above-mentioned metaheuristic algorithms are executed using a population size of 50 over a predefined number of maximum iterations, which is taken as 350 iterations.

A comparison of optimum designs obtained with different algorithms is tabulated in Table 1 for the investigated two cases. As presented in the table, all the algorithms in case (I) locate better solutions compared to case (II). In term of convergence rate, for all the algorithms slower convergence rates have been observed in case (II) compared to case (I) (Fig. 2). As a result it can be deduced that the general performance of the investigated algorithms deteriorates when the employed profile list is unordered.

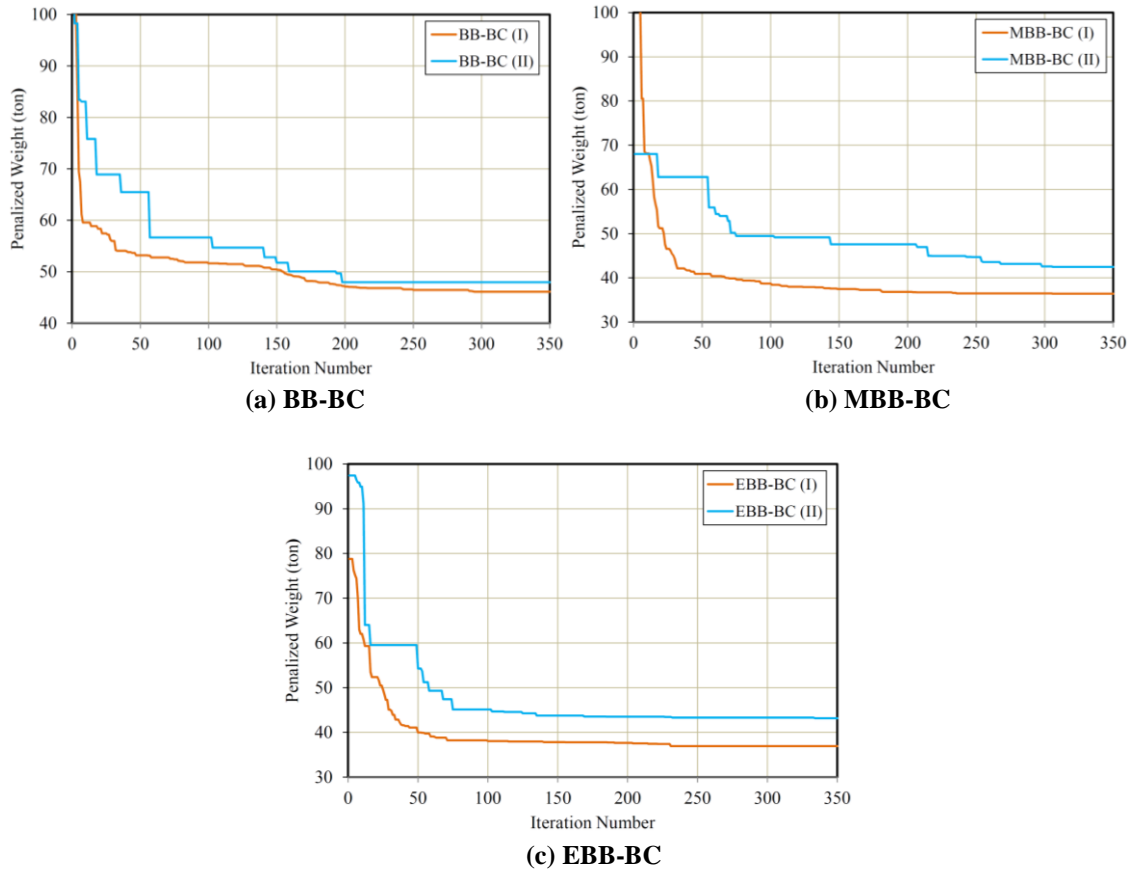


Figure 2: Convergence histories for ordered (case I) and unordered (case II) profile lists

IV. Conclusions

Numerous research studies have been conducted so far on developing new algorithms for practical design optimization of steel frames. In spite of the large number of proposed methodologies, only a few studies address non-algorithmic concerns, such as profile list ordering, affecting the general performance of the algorithms. In this study the effect of the order of sections in an available list of ready sections is investigated using stochastic search algorithms or metaheuristic techniques. Sensitivity of three recently proposed metaheuristic algorithms to different profile lists is investigated through practical sizing optimization of a 135-member steel frame according to AISC-LRFD⁸ specification. A wide-flange profile list composed of 268 ready sections was employed to size the frame members. In order to investigate the profile list ordering effect, first the optimization process is performed based on a set of ready sections ordered with respect to the cross sectional area values. Next, the profiles are reordered randomly in the list and the new profile list is utilized for design optimization. The results obtained using each metaheuristic algorithm are compared for both the ordered and unordered profile lists. The numerical results indicated that the general performance of the investigated algorithms deteriorates, both in terms of solution quality as well as convergence rate, when the employed profile list is unordered. It is worth mentioning that further research is required to investigate the effect of ordering the profile list with respect to the type of structural members (i.e. column, beam, bracing) and different cross sectional properties such as moments of inertia about principal axes as well as governing radius of gyration about the axis of buckling.

References

- ¹Saka, M. P., "Optimum design of steel frames using stochastic search techniques based on natural phenomena: a review", In: B.H.V. Topping (Ed.), *Civil Engineering Computations: Tools and Techniques*, Saxe-Coburg Publications, Stirlingshire, UK, pp. 105-147, 2007.
- ²Kirkpatrick, S., Gerlatt, C. D., Vecchi, M. P., "Optimization by simulated annealing", *Science*, 220, pp. 671-80, 1983.
- ³Goldberg, D. E., Samtani, M. P., "Engineering optimization via genetic algorithm", *Proceeding of the Ninth Conference on Electronic Computation*, ASCE, pp. 471-82, 1986.
- ⁴Michalewicz, Z., "Genetic algorithms + data structures = evolution programs", 3rd ed. Springer-Verlag, 1996.
- ⁵Schwefel, H-P., "Numerical optimization of computer models", Chichester, UK: John Wiley & Sons, 1981.
- ⁶Kennedy, J., Eberhart, R., "Particle swarm optimization", In: *IEEE international conference on neural networks*, IEEE Press, pp. 1942-48, 1995.
- ⁷Colomi, A., Dorigo, M., Maniezzo, V., "Distributed optimization by ant colony", In: *Proceedings of the first European conference on artificial life*, USA, pp. 134-142, 1991.
- ⁸American Institute of Steel Construction (AISC), "Manual of Steel Construction, Load & Resistance Factor Design", 2nd ed. Chicago, 1994.
- ⁹Kazemzadeh Azad, S., Hasançebi, O., Kazemzadeh Azad, S., "Upper Bound Strategy for Metaheuristic Based Design Optimization of Steel Frames", *Adv. Eng. Software*, 57, 19-32, 2013.
- ¹⁰Erol, O. K., Eksin, I., "A new optimization method: Big Bang-Big Crunch", *Adv. Eng. Software*, 37(2), 106-111, 2006.
- ¹¹Hasançebi, O., Kazemzadeh Azad, S., "Discrete size optimization of steel trusses using a refined big bang-big crunch algorithm", *Eng. Optim.*, 46, 61-83, 2014.
- ¹²Hasançebi, O., Kazemzadeh Azad, S., "An exponential big bang-big crunch algorithm for discrete design optimization of steel frames", *Comput. Struct.*, 110-111, 167-179, 2012.
- ¹³ASCE 7-98, Minimum design loads for buildings and other structures: Revision of ANSI/ASCE 7-95, American Society of Civil Engineers, 2000.

A preliminary design method for optimizing composite forward-swept wings

Christopher Bach* and Reda Jebari†

Aeronautics Department, Imperial College London, SW7 2AZ. UK.

Andrea Viti‡

ONERA, 912190 Meudon, France and Aeronautics Department, Imperial College London.

Rob Hewson§

Aeronautics Department, Imperial College London, SW7 2AZ. UK.

In this work, we describe a preliminary design method for optimizing composite forward-swept wings. It is intended for estimating possible weight savings due to aeroelastic tailoring in early aircraft design stages. The approach uses a simplified structural wing model based on the theory of thin walled anisotropic laminate cross-sections. This way, a cross-sectional stiffness matrix can be obtained which is used to couple the deformations with the aerodynamic forces. Bending-torsion coupling of the spar is used to avoid aeroelastic divergence, a typically encountered problem for forward swept wings. Optimization was undertaken for different sweep angles and Mach numbers, the weight of the wing spar being the objective function. A number of constraints were applied, including the avoidance of aero-elastic divergence. Results confirm that a positive bend-twist coupling constant is beneficial for mitigating aeroelastic divergence of forward-swept wings, and consequently structural mass reductions can be achieved.

I. Introduction

Aircraft wings have, with a few noteworthy exceptions [20, 22], traditionally been swept backwards rather than forwards. Sweep of wings is used to reduce the influence of compressibility effects at transonic speeds of modern commercial passenger aircraft. However, forward-swept wings (FSW) come with a number of design difficulties which are related to aeroelastic issues. These can be dealt with by stiffening the wing, or adding counter-weights, yet these measures entail significant weight penalties. The most dominant instability of FSW is aeroelastic divergence, which typically occurs before flutter or aileron reversal [4, 18].

If this issue can be addressed without a weight penalty, forward-swept wings have a number of advantages. These include better maneuverability at high angles of attack, a lower overall wave drag due to a better cross-sectional area distribution of the aircraft, and also the potential to deliver a decrease in vortex drag due to weaker vortices at the wing tips [19, 20]. The cabin layout can also be improved for smaller aircraft due to the more aft location of the wing root and therefore continuous spar, when compared to a rearward swept wing.

Due to their anisotropic characteristics, fibre composites can exhibit couplings between bending, twisting and extension. It is possible to tailor laminated composites for specific applications by controlling the fibre orientations and stacking sequences. Aeroelastic tailoring of FSW makes use of bend-twist coupling to mitigate aeroelastic divergence, improve aerodynamic performance and reduce the wing structural weight [2]. The work presented in this paper demonstrates a fast means of obtaining an early estimate of possible weight savings by using composite tailoring for FSW aircraft. A strip theory model is used to represent the aerodynamics. It is then coupled with a semi-analytical model for the structural response, which is derived from anisotropic shell theory. While we only consider aeroelastic divergence (being the dominant problem for FSW), other aeroelastic instabilities should nevertheless be taken into account at

*PhD Student

†former MSc Student in Composites

‡Marie Curie Early Stage Researcher and PhD Student

§Senior Lecturer

later design stages, using more accurate fluid-structure interaction models. For preliminary design, however, where designers often rely on empirical relationships, the use of analytical models allows optimizing for a large number of design variables, and analyzing trade-offs.

II. Related work

Across the years, aeroelastic tailoring of composite structures for FSW has been the subject of many studies [8, 14, 18, 24, 25]. Many studies that were based on semi-analytical models made simplifying assumptions. This work extends the applicability of such analytical models to span-wise nonlinear wing properties, so that an optimization of the laminate layups can be performed [2]. Lamination parameters (LPs) have already been used for optimizing the stacking sequences of laminated composites by other authors [11, 17]. This approach is advantageous, because it allows the operation on a twelve-dimensional space of continuous design variables, instead of a very large number of ply thicknesses and fibre orientation angles. An overview of manufacturing constraints for lamination-parameter-based optimization, and a ply blending algorithm can be found in the work of [16]. Also, the twelve lamination parameters are not entirely independent of one another, but constrained by physics. The feasible LP region is convex [5, 6]. For a set of ply angles restricted to $\{0^\circ, \pm 45^\circ, 90^\circ\}$, Diaconu and Sekine [7] derived explicit expressions for the feasible region, which are used as constraints in this work.

III. Static aeroelasticity of a forward-swept wing

Aeroelastic divergence is a static phenomenon. It is the dominating instability for forward-swept wings, owing to the fact that lift-induced upwards-bending of the wings leads to a further increase of the local angle of attack [4, 12]. Even before reaching the critical divergence dynamic pressure, considerable deformation may occur. This is usually undesirable from a structural and aerodynamic point of view. To prevent this, local stall and divergence constraints are used in the optimization, as well as a maximum-twist constraint of 5° along the wingspan.

The elastic response of the wings to aerodynamic and gravitational forces is hereafter modelled using a semi-analytical representation of a slender, thin-walled closed-section cantilevered beam model. This allows a direct coupling with the governing equations of aeroelasticity. The aerodynamic forces are also obtained analytically, using strip theory. Strip theory is an approximating model for an incompressible and inviscid flow over an aerofoil with a theoretically infinite wingspan. The analytical description of the aerodynamic forces using strip theory enables a quick evaluation of the divergence constraint, and enables a computationally cheap optimization to be undertaken, particularly since the focus of this work is obtaining a preliminary design estimate of possible weight savings by aeroelastic tailoring [9, 14]. However, higher-fidelity models which are able to capture three-dimensional effects could also be applied, e.g. when further aerodynamic analysis or the examination of other aeroelastic instabilities are of interest. The equations for the local lift and the local lift coefficient per unit chord c_l can then be formulated as following:

$$l(y) = q_\infty c(y) c_l(y) \quad \text{with} \quad c_l(y) = c_{l0}(y) + c_{l\alpha}(y) \alpha(y) \quad (1)$$

Here, c denotes the local chord length, q_∞ the dynamic pressure, and α is the local angle of attack. A detailed overview of the geometry is given in figure 1. To better distinguish between frames of reference, all quantities written with a bar (e.g. \bar{e}) refer to segments perpendicular to the \bar{y} axis (more generally: within the $\bar{x}\bar{y}\bar{z}$ frame of reference). Variables written without a bar refer to the standard xyz frame of reference. It is further assumed that there is an elastic axis, swept forward by an angle $\Lambda \leq 0$, that the deformations are small and the wing is slender (which is a valid assumption for high-aspect-ratio wings). Also, it is assumed that there is no rigid pre-twist of the wings, and that the cross-section does not exhibit any couplings other than bend-twist (which is ensured by exploiting particular symmetries of the panel stacking sequences). In this model, all loads are carried by the thin-walled rectangular wing box beam, which represents the spars and top and bottom panels (figures 2, 3). The joint with the fuselage is assumed to be rigid and is idealized a so-called effective root. This approximation is justified for slender wings [4, 24]. The resultant cross-sectional aerodynamic lift l is acting in z -direction on the aerodynamic centres (figure 2), which are located at a distance $\bar{e}(\bar{y})$ from the elastic axis. The resulting gravitational loads are acting on the centres of mass, positioned at a distance $\bar{d}(\bar{y})$ from the elastic axis. The external forces f_{ext} and moments t_{ext} due to lift and gravity can be expressed as following.

$$f_{ext}(y) = q_\infty c c_l - \mu n g \quad \text{and} \quad f_{ext}(\bar{y}) = f_{ext}(y) \cos \Lambda \quad (2)$$

$$t_{ext}(y) = q_\infty (e c c_l + c^2 c_{MAC}) + \mu n g d \quad \text{and} \quad t_{ext}(\bar{y}) = t_{ext}(y) \cos \Lambda \quad (3)$$

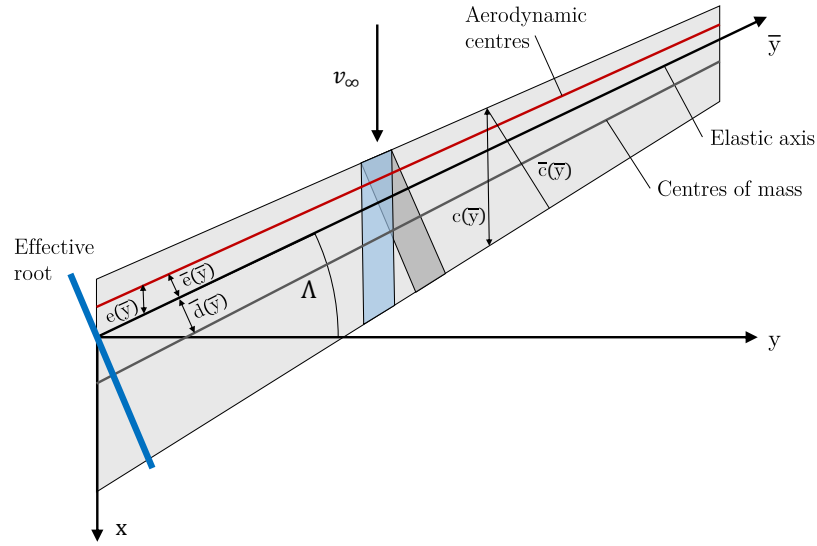


Figure 1: Geometry of a slender swept-forward wing [2] (notation based on [4])

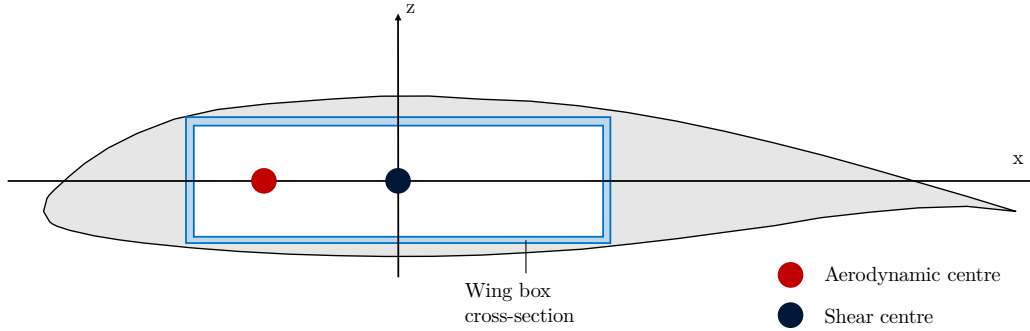


Figure 2: Schematic view of the wing box cross-section within the aerofoil, with the aerodynamic and shear centres highlighted.

Here, g is the gravitational acceleration, μ denotes the wing mass per unit length, n is the load factor, and $c_m AC$ is the aerofoil moment coefficient about its aerodynamic centre. This leads to the following set of equations for the bending and torsion moments \bar{M}_B and \bar{M}_T , where primes denote derivatives with respect to \bar{y} for better readability.

$$\bar{M}_T'(\bar{y}) = -t_{ext}(\bar{y}) \cos \Lambda \quad \text{and} \quad \bar{M}_B''(\bar{y}) = f_{ext}(\bar{y}) + t_{ext}'(\bar{y}) \sin \Lambda \quad (4)$$

A major finding from the structural model described in section IV, is that when particular symmetries of the rectangular cross-section are exploited, the following equations relate the moments to their respective curvatures. $\bar{\theta}(\bar{y})$ denotes the local wing twist angle about \bar{y} , and $w(\bar{y})$ describes the vertical displacement:

$$\begin{bmatrix} \bar{M}_T \\ \bar{M}_B \end{bmatrix} = \begin{bmatrix} GJ & K \\ K & EI \end{bmatrix} \begin{bmatrix} \bar{\theta}' \\ w'' \end{bmatrix} \quad (5)$$

A non-dimensional coupling constant κ is also often used to describe the bending-torsion coupling. It is defined as $\kappa = K/\sqrt{EIGJ}$. The resulting differential equations of aeroelasticity are:

$$(GJ\bar{\theta}')' + (Kw'')' = -(q_\infty(ecc_l + c^2 c_{mAC}) + \mu n g d) \cos^2 \Lambda \quad (6)$$

$$(EIw'')'' + (K\bar{\theta}')'' = (q_\infty cc_l - \mu n g) \cos \Lambda + \sin \Lambda \cos \Lambda (q_\infty(ecc_l + c^2 c_{mAC}) + \mu n g d)' \quad (7)$$

Since a closed-form solution can only be derived when specific wing properties are assumed [4, 12], the Ritz method is used to solve the equations. [2] describes the approach taken in further detail. It is based on applying Hamilton's principle to the homogeneous form of equations (6) and (7), and expresses

$\bar{\theta}$ and w using a weighted sum of shape functions:

$$w(\bar{y}) = \sum_{i=1}^{N_w} \eta_i \psi_i(\bar{y}) \quad \text{and} \quad \bar{\theta}(\bar{y}) = \sum_{j=1}^{N_\theta} \xi_j \varphi_j(\bar{y}) \quad (8)$$

The functions $\psi_i(\bar{y})$ and $\varphi_j(\bar{y})$ are chosen as the free-vibration modes of a clamped-free beam, as presented in [12] pp. 82ff.; pp 170ff. The coefficients α_i and β_i are given in table 1 for $1 \leq i \leq 5$.

$$\psi_i(\bar{y}) = \cosh(\alpha_i \bar{y}) - \cos(\alpha_i \bar{y}) - \beta_i (\sinh(\alpha_i \bar{y}) - \sin(\alpha_i \bar{y})) \quad (9)$$

$$\varphi_j(\bar{y}) = \sqrt{2} \sin\left(\frac{\pi(j-1/2)}{l}\right) \quad (10)$$

Table 1: Values of α_i , β_i , [12] p.83. Note: $l = b/(2 \cos \Lambda)$, where b is the wingspan.

	$i = 1$	$i = 2$	$i = 3$	$i = 4$	$i = 5$
$\alpha_i l$	1.87510	4.69409	7.85476	10.9955	14.1372
β_i	0.734096	1.01847	0.999224	1.00003	0.999999

By further introducing a vector of generalized displacements $\underline{\chi} = [\eta_1, \dots, \eta_{N_w}, \xi_1, \dots, \xi_{N_\theta}]^T$, the following system of equations can be obtained. The divergence dynamic pressure q_D can then be calculated as the solution of the corresponding eigenvalue problem, more specifically as the inverse of the largest positive eigenvalue of \mathbf{M} . Detailed expressions for the matrices can be found in [2]:

$$[\mathbf{A}]\underline{\chi} = ([\mathbf{A}_{stiff}] + q_\infty[\mathbf{A}_{aero}])\underline{\chi} = 0 \quad (11)$$

$$\frac{1}{q_\infty}\underline{\chi} = [\mathbf{M}]\underline{\chi} \quad (12)$$

This approach provides a fast criterion for checking whether divergence occurs prior to a specified cruise dynamic pressure, and is used as a constraint for optimization. The aeroelastic equations (6) and (7) are also solved numerically to obtain $\bar{\theta}$ and w' along the wing. Using $Q(\bar{y}) = \bar{M}_B'(\bar{y})$ and $\eta := \bar{y}/l$, we get:

$$Q(\eta)' = l(q_\infty c(\eta)c_l(\eta, \bar{\theta}(\eta), w'(\eta)) - \mu(\eta)ng) \cos \Lambda + \frac{d}{d\eta} \left(q_\infty e(\eta)c(\eta)c_l(\eta, \bar{\theta}(\eta), w'(\eta)) \right. \\ \left. + q_\infty c(\eta)^2 c_{mAC}(\eta) + \mu(\eta)ngd(\eta) \right) \sin \Lambda \cos \Lambda \quad (13)$$

The problem is then transformed to a set of first-order ordinary differential equations by choosing

$$\begin{bmatrix} \gamma_1 \\ \gamma_2 \\ \gamma_3 \\ \gamma_4 \\ \gamma_5 \end{bmatrix} = \begin{bmatrix} Q - \sin \Lambda \cos \Lambda (q_\infty ecc_l + q_\infty c^2 c_{mAC} + \mu ngd) \\ \bar{M}_B(\eta) \\ \bar{M}_T(\eta) \\ w'(\eta) \\ \bar{\theta}(\eta) \end{bmatrix} \quad (14)$$

This results in the following boundary value problem, with the corresponding boundary conditions for a clamped-free beam.

$$\underline{\gamma}'(\eta) = \begin{bmatrix} l(q_\infty cc_l - \mu ng) \cos \Lambda \\ l\gamma_1 + l \sin \Lambda \cos \Lambda (q_\infty ecc_l + q_\infty c^2 c_{mAC} + \mu ngd) \\ -l \cos^2 \Lambda (q_\infty (ecc_l + c^2 c_{mAC}) + \mu ngd) \\ \frac{l^2 (GJ\gamma_2 - K\gamma_3)}{EIGJ - K^2} \\ \frac{l(EI\gamma_3 - K\gamma_2)}{EIGJ - K^2} \end{bmatrix} \quad (15)$$

$$\gamma_4(0) = \gamma_5(0) = \gamma_2(1) = \gamma_3(1) = 0 \quad (16)$$

$$\left(\gamma_1 + \sin \Lambda \cos \Lambda (q_\infty (ecc_l + c^2 c_{mAC}) + \mu ngd) \right) \Big|_{\eta=1} = 0 \quad (17)$$

For span-wise uniform wing properties, the results showed good agreement with both the closed-form and the analytical approximation of its divergence boundary, as given by [12], pp. 161-167.

IV. Bending-torsion coupling of thin-walled closed-section composite beams

The structural response of the wing is modelled as that of a cantilever beam with thin-walled, rectangular cross-sections and span-wise varying dimensions. The wing is divided along the span into a discrete number of sections, with the lift about the quarter chord obtained from the sections' lift curve slopes. The wing spar was modelled as a thin-walled cantilever beam with rectangular cross sections. It was assumed to carry all the loads. In order to obtain the relationship between beam's deformations and the applied aerodynamic loads, a model is developed from the theory of anisotropic thin-walled closed-section beams presented by Salim and Davalos [21]. The resulting model relates the cross-sectional forces and moments to the respective curvatures via a global stiffness matrix. Figure 3 shows a schematic view of a beam cross-section. The coordinate system (\bar{x}, \bar{y}) is defined with the origin at the center of the cross-section. The z and w axes are also shown. The dimensions d_1 and d_2 represent the height and width of the cross-section, respectively. The thicknesses t_1 and t_2 are indicated for the vertical and horizontal walls. The nodes are numbered 1, 2, 3, and 4. The forces n and s are shown at the nodes.

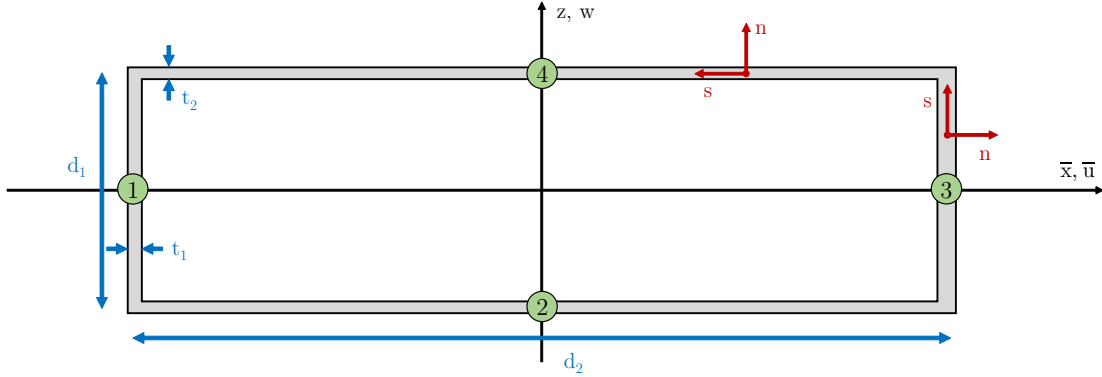


Figure 3: Description of the thin-walled wing box cross-section

Instead of stacking sequences and fibre angles, lamination parameters are used as design variables for the optimization within this paper. The twelve lamination parameters are directly related to the laminate stiffness matrices $[A]$, $[B]$ and $[D]$ via invariant laminate stiffness matrices $[\Gamma]_i$. Lamination parameters are defined as through-thickness integrals of the fibre orientation angles. In case of constant fibre angles within a single lamina, the relationship simplifies to a summation [23].

$$\begin{bmatrix} V_1^A \\ V_2^A \\ V_3^A \\ V_4^A \end{bmatrix} = \frac{1}{N} \sum_{k=1}^N \begin{bmatrix} \cos 2\theta_k \\ \sin 2\theta_k \\ \cos 4\theta_k \\ \sin 4\theta_k \end{bmatrix} \quad (18)$$

$$\begin{bmatrix} V_1^B \\ V_2^B \\ V_3^B \\ V_4^B \end{bmatrix} = \frac{2}{N^2} \sum_{k=1}^N \left(\left(\frac{N}{2} - k + 1 \right)^2 - \left(\frac{N}{2} - k \right)^2 \right) \begin{bmatrix} \cos 2\theta_k \\ \sin 2\theta_k \\ \cos 4\theta_k \\ \sin 4\theta_k \end{bmatrix} \quad (19)$$

$$\begin{bmatrix} V_1^D \\ V_2^D \\ V_3^D \\ V_4^D \end{bmatrix} = \frac{4}{N^3} \sum_{k=1}^N \left(\left(\frac{N}{2} - k + 1 \right)^3 - \left(\frac{N}{2} - k \right)^3 \right) \begin{bmatrix} \cos 2\theta_k \\ \sin 2\theta_k \\ \cos 4\theta_k \\ \sin 4\theta_k \end{bmatrix} \quad (20)$$

$$[A] = h \left([\Gamma_0] + [\Gamma_1]V_1^A + [\Gamma_2]V_2^A + [\Gamma_3]V_3^A + [\Gamma_4]V_4^A \right) \quad (21)$$

$$[B] = \frac{h^2}{4} \left([\Gamma_1]V_1^B + [\Gamma_2]V_2^B + [\Gamma_3]V_3^B + [\Gamma_4]V_4^B \right) \quad (22)$$

$$[D] = \frac{h^3}{12} \left([\Gamma_0] + [\Gamma_1]V_1^D + [\Gamma_2]V_2^D + [\Gamma_3]V_3^D + [\Gamma_4]V_4^D \right) \quad (23)$$

Only plies with fibre orientation angles restricted to $\theta_k \in \{0^\circ, \pm 45^\circ, 90^\circ\}$ are considered here, which results in $V_4^{ABD} = 0$, as $\sin(4\theta_k) = 0$. For manufacturing purposes, laminates are also required to have symmetrical layups in this work, which results in $V_{1,2,3,4}^B = 0$.

Armanios and Badir [1] found that making the top (4) and bottom (2) panels' stacking sequences antisymmetric about one another ($\theta_{ply}(z) = -\theta_{ply}(-z)$) produced the greatest bend-twist coupling constants κ of the cross-section. This was confirmed using the expressions derived for the structural model used in this work. Undesirable couplings with the bending moment about the z-axis can be eliminated by forcing the side panel layups to be symmetric about the z-axis, i.e. $\theta_{ply}(x) = \theta_{ply}(-x)$. Following from these findings, the top and bottom panel stacking sequences were made antisymmetric about another and the side panel stacking sequence were made symmetric about another. This produces the largest bend-twist couplings, eliminates other couplings, and also reduces the number of lamination parameter design variables to consider in the optimization.

As is typical for thin-walled cross-sections, the thicknesses t_1 and t_2 are small compared to the beam's height d_1 and width d_2 . Transverse shear and restrained warping were neglected, which was found to be either a conservative estimate when calculating the divergence dynamic pressure, or led to errors less than 2 % for slender wings [15]. Inspired by Gjelsvik [10] and Barbero et al. [3], further simplifications typical for thin-walled composite beams are introduced. These include neglecting any in-plane deformation of the cross-section, and considering each panel as a thin plate governed by the laws of linear elastic classical laminate theory. The normal stress N_s and bending moment M_s about the local coordinate \underline{s} are also neglected. By further neglecting non-classical effects, the resulting 9×9 global stiffness matrix reduces to a 4×4 matrix $[\mathbf{K}_r]$, which relates the beam's loads to its deformations. When the cross-sectional layup symmetries stated above are taken into account, the matrix further simplifies to:

$$\begin{bmatrix} \bar{N}(\bar{y}) \\ \bar{M}_T(\bar{y}) \\ \bar{M}_{B,\bar{x}}(\bar{y}) \\ \bar{M}_{B,z}(\bar{y}) \end{bmatrix} = \underbrace{\begin{bmatrix} EA & 0 & 0 & 0 \\ 0 & GJ & K & 0 \\ 0 & K & EI_f & 0 \\ 0 & 0 & 0 & EI_l \end{bmatrix}}_{[\mathbf{K}_r]} \begin{bmatrix} \bar{v}'(\bar{y}) \\ \bar{\theta}'(\bar{y}) \\ w''(\bar{y}) \\ \bar{u}''(\bar{y}) \end{bmatrix} \quad (24)$$

$$EA = 2d_1 A_z^{(1)} + 2d_2 A_z^{(2)} \quad (25)$$

$$GJ = 2 \left(\frac{d_1 d_2 t_1 t_2}{d_1 t_2 + d_2 t_1} \right)^2 \left(\frac{d_1}{t_1^2} A_s^{(1)} + \frac{d_2}{t_2^2} A_s^{(2)} \right) + 8 \left(d_1 D_s^{(1)} + d_2 D_s^{(2)} \right) \quad (26)$$

$$EI_f = \frac{d_1^2 d_2}{2} A_z^{(2)} + 2d_2 D_z^{(2)} \quad (27)$$

$$EI_l = \frac{d_2^2 d_1}{2} A_z^{(1)} + 2d_1 D_z^{(1)} \quad (28)$$

$$K = \frac{d_1^2 d_2^2 t_1}{d_1 t_2 + d_2 t_1} A_{sz}^{(2)} - 4d_2 D_{sz}^{(2)} \quad (29)$$

Where EA is the extensional stiffness, GJ the torsional stiffness and K the coupling stiffness between torsion and bending about the \bar{x} axis. EI_f and EI_l denote the bending stiffnesses about \bar{x} and z , respectively. The superscripts in brackets refer to the panel number (see figure 3). $A_x^{(i)}$ and $D_x^{(i)}$ depend on the $[\mathbf{A}]$ and the $[\mathbf{D}]$ stiffness matrices of each panel. Their exact expressions are:

$$\begin{bmatrix} A_z & A_{sz} \\ A_{sz} & A_s \end{bmatrix} = \begin{bmatrix} A_{11} - \frac{A_{12}^2}{A_{22}} & A_{13} - \frac{A_{12}A_{23}}{A_{22}} \\ A_{13} - \frac{A_{12}A_{23}}{A_{22}} & A_{33} - \frac{A_{23}^2}{A_{22}} \end{bmatrix} \quad (30)$$

$$\begin{bmatrix} D_z & D_{sz} \\ D_{sz} & D_s \end{bmatrix} = \begin{bmatrix} D_{11} - \frac{D_{12}^2}{D_{22}} & D_{13} - \frac{D_{12}D_{23}}{D_{22}} \\ D_{13} - \frac{D_{12}D_{23}}{D_{22}} & D_{33} - \frac{D_{23}^2}{D_{22}} \end{bmatrix} \quad (31)$$

The detailed derivation of all equations involves a very lengthy integration of various stiffness terms along the cross-section contour in \underline{s} , and is therefore omitted here. More information can be found in [2,13]. It is worth noting that the results obtained using this approach were compared to the thin-walled closed-section beam model described in [1], which was verified using FE simulations and experiments. For sufficiently thick panels (≥ 70 plies), the agreement was very good in general, with less than 1% difference in EA , GJ , EI_f and EI_l . With 8.5%, the coupling stiffness K exhibited larger variations between the models. These differences may also be partly owing to the fact that Armanios and Badir neglected the influence of the $[\mathbf{D}]$ matrix terms in their work.

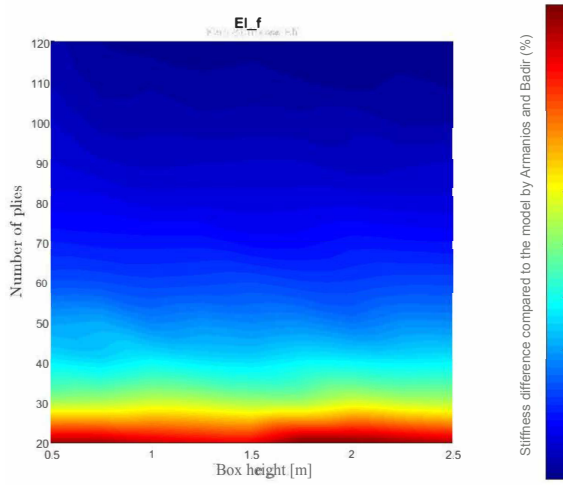


Figure 4: Relative difference in EI_f between the models [13]

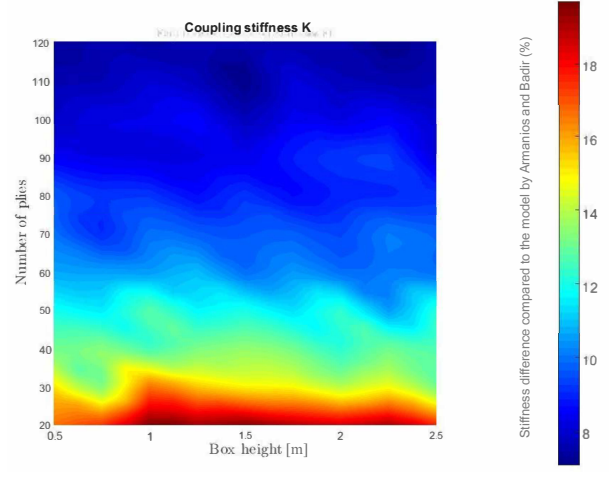


Figure 5: Relative difference in K between the models [13]

V. Optimization problem formulation

Optimization is undertaken on the composite stacking sequences, using a bi-level approach as presented by [17]. The number of plies in each of the pre-defined directions $\{0^\circ, \pm 45^\circ, 90^\circ\}$, and the V^D lamination parameters are used as the first level design variables, and are optimized using a hybrid approach that consists of a genetic algorithm (GA), and a subsequent gradient-based SQP-algorithm in MATLAB. A corresponding stacking sequence is matched to these parameters in a second step, using a permutation GA. The ply angles were restricted to the set of $\{0^\circ, \pm 45^\circ, 90^\circ\}$, as is typical in many industrial applications. The minimum weight was sought, subject to the constraints below:

- No aeroelastic divergence
- No stalling: $\alpha < \alpha_{stall}$ at all wing span locations
- Twist angle $\bar{\theta}(\bar{y}) \leq 5^\circ$ everywhere along the wing
- Lift equal to lift required $\pm 1\%$
- $\geq 10\%$ plies in each pre-defined direction
- No structural failure by the Tsai-Hill criterion (first-ply-failure, FPF)
- Feasible lamination parameter region as described by [7]

For this purpose, the wings are discretized into five span-wise segments with piecewise constant stacking sequences and panel thicknesses. Optimization runs were undertaken for varying amounts of wing sweep, ranging from -35° to 0° , and Mach numbers between 0.70 and 0.90.

Table 2: Chosen parameters (aircraft configuration)

Wingspan	30 m	Material	T300-914
Root chord	5 m	Safety factor	1.5
Taper ratio	0.25	Required lift	600,000 N
Airfoil	65410	Wingbox position (LE to wingbox)	1 m

Matching the total aerodynamic lift to the aircraft's weight is achieved by adjusting the wing's undeformed angle of attack α_r within pre-defined bounds of $[-1^\circ; 5^\circ]$. The divergence constraint is implemented using the Ritz method, and the deformations and local angle of attack are calculated by numerically solving the BVP (14-17). Deformations and strains are also calculated to assess structural failure and the reserve factor. A population size of 500 is used for the GA, with a stop condition of 100 stalled generations. Once the algorithm converges, the obtained optimum point is passed to a gradient-based SQP algorithm (*fmincon*) for further refinement. A permutation GA then matches a corresponding stacking sequence to the resulting V_D parameters [2]. All computations were run on 16 cores of the Imperial College Department of Aeronautics Linux cluster.

VI. Optimization results

Typical results showed the variation in the stiffness along the length of the wing as shown in figure 6. It is interesting to note that the positive coupling coefficient, κ , leads to a nose down twist of the wing in response to aerodynamically applied bending moments. A trend towards larger values of κ for increasing amounts of forward-sweep could be observed. The reason for this coupling is the fraction of 45° plies in the top panel (and a corresponding number of -45° plies in the bottom panel, as observed from the exterior of the wing-box). This is illustrated in figure 7 for a Mach number of 0.8. The relatively large percentage of 0° plies mitigates lift-induced bending, as it exhibits the greatest stiffness in direction of the elastic axis. Results also showed the bi-level optimization strategy to be more efficient than a computationally expensive approach of directly optimizing the stacking sequence of the composite spar.

The results also show a weight penalty for larger amounts of forward-sweep, particularly beyond -20° (figure 8). This indicates that the aeroelastic tailoring achieved through the optimization does not entirely avoid the divergence problem, therefore requiring an increase in stiffness and structural mass. The side panels of the optimized wings, forming the front and rear spars, generally have a larger thickness than the top and bottom panels. The side panels carry most of the shear loads, whereas the top and bottom panels are mainly loaded in compression and tension, respectively. The poor performance of composite materials in shear might therefore be a reason for producing designs with thicker spars. In real aircraft, the top and bottom panels as well as the front and rear spars may exhibit different thicknesses. The top panels typically require more plies to prevent buckling.

The results were compared to an optimized design achieved with $\{0^\circ, \pm 45^\circ, 90^\circ\}$ quasi-isotropic layups and no bend-twist coupling. This avoids comparisons with different materials and produces a reference design which overcomes the divergence problem by increasing the stiffnesses alone. The reference wing was optimized in a similar manner, but with the panel thicknesses being the only design variables. A structural weight saving of 13% was found for the wing spar, at a forward sweep angle of -25° and Mach 0.7. The mass was reduced from 760.67 kg to 663.82 kg through aeroelastic tailoring.

VII. Conclusions

A new preliminary design method for estimating possible weight savings through aeroelastic tailoring of forward-swept wings has been developed. It uses bending-torsion coupling which arises from the anisotropic stiffness properties of tailored laminated composites to mitigate aeroelastic divergence and structural failure. Lamination parameters are used as first-level design variables, and a corresponding stacking sequence is matched to the obtained parameters in a second post-processing step. Possible weight savings have been studied for a range of sweep angles and Mach numbers. The computationally cheap semi-analytical models allow for a fast optimization, at the cost of losing accuracy compared to high-fidelity fluid-structure-interaction coupled FE-CFD models. Positive values of the coupling constant κ , which produce a nose-down twist when the wings rise upwards due to lift, are beneficial for mitigating

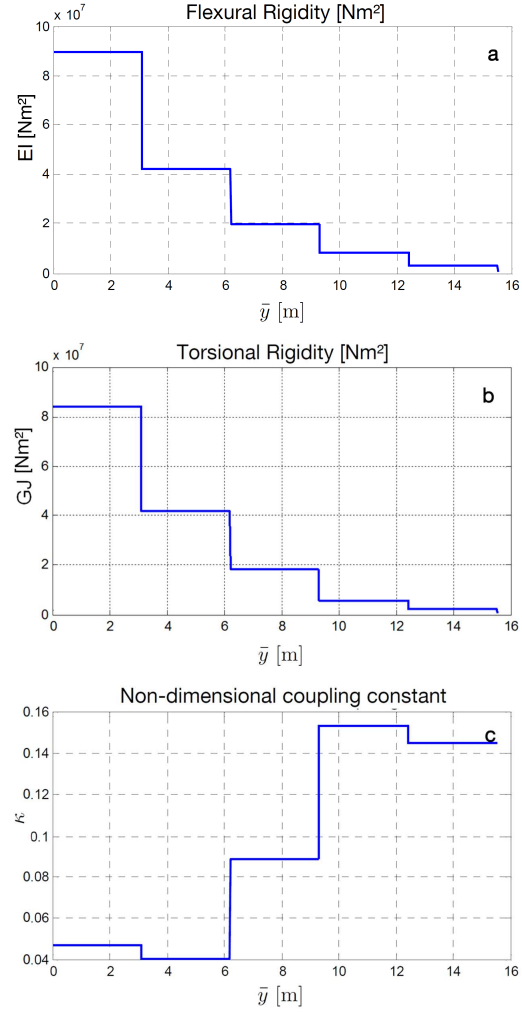


Figure 6: Optimum stiffnesses EI , G and κ . Results obtained for $\Lambda = -15^\circ$, $M_\infty = 0.8$

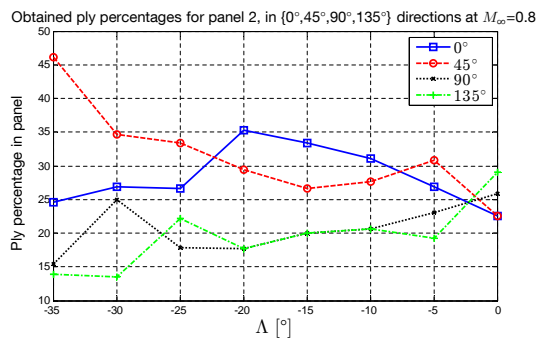


Figure 7: Ply percentages in top panel of wing discretization segment 2 vs. Λ , at $M_\infty = 0.8$.

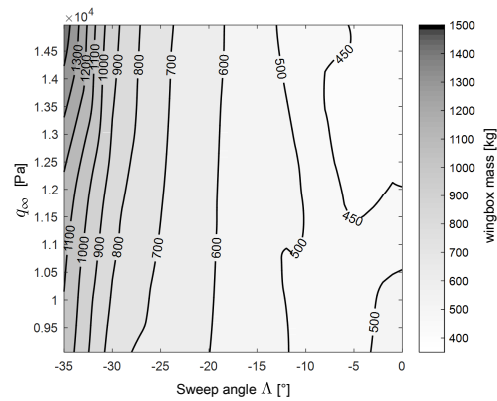


Figure 8: Obtained wingbox mass vs. Λ and dynamic pressure q_∞ .

divergence. Future work could include the consideration of aeroelastic instabilities other than divergence, and a more detailed analysis of the incorporation of manufacturing constraints such as ply blending.

References

- ¹Armanios E, Badir A. *Free vibration analysis of anisotropic thin-walled closed-section beams*, AIAA J, **33**:10, 1995.
- ²Bach C, Jebari R, Viti A, Hewson R. *Composite stacking sequence optimization for aeroelastically tailored forward-swept wings*, Struct Multidiscip O, **55**:105, 105-119, 2017.
- ³Barbero E J, Lopez-Anido R, Davalos J. *On the mechanics of thin-walled laminated composite beams*, J Compos Mater, **27**:8, 806-829, 1993.
- ⁴Bisplinghoff R L, Ashley H, Halfman R. *Aeroelasticity*, Dover Publishing, 1955.
- ⁵Bloomfield M, Herencia J, Weaver P. *On feasible regions of lamination parameters for lay-up optimization of laminated composites*, P Roy Soc Lond A Mat, **465**, 1123-1143, 2009.
- ⁶Diaconu C, Sato M, Sekine H. *Feasible region in general design space of lamination parameters for laminated composites*, AIAA J, **40**:3, 559565, 2002.
- ⁷Diaconu C, Sekine H. *Layup optimization for buckling of laminated composite shells with restricted layer angles*, AIAA J, **42**:10, 21532163, 2004.
- ⁸Dillinger J, Klimmek T, Abdalla M, Gürdal Z. *Stiffness optimization of composite wings with aeroelastic constraints*, J Aircraft, **50**:4, 1159-1168, 2013.
- ⁹Georgiou G, Vio G, Cooper J. *Aeroelastic tailoring and scaling using bacterial foraging optimisation*, Struct Multidiscip O, **50**:1, 81-99, 2014.
- ¹⁰Gjelsvik A. *The theory of thin walled bars*, Wiley, 1981.
- ¹¹Herencia J, Weaver P, Friswell M. *Lay-Up Optimization of Composite Stiffened Panels Using Linear Approximations in Lamination Space*, AIAA J, **46**:9, 2387-2391, 2008.
- ¹²Hodges D H, Pierce G A. *Introduction to Structural Dynamics and Aeroelasticity*, 2nd ed., Cambridge University Press, 2011.
- ¹³Jebari R. *Composite Stacking Sequence Optimization and Aero-elastic Tailoring of a Forward Swept Wing*, MSc thesis, Imperial College London Department of Aeronautics, 2015.
- ¹⁴Librescu L, Khdeir A. *Aeroelastic divergence swept-forward composite wings including warping restraint effects*, AIAA J, **26**:11, 1373-1377, 1988.
- ¹⁵Librescu L, Song O. *On the static aeroelastic tailoring of composite aircraft swept wings modelled as thin-walled beam structures*, Compos Eng, **2**, 497-512, 1992.
- ¹⁶Liu D, Toropov V, Barton D, Querin O. *Weight and mechanical performance optimization of blended composite wing panels using lamination parameters*, Struct Multidiscip O, **52**:3, 549-562, 2015.
- ¹⁷Liu D, Toropov V, Querin O M, Barton D C. *Bilevel Optimization of Blended Composite Wing Panels*, J Aircraft, **48**:1, 107-118, 2011.
- ¹⁸Lottati I. *Flutter and divergence aeroelastic characteristics for composite forward-swept cantilevered wing*, J Aircraft **22**:11, 1001-1007, 1985.
- ¹⁹Johnsen F A. *Sweeping Forward: Developing & Flight Testing the Grumman X-29A Forward Swept Wing Research Aircraft*, NASA Aeronautics Book Series, 2013.
- ²⁰Roskam J. *Roskam's Airplane War Stories: An Account of the Professional Life of Dr. Jan Roskam, Airplane Designer and Teacher*, DARcorporation, 2002.
- ²¹Salim H and Davalos J. *Torsion of open and closed thin-walled laminated composite sections*, J Compos Mater, **39**:6, 497-524, 2005.
- ²²Torenbeek E. *Synthesis of Subsonic Airplane Design* p. 37, Springer Science & Business Media, 2013.
- ²³Van Campen J. *Optimum lay-up design of variable stiffness composite structures*, PhD thesis, TU Delft, 2011.
- ²⁴Weisshaar T. *Aeroelastic stability and performance characteristics of aircraft with advanced composite sweptforward wing structures*, technical report, Virginia Polytechnic Institute and State University, 1978.
- ²⁵Weisshaar T. *Divergence of forward swept composite wings*, J Aircraft, **17**:6, 442-446, 1980.

Node-based shape optimization in aircraft preliminary design

D. Baumgärtner* and K.-U. Bletzinger[†]

Technical University of Munich, 80333 Munich, Germany.

A. Viti[‡] and A. Dumont[§]

ONERA The French Aerospace Lab, 92190 Meudon, France

We present applications of the Vertex Morphing Method to aircraft preliminary design. Vertex Morphing is a node-based shape optimization technique that unifies shape control, mesh-regularization and sensitivity filtering. Since it directly uses surface nodes of a given discrete model, it is particularly useful to explore the design space at a minimum modeling effort. It also allows for effective shape optimization where another parametrization is not obvious or even infeasible. In this context, the paper discusses two different applications of the Vertex Morphing Method. The first application comprises the aeroelastic shape optimization of a flexible wing. Given this multidisciplinary problem, we investigate the Vertex Morphing Method in terms of possible design improvements and quality of the final design. The second application is about the aerodynamic shape optimization of a forward-swept wing aircraft. This example highlights efficiency and applicability of the method in case of more complex geometries. Both examples eventually show that Vertex Morphing is a powerful alternative method to optimize or find shapes within aircraft preliminary design.

I. Introduction

The current state of the art in aerodynamic, aeroelastic or aerostructural shape optimization is dominated by CAD-based approaches or approaches utilizing morphing boxes.^{1–8} On the other hand CAD-free or node-based approaches, which were first investigated by e.g. Jameson,⁹ Pironneau and Mohammadi,¹⁰ have not reached broad industrial application so far, despite their promising characteristics, like for example high optimization potential, minimum modeling effort and efficient exploration of the design space. In previous European projects, namely FLOWHEAD (project no. 218626) and AMEDEO (project no. 316394), it was shown that a CAD-free or node-based parametrization using the Vertex Morphing Method¹¹ actually represents a very efficient and effective alternative to CAD-based approaches. Vertex Morphing allows to perform both shape optimization and form finding of fluid as well as structure problems in the context of industry-relevant applications (particularly also in the context of aircraft design¹²). Moreover, related research showed that both a CAD-based and a CAD-free approach using Vertex Morphing are two consistent parametrization techniques that may be transformed into each other¹³ or that may be combined towards a more effective overall shape optimization procedure.¹²

This paper presents recent advances in the application of the Vertex Morphing Method within aircraft preliminary design. In the first section a multidisciplinary aeroelastic shape optimization of a flexible ONERA M6 wing is discussed. This case is challenging since the shape here depends both on the initial choice of the geometry as well as the aerodynamically imposed structural deformation. The second part of the paper then discusses the aerodynamic shape optimization of a full aircraft configuration. Herein we aim consequently for a minimum modeling effort in favor of an improved performance regarding design space exploration.

*Ph.D. candidate, Chair of Structural Analysis

[†]Professor and head of Chair of Structural Analysis

[‡]Ph.D. candidate, Applied Aerodynamics Departement

[§]Research engineer, Applied Aerodynamics Departement

I.A. Software framework

All optimization runs described in this paper are realized using several software packages that are linked through a common python interface. This allows for a modular simulation environment in which individual packages can communicate either via direct memory interface or File-I/O. To drive the design process an implementation of the Vertex Morphing Method in the established open-source simulation framework Kratos¹⁴ is used. The implementation acts as a generic optimizer to perform node-based shape optimization using the Vertex Morphing Method. Moreover, it provides the common python interface. The optimizer is developed at the Technical University of Munich (TUM) and is dedicated to shape optimization of arbitrary geometries with possibly millions of design variables. Correspondingly, the implementation follows a concept with which unnecessary solver calls during the optimization may be avoided. As primal CFD solvers we apply the ONERA in-house code elsA^{15,16} as well as the open-source CFD code SU2.⁸ As primal structure solver we utilize Kratos again. Kratos and SU2 are used for the aeroelastic shape optimization of the flexible ONERA M6 wing, whereas Kratos and elsA are used in case of the aerodynamic shape optimization of the forward-swept wing aircraft.

II. Aeroelastic shape optimization of a flexible ONERA M6 wing

Generally, aerodynamic shape optimization of flexible structures, i.e. aeroelastic shape optimization, represents a challenge, since in this case the shape depends not just on initial geometric definitions, but also on the superposed flow-induced deformation of the structure. Therefore, aeroelastic shape optimization requires a modification of the structure's rigid or jig-shape such that the desired improvement appears in the *deformed state*. This is a non-trivial task and generally it becomes all the more difficult the higher the number of design variables controlling the shape in the optimization process. Hence it represents a particular challenge in node-based shape optimization. In this context, we in the following investigate the applicability of the Vertex Morphing Method within an aeroelastic scenario. Particular test case is a flexible ONERA M6 wing immersed in a compressible fluid flow.

II.A. Model

The geometry to be optimized is the well-known ONERA M6 wing. Different as in the classical analyses, however, we do not consider the wing to be rigid, but model it as a hollow shell structure clamped at the wing root. This is done to introduce an artificial fluid-structure interaction in the model so that the corresponding shape optimization becomes an aeroelastic problem. The rather simple wing structure was chosen since we are focusing here on the performance of the Vertex Morphing Method within aeroelastic cases. Therefore, any structure causing a bigger wing deflection is sufficient. For both the fluid analysis (CFD) and the structural analysis (CSM) we assume steady cruise conditions. Some details of the corresponding fluid and structure model are compiled in table 1 and 2. Analyzing the corresponding fluid-structure interaction (FSI) in this baseline configuration, we observe a wing tip deflection of around 6% of the wing span, see figure 1(a). All FSI simulations are done using a Gauss-Seidel approach with constant relaxation. Furthermore, all mesh-motions involved in the optimization problem, both due to the fluid-structure interaction and the shape modifications, are solved using a pseudo-elastic approach.

Table 1. Fluid model of ONERA M6 case

Governing equations	Steady 3D Euler
Freestream pressure	101325.0 N/m ²
Freestream temperature	288.15 K
Freestream Mach number	0.8395
Angle of attack	3.06 deg

Table 2. Structure model of ONERA M6 wing

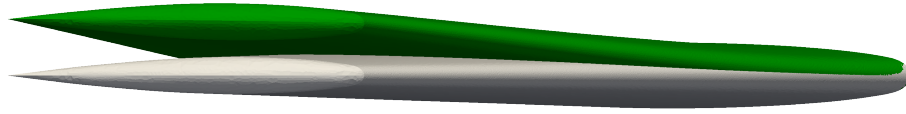
Governing equations	Steady geometrically nonlinear shell
Shell thickness / Span	$\sim 1/50$
Material	Saint Venant-Kirchhoff

Given this model the wing shape is to be aerodynamically optimized such that the near-field drag (c_d) is minimized whereas the lift (c_l) is not allowed to deviate from a constant target value (i.e. the c_l of the deformed baseline design). Since we are dealing with a coupled problem and we are choosing a multidisciplinary feasible solution approach, the coupled governing equations, i.e. in residual form

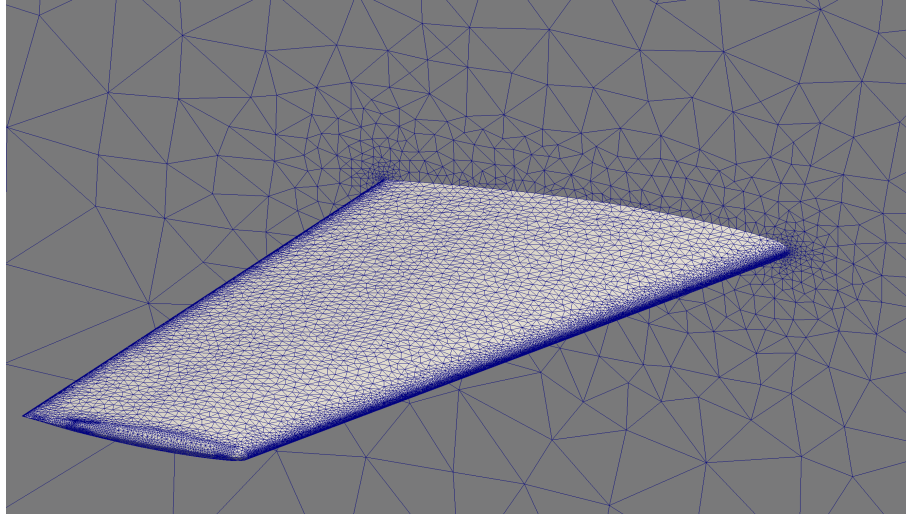
R_S for the structure and R_F for the fluid, have to be satisfied during the complete optimization. The corresponding optimization problem reads as follows:

$$\begin{aligned}
 \min \quad & J = c_d(\mathbf{x}) \\
 \text{w.r.t.} \quad & \mathbf{x} \\
 \text{s.t.} \quad & g = c_l - c_{l, \text{baseline}} = 0 \\
 & \mathbf{R}_F = 0 \\
 & \mathbf{R}_S = 0
 \end{aligned} \tag{1}$$

Herein J represents the objective function, g the constraint function and x the design variables. As design variables we choose all the given 18000 nodes on the discrete wing surface, see figure 1(b). We note, that the discrete shell model of the wing was created to match the fluid grid on the wing surface. Without affecting the investigations in this chapter, this rather pragmatic structural model avoids a mapping of state quantities on the interface. Generally, matching grids are the exception, so that in a node-based approach one would choose the nodes of the typically finer fluid mesh as design variables. This requires, however, a more sophisticated interface mapping between structure and fluid.



(a) Aeroelastic deformation (tip deflection corresponds to 6% of the wing span)



(b) Discrete jig shape (~ 18000 surface nodes)

Figure 1. Jig shape (grey, bottom) and deformed shape (green, top) of flexible ONERA M6 wing

To solve the optimization problem we apply a gradient-based approach, whereas the necessary surface sensitivities are computed by means of continuous adjoint sensitivity analysis. Since no coupled adjoint sensitivity analysis was available, a less accurate approach utilizing only aerodynamic sensitivities is applied. Herein, instead of computing the complete coupled sensitivities, we only compute the aerodynamic sensitivities but always in the deformed structure state. That is, in every optimization iteration we perform a complete FSI analysis to reach the current steady state of equilibrium and then evaluate the aerodynamic surface sensitivities of the deformed wing using SU2. These sensitivities are afterwards provided to the optimizer. The suggested shape update is then applied to the undeformed design and we start again to compute the deformed state of equilibrium.

To drive the actual optimization process we utilize a modified gradient projection method with constant step size. Hence we perform an unconstrained optimization in the tangent subspace of the constraint. To this end the objective gradient is modified by the constraint gradient as follows:

$$\begin{aligned}
 \tilde{\nabla} J &= \nabla J - (\nabla J \cdot \mathbf{n}_g) \cdot \mathbf{n}_g + g \|\nabla J\| \cdot \mathbf{n}_g \\
 \text{with } \mathbf{n}_g &= \frac{\nabla g}{\|\nabla g\|}
 \end{aligned} \tag{2}$$

This modification corresponds to a classical projection method, however, with one additional term (last term in equation (2)). The additional term is to penalize any deviation from the feasible domain or the target lift value respectively. In the following the results of the above described node-based shape optimization problem are presented.

II.B. Results

The quantitative results of the aeroelastic shape optimization are presented in figure 2. Herein we see the evolution of the drag and lift coefficient (c_d, c_l) during the aeroelastic or FSI optimization. First striking result is the significant improvement of the objective value (c_d) by almost 30% after around 190 optimization iterations. At the same time we observe only a slight but noticeably deviation of c_l from the target value ($\sim 0.3\%$). As a matter of fact, this deviation is a consequence of our simplified sensitivity analysis, where we neglect the actually involved coupling terms. The deviation, however, appears to be acceptable given the total quantitative improvement and the attractive computational savings linked to this simplified approach.

It is interesting to compare the FSI results to a classical aerodynamic optimization approach, in which the deformed state of the wing (i.e. the flight shape) is computed only once in the beginning and then used as a constant reference geometry for a subsequent single-disciplinary shape optimization using only aerodynamic sensitivities. Here, shape updates are always added to the deformed wing shape. In figure 2, this approach is referred to as CFD optimization. Comparing CFD and FSI optimization we see that the first performs slightly worse in terms of the objective value but seems to exactly maintain the target value for c_l . However, the CFD optimization neglects the influence of the changing shape on the wing deflection. As a matter of fact, if we again compute the equilibrium state of the hence optimized wing, we observe that the actual shape in equilibrium changes leading to a jump in the force coefficients. In particular we see that the c_l now is much further off the target value compared to the FSI optimization.

So from the quantitative results we may already conclude that a shape optimization process considering the fluid-structure interaction in the state analysis performs significantly better than a pure aerodynamic optimization process of only the flight shape. That is, even when coupled sensitivity analysis is not available, the shape optimization process in case of a flexible structure may be significantly improved by including the fluid-structure interaction into the analysis of the state equations, which typically may be achieved with only a minor effort compared to a fully coupled state and sensitivity analysis.

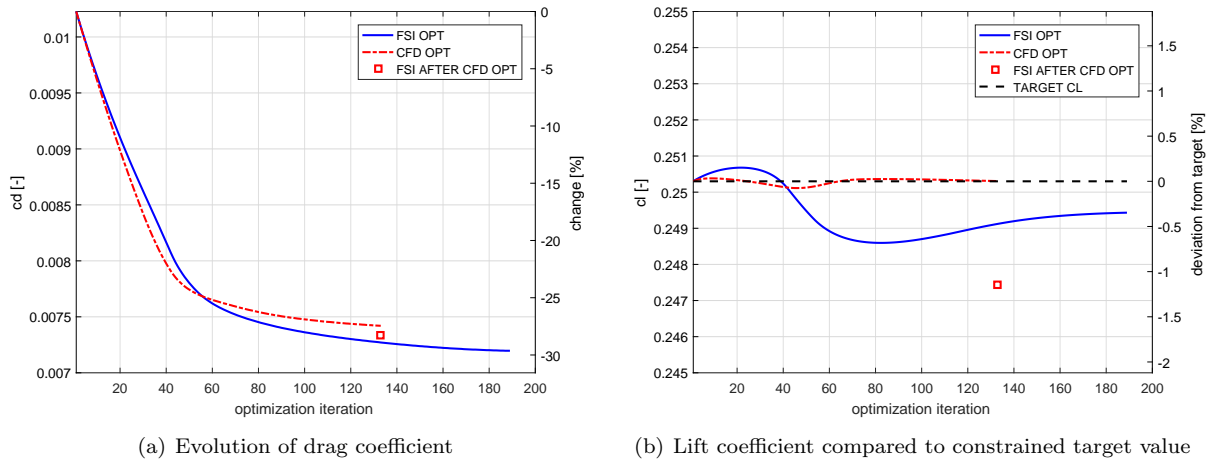


Figure 2. Comparison of results of a single disciplinary (CFD) and multidisciplinary (aeroelastic / FSI) node-based shape optimization of the ONERA M6.

Qualitatively the big improvement can be explained by a shock reduction on the wing surface. Figure 3 shows the surface pressure distribution (c_p) before and after the aeroelastic shape optimization each in the deformed wing state. Herein visible is the clearly alleviated shock region up to almost vanishing discontinuities.

Additional insight yields the comparison between the pressure distribution in the undeformed state and the deformed state. Therefore, figure 8 plots the pressure distribution over the wing's center profile in span-wise direction for different wing states, i.e. the deflected baseline wing design, the undeflected optimized wing and the deflected optimized wing. For the deflected baseline design we observe a clear pressure discontinuity leading to the shock front on the wing as seen before. After the optimization, we find that in the undeformed state the pressure gradient improved but still shows clear fluctuations.

Only in the deformed state of the optimized wing the pressure gradient eventually turns into a smooth curve and we obtain the final force coefficient values presented in figure 2. So obviously, by considering the fluid-structure interaction in the state analysis, the design changes proposed by the optimizer are such, that the objective value is improved while the constraint is met, each in the *deformed* state, or generally speaking under flight conditions. This exactly corresponds to the underlying motivation of such an aeroelastic (multidisciplinary) optimization approach.

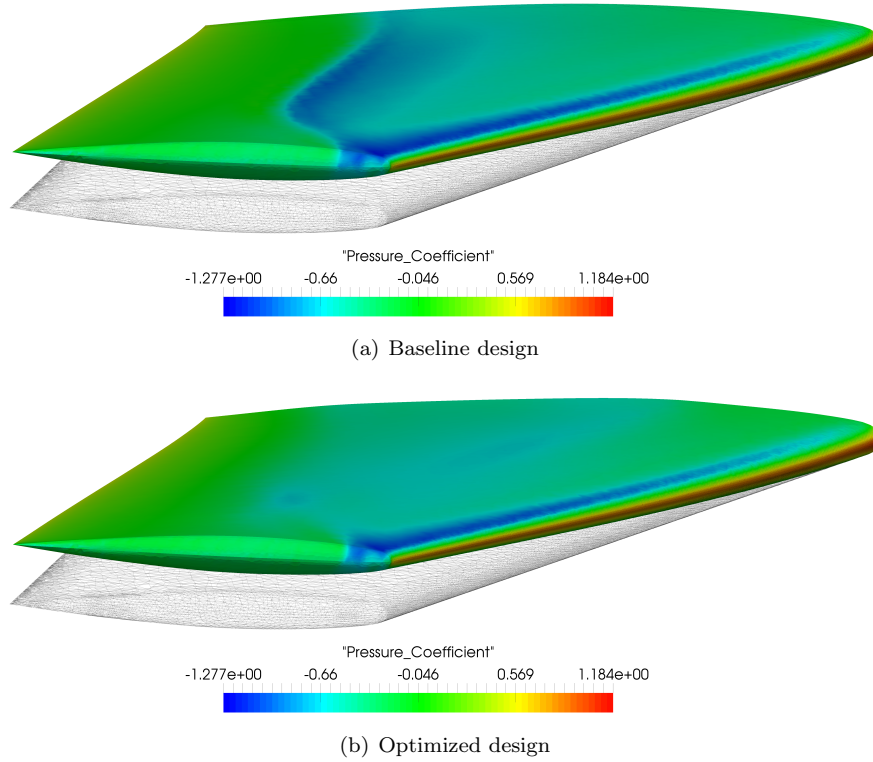


Figure 3. Surface pressure distribution before and after the optimization (each in the deformed wing state, the mesh indicates the undeformed wing)

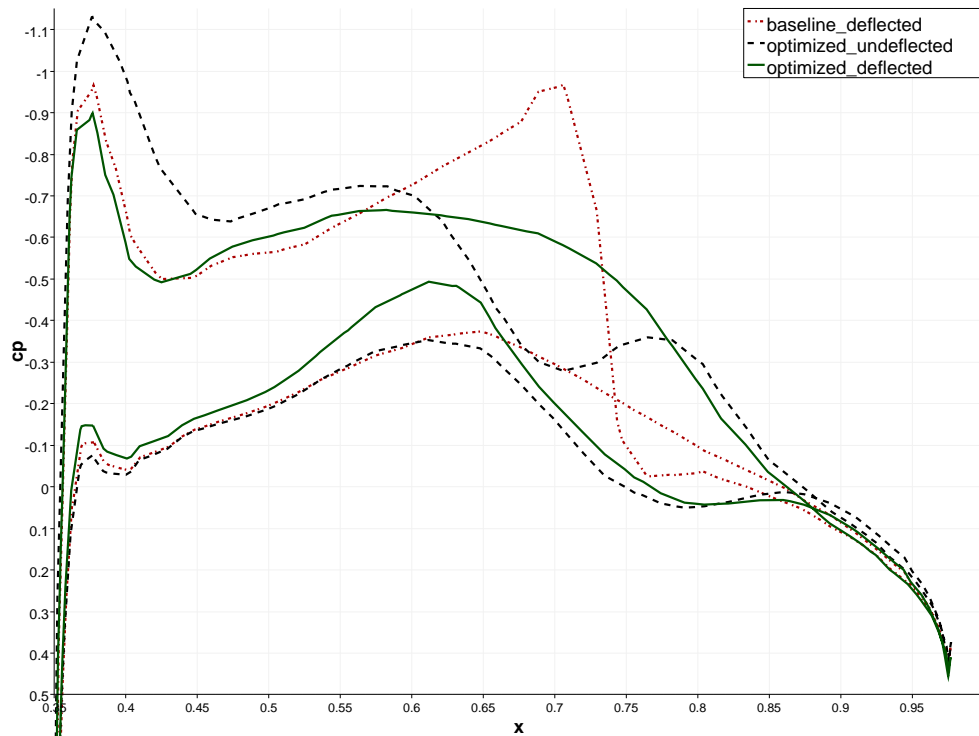


Figure 4. Pressure distribution over center profile of the wing in span-wise direction

Having observed the state changes from the baseline to the optimized design, we in the following want to analyze the actual changes in shape proposed by the optimizer. Figure 5 visualizes the shape changes for the final design after the optimization. From the figure we find three results that may be considered characteristic for the application of Vertex Morphing within shape optimization of wings:

First, we see that complex shape changes were introduced with very local adjustments according to the physical flow (compare the presented shape updates to the shock front seen in figure 3(a)). This very detailed adjustment of the wing shape is a consequence of the fine surface discretization and is difficult to achieve with another parametrization and in any case time consuming.

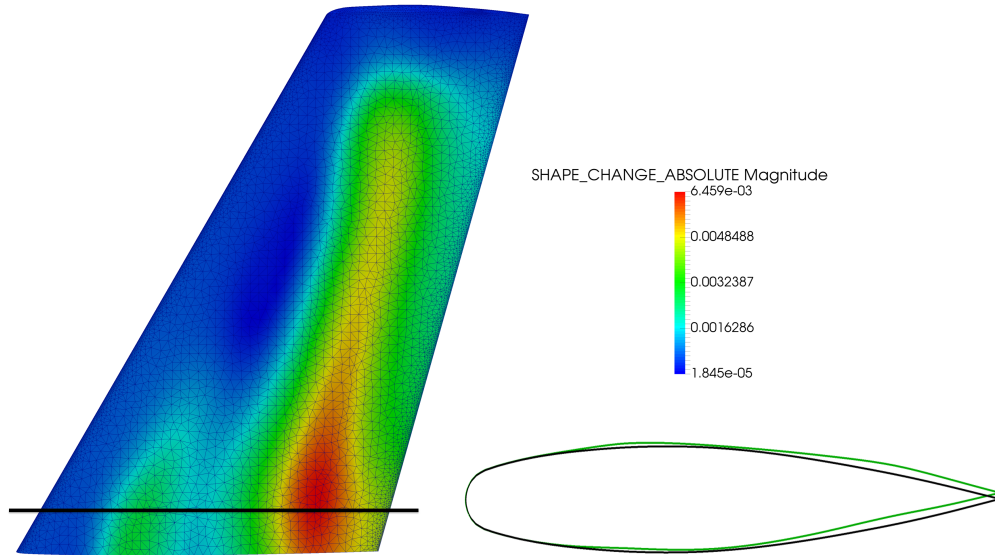


Figure 5. Shape change of the optimal (green) compared to the baseline design (black)

Second, we note that despite Vertex Morphing introduces shape change locally, we obviously obtain a globally continuous surface where previously defined sharp edges (i.e. the trailing edge) remain sharp. There are, however, no further discontinuities or geometric artifacts as one could expect from a node-based approach. Looking for example at the particular airfoil shown in figure 5, one clearly observes a smooth geometry (as a matter of fact we obtain C2-continuous surfaces here). The reason for this continuity is originated in the inherent filtering within the Vertex Morphing Method. This filtering generates smooth incremental shape updates from even highly discontinuous surface sensitivities during the optimization. Therefore, compare in figure 6 the suggested design updates with the original surface sensitivities for the first optimization iteration. These incremental smooth updates in total yield geometries whose continuity may be controlled by a proper choice of the included filter function.

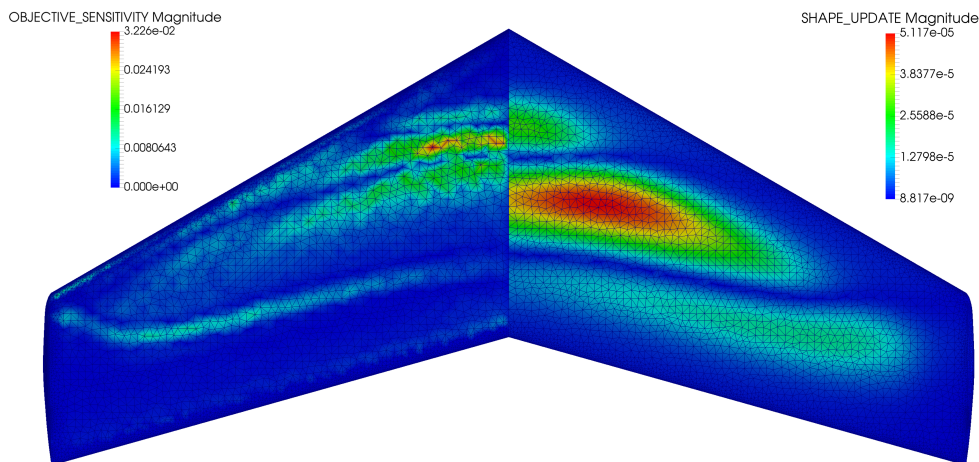


Figure 6. Effect of filtering in the Vertex Morphing method

Third, we observe that the wing thickness remains practically constant during the shape optimization process. While this holds for the complete wing, the airfoil in figure 5 indicates this exemplary. That is, indeed for every airfoil there is a changing chord line, but the thickness along the chord line remains constant. Again this result is a consequence of the inherent filtering of the Vertex Morphing Method. More precisely, we in this example chose a characteristic filter size that is significantly larger than the largest wing thickness so that the movements of the opposite surfaces are linked to each other. Note that by this approach, we are able to constrain the wing thickness without adding an explicit condition to the optimization problem described in (1).

From all the results in this chapter it is evident, that also in case of an aeroelastic shape optimization, where there is an additional dependency of the shape on the structural deformation, the Vertex Morphing Method allows for high optimization potential and effective design space exploration at simultaneously minimal modeling effort.

III. Aerodynamic shape optimization of an aircraft configuration

Having focused on a benchmark geometry so far, we in this section consider a case with more complex geometry.

III.A. Model

Particular application of interest is the aerodynamic shape optimization of a forward-swept wing aircraft with lifting fuselage design (figure 7, table 3). The problem is single-disciplinary in a sense that we are only interested in the aerodynamic performance. So the present shape does not depend on an additional structural deformation but only on geometric updates proposed by the optimizer.

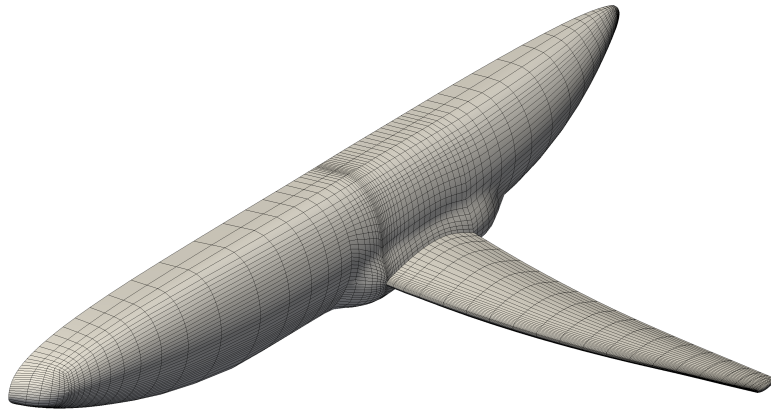


Figure 7. Surface discretization of forward-swept wing aircraft with lifting fuselage design (4085 surface nodes)

Table 3. Selected characteristics of the wing planform

Span	21.9 m
Quarter chord sweep	18.15 deg
Wing surface	160 m ²
Taper ratio	0.265
Aspect ratio	9.45

Some details of the fluid model are compiled in table 4.

Given this aircraft configuration we want to minimize drag while keeping lift on a constant target value. Aerodynamic shape optimization is particularly interesting in this case since the aircraft shows a strong shock inboard around the wing attachment to the fuselage close to the trailing edge (figure 8, left). This shock has a significant contribution to the overall wave drag. However, with given CAD-based shape optimization approaches it could not be reduced limiting the overall improvements. As a matter of fact, to allow for further optimization, not just the wing but also the complete inboard *with* parts of the

Table 4. Fluid model of forward-swept wing aircraft

Governing equations	Steady 3D Euler
Simulated altitude	35000 ft
Freestream Mach number	0.75
Angle of attack	1.33 deg

fuselage, like e.g. the fairing, need to be considered in the optimization. Introducing a parametrization, CAD-based or morphing boxes, which is able to control all these parts simultaneously while considering continuity requirements is very difficult and in any case time consuming. As a matter of fact, the lacking consistent parametrization of both parts, so the fuselage and the wing, was the main reason for the limited improvements so far. This motivates the application of the Vertex Morphing Method in this case. Using Vertex Morphing, the present optimization problem reads as follows:

$$\begin{aligned}
 \min \quad & J = c_{d,ff}(\mathbf{x}) \\
 \text{w.r.t.} \quad & \mathbf{x} \\
 \text{s.t.} \quad & g = c_l - c_{l,baseline} = 0 \\
 & \mathbf{R}_F = 0
 \end{aligned} \tag{3}$$

Herein $c_{d,ff}$ represents the physical drag of the aircraft (according to the far-field drag decomposition method FFD72^{17,18}). The target c_l is chosen to be the value from the baseline design. Since we consider preliminary design we choose the least restrictive set of design variables \mathbf{x} , i.e. all given 4085 nodes on the discrete surface of the aircraft (see figure 7). To run the optimization problem we again use the modified projection algorithm mentioned above. Sensitivity analysis is performed using a discrete adjoint approach. Mesh-motions in the CFD domain are handled using an analytic method and their influence on the sensitivity analysis is considered. Results of the corresponding shape optimization are presented in the following section.

III.B. Results

The quantitative results of this optimization are summarized in table 5. Herein we see that an overall improvement of the far-field drag coefficient of 21.71 % was reached. At the same time the constraint is satisfied, i.e. the lift coefficient only varies by 0.06 % compared to the baseline value. The table also shows that the improvement is due to both a decrease of the induced and a decrease of the wave drag, whereas the latter drops considerably by 86.61 %.

Table 5. Results after simultaneous shape optimization of entire aircraft geometry using Vertex Morphing

	cd far-field	cd wave	cd induced	cd spurious	cl pressure	iterations
baseline	157.91326E-4	30.40042E-4	127.51284E-4	143.48079E-4	0.63495	-
optimized	123.63205E-4	4.07163E-4	119.56042E-4	149.35479E-4	0.63534	172 primal 172 adjoint
change	-21.71 %	-86.61 %	-6.24 %	4.09 %	0.06 %	-

Looking at the optimized surface pressure distribution compared to the one from baseline design (figure 8), we find that the given drop in far-field drag is a result of the overall obtained very smooth pressure contours as well as the clearly alleviated shock regions. In fact pressure discontinuities were reduced almost all over the wing and in particular also inboard around its attachment to the fuselage, where the baseline design shows this strong shock.

Generally the above mentioned improved flow characteristics are a consequence of effective shape changes around the aerodynamically most critical parts of the aircraft. The most critical parts in the given problem are the wing as well as the belly-fairing or the fuselage section close to the wing attachment, respectively. For these areas we are given striking shape changes in the optimized design. For example the optimized wing geometry shows clear profile changes over the whole span, whereas the wing thickness was again kept constant through a proper choice of the filtering within the Vertex Morphing Method. Additional to the wing shape also the inboard and the belly-fairing were subjected to considerable shape modifications, see figure 9. Herein we see that the optimization suggests a more curved belly-fairing as well as more three-dimensional attachment profile of the wing. Particularly interesting to see is the

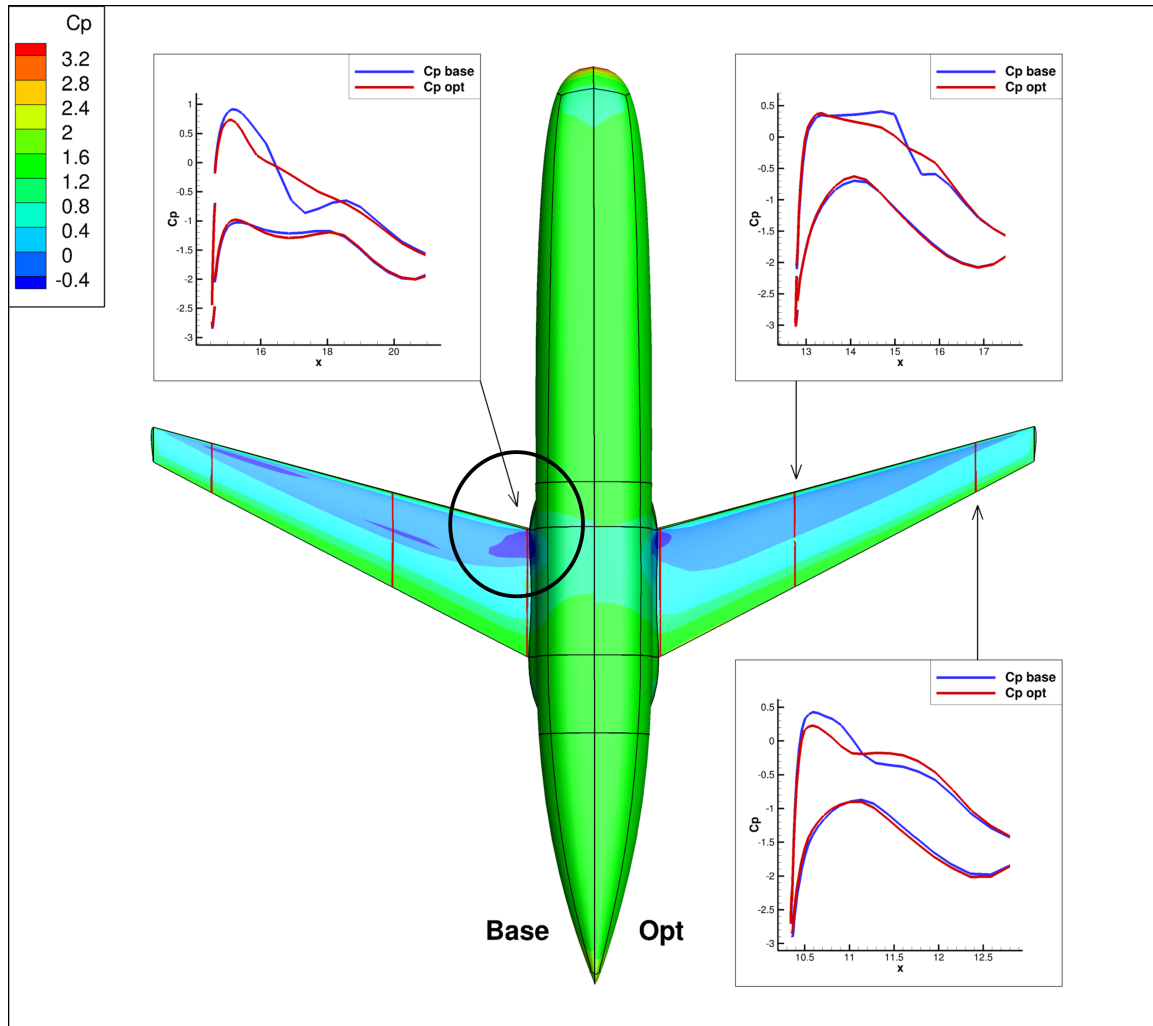


Figure 8. Surface pressure distribution of baseline (left) and optimized design (right). Note the significantly reduced shock inboard around the attachment of the wing to the fuselage.

complex shape change around the intersection between leading edge and fuselage. The resulting flow modification is responsible for the clearly alleviated inboard shock and hence for the above shown drop in wave drag.

Note generally, that we obtained smooth surfaces where smooth surfaces were given before, whereas sharp edges remained sharp and distinct. Note also, that apart from the previous discussed shape changes, the overall dimensions of the aircraft including the wings did not change, see figure 8. Moreover, we would like to emphasize that, despite the high design freedom, no uncontrolled shape modifications were introduced. That is, even so we did not introduce any dedicated parametrization, the Vertex Morphing Method generated valid design suggestions, which in turn provide a profound basis for actual design decisions. Finally we note that further design exploration is quickly possible by varying only the filter parameter and run the optimization again. Also geometric bounds may be taken into account, however, were not formulated in the scope of this paper.

IV. Conclusion

In this paper we showed that the Vertex Morphing Method allows to conveniently explore shape optimization potential of both simple and complex geometries within aircraft preliminary design. Hence significant shape improvements may be identified and new and possibly unexpected shapes may be found. A very practical feature in this context appeared to be the possibility to control the wing thickness without formulating explicit constraints.

Also, we found Vertex Morphing to be particularly useful to shape optimize free-form areas where another parametrization is difficult or even unknown. This opens a lot of new applications fields, for example within the scope of engine integration (aerodynamic shape optimization of pylons).

Furthermore, we have seen that Vertex Morphing may be successfully applied in an aeroelastic shape

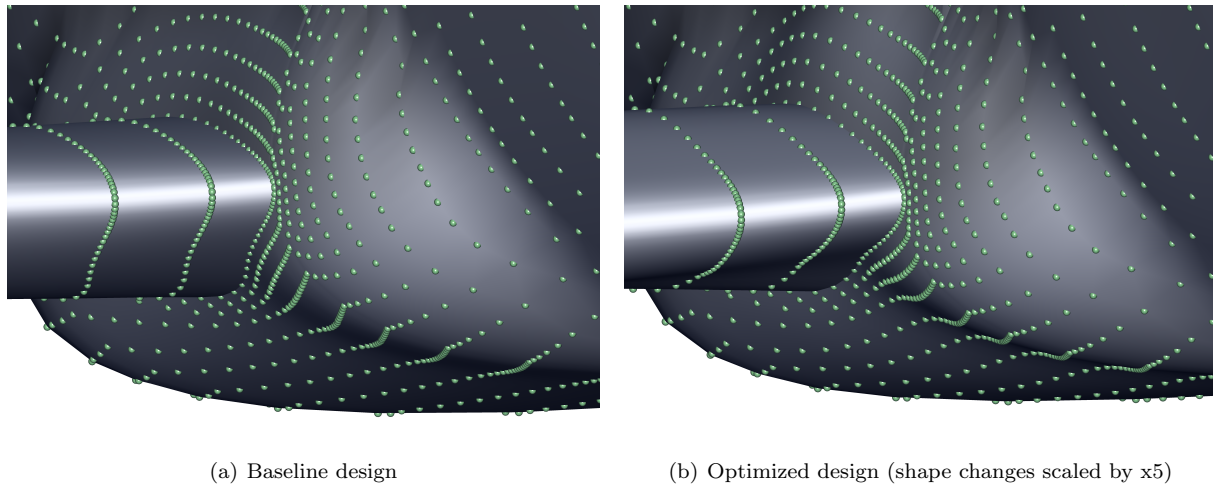


Figure 9. Optimized inboard design when shape optimizing entire aircraft geometry simultaneously using the Vertex Morphing Method (close-up view on belly-fairing and leading edge of the wing).

optimization process, where the shape is depending on the involved structural deformation. As a matter of fact, the corresponding interaction between fluid and structure does not negatively impact the morphing process itself, obviously, however, requires more elaborate state and sensitivity analysis. In this context we found that already a simplified aeroelastic process, including a reduced sensitivity analysis, which does not consider the present coupling terms but still the varying structural deformation, outperforms pure aerodynamic optimization of a selected flight shape. This is noteworthy since modeling such a simplified aeroelastic process requires only minor adjustments beyond the original aerodynamic optimization process whereas a complete multidisciplinary state *and* sensitivity analysis is far more elaborate.

Finally, from all the herein presented examples, we conclude that Vertex Morphing is an effective alternative method for shape optimization or form-finding within aircraft preliminary design.

Acknowledgements

This work was funded by the European Commission through the research project AMEDEO (Aerospace Multidisciplinarity Enabling Design Optimisation) under the FP7-PEOPLE Marie-Curie ITN 316394. The authors gratefully acknowledge all the financial and technical support provided by AMEDEO and the European Commission.

References

- ¹Lyu, Z., Kenway, G. K. W., and Martins, J. R. R. A., "Aerodynamic Shape Optimization Investigations of the Common Research Model Wing Benchmark," *AIAA Journal*, Vol. 53, No. 4, 2015.
- ²Kenway, G. K. W., Kennedy, G., and Martins, J. R. R. A., "A CAD-Free Approach to High-Fidelity Aerostructural Optimization," *13th AIAA/ISSMO Multidisciplinary Analysis Optimization Conference*, Reston, Virginia, 2010.
- ³Gaetan, K. W. K., Kennedy, G. J., and Martins, J. R. R. A., "Scalable parallel approach for high-fidelity steady-state aeroelastic analysis and adjoint derivative computations," *AIAA Journal*, Vol. 52, 2014, pp. 935–951.
- ⁴Carrier, G., Destarac, D., Dumont, A., Méheut, M., Din, I. S. E., Peter, J., Khelil, S. B., Brezillon, J., and Pestana, M., "Gradient-Based Aerodynamic Optimization with the elsA Software," *52nd Aerospace Sciences Meeting*, National Harbor Maryland USA, 2014.
- ⁵Abu-Zurayk, M. and Brezillon, J., "Shape Optimization Using the Aero-structural Coupled Adjoint Approach for Viscous Flows," *Evolutionary and deterministic methods for design, optimization and control (Eurogen 2011)*, Capua, Italy, 2011.
- ⁶Palacios, F., Alonso, J., Duraisamy, K., Colonno, M., Hicken, J., Aranake, A., Campos, A., Copeland, S., Economon, T., Lonkar, A., Lukaczyk, T., and Taylor, T., "Stanford University Unstructured (SU2): An open-source integrated computational environment for multi-physics simulation and design," *51st AIAA Aerospace Sciences Meeting*, Grapevine Texas USA, 2013, pp. 1–60.
- ⁷Palacios, F., Economon, T. D., and Alonso, J. J., "Large-scale aircraft design using SU2," *53rd AIAA Aerospace Sciences Meeting*, American Institute of Aeronautics and Astronautics, Reston Virginia USA, 2015, pp. 1–20.
- ⁸Economon, T. D., Palacios, F., Copeland, S. R., Lukaczyk, T. W., and Alonso, J. J., "SU2: An Open-Source Suite for Multiphysics Simulation and Design," *AIAA Journal*, Vol. 54, No. 3, 2015, pp. 1–19.
- ⁹Jameson, A., "Optimum aerodynamic design using control theory," *Computational Fluid Dynamics Review*, Vol. 3, 1995, pp. 495–528.
- ¹⁰Mohammadi, B. and Pironneau, O., *Applied Shape Optimization for Fluids*, Oxford University Press, 2nd ed., 2010.
- ¹¹Hojjat, M., Stavropoulou, E., and Bletzinger, K.-U., "The Vertex Morphing method for node-based shape optimization," *Computer Methods in Applied Mechanics and Engineering*, Vol. 268, 2014, pp. 494–513.

¹²Baumgärtner, D., Viti, A., Dumont, A., Carrier, G., and Bletzinger, K.-U., “Comparison and combination of experience-based parameterization with Vertex Morphing in aerodynamic shape optimization of a forward-swept wing aircraft,” *17th AIAA/ISSMO Multidisciplinary Analysis and Optimization Conference*, American Institute of Aeronautics and Astronautics, Washington D.C. USA, 2016, pp. AIAA-2016-3368.

¹³Bletzinger, K.-U., “A consistent frame for sensitivity filtering and the vertex assigned morphing of optimal shape,” *Structural and Multidisciplinary Optimization*, Vol. 49, No. 6, 2014, pp. 873–895.

¹⁴International Center for Numerical Methods in Engineering (CIMNE), *Kratos Multi-Physics*, <http://www.cimne.com/kratos/>, May 2016.

¹⁵Dumont, A., Ghazlane, I., Marcelet, M., Carrier, G., and Din, I. S. E., “Overview of Recent Development of Aeroelastic Adjoint Method for Civil Aircraft Wing Optimization at ONERA,” *ODAS, ONERA-DLR Aerospace Symposium*, Toulouse, France, 2011.

¹⁶Cambier, L. and Veillot, J. P., “Status of the elsA Software for Flow Simulation and Multi-Disciplinary Applications,” *46th AIAA Aerospace Science Meeting and Exhibit*, Reno Nevada USA, 2008.

¹⁷van der Vooren, J. and Destarac, D., “Drag/Thrust Analysis of Jet-propelled Transonic Transport Aircraft; Definition of Physical Drag Components,” *Aerospace Science & Technology*, Vol. 8, 2004, pp. 545–556.

¹⁸Destarac, D., “Far-field / Near-field Drag Balance and Applications of Drag Extraction in C.F.D.” *VKI Lecture Series, CFD Based Aircraft drag Prediction and Reduction*, Hampton VA, 2003.

Evolutionary Crashworthiness Topology Optimization of Thin-Walled Structures

Mariusz Bujny*

Technical University of Munich, Munich, 80333, Germany

Nikola Aulig†

Honda Research Institute Europe GmbH, Offenbach/Main, 63073, Germany

Markus Olhofer‡

Honda Research Institute Europe GmbH, Offenbach/Main, 63073, Germany

Fabian Duddeck§

Technical University of Munich, Munich, 80333, Germany

A basis for most of the state-of-the-art methods for crashworthiness topology optimization form voxel elements, being three-dimensional, regular brick finite elements. Such voxel-based optimization techniques lead to creation of so-called zigzag structures that are used as a reference for positioning of the structural beams. On the other hand, important vehicle body components are made of thin-walled sheet metal structures and the use of an optimized design obtained from any voxel-based optimization method as an inspiration for the final thin-walled structure is questionable and requires considerable manual post-processing. In this paper we propose a novel approach using evolutionary algorithms for optimization of thin-walled structures. For evaluation of the method, a 2D transverse bending of a rib-reinforced thin-walled structure is considered. A state-of-the-art Covariance Matrix Adaptation Evolution Strategy (CMA-ES), combined with a suitable representation, is used for optimization of the layout of the reinforcing ribs. The results show that evolutionary optimization algorithms can be efficiently used for topology optimization of crash-loaded thin-walled structures.

I. Introduction

Structural Topology Optimization (TO) has proven to be a valuable tool for identification of the best concepts in early phases of the design process. It is widely used in lightweight design of structures in automotive and aerospace industry, as well as in civil engineering, materials science and biomechanics. In particular, TO of crash-loaded structures in vehicles is a very challenging task, which requires still a lot of work to be done to develop accurate and efficient methods. Due to the continuous increase in computational resources, global stochastic search methods can be applied also in this field, resulting in flexible techniques able to deal with different optimization criteria.

Nowadays, due to the lack of reliable sensitivity information, state-of-the-art methods for crash TO use very strong assumptions about the underlying optimization problems. This is mainly motivated by very high complexity of crash phenomena, including contact and failure, which results in highly nonlinear, noisy and discontinuous responses, excluding even the use of finite-differencing to obtain the gradient information. As a result, gradient-based methods cannot be used and considerable simplifications are applied.

In Equivalent Static Loads Methods^{4,5,7,19} dynamic crash loads are replaced by static forces and standard TO approaches, taking advantage of efficient gradient-based optimizers, are used to find the best topology. In Ground Structure Approaches^{9,21} topologies evolve from initial layout of elementary structural components that undergo a simplified crash behavior. Fixed ground structure, however, highly

*Doctoral Candidate, Chair of Computational Mechanics.

†Scientist, Complex System Optimization & Analysis.

‡Chief Scientist, Complex System Optimization & Analysis.

§Professor for Computational Mechanics, Chair of Computational Mechanics.

limits the design space and the simplified crash models involve considerable calibration effort. In Graph and Heuristic Approaches,¹⁸ optimization is based on explicit finite element simulations, but topological changes are introduced based on heuristic rules derived from the expert knowledge. Efficient Hybrid Cellular Automata techniques^{8,15,16,20} homogenize energy distribution in the structure, which is again an arguable assumption and can be true only for selected cases. Recently, an attempt to use Evolutionary Algorithms (EA) together with the Level Set Method (LSM) for crash TO has been made.² The main advantage of using evolutionary optimization methods is the fact that they can be used to optimize arbitrary objective functions directly, without the need to introduce any additional assumptions. Nevertheless, evolutionary methods involve considerable computational costs, which become less important due to the increasing availability of high performance cluster computers. Furthermore, the computational costs can be considerably reduced with use of hybrid algorithms³ that exploit approximate gradient information obtained from structural or equivalent state¹ as well as any known heuristics.

Most of the techniques mentioned above use solid finite elements (voxels) in the models used in crash simulations. The basic idea in such cases is stated as follows: Firstly, define the design domain in the space that is not occupied with non structural vehicle elements such as wheels, engine, etc.; Secondly, fill the volume of the design space with voxels; Thirdly, eliminate redundant voxels by an iterative numerical optimization procedure. This results in creation of the zigzag structures that can be used as a reference for positioning of the structural beams. Such a design is assumed to be optimized with respect to the given objective (e.g. energy absorption, plastic deformation, etc.). These methods are very efficient, but involve several limitations. Usually, due to the heuristic assumptions, they can be applied only in optimization of selected cases, with strictly specified objectives and constraints. The zigzag structures demand considerable post-processing effort to satisfy the manufacturing requirements. Finally, important vehicle body components are made of thin-walled sheet metal structures. In such a case plastic buckling is the principal phenomenon that influences the crashworthiness behavior. In the optimization process based on voxel elements, structures made of thin metal sheets cannot be obtained, which leads to completely different phenomena, not corresponding to the buckling of thin-walled structures. As a result, the use of an optimized design obtained from any voxel-based optimization method as an inspiration for final thin-walled structure is questionable and a direct optimization of thin-walled structures would be favorable. In the following sections, we demonstrate how this can be achieved.

In this work, we propose a novel approach using EA for optimization of thin-walled structures. Unlike in the other approaches for crashworthiness TO of thin-walled structures,^{8,15,18} in evolutionary optimization methods, no heuristic assumptions about the properties of the optimization problem are made, and therefore, any actual quantifiable user defined objective function can be optimized directly.

The paper is structured as follows. In Section II the parametrization of the thin-walled structures and the algorithm for generation of shell finite element meshes are described. Section III defines the optimization problem and describes the optimization algorithm used in this work. Section IV presents the test cases. In Section V the results of the optimization are presented. The paper is concluded in Section VI.

II. Parametrization

The main focus of this work is development of a method for optimization of rib-reinforced, thin-walled extrusions. In such a case it is crucial to use an appropriate finite element model that would be able to capture complex physical behavior of the structure during the crash event. Unless the number of finite elements in the voxel-based approaches is very high, physical behavior cannot be captured properly and finite element models based on shell elements have to be used. As a result, the optimization approach has to be able to create different finite element meshes during the optimization process.

In this section, a simple, yet efficient and extensible parametrization and meshing algorithm have been proposed. In order to describe the structure, the representation is based on a set of thin-walled components, which can freely move in the design domain. The main idea for this type of parametrization was inspired by the voxel-based, level-set approach for crash TO.²

At the beginning of the optimization, the number of reinforcing ribs is defined and the ribs are distributed evenly inside a specified design domain. Each rib is described by 5 parameters (see Figure 1): x and y coordinate of the center of the rib (x_0, y_0), rotation angle with respect to the x -axis (θ), length (l) and thickness (t).

The optimization algorithm operates on a vector of design variables consisting of parameters defining each rib. In order to find the intersection points between the ribs, the equations of the collinear lines are found and multiple systems of two equations are solved. The intersection point has to lie inside the design domain and within the length of each rib. In order to avoid creation of very small finite elements, which

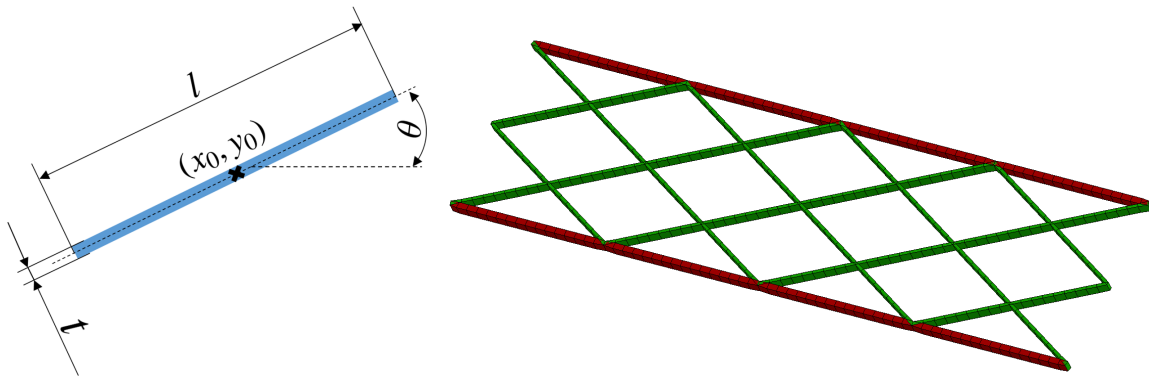


Figure 1: Parametrization of a single rib (left) and the initial shell finite element mesh (right).

determine the critical time step in explicit finite element simulations, we merge the intersection points and ends of the ribs, if they are too close to each other. This also limits the design space by eliminating the designs that would be difficult to manufacture. Finally, the nodes of the mesh are distributed as uniformly as possible along each rib and the corresponding finite element mesh is created. An algorithm implementing the above mentioned principles is presented below:

1. For each rib, find the equation of a collinear straight line. For each pair of ribs, find the intersection point between the corresponding lines and check if the resulting point lies within a distance lower than half of length from the centers of each rib. If yes, add the point to the list of intersection points.
2. Check the distance between each pair of intersection points. If the intersection points are closer to each other than a specified threshold, delete one of them from the list of intersection points.
3. For each intersection point, save the list of ribs intersecting at that point (two or more).
4. For each rib, compute the distance between each end and the intersection points belonging to the rib. If it is below a given threshold, e.g. half of the reference finite element size, move the end of the rib to the intersection point.
5. Distribute the nodes of the first layer of the finite element mesh along each rib. Using the reference element size, place the nodes possibly uniformly between end and intersection points of the ribs (see Figure 2).
6. Copy the first layer of nodes and move along the extrusion direction. Create the shell finite element mesh based on the generated nodes.

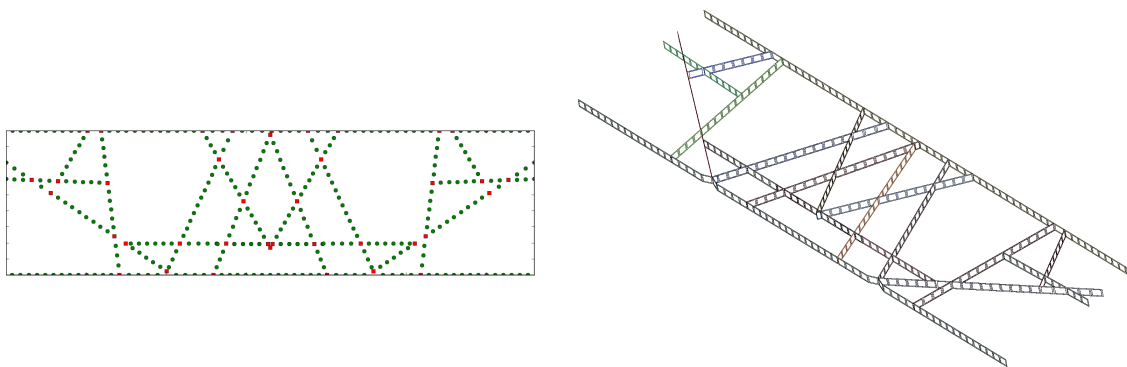


Figure 2: Intersection points between ribs (red squares) and the nodes of the finite element mesh (green points). Resulting finite element mesh (right).

The approach presented above can be easily extended to include curved ribs or ribs of arbitrary shapes by considering not only straight lines, but also arcs or splines. However, in order to keep the number of design variables on a low level, we consider straight ribs only.

III. Optimization

In this work, optimization problems of the following form are considered:

$$\begin{aligned} \min_{\mathbf{z}} f_{obj}(\mathbf{z}), \mathbf{z} \in \mathbb{R}^n; \\ \text{s.t. } \mathbf{r}(t) = \mathbf{0}; \\ g_j(\mathbf{z}) \leq 0, j = 1, \dots, p, \end{aligned} \quad (1)$$

where f_{obj} is the objective function to be minimized, g_j are the inequality constraints, \mathbf{z} denotes the vector of design variables and $\mathbf{r}(t) = \mathbf{0}$ corresponds to the dynamic equilibrium at time t .

In order to use EA for optimization of the constrained problem given by the Equation (1), a transformation of the fitness function according to the exterior penalty method^{6,22} is applied:

$$f(\mathbf{z}) = f_{obj}(\mathbf{z}) + c \sum_{j=1}^p \max(0, g_j(\mathbf{z})) \quad (2)$$

where c is a weighting constant used to penalize the infeasible designs. Additionally, bounds on parameters are imposed by applying a quadratic transformation of design variables.¹⁰

The optimization process is driven by the state-of-the-art Covariance Matrix Adaptation Evolution Strategy (CMA-ES).¹³ CMA-ES is a derandomized Evolution Strategy, which adapts the covariance matrix of the normal distribution used in the mutation step according to previous successful search steps.¹¹ The idea in this case is similar to the gradient-based quasi-Newton methods, which estimate the Hessian matrix iteratively as the optimization process progresses. In particular, CMA-ES is very efficient in minimizing unimodal functions,¹¹ but the superiority of the method on non-separable and ill-conditioned problems has been demonstrated, as well.¹³ An extension of the CMA-ES by the rank- μ -update^{14,17} allowed to use more effectively the information from large populations without influencing the performance when small populations are considered. In this research, we used the Python implementation¹² of this method.

IV. Test Cases

Test cases presented in this work are inspired directly by the Euro NCAP's side pole impact. In this type of crash, both the intrusion of the pole into the vehicle and the maximal deceleration associated with the crash event, which is crucial from the point of view of Head Injury Criterion (HIC), should be taken into account.

In this paper, a crash of a rectangular, rib-reinforced, aluminum structure is considered (see Figure 3). The structure is fixed at both ends and impacted in the middle by a cylindrical pole. Outer, horizontal walls remain unchanged and only the inner, reinforcing ribs are subject to optimization.

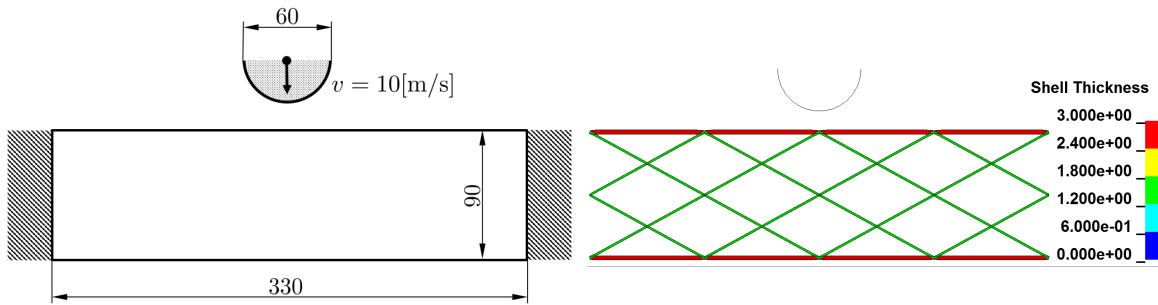


Figure 3: Optimization test case (left) and the corresponding LS-Dyna model (right).

Material properties and the setup of the test case are presented in Table 1. In each of the cases presented below, the initial design (Figure 3, right) consists of 16 reinforcing ribs corresponding to 80 design variables in the general case and 40 design variables if symmetry is imposed. The symmetry condition is applied in the parametrization, but a complete finite element model is used in the simulations in order to allow for a non-symmetric behavior of the structure. A maximal allowed thickness of a rib is equal to 3 [mm] and the ribs, whose thicknesses drop below 0.5 [mm] during the optimization are deleted from the structure. In case if the generated finite element mesh leads to a problem with stability of the simulation, the design is granted a high penalty, which eliminates it in the selection step of the CMA-ES. All of the design variables are normalized to obtain a similar impact of each parameter on the considered responses.

Property	Symbol	Value	Unit
Beam material density	ρ	$2.7 \cdot 10^3$	kg/m ³
Young's modulus	E	$7.0 \cdot 10^4$	MPa
Poisson's ratio	ν	0.33	-
Yield strength	R_e	241.0	MPa
Tangent modulus	E_{tan}	70.0	MPa
Pole velocity	v	10	m/s
Pole mass	m	4.7	kg
LS-Dyna termination time	t_{end}	12	ms

Table 1: Configuration of the test cases.

IV.A. Case 1

In the first case, the impactor's intrusion minimization problem with a mass constraint is considered. The formal definition of the optimization problem can be stated as follows:

$$\begin{aligned}
 &\min_{\mathbf{z}} (d_{max}(\mathbf{z})), \mathbf{z} \in \mathbb{R}^n; \\
 &\text{s.t. } \mathbf{r}(t) = \mathbf{0}; \\
 &\quad m(\mathbf{z}) \leq m_{req};
 \end{aligned} \tag{3}$$

where d_{max} is the maximal displacement of the pole (intrusion), m is the mass of the whole structure and m_{req} is the required mass of the optimized design.

IV.B. Case 2

The second case is the problem of mass minimization under the constraint on the maximal deceleration of the impactor. Additionally, in order to prevent removal of the whole structure by the optimization algorithm, a constraint requiring the velocity of the impactor to reverse at the end of the simulation has to be imposed. Alternatively, a constraint on the maximal intrusion of the pole could be imposed to play a similar role. The optimization problem in this case is formally defined as:

$$\begin{aligned}
 &\min_{\mathbf{z}} (m(\mathbf{z})), \mathbf{z} \in \mathbb{R}^n; \\
 &\text{s.t. } \mathbf{r}(t) = \mathbf{0}; \\
 &\quad a_{max}(\mathbf{z}) \leq a_{req}; \\
 &\quad v_{end}(\mathbf{z}) \geq 0
 \end{aligned} \tag{4}$$

where a_{max} is the maximal deceleration of the pole during the crash and a_{req} is the maximal allowed acceleration. The velocity of the pole at the end of the simulation is denoted by v_{end} .

V. Results

Below, the summary of the successful optimization runs for the two test cases described in Section IV are presented. For each case, the convergence plots resulting from averaging of fitness evolution of 10 different optimization runs are presented and the performance of the best optimized design is analyzed.

V.A. Case 1

Figure 4 shows the convergence of the fitness function in terms of generations (iterations of EA) and evaluations (finite element simulations). The layout of the ribs and their thicknesses have been shown in the Figure 5. It is clear that in this case the upper bound on the rib thickness plays a crucial role and is the main reason why double ribs were created. Interestingly, none of the ribs was deleted from the structure and their thicknesses were kept just above the threshold, below which they would be removed. This shows that also those components play an important role for the performance of the structure for this optimization case. The crash behavior of the structure is shown in Figure 11 (Appendix).

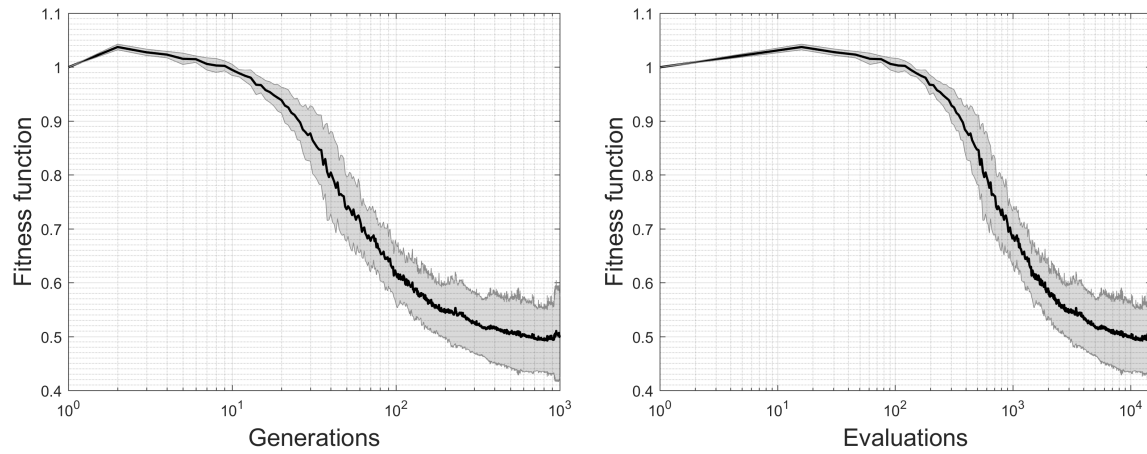


Figure 4: Convergence of the fitness function for CMA-ES(7,15), averaged over 10 optimization runs in terms of generations (left) and evaluations (right). Grey area corresponds to 2 standard deviations of the fitness function.

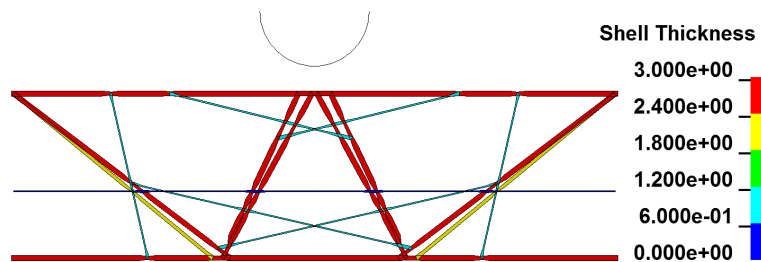


Figure 5: Rib layout and thickness distribution (in [mm]) for the best optimized design (test case 1).

Below, the comparison of the performance of the initial and the best optimized design in terms of intrusion is presented:

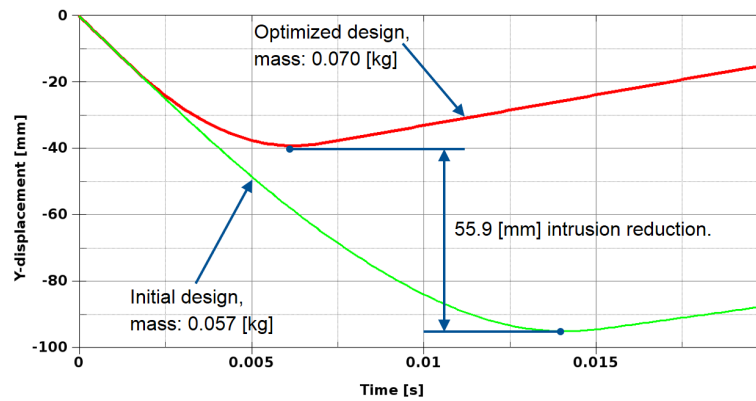


Figure 6: Intrusion of the impactor during the crash for the initial and the best optimized design (test case 1).

V.B. Case 2

Figure 7 presents the convergence of the optimization algorithm averaged over 10 optimization runs, as well. The optimization starts in the infeasible region and the optimizer needs quite a lot of time to satisfy the constraints. This is mainly caused by a very demanding constraint on the maximal acceleration, requiring it to remain almost constant throughout the whole crash event.

Rib layout and the thickness distribution for the best optimized design is presented in Figure 8. Deformation of the structure during the crash event and the equivalent stress field are shown in Figure 12 (Appendix). This test case demonstrates clearly merits of the proposed approach, which is able to develop a well-performing structure taking advantage of a complex buckling behavior. This would be

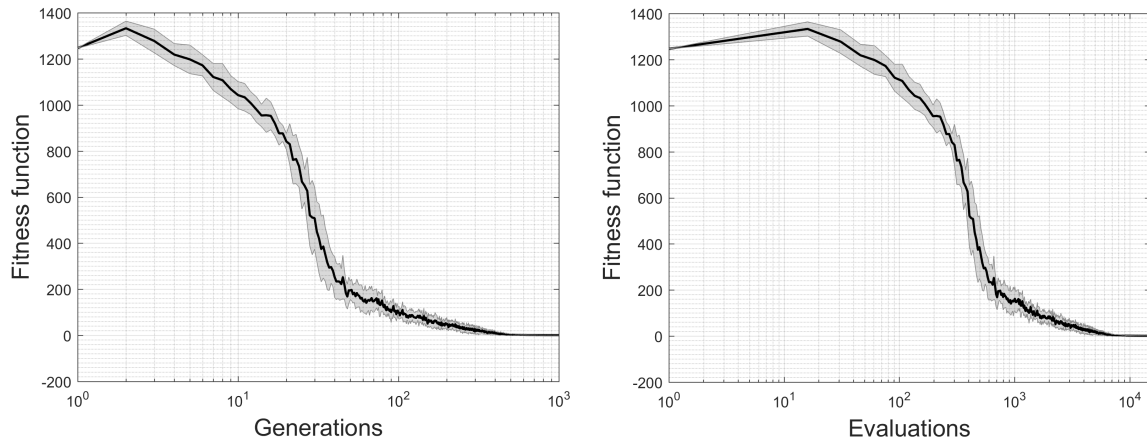


Figure 7: Convergence of the fitness function for CMA-ES(7,15), averaged over 10 optimization runs in terms of generations (left) and evaluations (right). Grey area corresponds to 2 standard deviations of the fitness function.

certainly not possible with a voxel-based approach, with a similar number of finite elements. Our method allows for a considerable reduction of computational costs and can capture complex buckling behavior of the thin-walled structures.

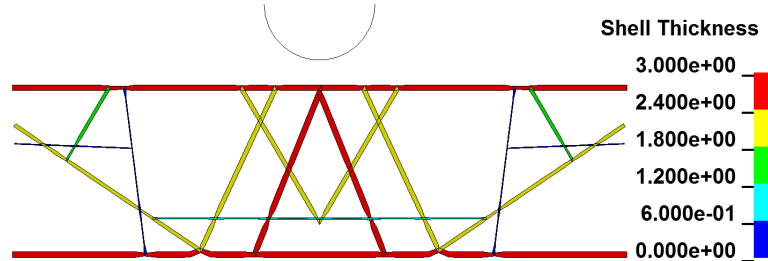


Figure 8: Rib layout and thickness distribution (in [mm]) for the best optimized design (test case 2).

Below, in Figure 9, the comparison of the performance of the initial and the best optimized structure in terms of maximal deceleration of the impactor is shown. Although the initial design does not satisfy the constraint requiring the reversal of the impactor's velocity after 12 [ms] and it takes much more time until it stops, the maximal deceleration of the pole is still considerably higher, whereas the mass of both structures is on a similar level. Obviously, this leads to much higher intrusion of the pole for the initial design (see Figure 10). The optimized structure shows virtually perfect crash behavior, with almost flat deceleration characteristics.

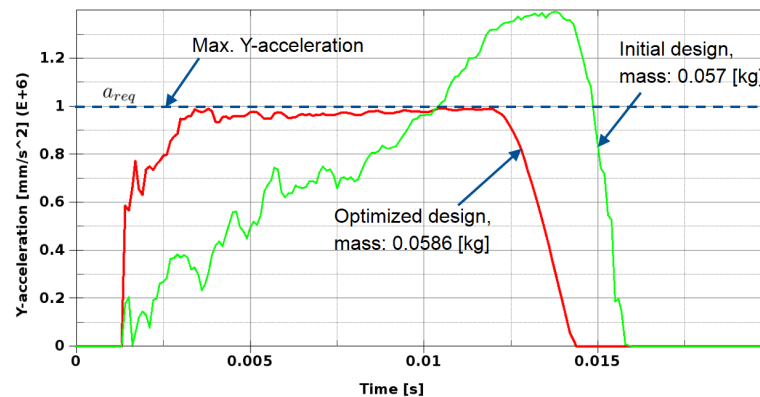


Figure 9: Deceleration of the impactor during the crash for the initial and the best optimized design (test case 2).

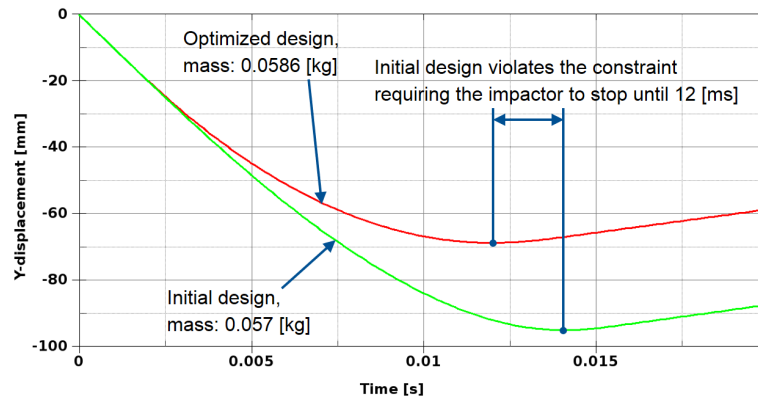


Figure 10: Intrusion of the impactor during the crash for the initial and the best optimized design (test case 2).

VI. Conclusion

In this paper, a novel approach, using Evolutionary Algorithms for optimization of thin-walled structures, is proposed. In this method, we address the problem of optimization of rib-reinforcements of the extruded, thin-walled structures. Each rib is parametrized with use of 5 parameters describing its position, rotation, length and thickness. An efficient meshing algorithm allows for an automatic creation of shell finite element meshes, which are used in the optimization. In this way the optimizer operates directly on shell meshes, which, unlike solid finite elements, can accurately capture complex buckling behavior of thin-walled structures at a reasonable computational cost. As a result, the method bridges the gap between the optimized topologies, which have to be interpreted in case of voxel-based approaches, and the final thin-walled structures used in the automotive industry.

The method has a wide range of potential applications in the automotive industry, including optimization of such components as crashboxes, bumpers, roof reinforcements or even seats. The flexibility of the method, giving the designer the freedom to choose any quantifiable objective functions and constraints, makes the application of the method in the other branches of industry very promising, as well. The higher flexibility legitimates the higher computational costs of Evolutionary Algorithms, which for many quality criteria are the only algorithms that can be used. Finally, very good scalability of Evolutionary Algorithms makes them applicable to real-world problems, being an attractive alternative to the state-of-the-art methods. In particular, in case of crashworthiness topology optimization, this means the possibility to eliminate the heuristic assumptions used in the state-of-the-art methods, leading potentially to considerable improvements in the design of crash structures.

Appendix

Case 1

Deformation of the best optimized design during the crash and the corresponding equivalent stress for the Case 1:

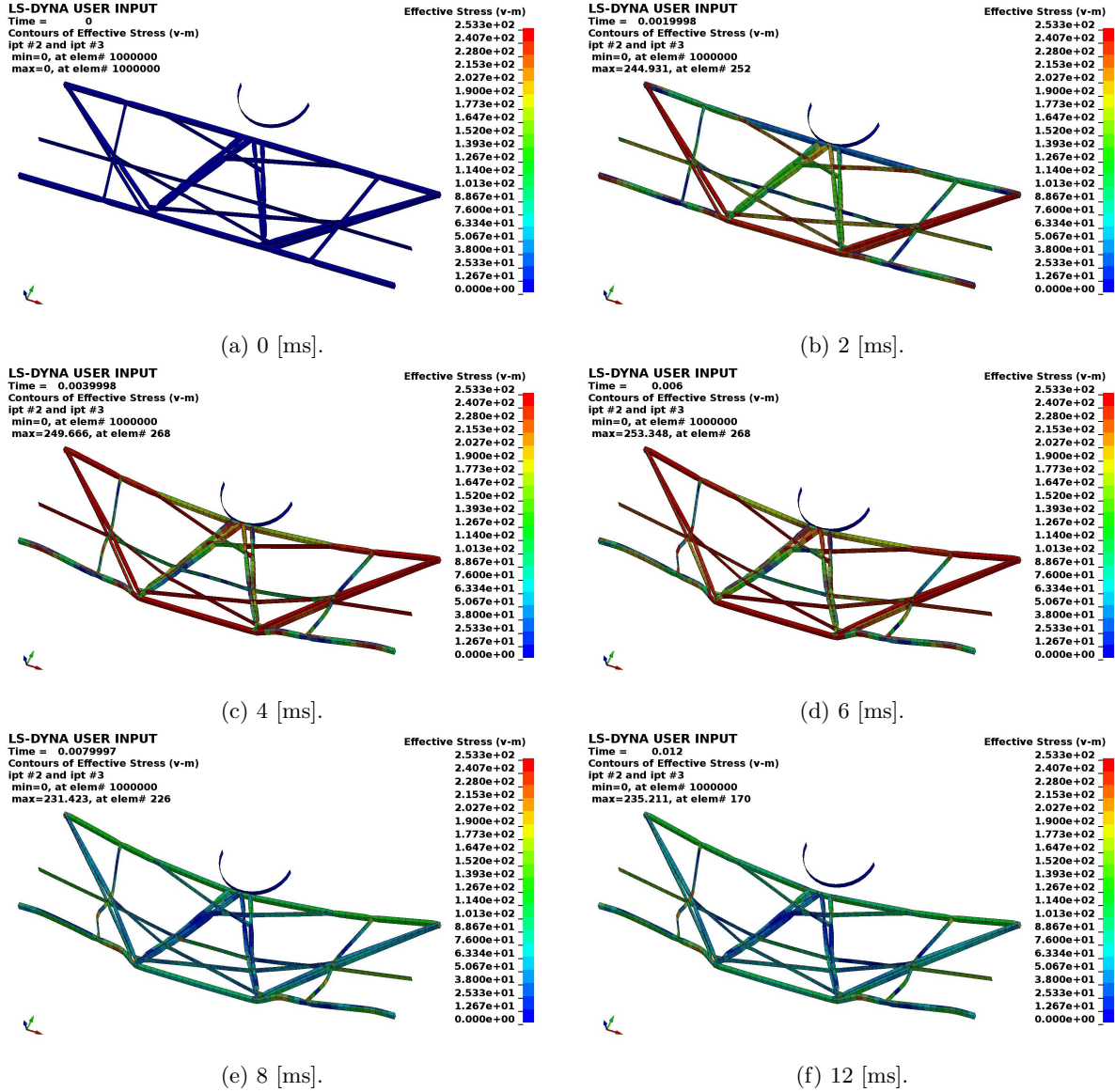


Figure 11: Deformation and the equivalent stress field for the best optimized design for the test case 1.

Case 2

Deformation of the best optimized design during the crash and the corresponding equivalent stress for the Case 2:

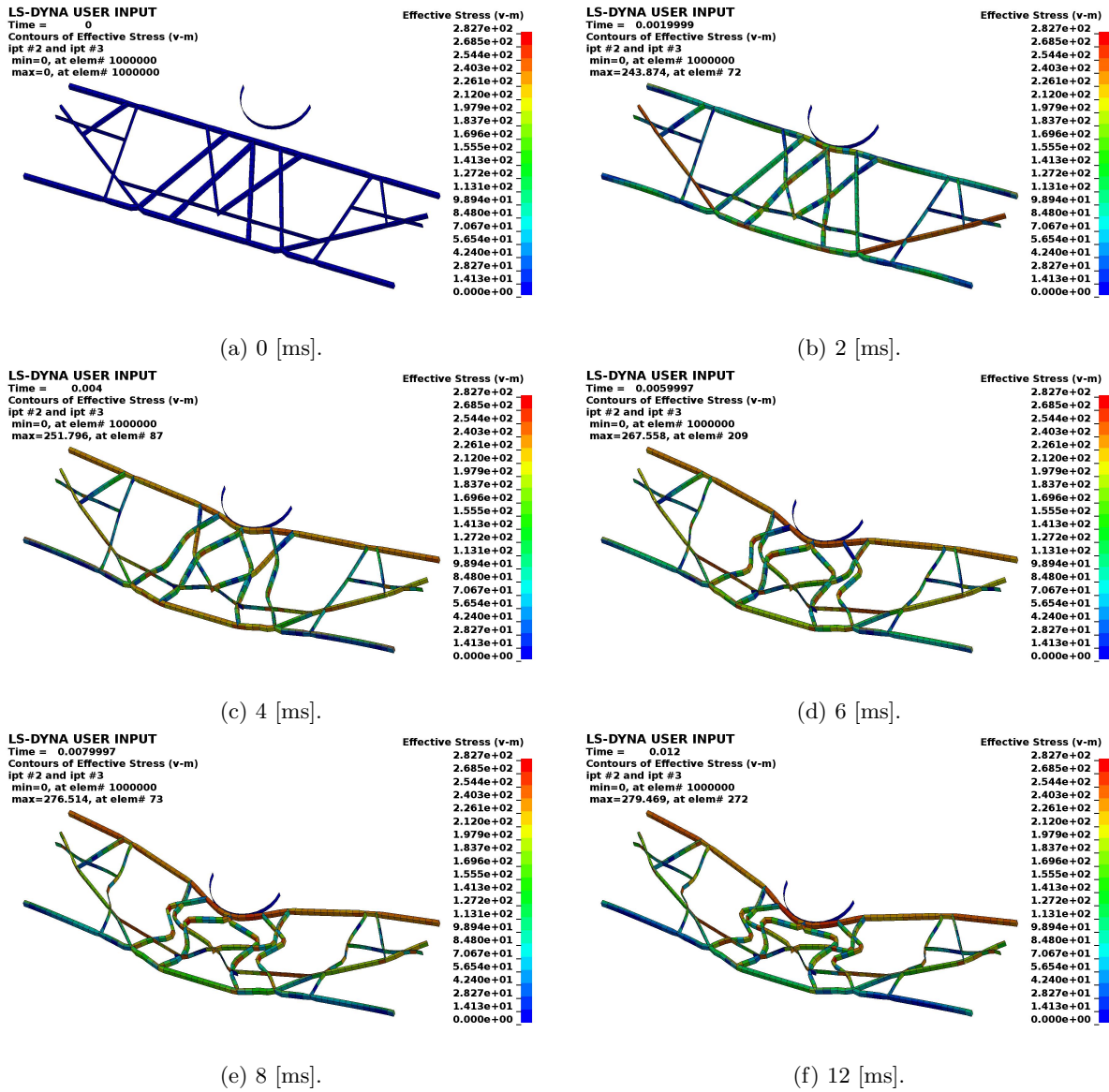


Figure 12: Deformation and the equivalent stress field for the best optimized design for the test case 2.

References

- ¹N. Aulig and M. Olhofer. Neuro-evolutionary topology optimization of structures by utilizing local state features. GECCO '14, pages 967–974, Vancouver, BC, Canada, 2014. ACM.
- ²M. Bujny, N. Aulig, M. Olhofer, and F. Duddeck. Evolutionary Level Set Method for Crashworthiness Topology Optimization. In *ECCOMAS Congress 2016*. European Community on Computational Methods in Applied Sciences, 2016.
- ³M. Bujny, N. Aulig, M. Olhofer, and F. Duddeck. Hybrid Evolutionary Approach for Level Set Topology Optimization. In *IEEE Congress on Evolutionary Computation*. IEEE, 2016.
- ⁴M. Cavazzuti, A. Baldini, E. Bertocchi, D. Costi, E. Torricelli, and P. Moruzzi. High performance automotive chassis design: a topology optimization based approach. *Structural and Multidisciplinary Optimization*, 44(1):45–56, 2010.
- ⁵J. Christensen, C. Bastien, and M. V. Blundell. Effects of roof crush loading scenario upon body in white using topology optimisation. *International Journal of Crashworthiness*, 17(1):29–38, 2012.
- ⁶C. A. Coello Coello. Theoretical and numerical constraint-handling techniques used with evolutionary algorithms: a survey of the state of the art. *Computer Methods in Applied Mechanics and Engineering*, 191(1112):1245–1287, 2002.
- ⁷F. Duddeck and K. Volz. A new topology optimization approach for crashworthiness of passenger vehicles based on physically defined equivalent static loads. In *Proceedings ICRASH conference, Milano, Italy*, 2012.
- ⁸F. Duddeck, S. Hunkeler, P. Lozano, E. Wehrle, and D. Zeng. Topology Optimization for Crashworthiness of Thin-walled Structures under Axial Impact Using Hybrid Cellular Automata. *Structural and Multidisciplinary Optimization*, 2015.
- ⁹H. Fredricson, T. Johansen, A. Klarbring, and J. Petersson. Topology optimization of frame structures with flexible joints. *Structural and Multidisciplinary Optimization*, 25(3):199–214, 2003.
- ¹⁰N. Hansen. CMA Evolution Strategy Source Code, 2016.
- ¹¹N. Hansen and A. Ostermeier. Completely Derandomized Self-Adaptation in Evolution Strategies. *Evolutionary Computation*, 9(2):159–195, 2001.
- ¹²N. Hansen. The CMA Evolution Strategy: A Comparing Review. In J. A. Lozano, P. Larrañaga, I. Inza, and E. Bengoetxea, editors, *Towards a New Evolutionary Computation*, number 192 in Studies in Fuzziness and Soft Computing, pages 75–102. Springer Berlin Heidelberg, Germany, 2006.
- ¹³N. Hansen and S. Kern. Evaluating the CMA Evolution Strategy on Multimodal Test Functions. In X. Yao, E. K. Burke, J. A. Lozano, J. Smith, J. J. Merelo-Guervós, J. A. Bullnaria, J. E. Rowe, P. Tiño, A. Kabán, and H.-P. Schwefel, editors, *Parallel Problem Solving from Nature - PPSN VIII*, number 3242 in Lecture Notes in Computer Science, pages 282–291. Springer Berlin Heidelberg, Germany, 2004.
- ¹⁴N. Hansen, S. Müller, and P. Koumoutsakos. Reducing the Time Complexity of the Derandomized Evolution Strategy with Covariance Matrix Adaptation (CMA-ES). *Evolutionary Computation*, 11(1):1–18, 2003.
- ¹⁵S. Hunkeler. *Topology Optimisation in Crashworthiness Design via Hybrid Cellular Automata for Thin-walled Structures*. PhD thesis, Queen Mary University of London, UK, 2013.
- ¹⁶C. K. Mozumder. *Topometry optimization of sheet metal structures for crashworthiness design using hybrid cellular automata*. PhD thesis, University of Notre Dame, USA, 2010.
- ¹⁷S. D. Müller, N. Hansen, and P. Koumoutsakos. Increasing the Serial and the Parallel Performance of the CMA-Evolution Strategy with Large Populations. In J. J. M. Guervós, P. Adamidis, H.-G. Beyer, H.-P. Schwefel, and J.-L. Fernández-Villacañas, editors, *Parallel Problem Solving from Nature — PPSN VII*, number 2439 in Lecture Notes in Computer Science, pages 422–431. Springer Berlin Heidelberg, Germany, 2002.
- ¹⁸C. Ortmann and A. Schumacher. Graph and heuristic based topology optimization of crash loaded structures. *Structural and Multidisciplinary Optimization*, 47(6):839–854, 2013.
- ¹⁹G.-J. Park. Technical overview of the equivalent static loads method for non-linear static response structural optimization. *Structural and Multidisciplinary Optimization*, 43(3):319–337, 2010.
- ²⁰N. M. Patel. *Crashworthiness Design Using Topology Optimization*. PhD thesis, University of Notre Dame, USA, 2007.
- ²¹C. B. W. Pedersen. Topology optimization design of crushed 2d-frames for desired energy absorption history. *Structural and Multidisciplinary Optimization*, 25(5-6):368–382, 2003.
- ²²S. S. Rao *Engineering Optimization: Theory and Practice*. John Wiley & Sons, 2009.

Multidisciplinary Design Optimization of Aero-Engine Fan Blades

Christopher Chahine^{*}

Von Karman Institute for Fluid Dynamics, Rhode-Saint-Genese, 1640, Belgium

Tom Verstraete[†]

Queen Mary University of London, London, E1 4NS, United Kingdom

and

Li He[‡]

University of Oxford, Oxford, OX2 0ES, United Kingdom

A multidisciplinary and multiobjective optimization of a transonic fan blade for a high bypass ratio turbofan engine is presented including aerodynamic as well as structural static and dynamic performance criteria. The optimization strategy applied is based on a two-level approach consisting of a Differential Evolution algorithm coupled to a Kriging metamodel in order to speed up the optimization process. High-fidelity performance evaluations are carried out by means of 3D Computational Fluid Dynamics and Computational Structural Mechanics analysis tools. Multiple key operating points are considered in the optimization process; aerodynamic performance is evaluated at top-of-climb and cruise conditions. Stresses are evaluated at take-off conditions, taking into account centrifugal and gas loads. Blade vibration is furthermore assessed over the entire operating range. Aerodynamic performance is separately evaluated for core and bypass flows in order to match the requirements specified by the engine cycle design.

I. Introduction

IN a modern high-bypass ratio turbofan engine the majority of the engine's thrust is generated by the fan, while only a small part (typically 10-20%) of the thrust is generated by the engine core. Hence, the main contribution to propulsive efficiency stems from the fan design with direct implications on specific fuel consumption (SFC) and overall engine efficiency. Besides the need to be aerodynamically efficient, fan blades are required to withstand considerable static and dynamic structural loads during operation. Their design is therefore a multidisciplinary problem which is further complicated by the fact that the involved disciplines have differing and often opposing requirements. In current industrial design practice, these disciplines are mostly handled separately from each other and the design progresses iteratively from one discipline to another until a satisfactory solution is found. The result is a time consuming and costly design process with the further disadvantage that interactions between disciplines are difficult to reveal. In contrast, this paper presents the application of a multidisciplinary and multiobjective optimization system to the design of a transonic fan blade for a typical modern high-bypass ratio turbofan engine. The optimization system enables the concurrent evaluation of aerodynamic and structural performance criteria, therefore facilitating the identification of the interaction of disciplines and allowing the design to progress towards global optimal solutions in a reduced design time.

Communicating Author: christopher.chahine@vki.ac.be

^{*} DPhil Candidate, Turbomachinery and Propulsion Department, Chaussee de Waterloo 72, 1640 Rhode-Saint-Genese, Belgium and Department of Engineering Science, University of Oxford, Osney Mead, Oxford, OX2 0ES, United Kingdom.

[†] Visiting Professor, School of Engineering and Material Science, Queen Mary University of London, E1 4NS Mile End Road, London, United Kingdom.

[‡] Professor, Chair of Computational Aerothermal Engineering, Department of Engineering Science, University of Oxford, Osney Mead, Oxford OX2 0ES, United Kingdom.

II. Optimization System

A flow chart of the optimization system used in present work is shown in Fig. 1. At the core of the in-house developed system are a multi-objective Differential Evolution algorithm (DE)¹, a database containing the design and performance parameters for the analyzed designs, several metamodels, including Radial Basis Functions, Artificial Neural Networks and Kriging, and a high-fidelity evaluation chain including a fully automatic geometry generation based on an in-house CAD library, automatic meshing and high-fidelity performance evaluations by Computational Fluid Dynamics (CFD) and Computational Structural Mechanics (CSM).

The optimization strategy is based on a two level approach. The first level comprises the DE optimization using exclusively the metamodel as a performance evaluator. During this stage, the metamodel simulates the output that would be obtained via the high-fidelity evaluation tools, but at negligible computational cost. This enables the evaluation of thousands of designs within a fraction of a second, therefore considerably reducing the computational cost that is associated with the usage of the evolutionary algorithm. DE, like other evolutionary algorithms, requires a large number of function evaluations to converge towards solutions of the optimization problem. An ordinary Kriging metamodel is used in this work.

The second level of the optimizer acts as a feedback loop to assess and improve the accuracy of the metamodel prediction. The idea is that the metamodel does not need to be equally accurate in the entire design space, but high accuracy is required in some critical regions, e.g. in the vicinity of optima and at boundaries of the feasible design space. To this end, the designs that perform best according to the metamodel prediction are passed on to the high-fidelity evaluation chain in order to be re-analyzed by CFD and CSM. The difference between the results of the high-fidelity evaluations and the metamodel predictions give a direct measure on the metamodel accuracy. The additional data obtained from the high-fidelity evaluations are subsequently added to the database which also acts as a knowledge base for the metamodel. A new iteration is then started with new metamodels being generated based on the now extended database.

An initial sampling of the design space for the generation of the first metamodels is performed by a fractional factorial Design of Experiments (DOE) consisting of 128 samples, each being analyzed by the high-fidelity evaluation chain. Further implementation details of the optimization system can be found in ²⁻⁴.

III. Fan Blade Parametrization

The shape of the fan blade is defined by parametric Bézier and B-Spline curves which specify the blade chord, blade angles, the thickness distributions at hub and tip sections and the profile stacking axis by lean and sweep, see Figs. 2 and 3.

The blade metal angles at the leading edge, trailing edge and an intermediate point as well as the chord length are defined by spanwise B-Spline curves, as shown in Fig. 2. Control points for these distributions are defined on four spanwise positions which are being fixed for three of the points at 0, 50 and 100% span. The spanwise position of the fourth control point is added as an optimization parameter in order to allow additional control of the blade geometry close to the bypass splitter. Some of the control points are directly defined as optimization

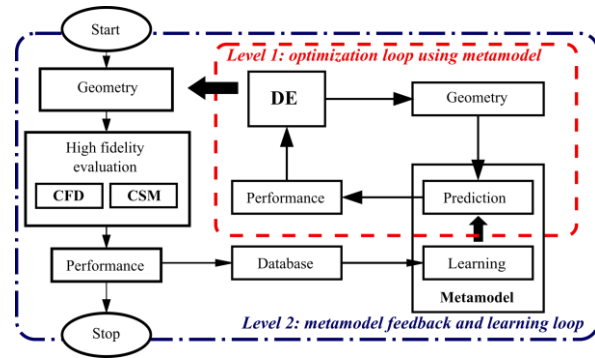


Figure 1: Flow chart of the optimization system

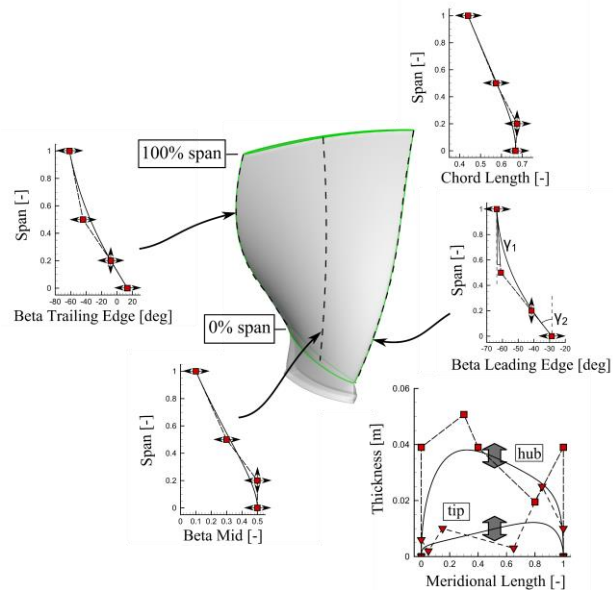


Figure 2: Parametrization of blade angles, chord length and thickness

parameters and are indicated with arrows, while others are defined via geometric dependencies to other control points (e.g. angles and distances).

The blade thicknesses at hub and tip sections are defined by B-Spline curves as shown in Fig. 2 and are designed based on Wennerstrom⁵. Both distributions can be scaled independently by a uniform scaling factor, therefore allowing thickness changes without altering the actual distributions.

In addition, the number of blades is allowed to be modified resulting in a total of 26 optimization parameters.

IV. Aerodynamic performance evaluations

The aerodynamic performance of the fan blade is computed using the commercially available 3D Reynolds-Averaged Navier-Stokes solver FINETM/Turbo. The fluid domain is discretized using a multi-block structured mesh consisting of about 2 million grid points and an average $y^+ = 3$. Turbulence is modelled with the one-equation model of Spalart and Allmaras.

To meet the aerodynamic design and off-design targets originating from the engine cycle design, the fan blade's performance is evaluated at two key flight conditions, namely top-of-climb (ToC) and cruise.

In total nine operating points are computed for each design, including four points on the ToC speedline and five points on the cruise speedline. An automatic convergence check is performed after each CFD computation to assess the mass flow error between domain inlet and outlet as well as the iteration errors of efficiency and pressure ratio. Only cases with sufficient convergence are subsequently assessed by an automatic postprocessing step, which extracts the required performance parameters needed by the optimizer. Non-converged cases are considered as failed and are automatically excluded from the optimization process.

The fluid domain of the fan blade including the bypass splitter is shown in Fig. 4. The fluid domain comprises one periodic section of the full annulus with periodic boundary conditions being applied at each side of the domain. Total pressure, total temperature, absolute inlet flow angle and turbulent kinematic viscosity are imposed as boundary conditions at the inlet. The low hub-to-tip radius ratio of the blade results in a transonic flow at all considered operating conditions with the relative inlet flow to the blade being subsonic for the lower part of the blade extending to about 50 percent span and supersonic for the remaining part of the blade up to the blade tip.

The flow at the subsonic root section (the portion of the blade feeding the engine core) is highly sensitive towards outlet pressure differences, requiring the mass flow to be imposed as the core outlet boundary condition in order to obtain a stable flow solution. In contrast, the static pressure is defined as boundary condition for the bypass outlet, with its spanwise variation being computed using the radial equilibrium law. Performance curves are computed by changing the bypass outlet static pressure.

V. Structural performance evaluations

The structural response of the fan blade including static stresses and vibrations is evaluated using the open-source finite element solver CalculiX⁶. An in-house unstructured meshing tool is applied to discretize the solid domain with quadratic tetrahedral elements, as shown in Fig. 5. The fan blade is modeled using material properties of Titanium (Ti-6Al-4V).

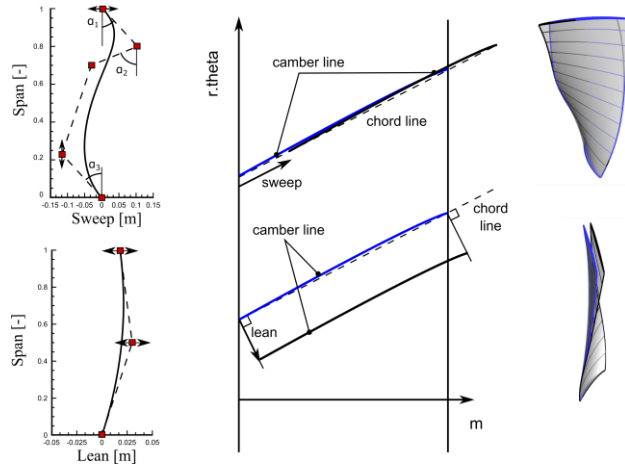


Figure 3: Lean and sweep definition and parametrization

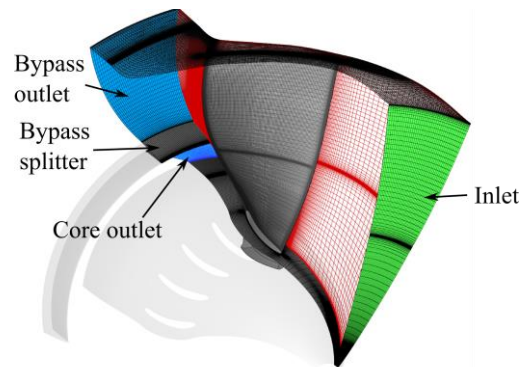


Figure 4: Fluid domain

A. Structural static performance evaluations

A static finite element computation including geometric non-linear effects is performed to evaluate the static stresses in the fan blade. The computation is performed at take-off conditions, where structural loads are at their peak values throughout the mission. The blade is subjected to centrifugal and gas loads whereas the gas loads are extracted from the converged take-off CFD computation of the baseline geometry and interpolated onto the FEM grid using an inverse distance weighting approach.

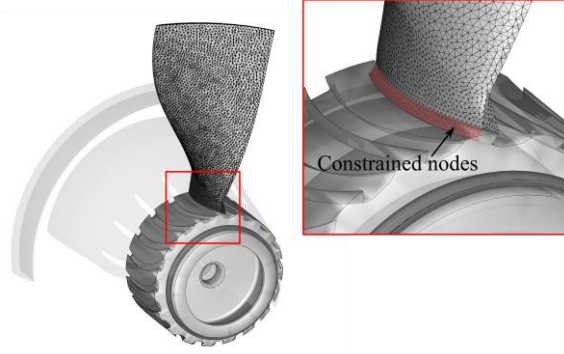


Figure 5: Meshed solid domain and its restraint in a typical disk

B. Vibration evaluations

In addition to the structural static evaluation, fan blade vibration is assessed at all previously mentioned key operating points: take-off, top-of-climb and cruise in order to assess the risk of high cycle fatigue failure. Natural frequencies of the fan blade are determined by means of modal analysis. A geometric non-linear static pre-stressing computation is performed prior to each modal analysis to take into account the non-linear effect of centrifugal forces on the blade stiffness at different rotational speeds. The Campbell diagram is used to compute the margins between excitation frequencies and blade natural frequencies at the rotational speeds associated with the aforementioned operating points. Excitations from one-per-revolution and two-per-revolution disturbances are considered covering possible sources like unbalance and inlet flow distortion due to cross-wind.

VI. Objectives and constraints

The optimization problem is composed of two objectives and a total of twelve aerodynamic and structural constraints. The first objective is the peak efficiency at cruise rotational speed, while the second objective is the stall margin of the fan blade. Both objectives are to be maximized, but are translated to an equivalent minimization problem as

$$obj_1 = -\eta_{cruise,peak} \quad (1)$$

$$obj_2 = -\frac{\dot{m}_{cruise,design} - \dot{m}_{cruise,stall}}{\dot{m}_{cruise,stall}} \quad (2)$$

Where η denotes the total-to-total isentropic peak efficiency of the blade at cruise rotational speed, $\dot{m}_{cruise,design}$ is the cruise design point mass flow and $\dot{m}_{cruise,stall}$ is the mass flow of the last converged CFD computation towards the stall limit of the blade, as shown in Fig. 6.

Four constraints are imposed to ensure that the operating range of the fan matches the engine cycle design requirements at cruise and top-of-climb. A top-of-climb evaluation point with a 6% stall margin with respect to the total pressure ratio is defined as shown in Fig. 6. This is the operating point where the required total pressure ratio is the highest throughout the mission.

Two constraints are therefore defined to ensure that the pressure ratios for core and bypass flows are not lower than the design requirements, which are defined as 1.7 for the bypass and 1.4 for the core flow. Additionally, the maximum absolute inlet Mach numbers and the maximum absolute flow angles at the

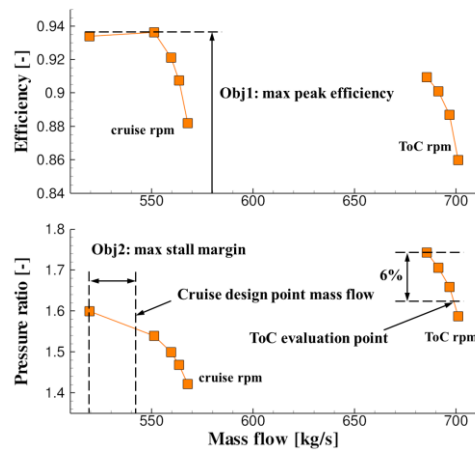


Figure 6: Definition of objectives and the top-of-climb evaluation point

bypass and core inlet are restricted to ensure that the stators located further downstream (outlet guide vane in the bypass and engine section stator in the core) receive a healthy inlet flow and performance improvements of the fan blade are not obtained at the cost of overall stage performance. The limits are set to a maximum Mach number of 0.9 and a maximum flow angle of 70 degrees measured with respect to the meridional plane. Maximum von Mises stresses in the fan blade are required to be lower than 800 MPa, leaving a 130 MPa dynamic stress margin towards the yield stress of the titanium alloy. Blade vibration is assessed at cruise, top-of-climb and take-off. A minimum required frequency margin between the first bending mode of the blade and the first harmonics of a one and two per revolution excitation are defined as constraint.

VII. Results

The optimization was run for 20 iterations, which equals a total of 290 high fidelity performance evaluations. The corresponding objective space is shown in Fig. 7, where each symbol represents one design analyzed by the high fidelity evaluation chain. Improved performance is obtained towards the lower left corner of the objective space, as both objectives need to be minimized. For visualization purposes the plot in Fig. 7 was scaled to show the set of feasible designs which are shaded in gray, therefore not all DOE samples are visible.

The baseline design is shown as orange diamond to provide a reference, although it has to be stressed that it violates multiple constraints and as such is not part of the feasible set of designs. However, the baseline design acted as the starting point for the definition of the design space and is therefore still a valuable sample to consider in order to assess the performance of the optimization system. Due to the high number of aerodynamic and structural constraints only three samples in the DOE database were feasible. Thus the initial challenge for the optimizer was the identification of the feasible region in the design space, which is coupled with the need for the generation of metamodels with sufficient prediction accuracy. About ten iterations were needed until all involved metamodels reached the required level of accuracy, therefore allowing the Differential Evolution algorithm to find feasible designs with improved objective function values. After 20 iterations the optimizer made considerable progress with respect to both objectives. A Pareto front is clearly identifiable in Fig. 7, showing the trade-off between peak efficiency and stall margin. As such, it is the task of the designer to choose a design from the Pareto front that best fulfills the design requirements. Here, a choice was made with a higher importance on the efficiency improvement, at the cost of only a slight improvement of stall margin. The chosen design was generated in the 20th iteration and is labeled as IT020_IND002 in Fig. 7. An efficiency improvement of 0.54 % and a stall margin improvement of 0.99 were obtained with respect to the baseline design.

A more detailed view on the global aerodynamic performances of the baseline design and IT020_IND002 is obtained from Fig. 8, where the performance maps of both designs are shown. The efficiency improvement is readily visible in the plot as well as a marginal and practically negligible stall margin increase. When comparing the efficiency curves, it is important to note that the baseline design did not satisfy the pressure ratio constraints

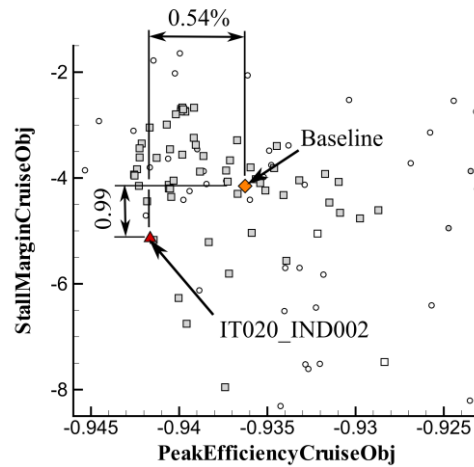


Figure 7: Objective space after 20 iterations. Circles indicate DOE samples while squares indicate designs generated during the optimization. Designs satisfying the constraints are shown with gray filling

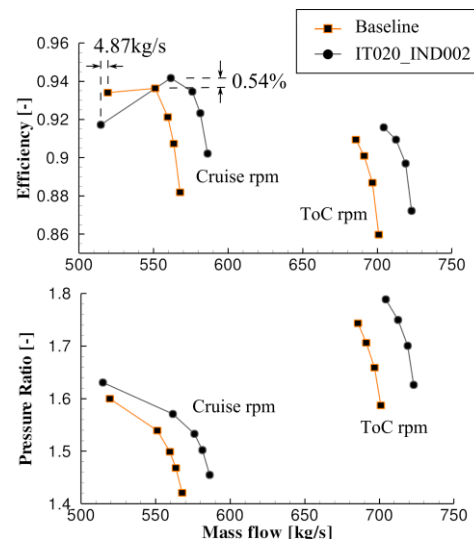


Figure 8: Performance maps of baseline and optimized designs

for the bypass and core flow. An overall increase of the pressure ratio was needed to reach the required pressure levels. As such, IT020_IND002 has both a higher pressure ratio and a higher peak efficiency.

Also in terms of structural performance the baseline design showed constraint violations, which mainly originated from the fact that it was solely designed based on aerodynamic considerations. A comparison of the von Mises stress distributions on the suction side surfaces of the baseline design and IT020_IND002 is shown in Fig. 9. Stresses exceeding the allowed static stresses of the titanium alloy are located at the connection of the airfoil section and the shank surfaces at the leading edge of the blade and on the suction side surface close to the trailing edge at about 80 percent chord. As shown on the right hand side of Fig. 9, the stresses in these regions were successfully reduced. The high stress values on the dovetail root surfaces are originating from the fixed nodes which are set as boundary conditions in the finite element computation. In reality, the dovetail root is in contact with the disk allowing small movements of the surfaces relative to each other. Fixing the nodes therefore artificially increases the stresses in these areas. For that reason, these stresses are not taken into account in the postprocessing step.

The vibration characteristics of the baseline design and IT020_IND002 are shown in the Campbell diagram plotted in Fig. 10. The diagram contains the eigenfrequencies of the first four blade eigenmodes and the excitation frequencies of the first five engine orders plotted versus the rotational speed. Due to centrifugal stiffening, a non-linear increase of the blade's eigenfrequencies with rotational speed is observed. As stated in section VI, a constraint is defined on the minimum required frequency margin between the first and second engine order excitations (1EO and 2EO) and the eigenfrequency of the blade's first bending mode (1F) at the three considered rotational speeds at cruise, top-of-climb and take-off. A dangerously low frequency margin exists between the eigenfrequency of the first bending mode (1F) of the baseline design and the first engine order at take-off rotational speed. To raise this margin above the constraint value the optimizer increased the stiffness of the blade resulting in globally higher eigenfrequencies for the optimized design.

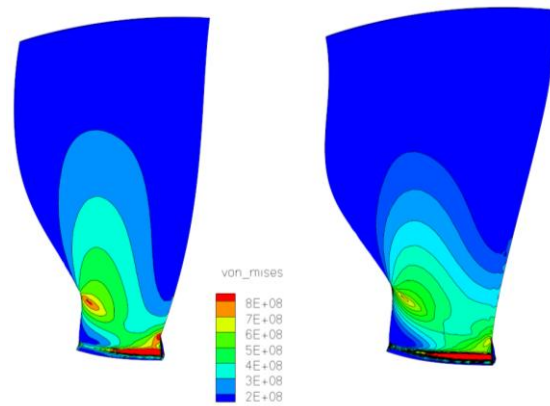


Figure 9: Von Mises stress distribution on the suction side surfaces of the baseline design (left) and the optimized design (right)

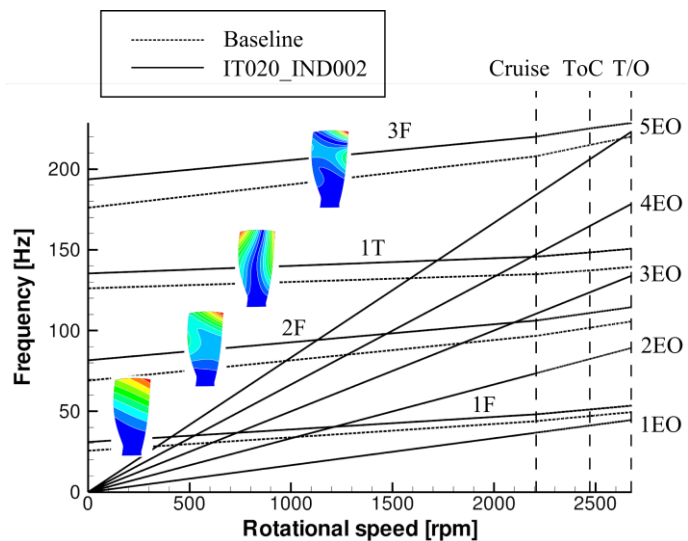


Figure 10: Campbell diagram

VIII. Conclusions

In this paper the application of a multidisciplinary and multiobjective optimization system to the design of a high-bypass ratio aero-engine fan blade is presented. A particular novelty in this work is the consideration of the bypass splitter in the fluid domain, therefore allowing the core and bypass flow requirements from the engine cycle design to be directly included in the optimization process. Aerodynamic and structural performance was considered at multiple key operating points, including cruise, top-of-climb and take-off.

The baseline design in this work was generated solely based on aerodynamic considerations. However, it was not attempted to satisfy all aerodynamic requirements in the manual aerodynamic design step. This task was

purposefully left to the optimization system, which was fulfilled flawlessly. The optimizer successfully identified the feasible region in the design space after 10 iterations (210 high fidelity evaluations) and subsequently improved both objectives until the optimization was stopped after 20 iterations. The final design chosen from the Pareto front has a cruise peak efficiency improvement of 0.54 % while satisfying all imposed structural and aerodynamic constraints.

Acknowledgments

The research leading to these results has received funding from the European Union Seventh Framework Programme (FP7/2007-2013) under grant agreement no [316394] (AMEDEO) and the EPSRC UK.

References

- ¹R. Storn, K. Price, "Differential Evolution - A simple and efficient adaptive scheme for global optimization over continuous Spaces", *Journal of Global Optimization* Vol. 11, No. 4, 1997, pp. 341–359.
- ²T. Verstraete, "CADO : a Computer Aided Design and Optimization Tool for Turbomachinery Applications", 2nd *International Conference on Engineering Optimization*, Lisbon, Portugal, 2010.
- ³T. Verstraete, "Introduction to Optimization and Multidisciplinary Design", *Introduction to Optimization and Multidisciplinary Design in Aeronautics and Turbomachinery*, VKI LS 2010-07, Von Karman Institute for Fluid Dynamics, Rhode-Saint-Genese, Belgium, 2010.
- ⁴T. Verstraete, "Multidisciplinary Optimization of Turbomachinery Components using Differential Evolution", *Introduction to Optimization and Multidisciplinary Design in Aeronautics and Turbomachinery*, VKI LS 2010-07, Von Karman Institute for Fluid Dynamics, Rhode-Saint-Genese, Belgium, 2010.
- ⁵Wennerstrom, A., *Design of Highly Loaded Axial Flow Fans and Compressors*, Concepts ETI, 2000, Chap. 5.
- ⁶CalculiX, A Free Software Three-Dimensional Structural Finite Element Program, Ver. 2.5, www.calculix.de

Optimisation for scaling up of plywood sandwich panels with rigid PU foam-cores

Kaspars Kalnins* and Gints Jekabsons†

Riga Technical University, Institute of Materials and Structures, Riga, Azenes st. 16/20, LV1048, Latvia

Edgars Labans‡

Delft University of Technology, Faculty Aerospace Engineering, Delft, Kluyverweg 1, 2629 HS, The Netherlands

Current paper deals with numerical analysis and optimisation with aim of scaling up of the mechanical and thermal behavior of rib-stiffened sandwich panels with plywood and PU foam core constituents. The effect of the skin and rib thicknesses and core density on mechanical and thermal properties has been analysed. Sandwich panel stiffness and of effective thermal conductivity were acquired by means of numerical models in ANSYS software. Parametrical optimisation of the cross section dimensions and material properties was performed to found the best trade-off between stiffness, structural weight and thermal properties. Comparing optimised sandwich structures with tradition plywood boards it is possible to found equivalent stiffness sandwich panels with weight reduction up to 35 % and effective thermal conductivity of 0.029 W/m*k (reference to 0.12 for solid plywood board).

I. Introduction

Wood based structural materials like timber beams, plywood and oriented strand board (OSB) are widely used in construction of housing and industrial building. Common practice of building large span load bearing floors and roofs currently heavy relies on assembly procedures inside construction site. In order to improve assembly time, quality and cost efficiency pre-fabricated wood based sandwich panels could be used instead. Thus several engineering challenges should be faced in designing of market oriented wood based sandwich panel.

Considering that there is several design variables for sandwich panel cross-section, the optimization allows to track the most efficient combinations of these variables. In addition to optimization of mechanical performance and mass, additional aspects like thermal/sound insulation and material/assembly cost should be addressed.

Advantages of stiffness and weight optimisation for sandwich panels with weak foam cores are described in several research articles^{1,2}. Optimisation of the rib-stiffened panels without any core filler is given in previous research by Labans and Kalnins³ where clear weight saving of more than 60 % comparing with reference plywood boards has been achieved. In additional optimisation results were experimentally validated by making 4-point bending tests on panel prototypes. This research was further extended by adding third optimization objective of thermal conductivity⁴. Novel contribution to design and optimisation of plywood based sandwich panels also has been provided in several recent articles^{5,6}.

In current research optimization of large scale (up to 4m) of wood based sandwich panels with plywood surfaces, stiffeners and natural foam core has been performed to find the most beneficial design regarding structural weight and cost efficiency. Manufacturing constraints, baseline of mechanical and thermal insulation performance also has been included in optimization constraints.

Communicating Author: kaspars.kalnins@sigmanet.lv

*Dr.sc.ing. Leading researcher, Institute of Materials and Structures

† Dr.sc.ing. Researcher, Institute of Materials and Structures.

‡ Dr.sc.ing. Researcher, Delft University of Technology

II. Methods and tools

Mechanical and thermal responses have been acquired by the means of numerical models based on Finite Element Method (FEM). Commercial software ANSYS has been employed for this purposes. Combined shell and solid element types have been combined for stiffness calculations with 4-node SHELL181 elements and 8-node SOLID185 elements. Thermal model of the cross-section numerically represented in 2D model with PLANE55 elements. Area load of 1.5 KPa applied on the sandwich surface corresponds to typical snow load magnitude in Latvia. Length of the panel has been fixed to 4 m – longest available plywood sheet size at local manufacturer. Restrictions on deflection and thermal conductivity values taken according Euro Code 5 for timber structures. The cross section of a corrugate panel has been characterised with five design variables as displayed in Figure 1.

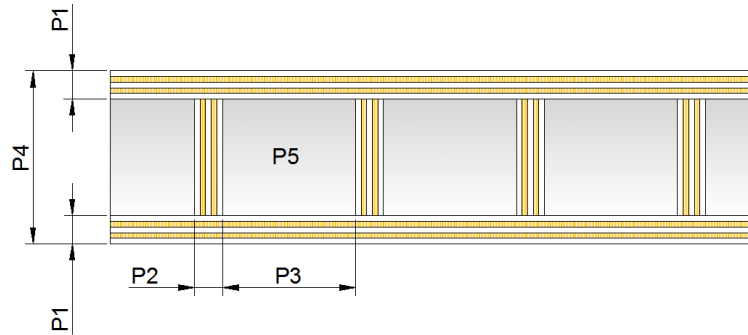


Figure 1. Design parameters

Separate parameter assigned for core density P5, which has linear relation with foam mechanical properties. Boundaries and units for each parameters are given in Table 1. Most of the variables except number of layers in plywood P1 and P2 are continuum variables. Range of mechanical properties for natural PU foams is based on the work of Kirpluks et al⁹.

Table 1. Design variables

Parameter	Lower bound	Upper bound	Step	Units
Number of surface plies - P1	5	9	2	-
Number of stiffener plies – P2	5	9	2	-
Stiffeners distance– P3	50	300	-	mm
Total section height – P4	80	200	-	mm
Foam E-modulus - P5	75	300	-	MPa

In present research a sequential space filling design based on Latin Hypercube with Means Square error criterion has been employed. Acquired responses have been approximated with ABFC method⁷ in VariReg software⁸. Two types of optimization have been considered Pareto optimality front – to evaluate relations between outputs and constrained design in order to find the most cost or weight efficient panel

III. Pareto optimality output

In present study Pareto optimality plots are considered as the most convenient ways to underline relationships and trends in design of rib-stiffened sandwich panel. As the cost, mass and deflection of the sandwich panels should be minimized it is very easy to find optimal spot in all graphs. Colour code allows to add fourth dimension of information, enhancing the output quality.

In Figure 1 it can be seen that the most optimal cross-section thickness lies in the region between 160 – 240 mm. Panels with lower thickness panels have increased deflection resulting in low stiffness, but extra thick cross-section lead to increased price of the structure.

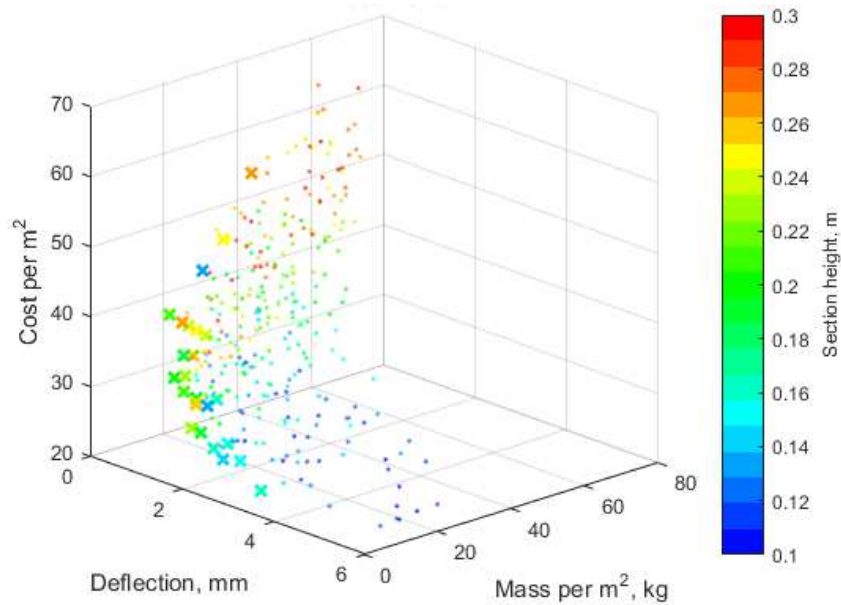


Figure 2. Pareto optimality front between deflection, mass and cost – influence of the section height

There is clearly visible trend in Figure 3 which shows that lowest foam's modulus of elasticity and therefore density is desirable. Apparently increase of the core performance by improving foam stiffness doesn't have a beneficial effect on none of the three response values.

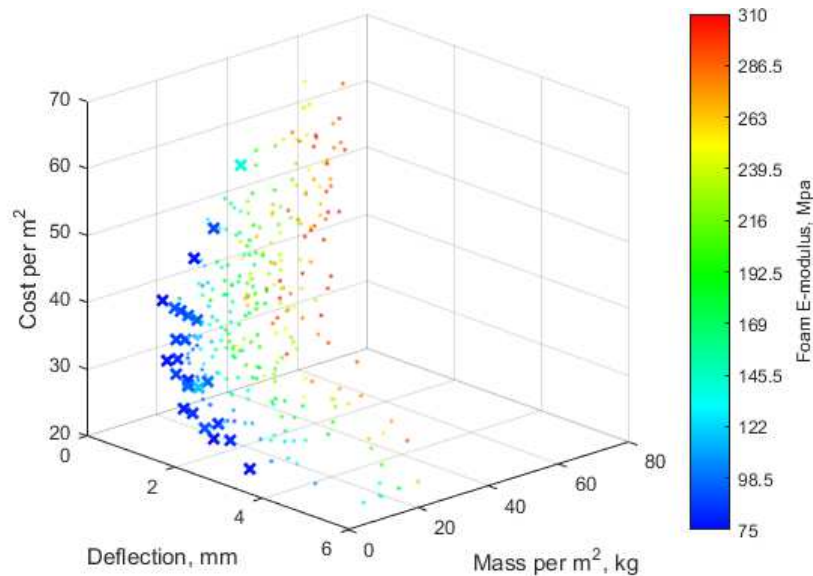


Figure 3. Pareto optimality front between deflection, mass and cost – influence of the foam modulus of elasticity

Number of stiffener layers in Figure 4 demonstrate that combination of variables with thicker vertical stiffeners and larger distance between them are more beneficial than dense array of stiffeners. However at large stiffener distances additional effect of shear stresses should be considered in the analysis

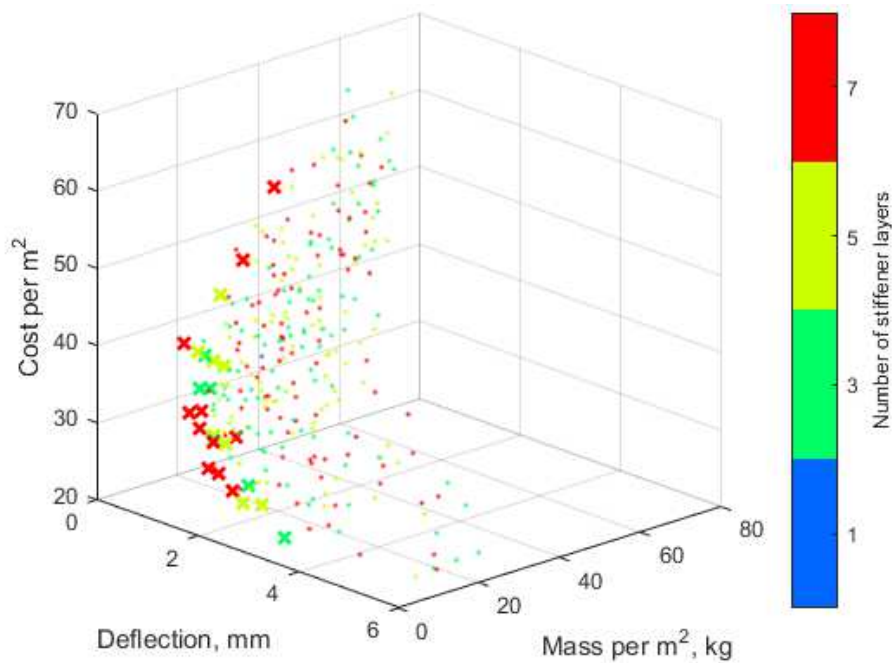


Figure 4. Pareto optimality front between deflection, mass and cost – influence of the number of stiffener layers

IV. Case study of roof panel parametrical optimisation

As the result of parametric optimization several feasible designs of wood based sandwich panels with 4 m span length has been elaborated. All designs pass deflection limitation of $1/300$ of the span length and thermal insulation requirements where overall heat transfer coefficient $< 0.23 \text{ W} / \text{m}^2\text{K}$.

Most effective lightweight sandwich panel could be made applying birch plywood with 4.1 mm thickness for skins and stiffeners. Overall thickness of the panel is 190 mm and distance between stiffeners – set to boundary value of 250 mm. In all cases lowest core foam stiffness and density is required. Although this design is the most cost and weight efficient, due to thin surfaces and stiffeners it could be not the most optimal for manufacturing and other non-structural reasons. In addition Design 2 and Design 3 were created applying one step higher face and rib thickness. Design shows that increased plywood thickness has only minor influence on price and self-weight. Weight difference between smallest and largest plywood thickness is about 12% and price difference even smaller – 8 %.

Table 2. Optimal design of the sandwich panels with plywood surfaces, stiffeners and PU foam core

	P1	P2	P3	P4	P5	Self weight per 1 m ² , kg	Price of materials per 1 m ² , EUR	U-value, (heat transfer coefficient) $\text{W}/(\text{m}^2 \text{K})$
Design 1	3	3	250	190	75	8.9	19.6	0.11
Design 2	5	5	250	160	75	9.6	20.7	0.12
Design 3	7	5	250	140	75	10.3	21.2	0.16

Cost saving for this type of sandwich panels could be reached mainly by substituting skin and/or stiffener material by cheaper alternative like OSB or high density fiber board(HDF) sheets. Although additional analysis should be applied to measure increment of manufacturing costs by number of material types applied. Possible design cases of the sandwich panel where plywood in core stiffeners are replaced by wood boards are given in Table 3. In this case variable P2 (Number of stiffener layers) is replaced by core stiffener thickness. Optimisation shows that such a modification reduce material price up to 5 % comparing to plywood core wall.

Table 3. Optimal design of the sandwich panels with plywood surfaces, wood stiffeners and PU foam core

	P1	P2 [mm]	P3	P4	P5	Self weight per 1 m ² , kg	Price of materials per 1 m ² , EUR	U-value, (heat transfer coefficient) W/(m ² K)
Design 4	5	8	250	165	75	11.8	18.8	0.17
Design 5	7	14	250	160	75	12.3	18.9	0.21

V. Conclusions

In current study large-scale plywood sandwich panels with natural PU foam core were studied numerically and parametric optimisation routines has been performed to study optimality trends and evaluate several possible designs for manufacturing scale-up of the panels. General trends were analysed applying Pareto optimality fronts. It has been found that most beneficial combinations of variables contains a foam core with minimal possible stiffness/density. Although foam filler do not provide outstanding stiffness/strength ratio, it greatly improves sandwich panel performance in transverse direction

Optimisation results of large scale sandwich panels demonstrate several possible design cases where lowest mass solution was possible applying plywood material, however lowest cost is reached by integrating timber board components in vertical core stiffeners. To maintain sufficient heat insulation level it is not possible to design sandwich panels with less than 160 mm cross-section thickness.

Acknowledgements

The research has received funding from Latvia state research program under grant agreement "Innovative and multifunctional composite materials for sustainable buildings (IMATEH)". Research was also partially supported by Forest Sector Competence Centre and Investment and Development Agency of Latvia according to the agreement.

References

- ¹Kawasaki, T., Zhang, M., Wang, Q., Komatsu, K. & Kawai, S., "Elastic moduli and stiffness optimization in four-point bending of wood-based sandwich panel for use as structural insulated walls and floors", *Journal of Wood Science*, vol. 52, no. 4, 2006, pp. 302-310.
- ²Fernandez-Cabo J.L., Majano-Majano A., San-Salvador Ageo L., Ávila-Nieto M. Development of a novel façade sandwich panel with low-density wood fibres core and wood-based panels as faces// *European Journal of Wood and Wood Products*, vol. 69, no. 3, 2011, pp. 459-470.
- ³Labans, E., Kalniņš, K. Experimental Validation of the Stiffness Optimisation for Plywood Sandwich Panels with Rib-Stiffened Core. *Wood Research*, 2014, Vol.59, Iss.4, pp.793-802.
- ⁴Labans, E., Kalniņš, K., Zudrags, K., Rudzīte, S., Kirpluks, M., Cabulis, U. Evaluation of plywood sandwich panels with rigid PU foam-cores and various configurations of stiffeners. In: *Proceedings of the 3rd International conference on Optimization and Analysis of Structures*, Estonia, Tartu, 23-25 August, 2015, pp.45-51.
- ⁵Sliseris, J., Frolovs, G., Rocens, K. & Goremikins, V."Optimal design of GFRP-plywood variable stiffness plate", *Procedia Engineering*, 2013 ,pp. 1060.
- ⁶Banerjee, S., Bhattacharyya, D., 2011: Optimal design of sandwich panels made of wood veneer hollow cores. *Composites Sci. Technol.* 71(4): 425-432
- ⁷Jekabsons G. Adaptive Basis Function Construction: an approach for adaptive building of sparse polynomial regression models. *Machine Learning*, Yagang Zhang (ed.), In-Tech, ISBN: 978-9533070339, pp. 127-156, 2010
- ⁸Jekabsons, G., and Lavendels, J., "Polynomial regression modelling using adaptive construction of basis functions," *IADIS International Conference, Applied Computing*, Algarve, Portugal, p. 8, 2008
- ⁹Kirpluks M, Cabulis U, Zeltins V, Stiebra L, Avots A. Rigid polyurethane foam thermal insulation protected with mineral intumescent mat. *Autex Res J.* 14(4):259-69, 2014

Aeroelastic tailoring for gust load alleviation

Paul Lancelot^{*} and Roeland De Breuker[†]

Faculty of Aerospace Engineering, Delft University of Technology, the Netherlands

This paper presents the results from the equivalent static load method applied to gust response optimisation of an aircraft wing. Through the different optimisation runs, it is assessed that gust load cases can be critical and are difficult to constrain with the sole use of static load cases. Several cases are evaluated with different gust parameters and wing boundary conditions. Effects of control efficiency and engine location are also studied.

I. Introduction

GUST encounter is among the most critical loads for an aircraft¹. The increasing aspect ratio of modern commercial aircraft wings and the weight reduction effort, generally result into increased wing sensitivity to dynamic loads. Loads mainly come from atmospheric conditions (gust loads) and from the action of the pilot/flight computer to control the aircraft (manoeuvre loads). The idea of load alleviation is not new and such a system has been in operation since the 70s². Lockheed engineers applied this technology on the C5 Galaxy to reduce fatigue load cycles on the wing structure as they had been underestimated during the design phase³. Therefore, load alleviation was used to save weight, because additional airframe reinforcement would have been needed otherwise. About the same time, Lockheed also implemented a similar system on its civil airliner, the L1011 Tristar, and nowadays, such features are common on civil aircraft to improve aircraft handling and passenger comfort². In combination with active load control using ailerons and spoilers, the wing structure can also be tailored in such way that it will relieve itself from the loads. This is achieved by a redistribution of the aerodynamics forces inward, caused by negative local angle of attack toward the wing tip. Backward swept wing genuinely exhibit this behaviour and the use of composite material can improve it furthermore. This was demonstrated in the work done by *Dillinger et al.*⁴. More generally, aeroelastic tailoring with composite materials has been a topic of research for many years now⁵.

In an industrial context, specific requirements are provided in the certification. It covers constraints related to structural strength and stiffness, aeroelastic instability (flutter, divergence) and minimum control effectiveness over the entire flight envelope. All civil aircraft must be able to comply, and yet be as light as possible. The certification provides static load cases and dynamic ones. However the structural sizing process is mostly driven by fixed loads and by aeroelastic instability constraints⁶. Taking dynamic load cases earlier in the design process could be beneficial in term of performance, as the work done by *Kenway et al.*⁷ shows that a wing optimised for fixed loads can failed when subjected to transient gust. However the main issue remains that these loads are generally dependent over the design itself. They are constantly changing during the optimisation, as the design evolve with it. Transient responses can also be computationally demanding and therefore costly to implement into current design optimisation process.

In this paper, the structural optimisation process of a wing that is designed for passive gust load alleviation is presented. To perform this optimisation, a gradient-based approach is preferred as the number of design variables is relatively large (≈ 180). However the computation of required sensitivity over a transient response is not an easy task⁸. The equivalent static loads (ESL) method formalised by *Kang et al.*⁹ is used to bypass this issue and provides optimised results for static and dynamics load cases. In the present work the method is used with little improvement regarding the original idea as described in the next section. Nonetheless, it is worth mentioning that examples of improved ESL method exist in the literature. For instance, load sensitivities can be derived using a first order Taylor expansion at each coupling iteration, in order to approximate the loads at the next steps and hence accelerate the convergence¹⁰. *Bettebghor et al.* proposed a different approach based on surrogate modelling⁸. Both of these works were applied to engine pylon sizing in the event of a “fan blade off”, a highly dynamic load case. ESL was extended to different scenarios, most of them summarized by *Park*¹¹. These include non-linear geometries, multi body dynamics, and crash and topology optimisation for the automotive industry.

Communicating Author: P.M.G.J.Lancelot@tudelft.nl

^{*} PhD Candidate.

[†] Assistant Professor.

The paper will first introduce a brief description of the optimisation mythology and then highlight how the wing structural sizing can be influenced by various parameters. These parameters are the different gust cases, the wing boundary conditions, the location of the engine along the span and the minimum control efficiency value.

II. Optimisation methodology

The optimisation process is built around the equivalent static load method. ESL relies on a weak coupling between the transient simulations and the optimiser. To reach convergence it requires several iterations where loads are updated along the new design. This method has the advantage to be easy to implement regardless of the different tools used in the loop. It can take advantage of already existing gradient based optimisation and aeroelastic analysis code and was already applied to similar aero structural problems where gust loads are introduced in the optimisations^{12,13,14}. The governing equation that needs to be solved for a gust analysis is the following:

$$M(x)\ddot{u}(t) + K(x)u(t) = f_{gust}(v_{\infty}, v_{gust}(t), \ddot{u}(t), \dot{u}(t), u(t)) \quad (1)$$

where u is the nodal displacement vector, M and K respectively the mass and the linear stiffness matrices which are dependent upon the design variables x and f_{gust} the aerodynamic forces due to a gust. Finally, v_{gust} is the vertical speed component of a transient gust and v_{∞} the flow speed in the far field. No structural damping is required as the damping forces are provided by the aerodynamic part. Once the displacements computed from Eq. (1), a set of equivalent static loads f_{eq} can be retrieved from the time steps identified in the elements strain history as the most the critical:

$$f_{eq} = K(x)u(t_i) \quad (2)$$

In the case of a free flying aircraft simulation, the structural displacements are obtained by removing the rigid body translations and rotations from the displacement vector of each grid points.

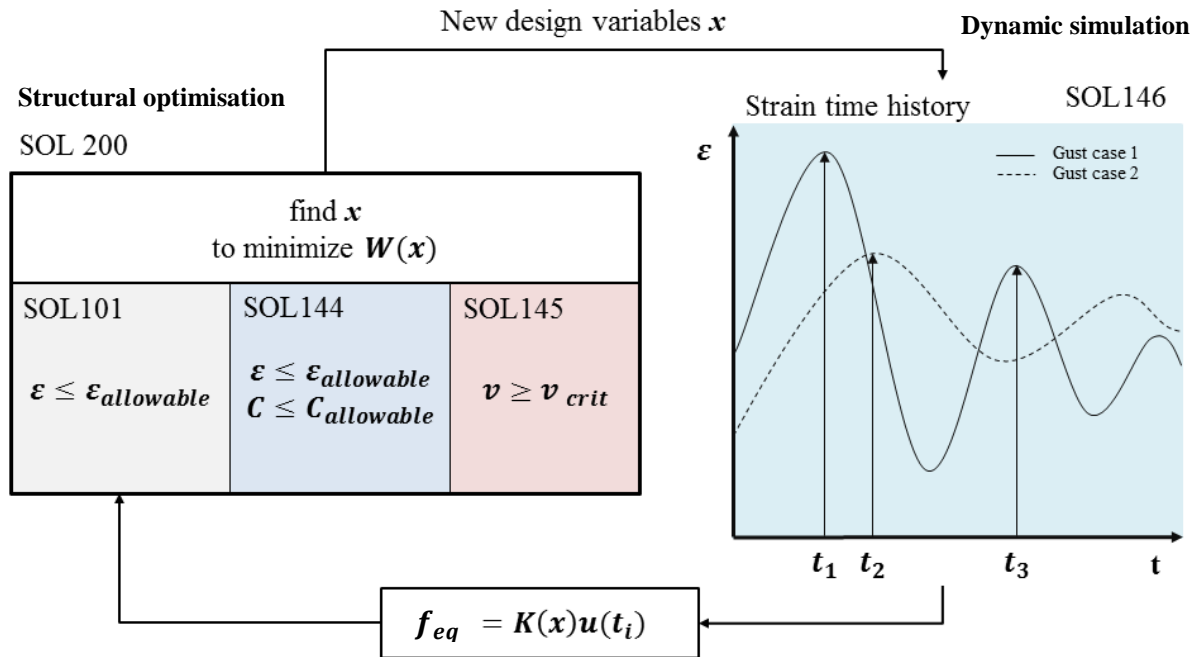


Figure 1: Schematic of the ESL method with the different NASTRAN solutions working together. The overall process is managed by a MATLAB script.

In the following example, described Figure 1, the loads are computed at each iteration with the transient aeroelastic module of NASTRAN, designated as the Solution 146¹⁵. This solution relies on the Doublet Lattice Method (DLM) to solve the gust analysis problem. Although Eq. (1) is given as time dependent, NASTRAN solves everything in the frequency domain before converting the output results (displacement, strains etc.) in the time domain. This method is limited to linear aerodynamic and structural computation only.

Once the set of ESL generated, they are sent to the optimiser module of NASTRAN (SOL200) to be treated as a static structural optimisation problem. SOL200 can also account for steady aeroelastic and flutter constraints, which are computed by the SOL144 and SOL145 NASTRAN modules. For these responses the optimiser can derived sensitivities and efficiently performed gradient based optimisation¹⁶. In this example the constraints are applied on strength ($\epsilon_{allowable}$), minimum static aileron efficiency ($C_{allowable}$) and minimum critical instability speed (v_{crit}). Buckling is not taking into account in the present work, although the authors acknowledge the influence that could have such constraints on the design and plan to implement it in future work.

The design variables used here are the panels' thickness (36 in total) and the laminations parameters. This formulation has been first introduced by *Tsai et al.*¹⁷ and is used as a representation of the [A,B,D] stiffness matrix from the classical lamination theory. As the optimisation is only done for the in-plane response (tension, compression and shear), only 4 laminations parameters per panel are necessary to fully describe any symmetrical stacking sequences. Laminations parameters are denoted V_1, V_2, V_3, V_4 and present the advantage to be continuous compared to discrete ply angles. This continuous formulation greatly helps the optimiser to perform its task but doesn't directly define a proper stacking sequence. This is usually done as a post processing step using a genetic algorithm, but is not achieved in the present work. Nonetheless, the retrieval of a feasible stacking sequence greatly influences the optimised results and will be included in a future work¹⁸.

Using a continuous formulation also requires using appropriate constraints for maximum strain. As the fibres orientations remain unknown, it is impossible to properly predict the actual failure envelope of a stacking sequence solely defines by its stiffness property. *IJsselmuiden et al.*¹⁹ proposed a formulation of the widely used Tsai-Wu failure criteria for the continuous optimisation, by defining the area of the failure envelope common to all the plies angle. This criterion is used for in the present work, but with a safety coefficient of 2, as shown on Figure 2. This is to avoid having an optimised wing too flexible and therefore with a non-linear behaviour. It is interesting to note that carbon fibre laminate has much more strength in compression than in tension, the effect of this can be seen in the optimisation results section 5.

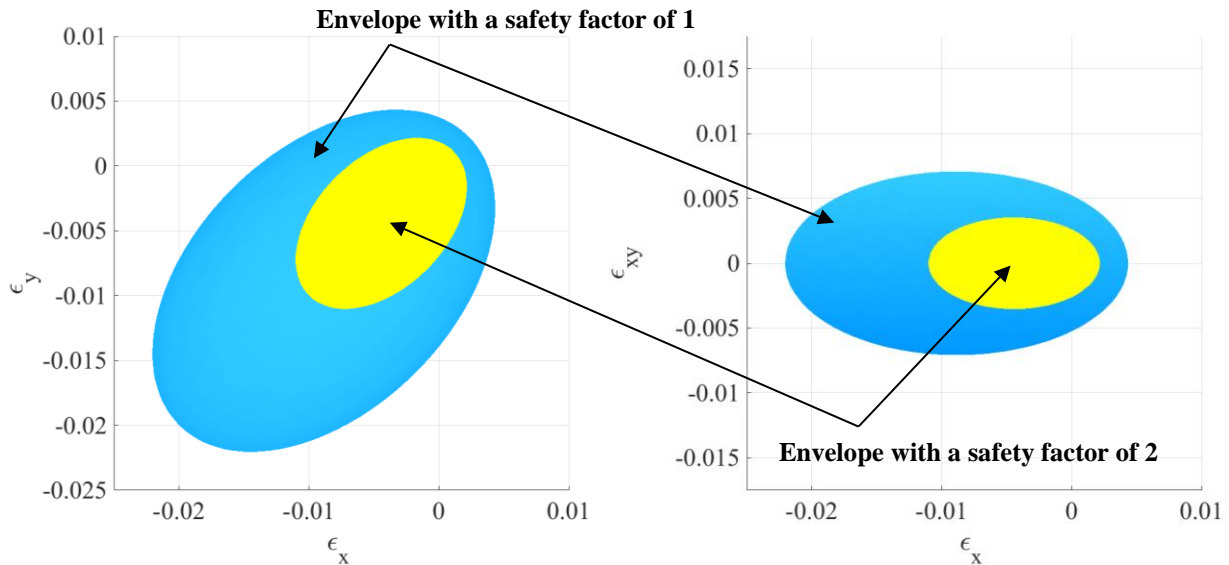


Figure 2: In plane failure envelope for Carbon-Epoxy (IM6). The methodology to compute these is detailed in the work by *IJsselmuiden et al.*¹⁹.

Flutter and static divergence are constrained up to speed of 220 m/s. However due to the wing geometry, these constraints weren't active and thus their influence not discussed in this paper. Control efficiency is also taken into account for some of the optimisation example. Control efficiency reflects how much root bending moment M can be obtained from a specific aileron deflection on a flexible wing. A 100% value represents the moment created by an aileron mounted on a rigid wing. This constrained is only used on static cases.

$$C_{allowable} = \frac{M_{Flex}}{M_{Ref}}$$

III. Model description and load cases

The aircraft model used for this study is a 90 seats regional turboprop, derived from existing model such as the ATR72 or the Bombardier Q400. The choice of such configuration is motivated by the current research done on this aircraft type within Clean Sky 1 & 2²⁰. Furthermore, as DLM method is used to compute the aerodynamic loads, a subsonic aircraft was preferred over a transonic configuration. The task of assigning specific aircraft data can seems arbitrary; however the mass properties need to be taken into account for the dynamic load cases. Therefore coherent model data are necessary to ensure valid results that could be extrapolated to more accurate model.

Wing span	30 m
Fuselage length	30 m
Wing surface	75 m ²
Wing aspect ratio	12
Mean aerodynamic chord	2.5m
Nominal Mach	0.6
Nominal altitude	25000ft
Fuselage + Tail empty weight	5t
Engine weight	1.5t × 2
Wing weight (ribs, LE/TE, flaps etc.)	2.05t × 2
Wing weight (skins and spars)	1t × 2
Total empty weight	14.1t
Maximum take-off weight	30t
Fuel weight	3.075t × 2
Pax and cargo weight	9.75t

Table 1: Weight and dimensions for the full aircraft. Note that the weight from the wing skins and spars can vary during the optimisation.

The FEA model is built of 801 CQUAD4 shell elements, 123 CONM2 concentrated mass and 41 RBE2 rigid body elements. Wing skins and spars are made of the CQUAD4 elements, while the ribs are defined by the RBE2 elements. Therefore the ribs properties are not optimized. This also reduces the number of degrees of freedom of the structure, as grid points on the same rib have the same displacement. Therefore, the size of the stiffness matrix K that needs to be extracted from the model is only 246×246 . The inertia properties of the fuselage are embedded within the concentrated mass card located at the centre of gravity of the aircraft.

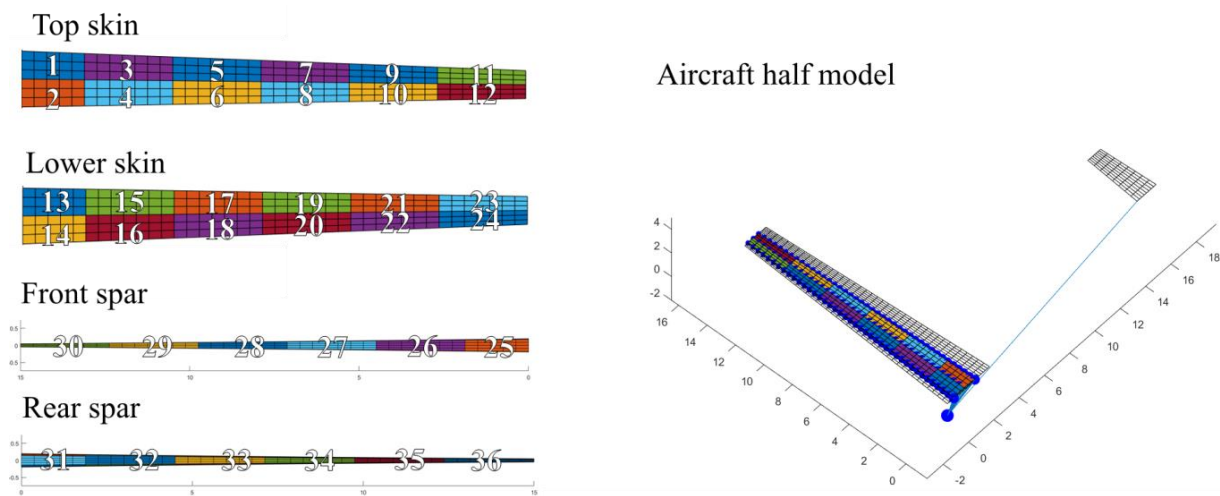


Figure 3: FEA model of the aircraft. The blue spheres represent the distributed concentrated mass. Numbers represent the panel properties IDs.

The Certification Specification 25 for large aircraft issued by EASA specifies “1-cos” gusts an aircraft needs to sustain²¹. The gust loads have to be defined with a half wave-length going from 9 to 110m. The gust amplitude is actually a function of its wave-length and altitude at which the aircraft is flying. Finding the critical gust cases over the entire flight envelope is a tricky matter as it requires to run many simulations, but recent work involves the use of reduced order model to solve that issue²². For the sake of simplicity, four gust cases are selected as the dynamic loads in this paper. The altitude, fuel loading and speed remain constant.

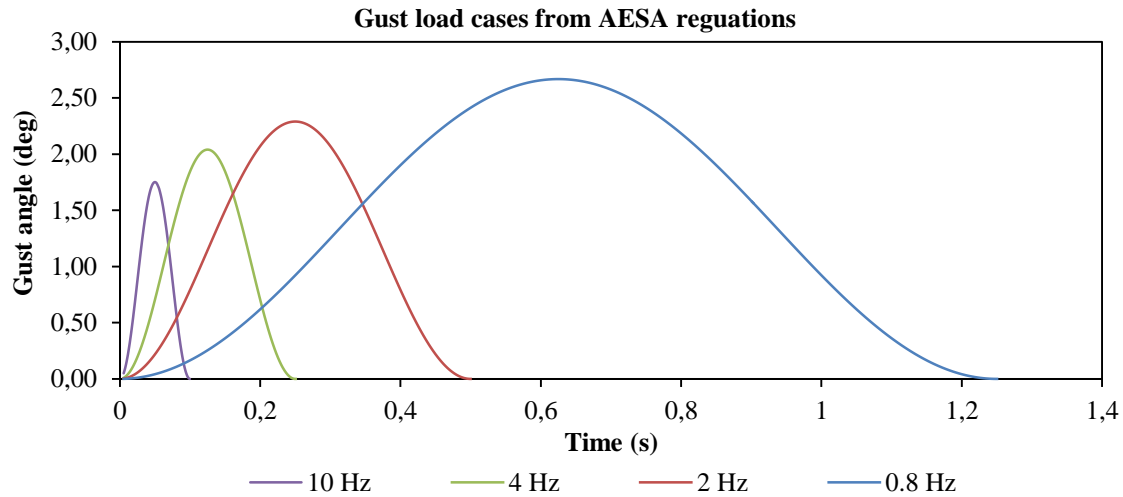


Figure 4: Gusts vary in amplitude and speed.

In addition to the gust load cases, static load cases are also applied. The static 2.5g load case is a well-known requirements used for aircraft structure certification. In the present work, an angle of attack of 4 degrees is sufficient to lift 30t of weight at cruise condition. The trim angle for the 2.5g load case is therefore about 10 degrees. Additional static load cases are used in some optimisation run to evaluate how they influence the tailoring. These static load cases and the associated angle of attacks are fixed during the optimisation. Dynamic load cases have a trim set to 0.

Static load cases

Load case number	True air speed	Frequency	Static load factor (g)	Aileron deflection in rad (deg)	Gust amplitude in rad (deg)
1	185 m/s	/	(0.01, 1.40, 2.50, 3.60, 4.60)	0	/
2	185 m/s	/	0	0.25 (14.3)	/

Transient load cases

3	185 m/s	10 Hz	0	0	0.0306 (1.67)
4	185 m/s	4 Hz	0	0	0.0356 (2.02)
5	185 m/s	2 Hz	0	0	0.04 (2.28)
6	185 m/s	0.8 Hz	0	0	0.0466 (2.66)

Flutter/Divergence load case

7	155 – 225 m/s	/	0	0	/
---	---------------	---	---	---	---

Table 2: Summary of the different load cases.

IV. Results

Several optimisations with different test cases were performed. Most aero structural optimisation is performed on a clamped wing but gust loads can also vary with the flight dynamic properties of the aircraft. As shown by *Reimer et al.*²³, a free flying aircraft will experience lower magnitude gust loads. The influence of the boundary conditions on the gust responses and on the resulting optimisation is assessed. By allowing the aircraft

half model to freely move in pitch and plunge, it was possible to recreate the symmetrical aero elastic behaviour of a full aircraft. It can be seen on Figure 5 that a free wing will be subjected to less root bending moment for a “slow” gust at 0.8Hz. In this configuration however, the peak amplitude on the load is achieved not during the initial gust response, but when the wing is going down again. This illustrates that flight dynamic can have an influence on the loads. While the loads are lower, this can actually change the outcome of the optimisation, as the wing box isn’t stressed the same way. It must be noted that the use of active pitch control could modify the flight behaviour and therefore the loads as well. However no active control is implemented in the present work.

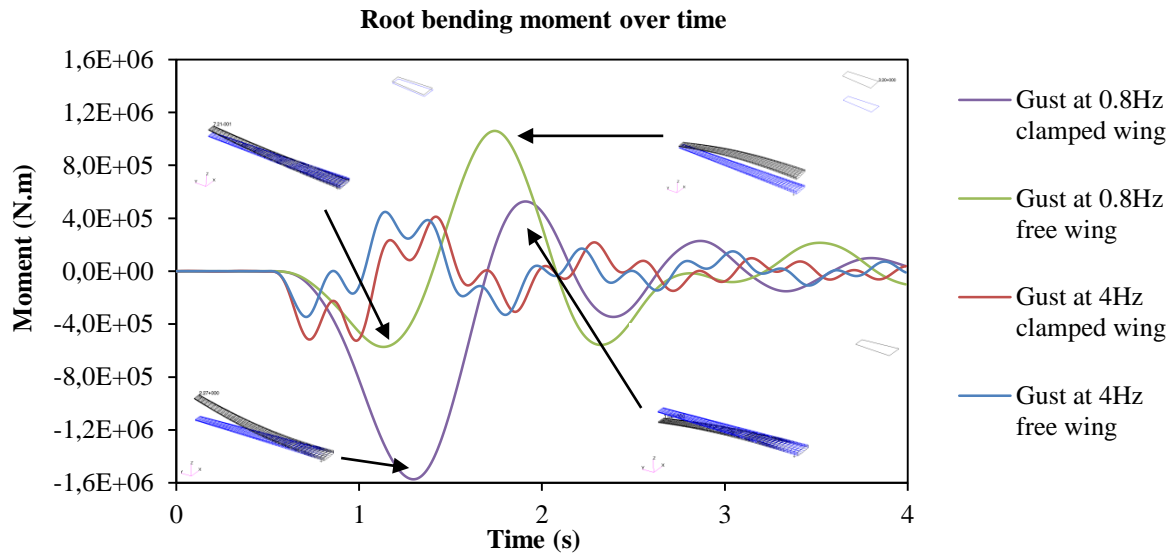


Figure 5: Root bending moment created by a gust encounter, for a clamped wing and a wing mounted on an aircraft with two degrees of freedom (pitch and plunge). All gusts start at 0.5 sec in the simulation.

If the wing is clamped, the maximum loads are going to be in tension in the lower skin and in compression in the top skin. Since buckling isn’t taken into account in the present work, composite panel are much stronger in compression than in tension. This results into lower thickness on the top skin. On the other hand, the free wing has its top skin stressed in tension which results in slightly higher thickness compared to the bottom skin on Figure 6. In term of weight, the optimised clamped wing is 6.7% heavier than the free wing as the plunge motion allows reducing some of the loads.

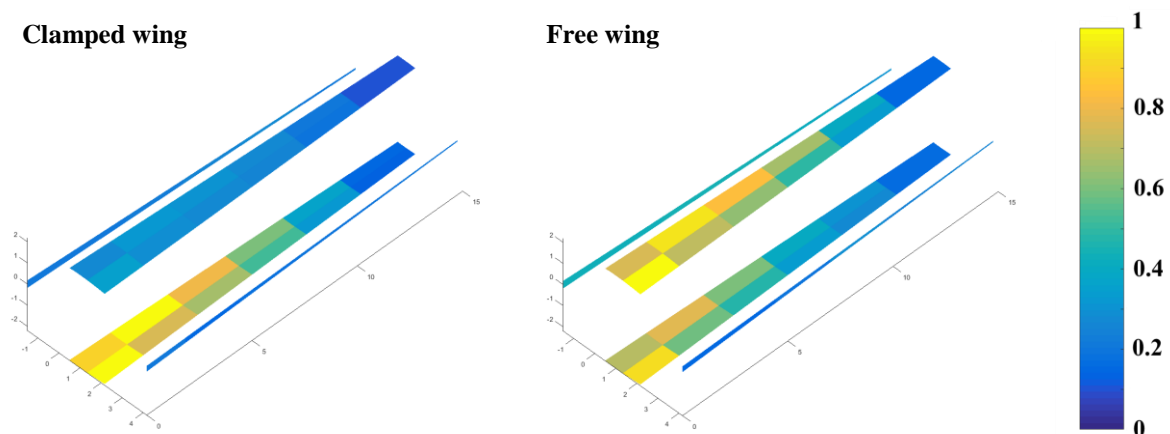


Figure 6: Normalised thickness distribution for two different configurations.

It can be noticed that the loads from “fast” gust are less impacted by the boundary conditions, and generate similar root bending moment. It is worth to mention that slow and fast gust don’t stress the wing at the same location. As shown on Figure 7, fast gusts tend to be more critical toward the wing tip, while slow one have more effect on the root. This is valuable information for whom designing wingtip devices for instance.

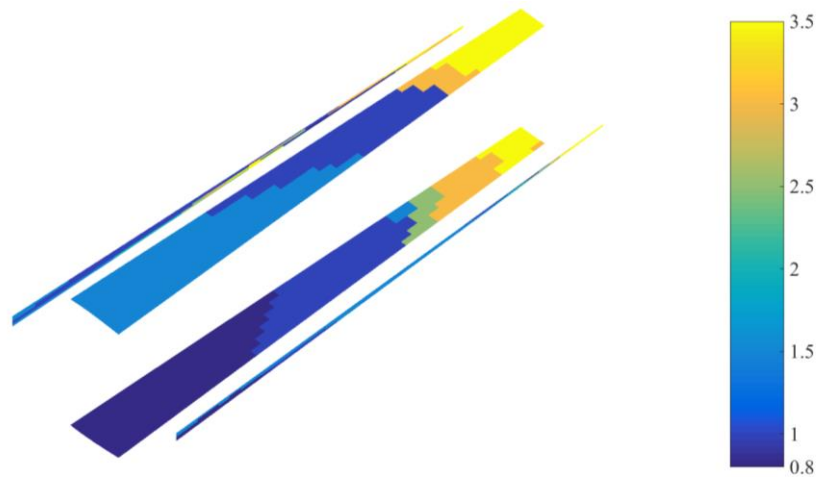


Figure 7: Criticality of different gust frequency (here in Hz) over the wing. This figure is obtained with additional load cases to better illustrate the dependency with the frequency.

Gust loads can be considered as flexible. Flexible loads are dependent over the design itself and can change during the optimisation as the design evolves. It also means that for the same gust and flight conditions, a stiff wing will more likely experience different loads compare to a flexible one. This is illustrated by running different optimisation problem, having the same gust cases, but with different static load conditions. Results on Figure 8 show the different constraints values for the different optimised design:

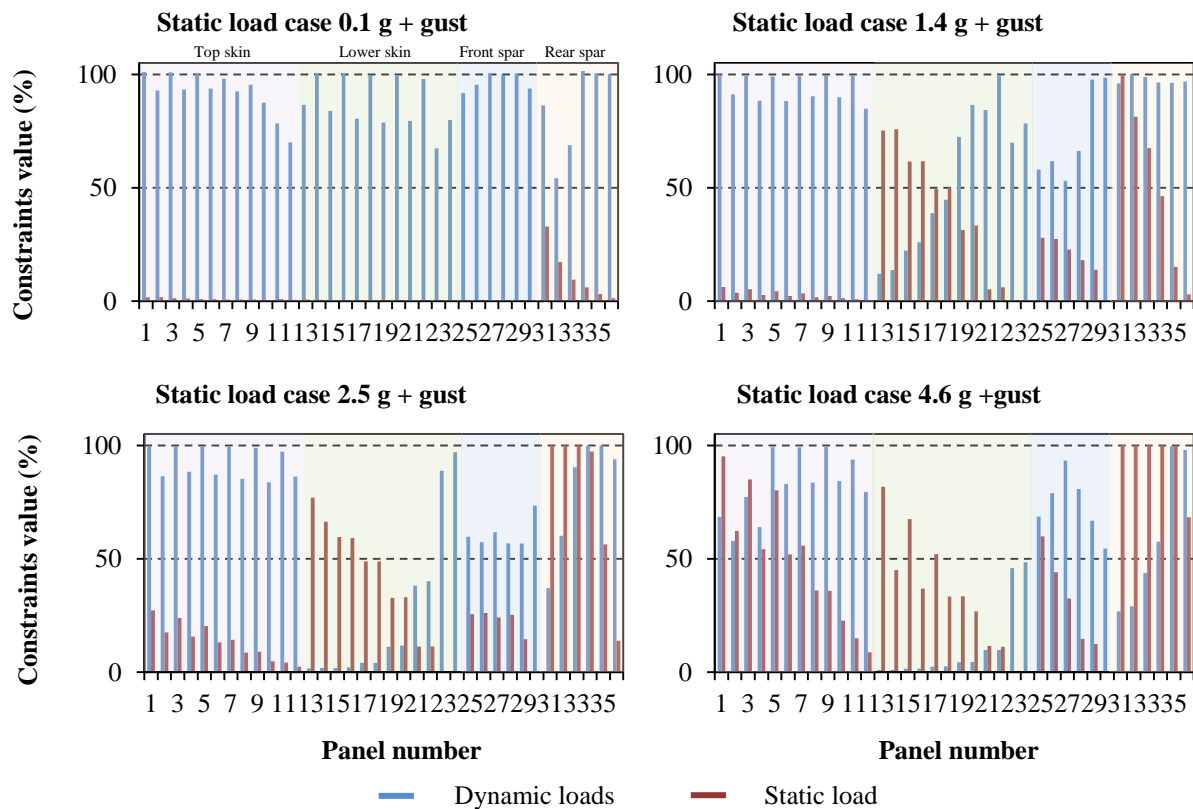


Figure 8: Constraint values for strength after optimisation.

Even with high static load some of the panels are more likely to be critical with respect of the dynamic loads. In this numerical experiment, the wing is free in pitch and plunge, therefore the top skin will be more critical to gust loads. On the other hand, the boundary conditions doesn't have any impact on the static load case, therefore the lower skin is more likely to be sized by these loads. We can also see that it is more difficult to reach an optimised design which is fully stressed, as the optimiser has to deal with a broader spectrum of load cases. Indeed, a high static load case will lead to a very stiff wing, therefore more sensitive to fast gust cases toward the

tip. When static load cases are removed, and the wing purely optimised for dynamic load cases, the wing tends to have lower natural frequency because less stiff. The wing is therefore sized for lower gust frequency, but with higher amplitude. When comparing the outcome of the different runs, it is clear that a high static load case induced a final higher optimised weight. On Figure 9 we can see that fast gust load root bending moment slightly increase with weight, while the root bending moment from gust at 0.8 Hz is decreasing. This can be seen as the influence on the tailoring from static load case.

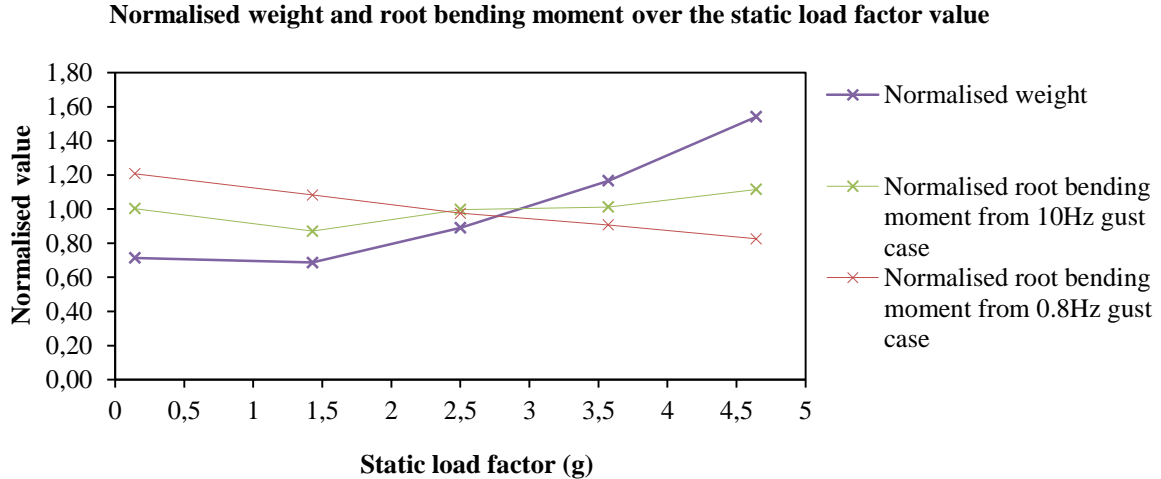


Figure 9: Summary of the weight and root bending moment of the different optimisation run.

As enunciated in chapter 2, the optimiser doesn't have the sensitivities, linking gust loads and design variables. However, for static aero elastic loads, NASTRAN is able to derive the appropriate sensitivities for such problem. Therefore, the optimiser will be able to aero elastically tailor the wing by inducing a negative twist distribution toward the tip in order to shift the lift inward, and therefore reduce root bending moment. This is achieved by moving the elastic centre toward the leading edge, usually by increasing the front spar thickness. If composite materials are used, the orientation of the fibres can also be used for that purpose. On Figure 10 we can see that once optimised for different static load cases and the gust loads, the optimised wing have a different behaviour under 2.5g. The one optimised for very high static loads will exhibit a negative twist distribution outward. On the other hands, the one optimised with only gust loads has the opposite behaviour. It can also be seen on both Figure 9 and Figure 10 that applying a small static load case is 1.4g has an effect on the optimised results.

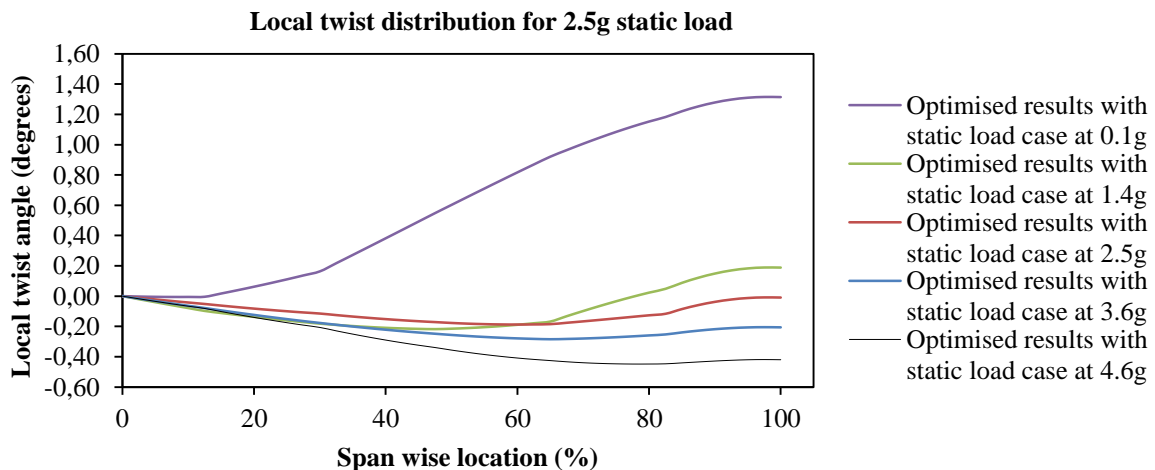


Figure 10: Local twist distribution for the different optimised results.

It is known that in order to reduce the root bending moment, engine and fuel can be shift outward to balance the lift. This is common practice in the aircraft industry and fuel system are design to accommodate such purpose, on the ground, and in flight ²⁴. Even if the engine location results in the trade-off between many parameters (such as the requirement to be able to take off with a single engine), the ability to optimise for

dynamic loads revealed an interesting trade-off. A single point mass that accounts for the engine, its nacelle and the propeller is moved along the span, roughly 1m ahead the front spar position. The wing is clamped to remove any effect from the flight dynamic. Both gust and static (2.5g) cases are used to run the optimisation. The results on Figure 11 shows that having the engine under the wing is beneficial in term of weight when located up to 40% of the span, with a reduction of the static root bending moment. Regarding the dynamic cases, having this extra mass hanging under the significantly change its dynamic behaviour. The engine mid-wing also reduces the root bending moment in the case of gust at 0.8Hz while slightly increase it for a fast gust. For clarity gust loads at 2Hz and 4Hz are not displayed on the charts but exhibit similar behaviour. The overall weight penalty after moving the engine passed 50% of the span is a good indication on where the engine should and shouldn't be.

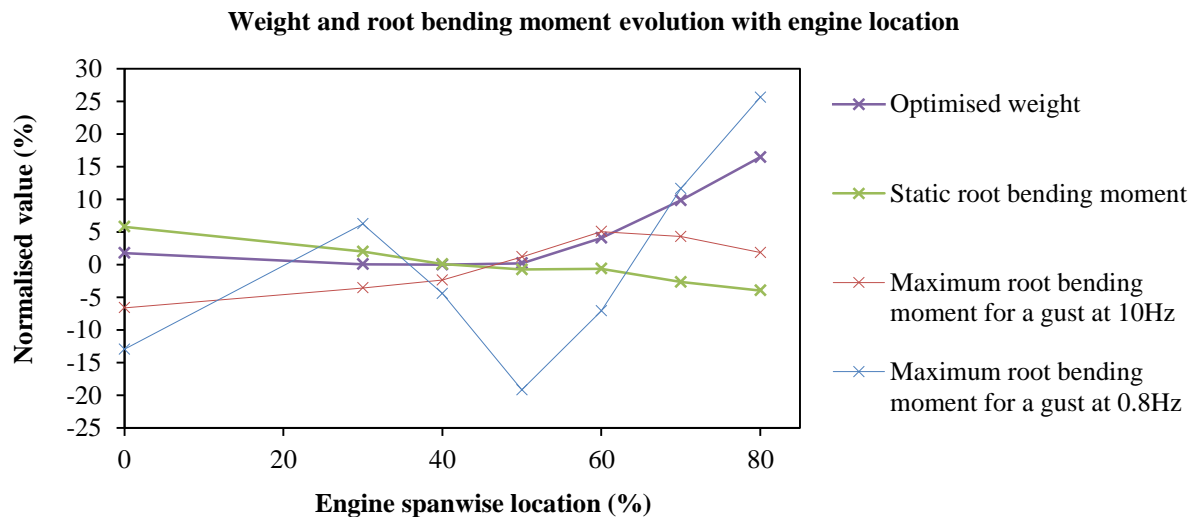


Figure 11: Summary of the weight and root bending moment of the different optimisation run.

Some optimisation cases were run with control efficiency as a constraint as well:

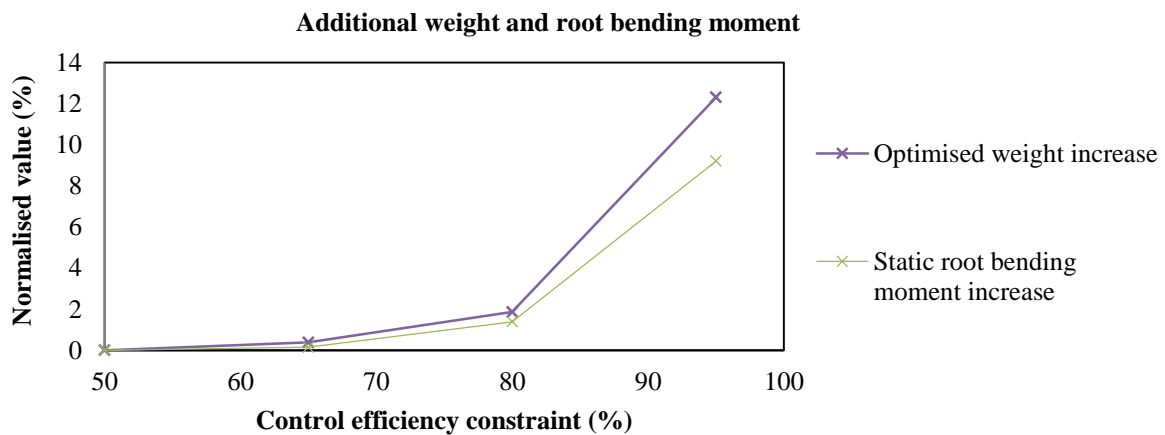


Figure 12: Summary of the weight and root bending moment of the different optimisation run.

On Figure 12 it is noticeable that trying to get close 100% aileron efficiency will require a stiffer wing (as shown on Figure 13), inducing more weight and lesser aero-elastic tailoring. As the present work only cover the control efficiency as a static load case, it already highlights the dilemma of having a very flexible wing, ideal to reduce gust loads passively, but with poor control effectiveness, requiring larger control surfaces, or the opposite.

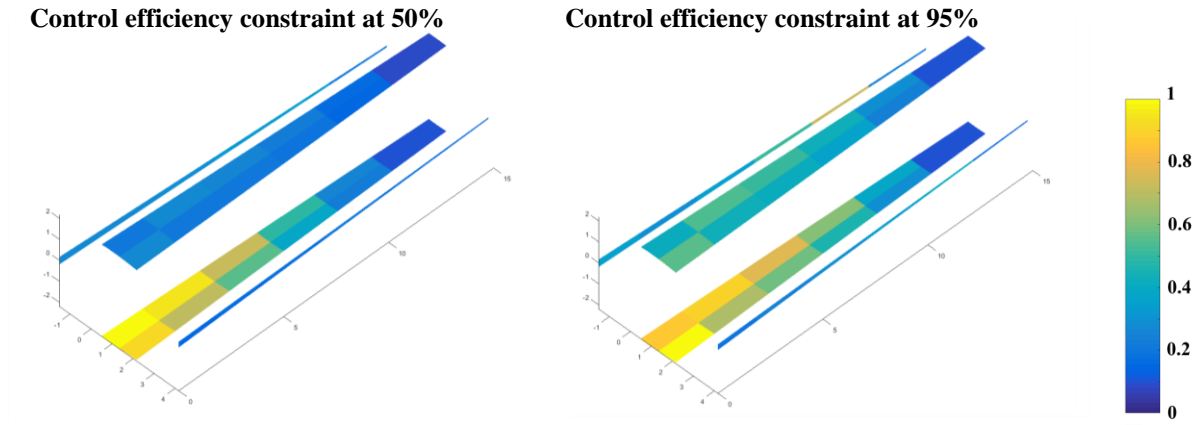


Figure 13: Normalised thickness distribution for two different configurations.

Regarding composite optimisation there are significant differences with the tailored results obtained by *Werter and De Breuker*²⁵ for instance, as these were obtained with static load cases only. Most of the tailoring appears to be done through thickness variations. In term of stiffness optimisation, as shown on Figure 14, the optimiser preferred to go for quasi-unidirectional laminates on the top and lower skin. This type of lay-up can in theory take very high loads in tension and compression. These results don't really vary as respect of different load cases or boundary conditions. On the spars we can see some variations in the stiffness. The laminates on the rear spars are most likely to have a stacking sequence close to $[\pm 45^\circ]_s$, very stiff in shear loading condition. The results would probably be different if panel buckling and manufacturing constraints were taken into account¹⁸.

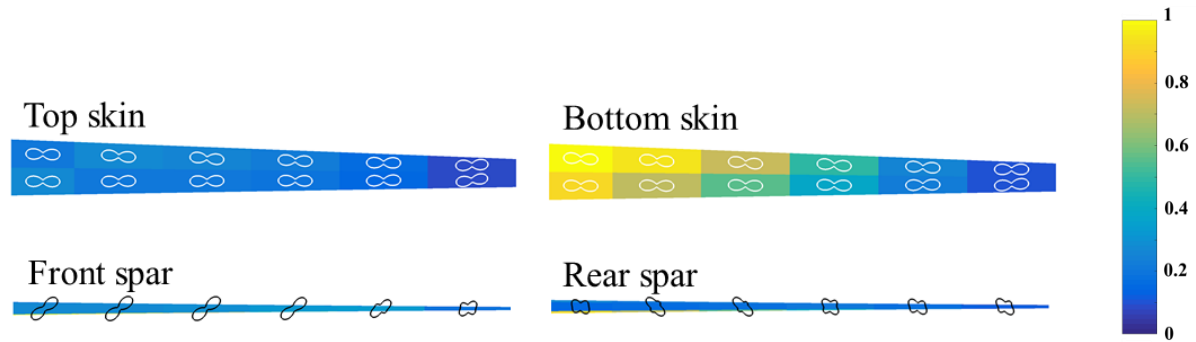


Figure 14: Stiffness distribution for two different configurations (the black and white shapes). The colour scale indicates the normalised thickness distribution.

The ESL method relies on a weakly coupled iterative scheme, convergence of the solution is therefore a major concern. The convergence rate and regularity of the optimisation results are related to many parameters. Among them, loads sensitivity to design changes between two iterations is critical. As shown on Figure 15, the use of an under relaxation factor can be a solution to help the convergence. In this scenario, the design variables x_i at the iteration n are multiply by 0.25 and added to 0.75 of the design variables at $n-1$.

Convergence history of the objective and constraints values

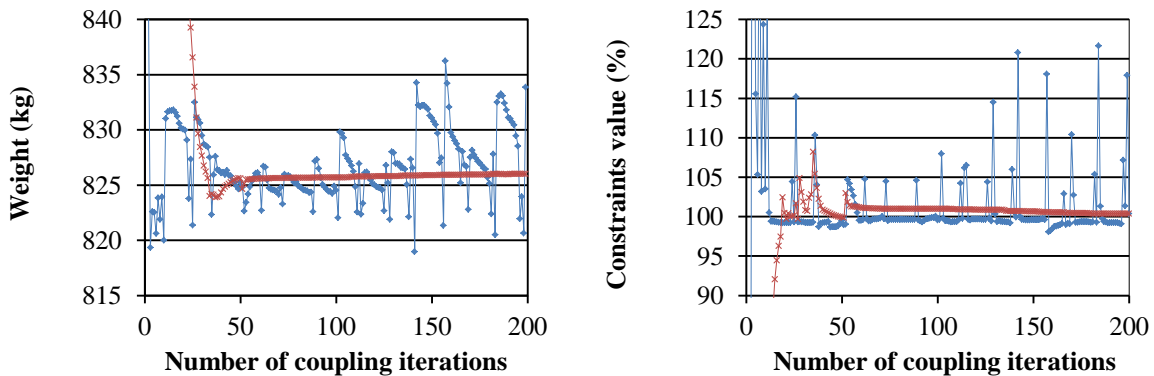


Figure 15: Red symbols are the results with under relaxation factor, and the blue ones without it.

Finally, as shown on Figure 8, 15 and 16, the ESL method is able to comply quite well with structural constraints. In the present work, only 36 design patches were optimised, therefore the final design cannot be fully stressed. However, by adding more design variables, this is something that could be reached with limited extra computational cost thanks to the use of a gradient based optimiser. It can also be shown with Figure 16 that loads tend to vary in space much quicker at the tip than at the root, meaning that the design patches would need to be smaller nearby the tip.

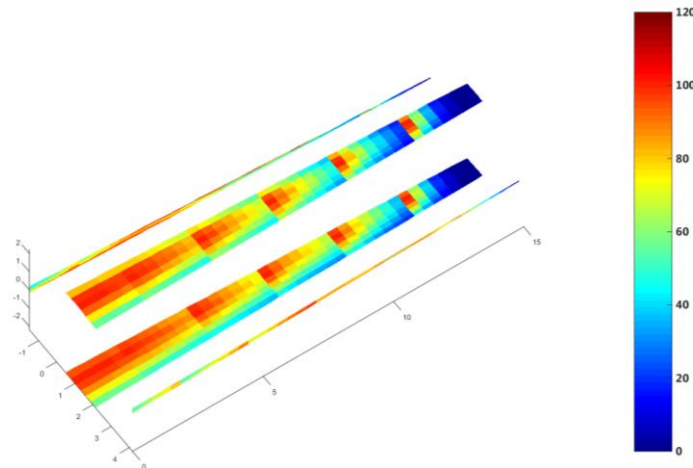


Figure 16: Maximum strength constraint value (%) for a wing optimised with dynamic loads.

V. Conclusion

This paper demonstrates that the ESL method can be applied to size aircraft wing structure for dynamic load cases. Through the different optimisation run, results shows that gust load cases can be critical for the structure and are difficult to constrain with the sole use of static load cases. Fast gust loads tend to be critical at the tip, slow ones at the root. One interesting matter is that the boundary condition of the wing (clamped or free flying) can affect the slow gust loads, but has a limited impact on the fast load cases. Most of the tailoring is done through the thickness distribution, rather than fibres orientations. Though, it is important to keep in mind that in the present work, only strength constraints are used for the structural sizing, therefore panel buckling, manufacturing constraints and other practical requirements related to composite structure are ignored. This will be included in a future work and will likely change the outcome of the optimisation. The ESL method also allows for interesting trade-off for the engine location. Finally this method can be implemented into an MDO framework and easily be combined with existing tools.

Acknowledgements

Part of this work has been supported by funding from the People Programme (Marie Curie Actions) of the European Union's Seventh Framework Programme FP7 2012 under REA Grant agreement n°316394. This work also received funding from the ReLOAD project, part of the Clean Sky 2 European research program. The authors would like also to thank Dr. Terence Macquart from the University of Bristol and Marco Tito Bordogna from ONERA/TUD for their help on the editing of this paper.

References

- ¹Hoblitz, F.M. "Gust Loads on Aircraft: Concepts and Applications", American Institute of Aeronautics and Astronautics, 1988.
- ²Regan, C.D. and Jutte, C.V. "Survey of Applications of Active Control Technology for Gust Alleviation and New Challenges for Lighter-weight Aircraft", NASA technical report 216008, 2012.
- ³Disney, T. E. "C-5A Active Load Alleviation System", J. Spacecr. Rockets. 14, pp. 81–86, 1977.
- ⁴Dillinger, J.K.S., Klimmek, T., Abdalla, M.M. and Gürdal, Z. "Stiffness Optimization of Composite Wings with Aeroelastic Constraints", J. Aircr. 50, pp. 1159–1168, 2013.
- ⁵Jutte, C. and Stanford, B.K. "Aeroelastic Tailoring of Transport Aircraft Wings: State-of-the-Art and Potential Enabling Technologies", NASA technical report 218252, 2014.

- ⁶Grihon, S., Krog, L. and Bassir., D. "Numerical Optimization applied to structure sizing at AIRBUS A multi-step process", *Int. J. Simul. Multidisci. Des. Optim.* 3, pp. 432-442, 2009.
- ⁷Kenway, G., Kennedy, G. & Martins, J. "Aerostructural optimization of the Common Research Model configuration", in proceeding of 15th AIAA/ISSMO Multidisciplinary Analysis and Optimization Conference, American Institute of Aeronautics and Astronautics, Atlanta, GA, 2014.
- ⁸Bettebghor, D. and Blondeau, C. "Prise en compte de la flexibilité des cas de charges dimensionnants en optimisation de structure", in proceeding of 11e Colloque National en Calcul des Structures, Giens, 2013.
- ⁹Kang, B. S., Choi, W. S. & Park, G. J. "Structural optimization under equivalent static loads transformed from dynamic loads based on displacement", *Comput. Struct.* 79, pp. 145–154, 2001.
- ¹⁰Grihon, S. "VIVACE" project final report, pp. 36, 2007.
- ¹¹Park, G.-J. "Technical overview of the equivalent static loads method for non-linear static response structural optimization", *Struct. Multidiscip. Optim.* 43, pp. 319–337, 2010.
- ¹²Daoud, F., Petersson, O., Deinert, S. and Bronny, P. "Multidisciplinary Airframe Design Process: Incorporation of steady and unsteady aeroelastic loads", in proceeding of 12th AIAA Aviation Technology, Integration, and Operations (ATIO) Conference and 14th AIAA/ISSMO Multidisciplinary Analysis and Optimization Conference, American Institute of Aeronautics and Astronautics, 2012.
- ¹³Wildschek, A., Haniš, T. and Stroscher, F. " L_{∞} -Optimal feedforward gust load alleviation design for a large blended wing body airliner", *Progress in Flight Dynamics, GNC, and Avionics.* 6, pp. 707-728, 2013.
- ¹⁴Kim, Y.I., Park, G.J., Kolonay, R.M., Blair, M. and Canfield, R.A. "Nonlinear Dynamic Response Structural Optimization of a Joined-Wing Using Equivalent Static Loads", *J. Aircr.* 46, pp. 821–831, 2009.
- ¹⁵MSC.Software Corporation. MSC Nastran 2014 Aeroelastic Analysis User's Guide, 2014.
- ¹⁶MSC.Software Corporation. MSC Nastran 2012 Design Sensitivity and Optimization User's Guide, 2012.
- ¹⁷Tsai, S.W. and Pagano, N.J. "Invariant properties of composite materials", *Def. Tech. Inf. Cent.*, 1968.
- ¹⁸Macquart, T., Bordogna, M.T., Lancelot, P. and De Breuker, R. "Derivation and application of blending constraints in lamination parameter space for composite optimisation", *Compos. Struct.* 135, pp. 224–235, 2016.
- ¹⁹Ijsselmuiden, S.T., Abdalla, M.M. and Gürdal, Z. "Implementation of strength based failure criteria in the lamination parameter design space", *AIAA J.* 46, pp. 1826–1834, 2008.
- ²⁰Regional Aircraft | Clean Sky. Available at: <http://www.cleansky.eu/content/page/regional-aircraft>
- ²¹European Aviation Safety Agency. Certification Specifications Large Aeroplanes, Amendment 18, 2016.
- ²²Castellani, M., Lemmens, Y. & Cooper, J. E. "Parametric reduced-order model approach for simulation and optimization of aeroelastic systems with structural nonlinearities" *Proc. Inst. Mech. Eng. Part G J. Aerosp. Eng.*, vol. 230 no. 8, pp. 1359-1370, 2015.
- ²³Reimer, L., Ritter, M., Heinrich, R. & Krüger, W. "CFD-based Gust Load Analysis for a Free-flying Flexible Passenger Aircraft in Comparison to a DLM-based Approach", in proceeding of 22nd AIAA Computational Fluid Dynamics Conference, American Institute of Aeronautics and Astronautics, 2015.
- ²⁴Langton, R., Clark, C., Hewitt, M. and Richards, L. "Aircraft Fuel Systems", Wiley, 2009.
- ²⁵Werter, N.P.M. and De Breuker, R. "A novel dynamic aeroelastic framework for aeroelastic tailoring and structural optimisation", *Compos. Struct.* 158, pp. 369–386, 2016.

Probabilistic Analysis of Topologically Optimized Structures Considering Geometric Imperfections

Julian Kajo Lüdeker* and Dr. Benedikt Kriegesmann[†]

Hamburg University of Technology, Hamburg, 21073, Germany

A method is presented to automatically parameterize the geometry obtained by topology optimization using NURBS. The NURBS representation is used to capture the random deviations of the geometry such that it can be used for probabilistic analyses. The coordinates of the NURBS control points are considered as random parameters, which are highly correlated. Their joint probability distribution is obtained by fitting the control points to measurement data. A transformation technique is employed which efficiently describes the distribution by a significantly reduced number of random parameters. These transformed random parameters are considered as input parameters for a semi-analytic probabilistic analysis. The probabilistic approach is demonstrated for an 2D example structure, where the maximal stress is considered as output of the probabilistic analysis. The results of the semi-analytic approach compare well with results obtained from a Monte Carlo simulation, while being much more efficient. The whole workflow is fully automated, including meshing and Finite Element analysis of the NURBS representations, which allows embedding the probabilistic analysis in a robust design optimization framework.

Nomenclature

\mathcal{C}	Candidates list
e_{ij}	Finite element at ij -th position
$f_{\mathbf{Z}}$	Joint probability density function of \mathbf{Z}
f_{Z_i}	Probability density function of Z_i
$g(\mathbf{z})$	Objective function of probabilistic analysis
$\mathcal{N}(e_{ij})$	Neighborhood of element e_{ij}
n_i	Entry of \mathbf{N}
r	Rank of Σ and length of \mathbf{Z}
w, w_α, w_β	Weight functions
\mathbf{X}	Random vector
\mathbf{x}	Realization of the random vector \mathbf{X}
$x_{c,i}$	x -coordinate of the i -th NURBS control point
$y_{c,i}$	y -coordinate of the i -th NURBS control point
\mathbf{Z}	Normalized, uncorrelated random vector
\mathbf{z}	Realization of the random vector \mathbf{Z}
α, β	Angles between gradient directions and neighbor position
ρ_{ij}	Normalized density of the corresponding element
Σ	Covariance matrix
σ_g^2	Variance of g
$\boldsymbol{\mu}$	Mean vector
$\mu_{i,k}$	k -th central moment of Z_i
μ_g	Mean value of g
$\nabla_{\mathbf{x}} \rho_{ij}$	Density gradient at element e_{ij}

*Research Assistant, New design and sizing methods for hybrid airframe structures, Hamburg University of Technology, Am Schwarzenberg-Campus 4, D-21073 Hamburg

[†]Juniorprofessor, New design and sizing methods for hybrid airframe structures, Hamburg University of Technology, Am Schwarzenberg-Campus 4, D-21073 Hamburg

I. Introduction

The industrialization of additive layer manufacturing has raised the intention of aircraft industry for topology optimization, as it allows manufacturing arbitrary shapes of structures. Standard topology optimization using the SIMP approach minimizes the compliance for a given volume fraction.¹ Several works enhanced topology optimization for considering stress constraints,^{2,3} as this is more relevant for practical application than the stiffness. However, these approaches do not consider the sensitivity with respect to uncertainties and therefore provide designs with little robustness. Kharmanda et al. suggested combining reliability based design optimization with topology optimization, which is referred to as reliability-based topology optimization (RBTO).⁴ Other studies followed this idea and confirmed the finding that the design obtained from RBTO can differ significantly from the one obtained using classical topology optimization.^{5,6} In these publications only parameters were considered as random which are independent of the design, such as Young's modulus, load magnitude and the size of the design space. Especially the geometry is challenging to be considered as random within RBTO, but it is known to have an effect on stability and fatigue performance. Schevenels et al.⁷ included geometric deviations within a robust topology optimization by applying a random field that perturbs the threshold of a Heaviside projection function, which results in a spatial variation of thicknesses. They showed that indeed a design is obtained that is less sensitive with respect to geometric imperfections. However, the random geometric deviations are distributed equally over the whole design space and independent of the specimen design. In subsequent works Lazarov et al.^{8,9} suggested ways to increase the efficiency of the embedded probabilistic analysis, but the same approach is followed for introducing geometric imperfections in the optimization. If a probabilistic sizing approach is supposed to be followed, the question is in how far the random input parameters are representative for real scatter of geometry. This question can only be answered by validating a probabilistic analysis with test data, considering the final design of the topology optimization. The present work suggests a procedure to describe the discretized result of a topology optimization and measurements of manufactured specimen by the same parameterization, namely by Non-Uniform Rational B-Splines (NURBS). The NURBS representation is then used to describe the randomness of geometry in a fast probabilistic analyses. The procedure is demonstrated by application to a 2D example.

II. Parameterization of Topologically Optimized Geometry

In the following section, a procedure is described to provide a NURBS representation based on the normalized density distribution given by the SIMP method.

II.A. Geometry from density gradients

The SIMP approach provides a normalized density distribution of an uniform finite element mesh of $n \times m$ elements e_{ij} (figure 1a). Based on these densities ρ_{ij} of each element, the gradient can be approximated using a finite differences scheme. In order to ensure a high gradient at the edge of the design space, the finite element mesh is surrounded by zero density elements.

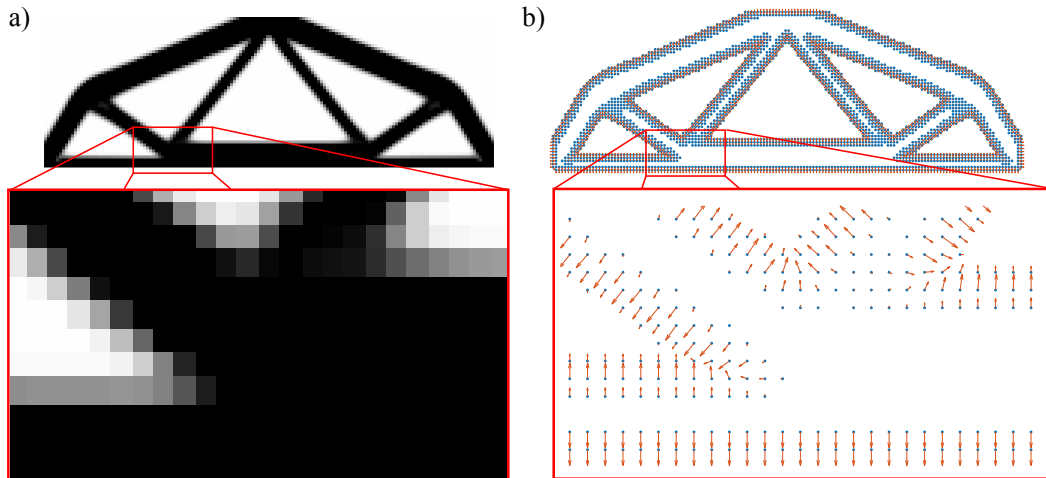


Figure 1. Density distribution (a) as a typical result of the topology optimization using the SIMP approach and the corresponding density gradients (b).

$$\nabla_{\mathbf{x}} \rho_{ij} = \frac{\partial \rho_{ij}}{\partial \mathbf{x}} \approx \begin{bmatrix} \frac{\rho_{i-1,j} - \rho_{i+1,j}}{\Delta x_1} \\ \frac{\rho_{i,j-1} - \rho_{i,j+1}}{\Delta x_2} \end{bmatrix} \quad (1)$$

An example of the gradient field is shown in figure 1b. The first step of the geometric interpretation is to find and sort the elements that describe the contour of the structure. The idea of the algorithm is to identify the contours by "drawing" lines along the maximum gradients, resulting in an array of lines described by the position \mathbf{x}_{ij} of the elements e_{ij} . At the beginning, the candidate list is given by all elements for which the norm of the density gradient is larger than some value ϵ , which is chosen to equal 0.1.

$$\mathbf{C} = \{e_{ij} | |\nabla_{\mathbf{x}} \rho_{ij}| > \epsilon\} \quad (2)$$

While the candidate list is not empty $\mathbf{C} \neq \emptyset$, the element with the maximum gradient is chosen as a starting point $\mathbf{e}_{start} = \{e_{ij} | \max(|\nabla_{\mathbf{x}} \rho_{ij}|)\}$. Then, an iterative procedure follows the contour of the structure by checking the neighborhood of the last chosen element $\mathbf{N}(e_{ij}) = \{n_i\} = \{e_{kl} | (|i-k| \leq 1) \cup (|j-l| \leq 1)\} / e_{ij}$ and picking the one with the highest weight $w(n_i)$.

$$w(n_i) = w_{\alpha}(\alpha(e_{ij}, n_i)) w_{\beta}(\beta(n_i, e_{ij})) |\nabla_{\mathbf{x}} \rho(n_i)|^p \quad (3)$$

$$w_{\alpha}(\alpha) = \sin |\alpha| + \frac{a}{\pi} |\alpha| \quad (4)$$

$$w_{\beta}(\beta) = \sin |\beta| - \frac{a}{\pi} |\beta| + a \quad (5)$$

This weight is based on the norm and the directions of the current elements and its neighborhoods gradients. The directions are weighted by w_{α} and w_{β} , which uprate elements that are more tangential to the gradients direction. Both functions and the definition of the corresponding angles α and β are shown in figure 2. The criteria defined by equation 3 appears to be stable by a usage of constant values $a = \frac{1}{4}$ and $p = 4$, for different density distributions achieved by the twodimensional SIMP method. For more accurate representations of complex fillets it is beneficial to reduce the weight of the gradient norm by decreasing p .

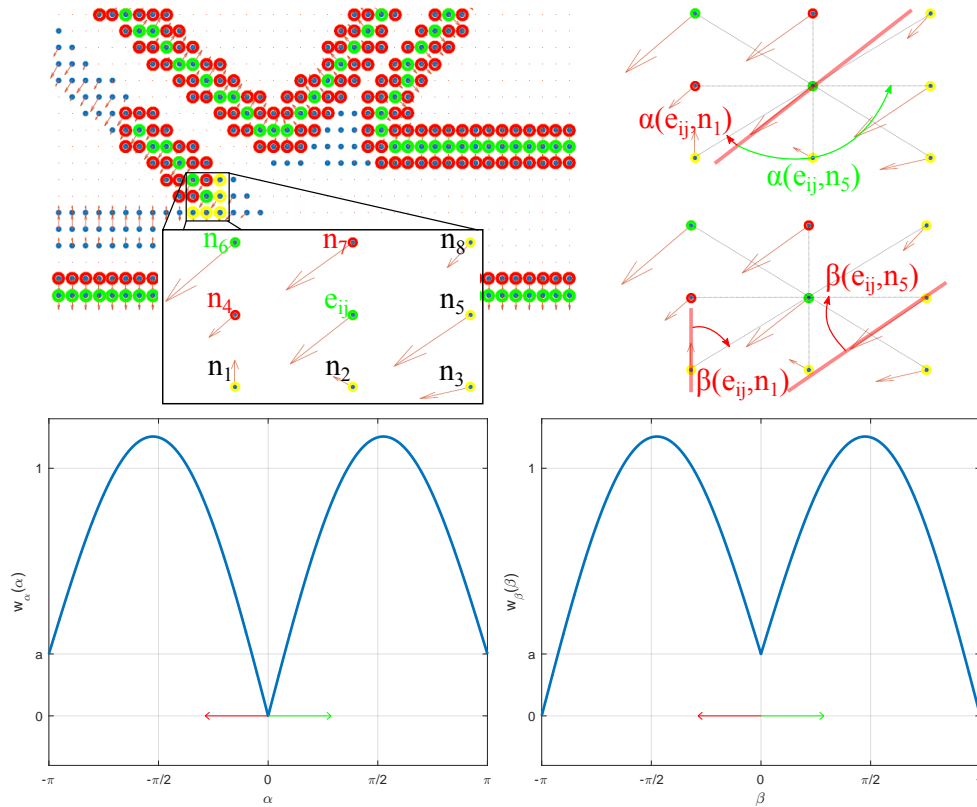


Figure 2. Defintion of α and β and the corresponding weight functions w_{α} and w_{β} for $a = \frac{1}{4}$.

All other elements of the current neighborhood are deleted from the candidates list. If the neighborhood of the current element is empty, the line is closed by adding the starting point to the end of the line. This procedure is repeated, until the candidates list is empty.

The described algorithm provides polygons represented by the green points in figure 3a. Only the important nodes of these polygons are used for the control points of the NURBS curvatures. These points

are determined based on the differences between the directions of the density gradients compared to its direct neighbors.

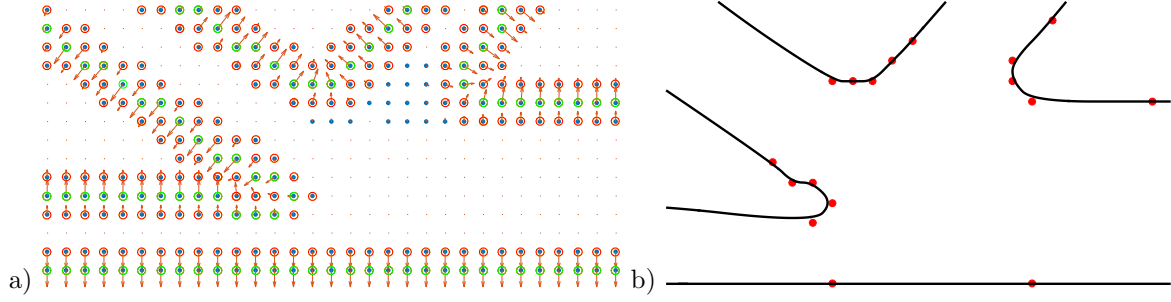


Figure 3. Elements that are chosen by the algorithm (for $a = \frac{1}{4}, p = 2$) to represent the contour lines (green), elements that have been deleted from the candidate list (red) (a) and the corresponding NURBS (control points in red)(b).

II.B. Meshing the NURBS representation

Given the NURBS representation, the geometry is meshed with triangle elements using the algorithm published in Ref. [10, text]. For the finite element simulation, linear elements with reduced integration are used. The meshing algorithm is called such that the mesh density increases towards the edges (see figure 4).

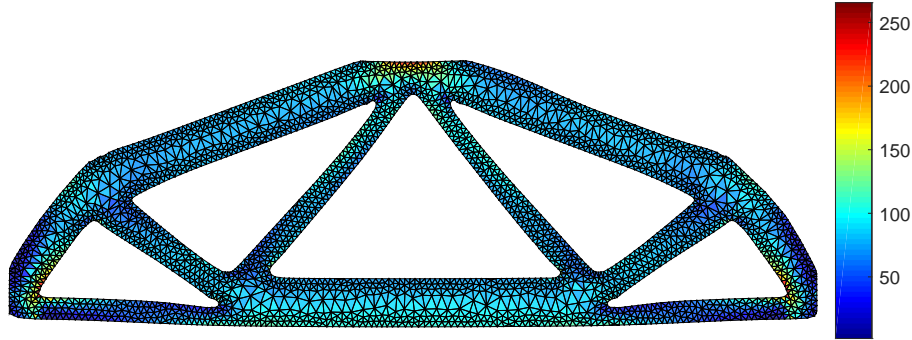


Figure 4. Finite Element model with von Mises stresses.

III. Probabilistic analysis

In this section, the probabilistic analysis approach is described to determine the stochastic distribution of the maximal occurring stress due to the scatter of the geometry. The mechanical system considered is the MBB beam with isotropic material properties.

III.A. Distribution of Geometric Scatter

The scatter of geometry is described by the coordinates of the control points of the NURBS $x_{c,i}$ and $y_{c,i}$, which are summarized in the random vector \mathbf{X} .

$$\mathbf{x} = (x_{c,1}, y_{c,1}, \dots, x_{c,i}, y_{c,i}, \dots, x_{c,p}, y_{c,p})^T \quad (6)$$

Given a sample of manufactured specimens, the control point coordinates are adjusted to describe the geometry of the specimen. Consider exemplarily the two control points A and B shown in figure 5a. For each specimen, the control points have different positions and therefore a scatter is obtained for each coordinate of each control point. The scatter of the x -coordinates of the points A and B is shown in figure 5b. Obviously, there is a strong correlation of the positions of both points, as one would expect. From each specimen, a realization \mathbf{x} of the random vector \mathbf{X} is obtained. From these realizations, the mean vector $\boldsymbol{\mu}$ and the covariance matrix $\boldsymbol{\Sigma}$ of random vector \mathbf{X} are estimated. These are used for transforming the random vector \mathbf{X} to the random vector \mathbf{Z} , by

$$\mathbf{X} = \boldsymbol{\Sigma}^{\frac{1}{2}} \mathbf{Z} + \boldsymbol{\mu} \quad (7)$$

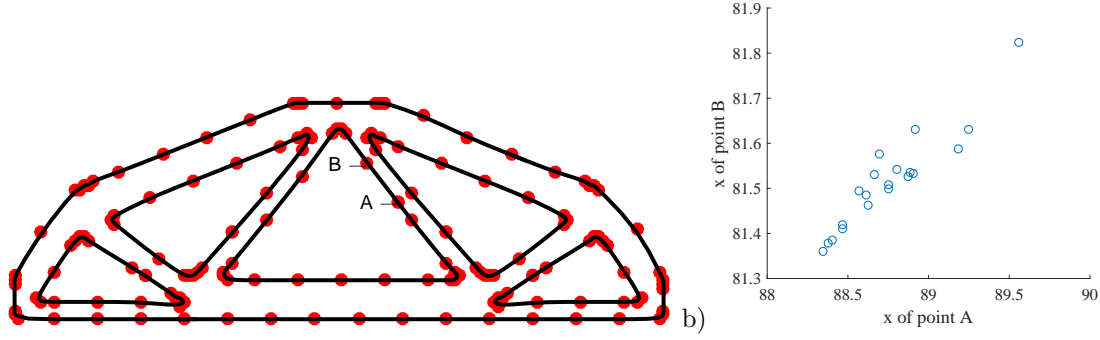


Figure 5. Control points A and B considered exemplarily (a). Ant hill plot of the x coordinates of control points A and B for the 20 virtual samples (b).

The root of the covariance matrix $\Sigma^{\frac{1}{2}}$ can be determined from the spectral decomposition of Σ .

$$\Sigma = Q D Q^T \quad (8)$$

The matrix Q consists of the eigenvectors of Σ and D is a diagonal matrix with the eigenvalues of Σ . The transformation (7) can be written as

$$X = Q D^{\frac{1}{2}} Z + \mu \quad \Sigma = Q D Q^T \quad (9)$$

The random vector Z has uncorrelated entries with a mean value of 0 and a standard deviation of 1. Furthermore, when using (9) the length of Z is smaller than the number of measurements used to build the covariance matrix.¹¹ The reason is that the rank r of Σ is smaller than the number of measurements. Given a random vector X of length n , then $Q \in \mathbb{R}^{n \times r}$ and $D \in \mathbb{R}^{r \times r}$. Hence, this transformation significantly reduces the number of parameters required to describe geometric imperfections. In the present case, $p = 158$ control points are used and X has a length of $n = 2p = 316$. Since 20 specimens are considered to build μ and Σ , Z has a length of only $r = 19$. Hence, for the probabilistic analysis, only 19 parameters are used to fully describe the observed scatter of geometry.

III.B. Probabilistic Approach

For the probabilistic analysis, the incomplete second order approach¹² (ISOA) is utilized, which is an extension of the first-order second-moment¹³ (FOSM) method. The objective function $g(\mathbf{x})$ is approximated by a Taylor series at the mean vector μ . Here, g shall be considered as a function of the vector \mathbf{z} , which is obtained from the transformation Eq. (7). Hence, the Taylor series at of $g(\mathbf{z})$ is expanded at $\mathbf{0}$.

$$g(\mathbf{z}) = g(\mathbf{0}) + \sum_{i=1}^r g_{,i} z_i + \frac{1}{2} \sum_{i=1}^r \sum_{j=1}^r g_{,ij} z_i z_j + \dots \quad (10)$$

For the partial derivatives at the origin, the following abbreviations are introduced.

$$\left. \frac{\partial g(\mathbf{z})}{\partial z_i} \right|_{\mathbf{z}=\mathbf{0}} = g_{,i} \quad \left. \frac{\partial^2 g(\mathbf{z})}{\partial z_i \partial z_j} \right|_{\mathbf{z}=\mathbf{0}} = g_{,ij} \quad (11)$$

Inserting the second-order Taylor series in the equation of the mean value of the objective function μ_g , an approximation of the mean value is obtained.

$$\mu_g = \int_{-\infty}^{\infty} g(\mathbf{z}) f_Z(\mathbf{z}) d\mathbf{z} \approx \underbrace{g(\mu)}_{\text{FOSM}} + \frac{1}{2} \sum_{i=1}^r \frac{\partial^2 g(\mu)}{\partial z_i^2} \text{var}(Z_i) \quad (12)$$

Here, the $\mu_{i,k}$ is the k -th (central) moment of the i -th entry of Z . (Note that since the mean value of z_i equals 0, the non central moment equals the central moment.)

$$\mu_{i,k} = \int_{-\infty}^{\infty} z_i^k f_{Z_i}(z_i) dz_i \quad (13)$$

In the same manner, the second-order approximation of the variance is obtained.

$$\begin{aligned}
 \sigma_g^2 = \text{var}(g(\mathbf{Z})) &= \int_{-\infty}^{\infty} (g(\mathbf{z}) - \mu_g)^2 f_{\mathbf{Z}}(\mathbf{z}) d\mathbf{z} \\
 &\approx \underbrace{\sum_{i=1}^r g_{,i}^2 \mu_{i,2} + g_{\mu}^2 - \mu_g^2 + g_{\mu} \sum_{i=1}^r g_{,ii} \mu_{i,2}}_{\text{FOSM}} + \sum_{i=1}^r g_{,i} g_{,ii} \mu_{i,3} + \frac{1}{4} \sum_{i=1}^r g_{,ii}^2 \mu_{i,4} \\
 &\quad + \frac{1}{2} \sum_{i=1}^r \sum_{j=i+1}^r g_{,ii} g_{,jj} \mu_{i,2} \mu_{j,2} + \underbrace{\sum_{i=1}^r \sum_{j=i+1}^r g_{,ij}^2 \mu_{i,2} \mu_{j,2}}_{G_{ij}}
 \end{aligned} \tag{14}$$

When using the incomplete second order approach (ISOA), the term G_{ij} is neglected for the sake of efficiency. When the derivatives need to be estimated by central difference, $2n + 1$ evaluations of the objective function need to be performed. When including term G_{ij} , mixed partial derivatives need to be estimated, which requires another $\frac{1}{2}(n^2 - n)$ evaluations of the objective function. For validation of the above described approach, also a standard Monte Carlo simulation is performed. Also here the transformation Eq. (7) is used to consider the uncorrelated random vector \mathbf{Z} . The Kolmogorov-Smirnov test (see, e.g., Ref.¹⁴) is used to determine the stochastic distributions that describes observed scatter best. These distributions are then used to generate samples $\mathbf{z}^{(k)}$, for which the objective function is evaluated and a discrete distribution of g is obtained.

III.C. Results

For the present work, no measurements of manufactured specimens are available. Therefore, virtual specimens have been generated by perturbation the initial geometry. The subsequent steps however are the same, but an experimental validation of the procedure is pending. In figure 6 the ideal structure (black

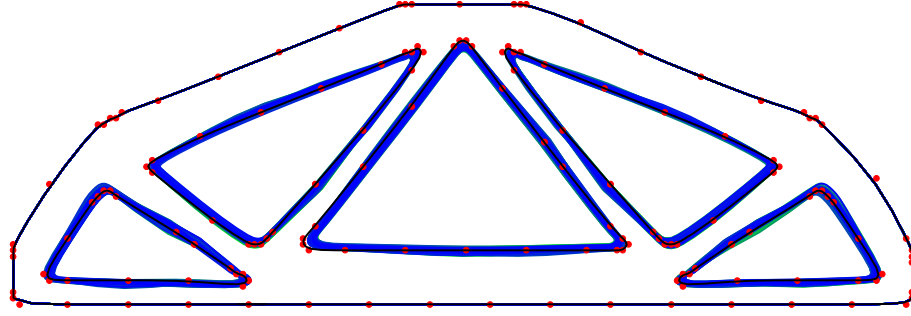


Figure 6. Virtual test specimens.

line) and the NURBS control points (red points) are plotted together with 20 perturbed geometries (blue lines), which serve as virtual test specimen. For each virtual specimen the maximal stress is determined, which is considered as the pseudo test series in the following. From the virtual test specimens, the stochastic distributions of the NURBS control points are determined, which serve as input data for the probabilistic analyses. In figure 7 the cumulative distributions obtained from the pseudo test series, a Monte Carlo simulation with 400 realizations and the FOSM and ISOA results are plotted. Since with FOSM and ISOA only mean value and variance of the maximal stress are determined, normal distribution is assumed in order to gain a distribution function. In table 1 the corresponding stochastic moments are summarized. While the FOSM method overestimate the mean value, all other values compare well. The ISOA, which requires $2n + 1 = 39$ finite element simulation, provides as good results as the Monte Carlo simulation.

Table 1. Stochastic moments of the maximal stress.

	Mean value	Standard deviation
Pseudo tests	250.8	7.8
Monte Carlo	248.3	9.5
FOSM	257.7	7.1
ISOA	252.5	7.5

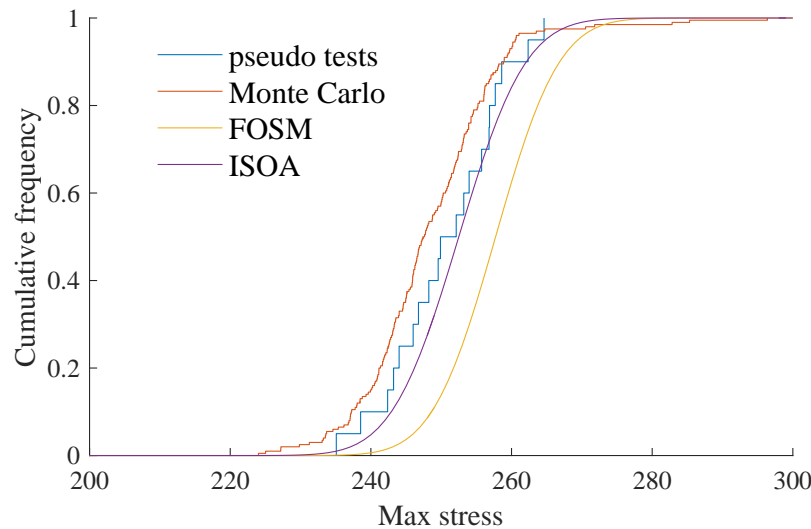


Figure 7. Cumulative distribution of the maximum stress.

IV. Conclusion

An efficient procedure is presented to capture the randomness of geometric imperfections for probabilistic analyses of topologically optimized structures. The Taylor series based fast semi-analytic approach is validated by comparison with a Monte Carlo simulation. For the current example, the second order approach provides much better accuracy than the first order approach at the same computational cost. The procedure can be easily integrated into a reliability based shape optimization of complex structures. A 2D example is considered in the current paper. In general, the procedure is applicable to 3D problem, but an automated generation of a NURBS representation will required significant additional development effort.

References

- ¹Bendsøe, M. P. and Kikuchi, N., "Generating optimal topologies in structural design using a homogenization method," *Computer Methods in Applied Mechanics and Engineering*, Vol. 71, No. 2, Nov. 1988, pp. 197–224.
- ²Duysinx, P. and Sigmund, O., "New developments in handling stress constraints in optimal material distribution," *American Institute of Aeronautics and Astronautics*, Vol. Paper 98-4906, 1998, pp. 10.
- ³Holmberg, E., Torstenfelt, B., and Klarbring, A., "Stress constrained topology optimization," *Struct Multidisc Optim*, Vol. 48, 2013, pp. 33–47.
- ⁴Kharmanda, G., Olhoff, N., Mohamed, A., and Lemaire, M., "Reliability-based topology optimization," *Structural and Multidisciplinary Optimization*, Vol. 26, No. 5, 2004, pp. 295–307.
- ⁵Jung, H.-S. and Cho, S., "Reliability-based topology optimization of geometrically nonlinear structures with loading and material uncertainties," *Finite Elements in Analysis and Design*, Vol. 41, No. 3, 2004, pp. 311–331.
- ⁶López, C., Baldomir, A., and Hernández, S., "Deterministic versus reliability-based topology optimization of aeronautical structures," *Structural and Multidisciplinary Optimization*, 2015.
- ⁷Schevenels, M., Lazarov, B. S., and Sigmund, O., "Robust topology optimization accounting for spatially varying manufacturing errors," *Computer Methods in Applied Mechanics and Engineering*, Vol. 200, No. 4952, 2011, pp. 3613–3627.
- ⁸Lazarov, B. S., Schevenels, M., and Sigmund, O., "Topology optimization with geometric uncertainties by perturbation techniques," *International Journal for Numerical Methods in Engineering*, Vol. 90, No. 11, 2012, pp. 1321–1336.
- ⁹Lazarov, B. S., Schevenels, M., and Sigmund, O., "Topology optimization considering material and geometric uncertainties using stochastic collocation methods," *Structural and Multidisciplinary Optimization*, Vol. 46, No. 4, 2012, pp. 597–612.
- ¹⁰Persson, P.-O., *Mesh generation for implicit geometries*, Ph.D. thesis, Massachusetts Institute of Technology, Boston, MA, 2005.
- ¹¹Kriegesmann, B., *Probabilistic Design of Thin-Walled Fiber Composite Structures*, Mitteilungen des Instituts für Statik und Dynamik der Leibniz Universität Hannover 15/2012, ISSN 1862-4650, Gottfried Wilhelm Leibniz Universität Hannover, Hannover, Germany, 2012.
- ¹²Kriegesmann, B., Rolfes, R., Hühne, C., and Kling, A., "Fast Probabilistic Design Procedure for Axially Compressed Composite Cylinders," *Composites Structures*, Vol. 93, 2011, pp. 3140–3149.
- ¹³Elishakoff, I., van Manen, S., Vermeulen, P. G., and Arbocz, J., "First-Order Second-Moment Analysis of the Buckling of Shells with Random Imperfections," *AIAA journal*, Vol. 25, No. 8, 1987, pp. 1113–1117.
- ¹⁴Haldar, A. and Mahadevan, S., *Probability, Reliability and Statistical Methods in Engineering Design*, John Wiley & Sons, New York ; Chichester England, 1st ed., Nov. 1999.

Computational Design for Micro Fluidic Devices using a Tightly Coupled Lattice Boltzmann and Level Set-Based Optimization Algorithm

David J. Munk* and Gareth A. Vio[†]

The University of Sydney, Sydney, 2006, Australia

Timoleon Kipouros[‡] and Geoffrey T. Parks[§]

University of Cambridge, Cambridge, CB2 1PZ, United Kingdom

Recently the study of micro fluidic devices has gained much interest in various fields from biological to engineering. The reason for this increased interest can be attributed to the technological progress in machining, allowing complex geometries to be manufactured, and the need for miniaturized devices in combustion and chemical analysis. These devices are concerned with low Reynolds number flows, resulting in a laminar flow regime, having dimensions that range from millimeters to micrometers. Although micro fluidic devices can be implemented for mixing of multiple fluid species, this work is particularly interested in the mixing of two non-reacting iso-thermal and incompressible fluids. Therefore, whilst diffusivity dictates the mixing in low-Reynolds-number flows, in this case the mixing is governed only by turbulence. Thus, the mixing can be enhanced by using active or passive devices, such as moving parts or multi-holed baffle plates. In this study passive devices are considered, due to their ease of integration and stable operation, compared with active devices, which require an energy input in order to mix the flows. Complex geometries are required due to the presence of components in the direction of the flow which stretch and fold the fluid over the cross-section of the channel enhancing the turbulence of the system. Hence, areas of high stress are present due to the geometrical non-linearity of the micro fluidic devices and high pressure ratios. This article develops a novel framework for a topology optimization algorithm that is coupled directly to the Lattice Boltzmann method, used for simulating the flow in the micro fluidic device, for the objective of minimum compliance. This study focuses on the effect of the fluid-structural interactions by comparing the optimization results obtained by fully coupled, where the loads are updated directly by the change in topology, and uncoupled, no update in the load, solutions on the design of micro fluidic devices. The final compliance for both cases are compared and a trade-off is made between minimum compliance and computation time.

I. Introduction

Topology optimization of continuum structures, through material distribution methods, is the most challenging, yet the most rewarding economically as there are no restrictions on the design, compared with other types of structural optimization.¹ For this reason, structural topology optimization has developed rapidly in the past two decades, diversifying its application to almost all fields of engineering and design. However, the application of topology optimization to the design of micro fluidic devices is limited due to the many design iterations, which reduce the problem size such that acceptable execution times are achieved.² Further, the problem is complicated by the fluid-structural interactions (FSI) present between the mixing device and the flow. This presents a more complicated problem to the traditional topology optimization methods, which seek to find the maximum stiffness using a given amount of material and predefined fixed loading,^{3–5} since the load location, direction and magnitude are dependent on the topology. The difficulty in applying a design dependent pressure load to a topology optimization problem lies

*Research Student, AMME, the University of Sydney, NSW, 2006, Australia.

[†]Senior Lecturer, AMME, the University of Sydney, NSW, 2006, Australia.

[‡]Research Fellow, EDC, University of Cambridge, Cambridge, CB2 1PZ, United Kingdom.

[§]Reader, EDC, University of Cambridge, Cambridge, CB2 1PZ, United Kingdom.

in determining the surface which the pressure load acts over.⁶ There exist many different methods in the literature for applying design dependent pressure loads in a topology optimization framework. For example, Chen and Kikuchi⁷ implemented the pressure loading with a fictitious thermal loading, where they used a dryness coefficient to identify the fluid and solid regions. Sigmund and Clausen⁸ modelled the fluid region as a hydrostatic incompressible fluid. An extra design variable is introduced for each element to determine the phase of the region. They apply a fluid volume fraction, alike that of the material volume fraction that is commonly used. However, level set-based topology optimization methods^{9,10} naturally lend themselves to the application of topology optimization with pressure loads, as they implicitly define the material boundaries in their formulation. Level set algorithms maintain the discrete nature of the optimization problem, which leads to significant advantages over density-based algorithms.¹¹ Moreover, the non-slip boundary condition is implemented, removing the need for interpolation schemes and continuation methods, giving significant computational savings since flow is only modelled in fluid regions, i.e. no porous material. Therefore, this paper employs a level set-based topology optimization method, which solves a reaction-diffusion equation based on the topological derivative of the objective to update the level set function.¹² This is different from the conventional level set-based approaches,^{13,14} which solve the Hamilton-Jacobi equation to update the level set function. Therefore, topological changes that generate new boundaries during the optimization procedure are permitted and re-initialization of the level set function, typically required in Hamilton-Jacobi based approaches to ensure accuracy, is not necessary. Further, through the use of a regularization parameter in the reaction-diffusion equation, qualitative control of the geometrical complexity, i.e. hole size, can be employed. Thus, innovative structural designs can be developed and coupled to the fluid solver. Typically, a fluid problem is discretized by finite volume, finite element or discontinuous Galerkin methods.¹⁵ These methods have difficulty with complex 3D geometries, since they require fine body fitted meshes. Moreover, these approaches are not easily applied to multiphase flows with variable complex interfaces. Conversely, Lattice Boltzmann methods (LBM) are built around the concept of solving a discrete Boltzmann equation on Cartesian grids. Therefore, complex geometries can be easily handled with the LBM.¹⁶ The LBM has been proven to converge to the incompressible Navier-Stokes equations for the low Mach number regime and recently has gained broad recognition for the calculation of micro fluids, multi-phase problems and flows through porous media.^{16,17} The geometry in the LBM is defined by switching specific nodes of the mesh on and off and applying a bounce back boundary condition. This inherent boundary approach of the LBM makes it an ideal candidate for topology optimization techniques, where complex structures are expected to appear. This article presents an optimization framework for mixing within a micromixer device using the LBM. The code has been tested by Djenidi¹⁸ and is used in this work because its stability has been shown. Further, the code has been successfully validated against Ansys CFX, a commercial code, and with the study performed by Moghtaderi *et al.*,¹⁹ which work under similar conditions. The problem of low-Reynolds-number mixing has been previously addressed using both the finite element² and the Lattice Boltzmann method.²⁰ However, the latter is limited to 2D channel flows and represents low topological complexity. Level set methods have been employed in the topology optimization of steady-state Navier-Stokes flows.²¹ However, the authors stated that remeshing the fluid domain, extending the velocity and re-initializing the level set function incurred computational costs that limited their model. In this study the fluid and structural mesh are identical, eliminating the need for any spline or mesh interpolating, greatly reducing the computational cost of the optimization process. This allows information to be passed directly between the structural and fluid solvers. This study presents a numerical framework for the design of micro fluidic devices using a level set-based topology optimization algorithm and a Lattice Boltzmann method. To the best of the authors knowledge, movable 3D fluid-structure interfaces applied to design dependent load problems with level set structural topology optimization are considered here for the first time. The effect of fluid structural interactions is analyzed, by updating the fluid solver with the change in topology driven by the optimization algorithm. The method presented shows good convergence for the minimum compliance objective and avoids remeshing, interpolation schemes and continuation methods, which were found to be computationally prohibitive in previous studies.^{11,21}

II. Numerical Procedure

This section outlines the methodology employed in the present work, beginning with the topology optimization method used to solve the minimum compliance problem. This is followed by a description of the Lattice Boltzmann method which simulates the fluid dynamics. Finally the numerical framework is presented, highlighting the coupling between the fluid and structural solvers.

II.A. Topology Optimization

The conventional level set topology optimization methods solve the Hamilton-Jacobi equation to update the level set function, limiting these methods to shape optimization, as only the present structural boundaries are updated.²² To overcome this shortcoming Allaire *et al.*²³ introduced the bubble method²⁴ to the level set based shape topology optimization algorithm in order to allow topological changes. However, the introduction of new holes during the optimization process is facilitated by pre-defined parameter values, which have been proven to be difficult to define, as they often show a strong dependency on the optimal configurations obtained.²⁵ Yamada *et al.*¹² propose a new level set-based approach, modelled off the concept of the phase field method and using a reaction-diffusion equation to update the level set function. This permits topological changes during the optimization procedure and has a minimal dependency on initial configurations and mesh sizes. Structural optimization problems define a domain, Ω , which consists of a material domain, a void domain and boundaries Γ :

$$F(\Omega) = \int_{\Omega} f_d(i, \mathbf{x}) d\Omega + \int_{\Gamma} f_b(i, \mathbf{x}) d\Gamma \quad (1)$$

where f_d and f_b are real functions defined for domain Ω and boundary Γ respectively. \mathbf{x} represents a vector of state variables, i , located inside domain Ω . Topology optimization is therefore a material distribution problem within a fixed design domain, D , where the design variables are defined by:

$$\mathbf{x}(i) = \begin{cases} 1 & \forall i \in \Omega \\ 0 & \forall i \in D \setminus \Omega \end{cases} \quad (2)$$

The above optimization problem allows topological changes, such as an increase or decrease in the number of holes, as well as changes in the shape of the boundaries Γ . However, since the design variables, \mathbf{x} , are defined as a subset of a bounded Lebesgue space, L^∞ , continuity cannot be guaranteed. Therefore, the obtained solutions can be discontinuous at every point in the design domain. This ill-posed nature of the optimization problem is due to a lack of regularity of admissible shapes, rendering a solution nonexistent. To overcome this issue the optimization problem must be regularized, such that a solution can exist. The homogenization²⁶ and Solid Isotropic Material with Penalization (SIMP)²⁷ methods are popular techniques used to regularize optimization problems. In both approaches, optimized configurations are represented by continuous design variables that range from 0 to 1, which represent the density distribution of the material. Thus, the final topologies often contain intermediate density values, where the presence of the structure is not well defined. Further problems occur when defining boundary conditions and fluid-solid interfaces at the structural boundaries as the structural boundaries are not clearly expressed. Level set methods fundamentally overcome this problem, since the boundaries of the optimal configuration are represented implicitly using a level set function (Figure 1).

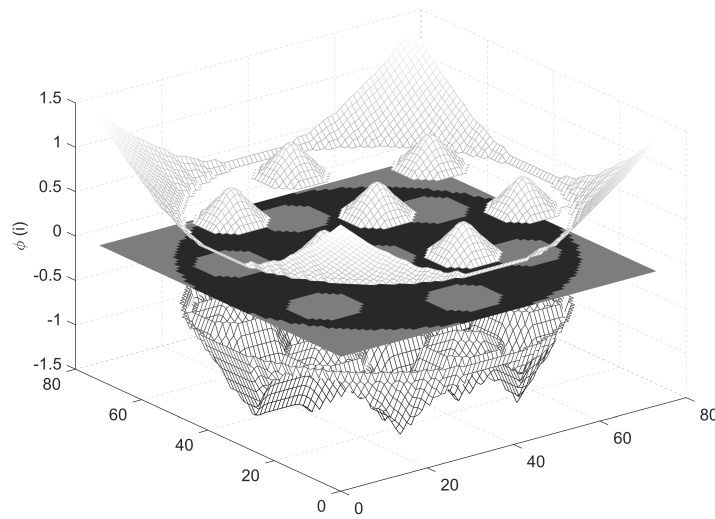


Figure 1. Level Set Function ϕ and Design Domain D

The iso-surface ϕ of the level set function can be defined by:

$$\begin{aligned} -1 \leq \phi(i) < 0 & \quad i \in \Omega \notin \Gamma \\ \phi(i) = 0 & \quad \forall i \in \Gamma \\ 0 < \phi(i) \leq 1 & \quad \forall i \notin \Omega \end{aligned} \quad (3)$$

The level set function is used to represent the boundaries of the structure, where negative values represent solid material, i.e. $\mathbf{x}(i) = -1$, positive values represent void material, $\mathbf{x}(i) = 1$, and zero represents the structural boundary (Figure 1). The level set function is bounded by: $\phi(i) \in [-1, 1]$ for regularizing the optimization problem. Thus, the optimization problem that minimizes an objective function, O , under an inequality constraint, G , can be formulated using the level set function, ϕ , as follows:

$$\begin{aligned} O(\mathbf{x}) &= \int_{\Omega} f_d(i, \mathbf{x}) d\Omega + \int_{\Gamma} f_b(i, \mathbf{x}) d\Gamma \\ \text{subject to } G(\mathbf{x}) &= \int_D g(i, \mathbf{x}) d\Omega - G_{max} \leq 0 \end{aligned} \quad (4)$$

where g is the density function and G_{max} is the maximum value that $\int_D g(i, \mathbf{x}) d\Omega$ can take. An unconstrained optimization problem is now formed using Lagrange's method of undetermined multipliers:

$$\check{O}(\mathbf{x}, \phi) = O + \lambda G \quad (5)$$

where λ is the Lagrange multiplier. The Karush-Kuhn-Tucker (KKT) conditions of this optimization problem are defined by:

$$\check{O}' = 0, \quad \lambda G = 0, \quad \lambda \geq 0, \quad G \leq 0 \quad (6)$$

where \check{O}' represents the derivative of the Lagrangian. For most problems it is not possible to find optimized solutions directly, therefore the optimization problem is replaced with a time evolution equation, by introducing a numerical time, t , and updating the level set function by solving this equation, ultimately obtaining an optimized configuration. To introduce the fictitious time, t , into the optimization problem, it is assumed that the variation of the level set function is proportional to the derivative of the Lagrangian, thus:

$$\frac{\partial \phi}{\partial t} = -K \check{O}' \quad (7)$$

where K is a constant that satisfies $K > 0$. Yamada *et al.*¹² showed as long as this constraint is satisfied the value of K has minimal effect on the final topology. However, this optimization problem is ill-posed; therefore, a regularization term is added to smooth out the problem. Thus, Eq. 7 is reformulated as a reaction diffusion equation:

$$\frac{\partial \phi}{\partial t} = -K(\check{O}' - \tau \nabla^2 \phi) \quad (8)$$

where $\nabla^2 \phi$ is the diffusive term which ensures smoothness of the level set function and τ is the regularization parameter which affects the degree of this diffusivity. Hence, larger values of τ provide increased diffusivity for the level set function; therefore, by appropriately setting τ excessive geometrical complexity can be prevented. Further, since the level set function is constrained between upper and lower limits, $\phi \in [-1, 1]$, the smoothing function only operates on points that are close to the structural boundaries. The optimized configuration can now be obtained by solving the time evolution problem given in Eq. 8. In this method the topological derivative, $d_t \check{O}$, is implemented for \check{O}' . The topological derivative is a measure, $meas()$, of the influence when a hole Ω_δ with radius δ is created at a certain point in the design domain Ω . Γ_δ represents the boundary of the hole. Thus, the topological derivative of the objective function O is defined by:

$$d_t O = \lim_{\delta \rightarrow 0} \frac{(O + \Delta O) - O}{meas(\Omega \setminus \Omega_\delta) - meas(\Omega)} \quad (9)$$

Further, the topological derivative for the Lagrangian, \check{O} , is given by:

$$d_t \check{O} = \lim_{\delta \rightarrow 0} \frac{\Delta \check{O}}{\frac{4\pi\delta^3}{3}} = \tilde{u}_{i,j}^0 A_{ijkl} u_{k,l}^0 - \lambda \quad (10)$$

where $\tilde{u}_{i,j}$ and λ are Lagrange multipliers and the superscript 0 indicates the value without creating holes. A_{ijkl} is defined as:

$$A_{ijkl} = \frac{3(1-\nu)}{2(1+\nu)(7-5\nu)} \left[\frac{-(1-14\nu+15\nu^2)E}{(1-2\nu)^2} \delta_{ij}\delta_{kl} + 5E(\delta_{ik}\delta_{jl} + \delta_{il}\delta_{jk}) \right] \quad (11)$$

where ν is the Poisson's ratio and E is the Young's modulus of the material. The interested reader is advised to seek out²⁸ for an in-depth derivation of the topological derivative. Therefore, the reaction diffusion equation, Eq. 8, becomes:

$$\frac{\partial \phi}{\partial t} = -K(-Cd_t\ddot{O} - \tau \nabla^2 \phi) \quad (12)$$

C is introduced to normalize the sensitivities such that a value for τ can be chosen regardless of the problem being solved. Therefore, C is defined by:

$$C = \frac{\int_D d\Omega}{\int_D |d_t O| d\Omega} \quad (13)$$

Through the finite difference approach the reaction diffusion equation is discretized in the time domain by:

$$\frac{\phi(t + \Delta t) - \phi(t)}{\Delta t} - \tau \nabla^2 \phi(t + \Delta t) = Cd_t\ddot{O} + \frac{\phi(t)}{\Delta t} \quad (14)$$

where Δt is a time step in the fictitious time domain t . By using the finite element method, Eq. 14 can be discretized into the following form:

$$\mathbf{T}\Phi(t + \Delta t) = \mathbf{Y} \quad (15)$$

where $\Phi(t)$ is a vector of the nodal values of the level set function at time t . \mathbf{T} is the stiffness matrix for the reaction diffusion equation and can be defined along with matrix \mathbf{Y} as:

$$\mathbf{T} = \bigcup_{\varepsilon=1}^N \int_{V_\varepsilon} \left(\frac{1}{\Delta t} \mathbf{N}^T \mathbf{N} + \nabla \mathbf{N}^T \tau \nabla \mathbf{N} \right) dV_\varepsilon \quad (16)$$

$$\mathbf{Y} = \bigcup_{\varepsilon=1}^N \int_{V_\varepsilon} \left(Cd_t\ddot{O} + \frac{\phi(i, t)}{\Delta t} \right) \mathbf{N} dV_\varepsilon \quad (17)$$

where N is the number of elements in the design domain, V_ε is the volume of an element, ε is the element number and \mathbf{N} is the interpolation function for the level set function. Thus, the level set function is updated using Eq. 15.

Finally, the volume constraint, $G(\mathbf{x})$, is dealt with using an augmented Lagrangian method, where the Lagrange multiplier, λ , is updated according to:

$$\lambda = \frac{\int_D d_t O d\Omega}{\int_D d\Omega} e^{[p(\frac{G}{G_{max}} + d)]} \quad (18)$$

where p and d are constant penalty parameters that adjust the position of the curve. When the constraint is sufficiently satisfied, i.e. when the value of G is small, the value of λ approaches 0. The sensitivity of the constraint function then becomes small compared to the sensitivity of the objective function in Eq. 5. In this case, the optimization is primarily affected by the value of the objective function. Conversely, when the constraint is far from being satisfied, the value of λ becomes large, causing the optimization to be primarily affected by the need to satisfy the constraint. However, to stabilize the convergence when the volume fraction is greater than the maximum allowable volume fraction, V_{max} , the volume constraint is relaxed according to:

$$G = \int_D \mathbf{x} d\Omega - V_{max} - (V_0 - V_{max}) \max \left(0, 1 - \frac{itr}{n_{vol}} \right) \leq 0 \quad (19)$$

where itr is the current iteration number, n_{vol} is the number of iterations set for the structure to satisfy the volume constraint and V_0 is the volume fraction of the structure. Therefore, the volume constraint is relaxed such that the constraint is gradually tightened during the first n_{vol} iterations.

II.B. Lattice Boltzmann Method

The Lattice Boltzmann method is a numerical scheme used for simulating fluid flows and modeling physics in fluids. The fundamental concept of the LBM is to construct kinetic models, based on Newton's laws, which incorporate the essential physics of microscopic processes such that the macroscopic processes are correctly modelled. Hence, the fluid is considered as a finite number of molecules whose motion is governed by Newton's laws of dynamics. Since the number of molecules of a particular gas is usually in

the order of Avogadro's number it is near impossible to simulate all particles individually.^{29,30} Therefore, the averages of a sample of molecules are simulated, passing from a microscopic to a mesoscopic scale, making it possible to obtain macroscopic values such as the fluid density and velocity from the moments of the velocity distribution functions that express the distribution state of the particles.

The LBM uses a discretized Boltzmann equation, known as the Lattice Boltzmann Equation (LBE), which can represent macroscopic properties by incorporating velocity distribution functions. The lattice used in this work is the D3Q19 lattice, meaning three dimensions and 18 moving particles per node with one rest node. The Boltzmann equation can be represented using the velocity distribution function, $f(x, t, \gamma)$, by:

$$Sh \frac{\partial f}{\partial t} + \gamma \cdot \nabla f = Q(f) \quad (20)$$

where Sh is the Strouhal number, t represents the time, x and γ represent the gas particle position and velocity respectively and Q , known as a collision operator, exhibits the effect of collision between the particles. For simplicity and without losing any generality, the Bhatnagar-Gross-Krook (BGK) collision model³¹ is used:

$$Q(f) = -\frac{1}{\tau_B}(f - f^{eq}) \quad (21)$$

where τ_B is the dimensionless relaxation time, which represents the average time until the next collision. f^{eq} is a Maxwell distribution and can be expressed as a local equilibrium solution of the Boltzmann equation:

$$f^{eq} = \frac{\rho}{T^{\frac{d}{2}}} e\left(-\frac{|\gamma - u|^2}{T}\right) \quad (22)$$

where ρ and u represent the fluid density and velocity, T is the temperature, assumed constant for the isothermal condition, and d is the number of spatial dimensions. From kinetic theory, the macroscopic variables in the flow field can be derived from the moments of the velocity distribution function with respect to the velocity field E :

$$\rho = \int_E f d\gamma, \quad u = \frac{1}{\rho} \int_E \gamma f d\gamma \quad (23)$$

The fundamental concept of the LBM is the discretization of the infinite set of particle velocities, γ , in Eq. 20. This allows the calculation of macroscopic quantities from the moments of a finite number of velocity distribution functions to be obtained as solutions of the Navier-Stokes equations. Thus, the discretization of the Boltzmann equation, Eq. 20, in time, t , and space at the lattice site x is:

$$f_\alpha(x + \gamma_\alpha \cdot \Delta t, t + \Delta t) - f_\alpha(x, t) = -\frac{1}{\tau_B} \cdot [f_\alpha(x, t) - f_\alpha^{eq}(x, t)] \quad \text{for } \alpha = 0 \dots 18 \quad (24)$$

where Δt is the time step and α is the number of particles per node. If the velocity is low or the flow has a small Mach number, the discrete local equilibrium distribution function f_a^{eq} obtained by the Maxwell distribution, Eq. 22, can be approximated as a Taylor expansion:³²

$$f_\alpha^{eq} = w_\alpha \rho \left[1 + 3 \cdot \gamma_\alpha \cdot u + \frac{9}{2} (\gamma_\alpha \cdot u)^2 - \frac{3}{2} \gamma_\alpha \cdot \gamma_\alpha \right] \quad (25)$$

where w_α are the weights as reported in.³³ The density ρ and fluid velocity u are obtained from the following moments of the velocity distribution functions:

$$\rho = \sum_{\alpha=0}^{18} f_\alpha, \quad u = \frac{1}{\rho} \sum_{\alpha=0}^{18} \gamma_\alpha f_\alpha \quad (26)$$

The left hand side of the discretized Boltzmann equation makes the streaming operation: the particles move from one node to the nearest neighbors along the velocity directions α . The right hand side represents the collision term, evaluated using the BGK collision model, Eq. 21, and describes the redistribution of the particles at each node for every time step. The Lattice Boltzmann equation is solved according to these two processes, where the collision step is evaluated as:

$$f_\alpha^{new} = f_\alpha(x, t) - \frac{1}{\tau_B} \cdot [f_\alpha(x, t) - f_\alpha^{eq}(x, t)] \quad (27)$$

where $f_\alpha^{eq}(x, t)$ is evaluated using the Taylor expansion of the Maxwell distribution, Eq. 25. The second step is the streaming operation, which means the transfer of the particle distribution $f_\alpha^{new}(x, t)$ to the particle distribution function at the next time step:

$$f_\alpha^{new}(x + \gamma_\alpha \cdot \Delta t, t + \Delta t) = f_\alpha^{new}(x, t) \quad (28)$$

The relaxation time, τ_B , is related to the kinematic viscosity, κ , of the fluid via:

$$\kappa = \frac{2 \cdot \tau_B - 1}{6} \quad (29)$$

Therefore, the relaxation time cannot be less than $\tau_B = 0.5$, as this would cause the viscosity to become negative, which is not possible. Consequently, the following Lattice Boltzmann equation is obtained:

$$f_\alpha^{new}(x + \gamma_\alpha \cdot \Delta t, t + \Delta t) = f_\alpha(x, t) - \frac{1}{\tau_B} \cdot [f_\alpha(x, t) - f_\alpha^{eq}(x, t)] \quad (30)$$

Eq. 30 is solved to simulate the fluid dynamics of the system.

II.C. Numerical Framework

The numerical framework, which couples the topology optimization algorithm, Section II.A, with the Lattice Boltzmann flow solver, Section II.B, is shown in Figure 2. The problem is defined, setting the initial topology and boundary conditions for the test case. The geometry is passed onto the flow solver, which outputs the pressures, and ultimately the forces, being applied to the topology. The current topology and loads are passed onto the Finite Element Method (FEM) module, which defines the structural boundary conditions and outputs the compliance of the structure. This is passed onto the topology optimization algorithm which calculates the sensitivities and updates the topology of the structure for the next iteration.

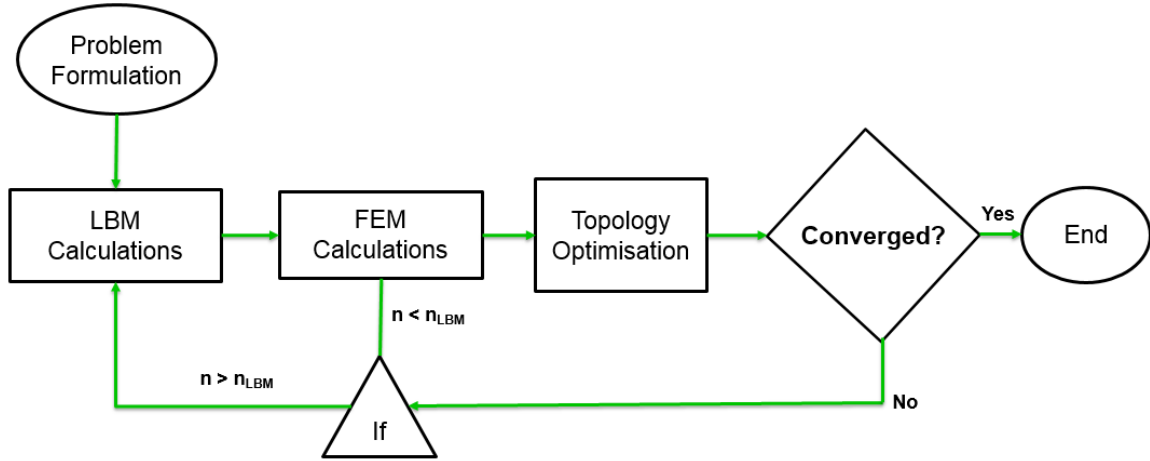


Figure 2. Numerical Framework for Coupled LBM-Topology Optimization

The numerical framework (Figure 2) consists of two loops. The first is between the topology optimization algorithm and the FEM module, which is performed at every iteration. The second loop passes the updated topology back into the LBM flow solver. Due to the computational penalty of the LBM solver, the second loop is performed only after every n_{LBM} iterations. This is a predefined parameter, which ensures the topology has changed significantly, such that the loads are required to be updated. A trade-off between reduction in compliance and computation time is given in the results (Section III).

III. Results and Discussion

In this section the results of the numerical framework are presented, along with a discussion and summary of the findings of this study. The case study analyzed in this work is detailed, followed by the results of the uncoupled and then coupled algorithm. Lastly, a trade-off is given on the improvement of the objective versus the computation time required for modelling of the fluid-structure interactions.

III.A. Case Study

The micro-reactor model used in this study is a baffled micro-reactor, as depicted in Figure 3. The model consists of a tubular vessel fitted with a fuel inlet tube, located co-axially in the main vessel, and a multi-holed baffle plate through which the oxidizer is introduced. The fluid domain and layout of the micro-reactor model is shown in Figure 3.

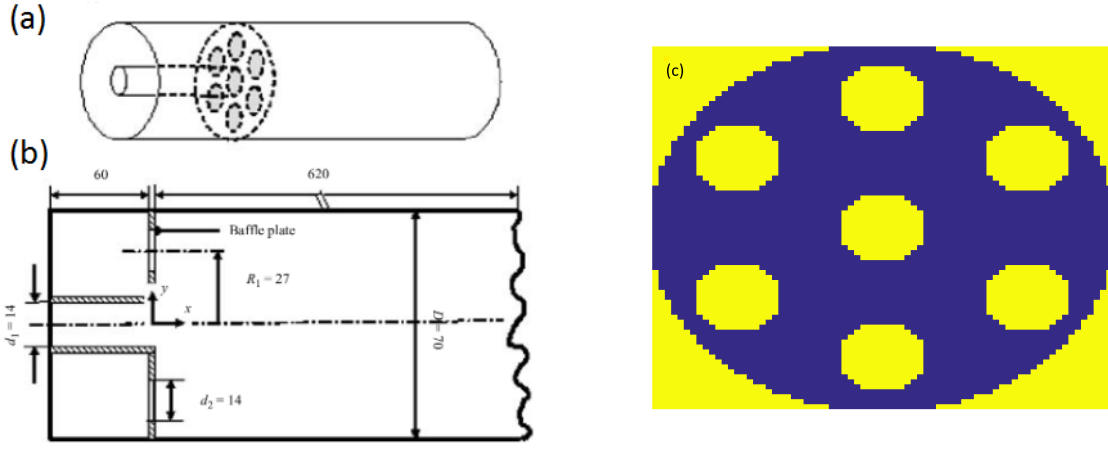


Figure 3. (a) Fluid Domain and (b) Layout of the Micro-Reactor Model³⁴ (c) Multi-Holed Baffle Plate

The dimensions of the fluid domain (Figure 3) are expressed in LBM nodes, where the dimensions of the lattice are $680 \times 73 \times 73$ lattice units, with additional nodes used for the wall, in the x , y and z directions, respectively. The baffle is located 60 lattice units downstream of the flow inlet (Figure 3). The imposed inlet conditions are the velocities of the flow in the inlet tube and annulus area. At the outlet a convective boundary condition is applied, based on the velocity. The no-slip conditions at the walls are implemented by modelling them as full-way bounce-back. The mass flow rate between the inner tube and annulus is set to 5% to mimic the experiments performed by Moghtaderi.¹⁹ The total number of iterations used for the LBM simulations is 4000, since stability is achieved and the code has been validated against Navier-Stokes simulations using a commercial code, Ansys CFX,¹⁸ and experimental analysis.¹⁹

The topology optimization algorithm is applied to the multi-holed baffle plate (Figure 3(c)) to maximize its stiffness for a given volume fraction. Therefore, the finite element analysis is performed on the baffle only. The plate is modelled using four-node quadrilateral elements, with all six degrees of freedom active. Hence, membrane, bending and transverse shear stresses are present. A clamped boundary condition, i.e. all six degrees of freedom are restrained, along the boundary of the baffle. The boundary of the central hole is designated as non-designable for the topology optimization, since this is determined by the fuel line and inlet conditions, which have been constrained in the fluid domain to be identical to the previous numerical¹⁸ and experimental¹⁹ studies.

III.B. Non-Coupled Solution

First, the problem with no feedback to the fluid solver is analyzed. Therefore, the LBM is only performed once on the initial structure to obtain the pressure loads, which remain unchanged throughout the optimization. This represents the simplest and hence most computationally efficient case. The initial structure is shown in Figure 3(c). A regularization parameter, $\tau = 10^{-5}$, and volume constraint iteration number, $n_{vol} = 50$, are defined before the level-set topology optimization method, Section II.A, is performed. The convergence history for the uncoupled topology optimization problem is given in Figure 4.

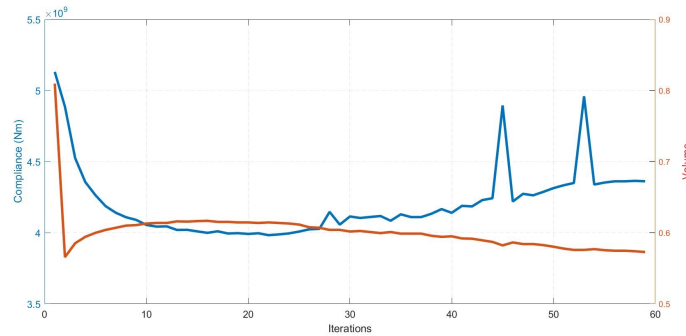


Figure 4. Convergence History for Uncoupled Problem

The sequence takes 59 iterations to converge to a final solution having a compliance of $4.361(10^9)Nm$. This is approximately 15% less than the initial structure, which has a compliance of $5.13(10^9)Nm$. Due to the addition of the regularization term, τ , it is not possible to guarantee that the objective function will monotonically decrease; further, since the volume constraint is relaxed for the first 50 iterations the objective decreases below the minimum before increasing again as the volume constraint is tightened. The 'jumps' observed in the objective (Figure 4) are a result of multiple holes combining to form one large hole, this behavior is characteristic of discrete methods.³ The initial and final topology for the uncoupled problem is shown in Figure 5.



Figure 5. Initial Topology (left) and Final Topology (right)

The final topology shows a much more complex structure (Figure 5), creating load paths to increase the stiffness of the baffle. All six holes from the original structure have been maintained; however, the topologies of the holes differ significantly. Further, four smaller holes have been added to the baffle. The strain energy distributions on the final and initial topologies are given in Figure 6.

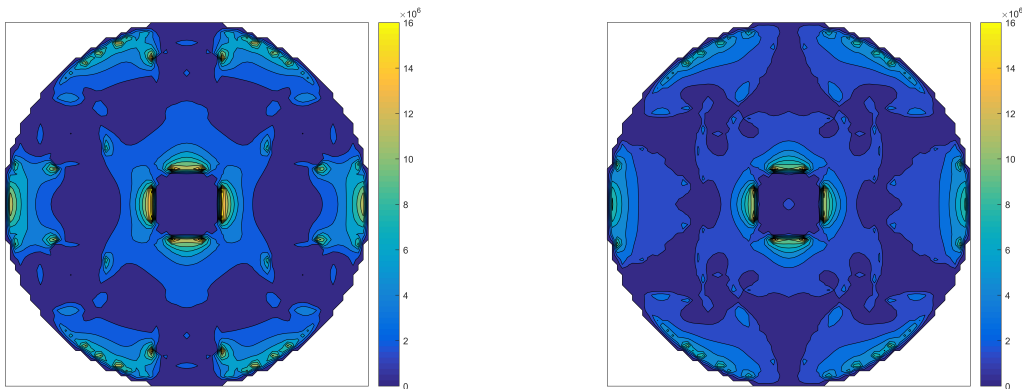


Figure 6. Initial Strain Energy Distribution (left) and Final Strain Energy Distribution (right)

The initial strain energy distribution shows several concentrated regions around the holes, where the overall stress is significantly higher compared to the rest of the structure. Comparatively, the optimized topology significantly reduces these concentrated zones (Figure 6), especially if the center hole is ignored, since this region is non-designable (Section III.A). The material is being used more effectively in the optimized structure since there are fewer zones of energy concentration. Therefore, the optimizer is able to improve the structural design of the baffle, by reducing the compliance and spreading out the loads more evenly through improved load paths.

The improvement gained by the optimization is significant as the baffle has become 15% more stiff compared with the original design. However, this was done without updating the pressure loads on the structure, meaning it is being optimized for the initial load case and not the actual load case, which develops with the topology. Further, the fluid-structural interactions are not being considered as the flow physics are not updated with the structure. Therefore, in the next section the coupled solution is presented where the flow is updated with the changing topology.

III.C. Coupled Solution

Here the coupled solution is presented; this means an extra parameter is defined, n_{LBM} , which determines when the LBM is solved to update the pressure loads on the structure. In this study two separate analyses are performed to test the effect of n_{LBM} on the final solution. First, an $n_{LBM} = 10$ is employed, meaning every 10 iterations the LBM is performed. The optimization parameters are kept constant from the previous analysis, i.e. $\tau = (10^{-5})$ and $n_{vol} = 50$. The convergence history for the coupled topology optimization problem is given in Figure 7.

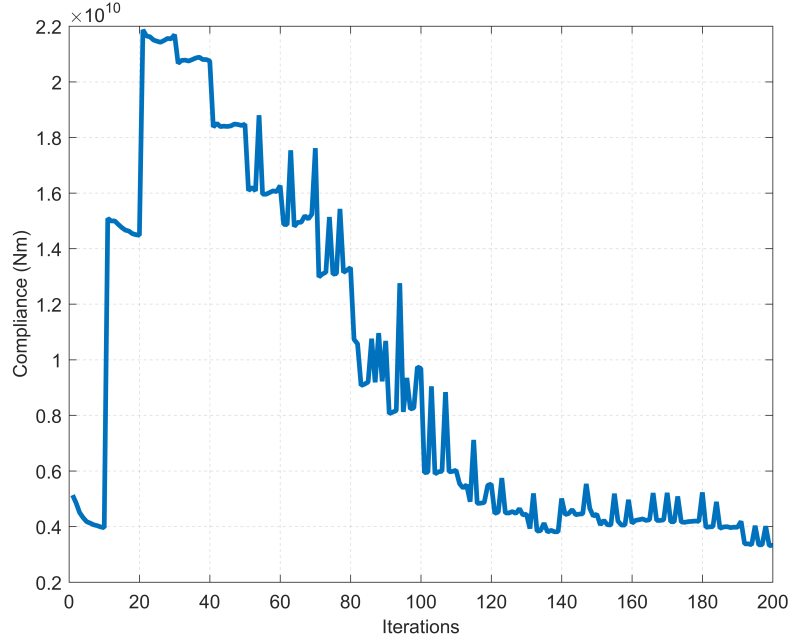


Figure 7. Convergence History for Coupled Problem ($n_{LBM} = 10$)

The step jumps in the compliance occur after the pressure loads are updated by running the LBM. Figure 7 shows that the solution is particularly sensitive in the early iterations and initially updating the loads increases the compliance. However, once the structure starts to converge the jumps become less noticeable and the compliance starts to decrease. The final compliance for the coupled solution is $3.328(10^9)Nm$, which is a 35% reduction from the compliance of the initial structure and a 24% reduction from the uncoupled solution. However, the number of iterations have been increased from 59 to 200, resulting in 20 LBM runs. Therefore, although the structure is improved the computational efficiency has been reduced, as is expected for a coupled solution. The final topology for the coupled problem is shown in Figure 8.



Figure 8. Final Topology for Coupled Case ($n_{LBM} = 10$)

The final topology for the coupled case (Figure 8) differs significantly compared to the uncoupled solution (Figure 5). Namely, the coupled solution has added two larger holes along the mid horizontal

plane, which are not present in the uncoupled case. Further, the holes have become less triangular, reducing the sharp corners in the topology. Nevertheless, there are still some similarities between the two topologies, which increase their stiffness compared to the initial structure. The four small holes have reappeared in the coupled case, though in the coupled case they are smaller. Furthermore, the six holes which are maintained from the initial structure have an overall similar topology between the coupled and uncoupled solutions, with the coupled case reducing the sharpness of the corners. The strain energy distributions on the coupled and uncoupled topologies are given in Figure 9.

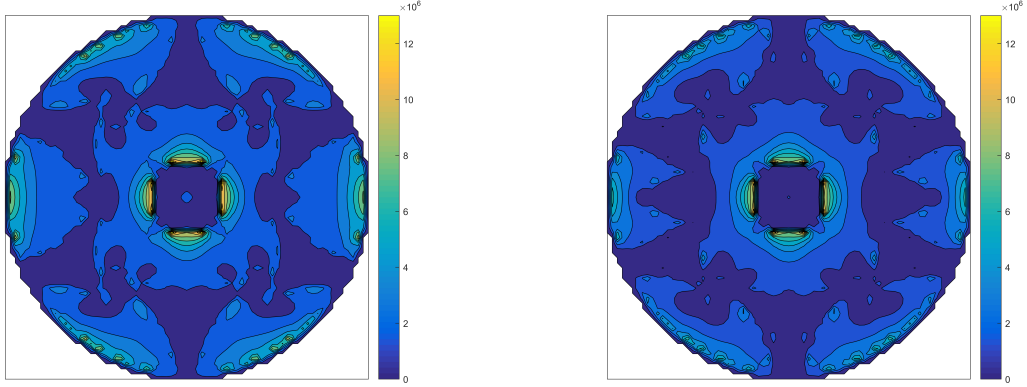


Figure 9. Uncoupled Strain Energy Distribution (left) and Coupled Strain Energy Distribution ($n_{LBM} = 10$) (right)

Figure 9 compares the strain energy distributions of the coupled and uncoupled results, with an equal scaling of the strain energy distribution. The coupled solution further reduces the strain energy concentrations, compared with the uncoupled solution. Therefore, the material is being used more effectively in the optimized structure using a coupled analysis. This indicates that the fluid-structural interactions play an important role in the design of the baffle for the micro fluidic device. Finally, the final design achieved is 24% stiffer than the final design found using the uncoupled framework and 35% stiffer compared to the initial design.

Lastly, the coupled optimization is performed; however, with a Lattice Boltzmann iteration number of $n_{LBM} = 5$ to assess its effect on the optimization of the baffle. The last analysis showed jumps in the objective function when the LBM was solved to update the pressure loads, therefore if the LBM is run more frequently, and hence the topology is less altered between solutions, these jumps should be reduced, reducing the overall number of iterations required for the optimization. The convergence history for the coupled topology optimization problem is given in Figure 10.

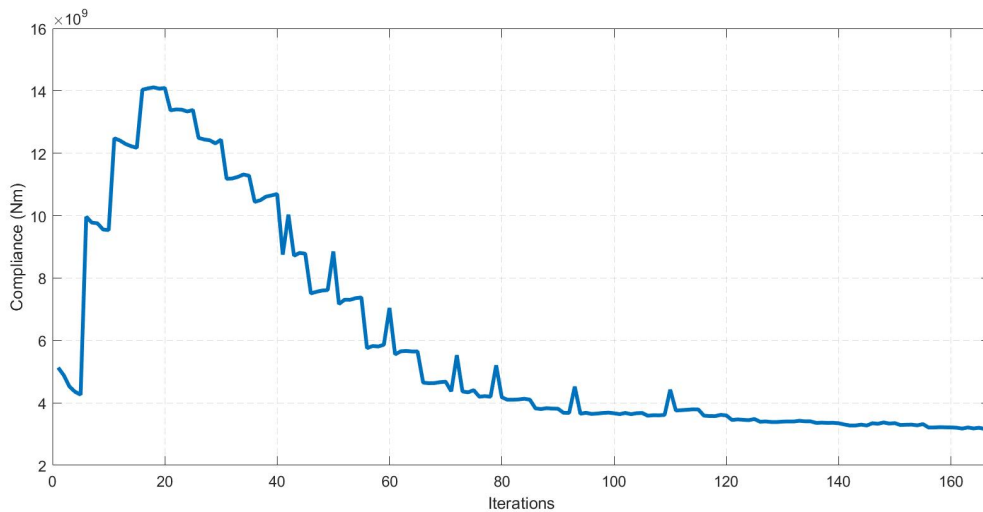


Figure 10. Convergence History for Coupled Problem ($n_{LBM} = 5$).

The step jumps in the compliance after the loads have been updated are still present; however, the magnitude difference of these jumps is reduced compared to the previous case (Figure 7). Further, the solution is still more sensitive to the load updates in the early iterations. This indicates that once the

structure begins to converge the fluid dynamics also converges to a steady solution. The final compliance is determined to be $3.125(10^9)Nm$, which is 39% lower than the initial structure, 28% lower compared to the uncoupled solution and 6% lower than the coupled solution with $n_{LBM} = 10$. Further, the number of iterations has been reduced to 167 compared with 200 for the previous analysis. This confirms the hypothesis of more frequent LBM runs resulting in fewer overall iterations, since the structure does not converge on inaccurate pressure loads for as long. However, because the flow solver is implemented more frequently this results in 33 LBM runs, compared with 20 for the previous analysis. Therefore, although the structure is improved the computational efficiency has been reduced. The final topology for the coupled problem with $n_{LBM} = 5$ is shown in Figure 11.



Figure 11. Final Topology for Coupled Case ($n_{LBM} = 5$).

The final topology for the coupled case with ($n_{LBM} = 5$) (Figure 11) again differs significantly compared to the uncoupled solution (Figure 5); however, it is similar to the coupled solution with $n_{LBM} = 10$ (Figure 8). Again, the coupled solution has added the two larger holes along the mid horizontal plane; however, in this case they are smaller compared with the topology shown in Figure 8. The four small holes are again present in this case, though they are bigger compared with the $n_{LBM} = 10$ coupled solution. Furthermore, the six holes which are maintained from the initial structure have an overall similar topology between all solutions, with the coupled cases reducing the sharpness of the corners. The strain energy distributions on the two coupled topologies are given in Figure 12.

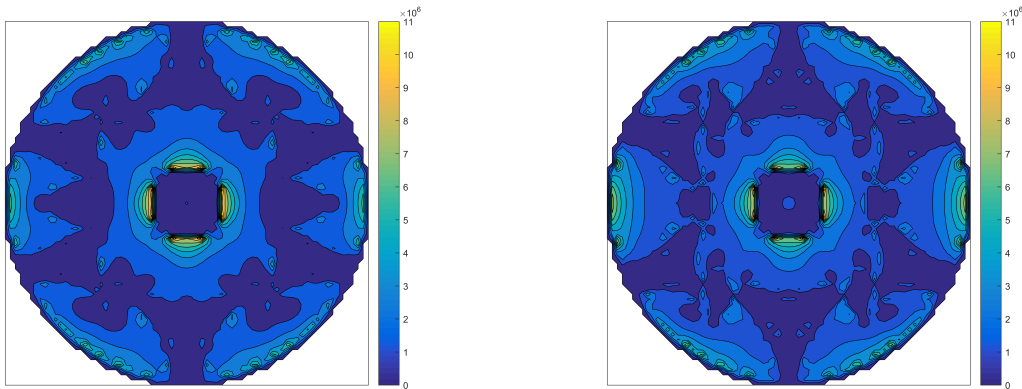


Figure 12. Coupled Strain Energy Distribution ($n_{LBM} = 10$) (left) and ($n_{LBM} = 5$) (right).

Figure 12 compares the strain energy distributions of the two coupled results, with an equal scaling of the strain energy distribution. The $n_{LBM} = 5$ coupled solution further reduces the strain energy concentrations, compared with the $n_{LBM} = 10$ solution. Therefore, the material is being used more effectively in the optimized structure using a coupled analysis with a smaller n_{LBM} . This further indicates that the fluid-structural interactions play an important role in the design of the baffle for the micro fluidic device, since the final design achieved is 6% stiffer than the final design found using the $n_{LBM} = 10$ coupled framework and 39% stiffer compared to the initial design. This is a significant improvement compared with the uncoupled solution, which was only able to increase the stiffness of the baffle by 15%.

From this analysis the fluid-structure interactions have a significant effect on the design of the baffle for the micro fluidic device. The improvement in stiffness was more than doubled when the interactions were included in the optimization. Further, the fewer iterations between LBM runs improves the final design as the structure does not deviate from the optimal flow conditions as much. However, this improvement is less significant than that achieved between the uncoupled and coupled solution. It must be noted that a coupled solution is less computationally efficient as it requires multiple LBM runs to update the fluid dynamics with the change in topology. Finally, fewer iterations between LBM solutions in the optimization algorithm does result in fewer overall iterations, however not in fewer LBM runs. The next section summarizes the key results from the uncoupled and coupled solutions, comparing improvement in the objective function with computational efficiency for the different cases.

III.D. Trade-Off

Finally, the results of the algorithm are summarized, comparing computational efficiency with the optimality of the final structure. The uncoupled results produced the least compliant structure; however, it was able to improve the design compared with the initial configuration. Since, the fluid-structural interactions were not considered and hence the pressure loading was not updated, this case only required one LBM simulation to obtain the initial loads. Further, the number of iterations required for convergence was lower compared with the coupled solutions. Therefore, this represents the most computationally efficient solution possible. This is as expected since the uncoupled case is the simplest and least accurate; it is predictable that increased nonlinearity in the model will increase the number of iterations required to obtain a solution. Thus, if only small improvements are required, towards the end of the design cycle where changes become costly, the uncoupled solution is recommended.

The coupled solutions were also able to improve the design compared with the initial configuration. Furthermore, both coupled solutions represented a significant improvement in compliance compared to the uncoupled structure, with a 24% and 28% increase in stiffness compared with the uncoupled case for the $n_{LBM} = 10$ and $n_{LBM} = 5$ solutions, respectively. However, the coupled results required more iterations to achieve convergence compared with the uncoupled case and a significant increase in the number of LBM simulations. Nevertheless, decreasing the number of iterations between LBM simulations resulted in a decrease in the number of optimization iterations. However, the reduction in iterations was not significant enough to reduce the number of LBM simulations required for the coupled cases. Thus, the coupled framework is beneficial in the conceptual design phase, when multiple structures are being considered. Table 1 summarizes the results of this work.

Table 1. Summary of Results for the Multiple Levels of Coupling

Optimization Method	Minimum Compliance (Nm)	Iterations	Number of LBM runs
Uncoupled	4.361(10^9)	59	1
Coupled ($n_{LBM} = 10$)	3.328(10^9)	200	20
Coupled ($n_{LBM} = 5$)	3.125(10^9)	167	33

IV. Conclusion

A numerical framework for a coupled fluid-structural topology optimization problem has been presented with the baffle plate of a micro fluidic device being optimized. A level set topology optimization algorithm is used due to its discrete nature and hence clear description of fluid-structural boundaries. Previous studies have focused on simplified two dimensional problems due to the intensive computation required. Further, the application of topology optimization to the design of micro fluidic devices has been handicapped by the numerous design iterations required; reducing the problem size so that acceptable execution times are achieved.² The literature shows that topology optimization has been applied to solve many structural and multiphysics problems;³ however, many topics are still open to research, such as design dependent pressure loading.³⁵

An uncoupled analysis was performed with the objective of maximizing the stiffness of the baffle. This analysis proved to be the most computationally efficient, since only one LBM simulation was required. Further the uncoupled problem had the fewest amount of iterations to achieve convergence. The compliance was reduced by 15% from the initial design, thus proving to be a better design without a high computational burden. It was suggested that this analysis would be most beneficial towards the end of the design process when large changes are not permitted.

A coupled analysis was also performed, where the pressure loads on the baffle were updated with the

change in structural topology. Thus, the fluid-structure interactions were considered in the optimization of the baffle; however, this increased the computational burden of the algorithm as multiple LBM simulations are required. Two coupled solutions were performed, with an $n_{LBM} = 10$ and with an $n_{LBM} = 5$. When the number of iterations between LBM runs was decreased a better final solution was achieved, having a reduction in compliance of 39% and 35% compared to the initial design for $n_{LBM} = 5$ and $n_{LBM} = 10$, respectively. Further, the number of iterations required for convergence was reduced from 200 to 167. However, this did not result in a reduction in the computational cost of the algorithm, as more LBM simulations were required. It was suggested that this analysis would be most beneficial at the conceptual phase of the design process when several structural concepts are being considered.

The work presented here brings high fidelity methods, such as Lattice Boltzmann flow simulations, forward to the conceptual/preliminary design stage. Further, multiple disciplines are coupled in a topology optimization analysis to better simulate the physics of the problem to achieve the best possible design. This type of analysis is key for the continued application of topology optimization to real design problems.

Acknowledgements

D. J. Munk thanks the Australian government for their financial support through the Endeavour Fellowship scheme.

References

- ¹Huang, X., and Xie, M., *Evolutionary Topology Optimisation of Continuum Structures: Methods and Applications*, 1st ed., John Wiley and Sons, 2010.
- ²Andreason, C. S., Gersborg, A. R., and Sigmund, O., "Topology Optimization of Microfluidic Mixers," *International Journal for Numerical Methods in Fluids*, Vol. 61, 2009, pp. 498-513.
- ³Sigmund, O. and Maute, K., "Topology Optimization Approaches: A Comparative Review," *Journal of Structural and Multidisciplinary Optimization*, Vol. 48, 2013, pp. 1031-1055.
- ⁴Deaton, J. and Grandhi, R. V., "A Survey of Structural and Multidisciplinary Continuum Topology Optimization: post 2000," *Journal of Structural and Multidisciplinary Optimization*, Vol. 49, 2014, pp. 1-38.
- ⁵Munk, D. J., Vio G. A. and Steven, G. P., "Topology and Shape Optimization Methods using Evolutionary Algorithms: A Review," *Journal of Structural and Multidisciplinary Optimization*, Vol. 52, 2015, pp. 613-631.
- ⁶Edmund, L. and Martins, J. R. R. A., "Structural Topology Optimization with Design Dependent Pressure Loads," *Computational Methods in Applied Mechanical Engineering*, Vol. 233-236, 2012, pp. 40-48.
- ⁷Chen, B. C. and Kikuchi, N., "Topology Optimization with Design-Dependent Loads," *Finite Elements in Analysis and Design*, Vol. 37, 2001, pp. 57-70.
- ⁸Sigmund, O. and Clausen, P. M., "Topology Optimization using a Mixed Formulation: An Alternative Way to Solve Pressure Load Problems," *Computer Methods in Applied Mechanics and Engineering*, Vol. 196, 2007, pp. 1874-1889.
- ⁹Allaire, G., Jouve, F. and Toader, A.-M., "Structural Optimization using Sensitivity Analysis and a Level-Set Method," *Journal of Computational Physics*, Vol. 194, 2004, pp. 363-393.
- ¹⁰Wang, M. Y., Wang, X. and Guo, D., "A Level Set Method for Structural Topology Optimization," *Computer Methods in Applied Mechanical Engineering*, Vol. 192, 2003, pp. 227-246.
- ¹¹Challis, V. J. and Guest, J., "Level Set Optimization of Fluids in Stokes Flow," *International Journal for Numerical Methods in Engineering*, Vol. 79, 2009, pp. 1284-1308.
- ¹²Yamada T., Izui, K., Nishiwaki, S. and Takezawa, A., "A Topology Optimization Method Based on the Level Set Method Incorporating a Fictitious Interface Energy," *Computer Methods in Applied Mechanical Engineering*, Vol. 199, 2010, pp. 2876-2891.
- ¹³Allaire G., "Shape Optimization by the Homogenization Method," *Applied Mathematical Sciences*, Vol. 146, 2002, Springer, New York.
- ¹⁴Osher, S. J. and Sethian, J. A. "Fronts Propagating with Curvature Dependent Speed: Algorithms Based on Hamilton-Jacobi Formulations," *Journal of Computational Physics*, Vol. 79, 1988, pp. 12-49.
- ¹⁵Laniewski-Wollk, L. and Rokicki, J., "Adjoint Lattice Boltzman for Topology Optimization on Multi-GPU Architecture," *Computers and Mathematics with Applications*, Vol. 71, 2016, pp. 833-848.
- ¹⁶Pan, C., Luo, L.-S. and Miller C. T., "An Evaluation of Lattice Boltzmann Schemes for Porous Medium Flow Simulations," *Computers and Fluids*, Vol. 35, 2006, pp. 898-909.
- ¹⁷Lee, T. and Lin, C.-L., "A Stable Discretization of the Lattice Boltzmann Equation for Simulation of Incompressible Two-Phase Flows at High Density Ratio," *Journal of Computational Physics*, Vol. 206, 2005, pp. 16-47.
- ¹⁸Djenidi, L. and Moghtaderi, B., "Numerical Investigation of Laminar Mixing in a Coaxial Microreactor," *Journal of Fluid Mechanics*, Vol. 568, 2006, pp. 223-243.
- ¹⁹Moghtaderi, B., Shames, I. and Djenidi, L., "Microfluidic Characteristics of a Multi-Holed Baffle Plate Micro-Reactor," *International Journal of Heat and Fluid Flow*, Vol. 27, 2006, pp. 1069-1077.
- ²⁰Makhija D., Pinggen, G., Yang, R. and Maute, K., "Topology Optimization of Multi-Component Flows using a Multi-Relaxation Time Lattice Boltzmann Method," *Computers and Fluids*, Vol. 67, 2012, pp. 104-114.
- ²¹Zhou, S. and Li, Q., "A Variational Level Set Method for the Topology Optimization of Steady-State Navier-Stokes Flow," *Journal of Computational Physics*, Vol. 227, 2008, pp. 10178-10195.
- ²²van Dijk, N. P., Maute, K., Langelaar, M. and van Keulen, F., "Level Set Methods for Structural Topology Optimization: A Review," *Structural and Multidisciplinary Optimization*, Vol. 48, 2013, pp. 437-472.

- ²³Allaire, G., Gournay, F., Jouve, F. and Toader, A.-M., "Structural Optimization using Topological and Shape Sensitivity via a Level Set Method," *Control and Cybernetics*, Vol. 34, 2005, pp. 59-80.
- ²⁴Eschenauer, H. A., Kobelev, V. V. and Schumacher, A., "Bubble Method for Topology and Shape Optimisation of Structures," *Structural Optimisation*, Vol. 8, 1994, pp. 42-51.
- ²⁵Yaji, K., Yamada, T., Yoshino, M., Matsumoto, T., Izui, K. and Nishiwaki, S., "Topology Optimization using the Lattice Boltzmann Method Incorporating Level Set Boundary Expression," *Journal of Computational Physics*, Vol. 272, 2014, pp. 158-181.
- ²⁶Bendsoe, M.P. and Kikuchi, N., "Generating Optimal Topologies in Structural Design using a Homogenization Method," *Computer Methods in Applied Mechanics and Engineering*, Vol. 71, 1988, pp. 197-224.
- ²⁷Bendsoe, M.P., "Optimal Shape Design as a Material Distribution Problem," *Structural and Multidisciplinary Optimization*, Vol. 1, 1989, pp. 193-202.
- ²⁸Otomori, M., Yamada, T., Izui, K. and Nishiwaki, S., "MATLAB Code for a Level Set-Based Topology Optimization Method using a Reaction Diffusion Equation," *Structural and Multidisciplinary Optimization*, Vol. 51, 2015, pp. 1159-1172.
- ²⁹Succi, S., *The Lattice Boltzmann Equation for Fluid Dynamics and Beyond*, 1st ed., Oxford University Press, 2001.
- ³⁰Cercignani, C., *Theory and Application of the Boltzmann Equation*, 1st ed., Scottish Academic Press, 1975.
- ³¹Bhatnagar, P. L., Gross, E. P. and Krook, M., "A Model for Collision Processes in Gases. I. Small Amplitude Processes in Charged and Neutral One-Component Systems," *Physical Review*, Vol. 94, 1954, pp. 511-525.
- ³²Chen, S. and Doolen, G. D., "Lattice Boltzmann Method for Fluid Flows," *Annual Review for Fluid Mechanics*, Vol. 30, 1998, pp. 329-364.
- ³³Wolf-Gladrow, D. A., *Lattice-Gas Cellular Automata and Lattice Boltzmann Models*, 1st ed., Springer, Berlin, 2000.
- ³⁴Tsotskas, C., Kipouros, T. and Savill, M. A., "Fast Multi-Objective Optimisation of a Micro-Fluidic Device by using Graphics Accelerators", *Procedia Computer Science*, Vol. 51, 2015, pp. 2237-2246.
- ³⁵Picelli, R., Vicente, W. M. and Pavanello, R. "Bi-directional Evolutionary Structural Optimization for Design-Dependent Fluid Pressure Loading Problems", *Engineering Optimization*, Vol. 47, 2015, pp. 1324-1342.

Incorporation of Bird Strike Requirements in MDO of an Aircraft Wing using Sub-space Metamodels

Jonathan Ollar¹, Royston Jones²,

Altair Engineering Ltd, Leamington Spa, CV32 4JG, United Kingdom

Vassili Toropov³

Queen Mary University of London, London, E1 4NS, United Kingdom

A metamodel based multidisciplinary design optimisation of a conceptual aircraft wing model is presented. The disciplines considered are bird impact at a number of critical locations along the leading edge as well as static bending and twisting stiffness of the wing. The bird strike simulations are many times more costly in terms of computational budget than the static load cases and as 100 sizing design variables are considered the problem may become very expensive. The multidisciplinary design optimisation is carried out using a method previously proposed by the authors for taking into account disparity in design variable dependence of the disciplines. This design variable dependence is specified by the designer and used to build metamodels in only the space of the significant variables to each discipline. This means that the number of required points for each metamodel, and the associated computational cost for their evaluation, can be reduced. The method is implemented within the optimisation framework known as the mid-range approximation method together with a recovery mechanism for erroneous identification of significant variables. It is shown that, by using the proposed approach to take into account the local design variable dependence of the individual bird strike simulations, the optimisation can be carried out to a much reduced computational budget to what would otherwise be required.

1. Introduction

This paper presents an efficient method of incorporating bird strike as well as stiffness requirements in multidisciplinary optimisation of an aircraft wing including 100 sizing design variables. Bird strike simulations are typically several times more costly than stiffness simulations and as the bird can potentially impact the wing at any location along the leading edge, one has to consider several simulations of the bird impacting critical locations in the same optimisation. Furthermore, gradients of the response functions are not available. This makes the computational cost of the bird strike requirements in the multidisciplinary optimisation problem disproportionately large compared to the stiffness requirements.

In this work, advantage is taken of the fact that each bird impact is a local event, influencing only a small part of the wing, and hence only a small number of the design variables. A method, previously proposed by the authors [1–3], for making use of disparate design variable dependence of the individual disciplines in multidisciplinary optimisation is here used to reduce the number of required evaluations, and hence the overall computational budget of the optimisation. Meta-models are built considering only a subset, of the full set of design variables, significant to the individual disciplines. The method relies on the designer to identify the significant variables for each load case through, for instance, engineering judgement or initial ranking studies. However, if such identification is erroneous a recovery mechanism, implemented as part of a trust-region strategy, is used to recover from resulting metamodeling errors by updating the values of the insignificant variables to align with the current best point at the end of each iteration.

¹Research Engineer, Altair ProductDesign & PhD candidate, Queen Mary University of London.

²Exec VP European Operations & Global CTO, Altair ProductDesign.

³Professor of Aerospace Engineering, School of Engineering and Materials Science.

2. Mid-range approximation method

The mid-range approximation method (MAM), also known as the multi-point approximation method, was originally reported by [4, 5] and [6]. The MAM solves a typical constrained optimisation problem in the form:

$$\begin{aligned} & \underset{\mathbf{x}}{\text{minimize}} && f_0(\mathbf{x}) \\ & \text{subject to} && f_j(\mathbf{x}) \leq 1, \quad j = 1, \dots, m \\ & && A_i \leq x_i \leq B_i, \quad i = 1, \dots, n \end{aligned} \quad (1)$$

where $f_0(\mathbf{x})$ is the objective function, $f_j(\mathbf{x})$ is the j -th constraint, \mathbf{x} is the vector of design variables and A_i and B_i are the upper and lower bounds respectively on the design variable x_i . The optimisation problem (1) is replaced by a sequence of approximate sub-problems defined as:

$$\begin{aligned} & \underset{\mathbf{x}}{\text{minimize}} && \tilde{f}_0^k(\mathbf{x}) \\ & \text{subject to} && \tilde{f}_j^k(\mathbf{x}) \leq 1, \quad j = 1, \dots, m \\ & && \left. \begin{aligned} A_i^k &\leq x_i \leq B_i^k \\ A_i^k &\geq A_i \\ B_i^k &\leq B_i \end{aligned} \right\} \quad i = 1, \dots, n \end{aligned} \quad (2)$$

where k denotes the current iteration number. $\tilde{f}_0^k(\mathbf{x})$ is a metamodel of the objective function and $\tilde{f}_j^k(\mathbf{x})$ is a metamodel of the j -th constraint function, both considered valid only in the current trust region. A_i^k and B_i^k are the bounds of the current trust region where the sub-problem (2) is solved for the current iteration. The solution procedure for each sub-problem consists of sampling, creating metamodels, solving the approximate optimisation problem and determining a new location and size of the trust region for the next iteration. The trust region will move and change size after each iteration until the termination criterion is reached. Figure 1 illustrates the history of trust regions through the sequence of sub problems in two dimensions. The trust region strategy has gone through several developments to account for the presence of numerical noise in the response function values [7, 8], occasional simulation failures [9], and improvements for high performance computing [10]. In this work a doe technique based on extensible lattice sequences [11], and a kriging metamodeling technique as outlined in [12], is used.

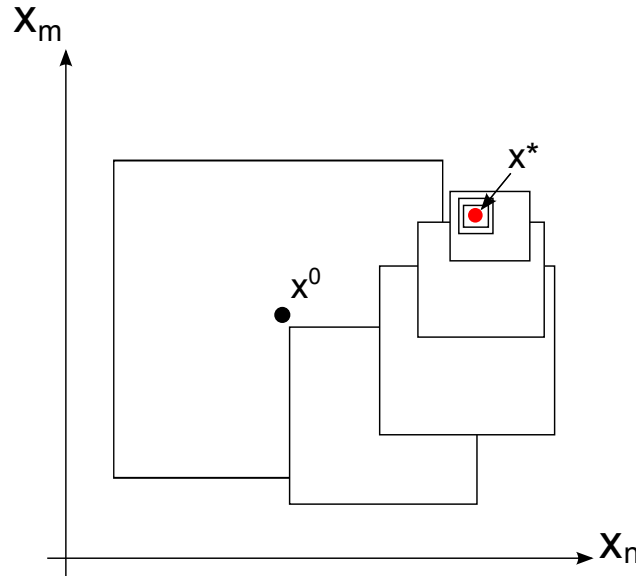


Figure 1: Typical history of the trust regions. In every iteration of the optimization process the new trust region is centered around the current solution and either kept the same size, reduced or enlarged.

3. Sub-space metamodels

Suppose that the responses belonging to a discipline in the MDO problem only depend on a subset of the full set of design variables, i.e. a set of the variables has none or very little influence on the responses of the particular discipline. An example of this from the automotive industry can be seen in Figure 2. The figure shows the results from a simulation of a vehicle subjected to a front crash load case. Each element is coloured according to its level of internal energy. It can be concluded that, as can be expected, the energy absorption is concentrated in the front of the vehicle and is not much affected by the rest of the structure. A conceptual partitioning based on design variable dependence for four common automotive disciplines, *Front Crash*, *Side Crash*, *Rear Crash* and *Noise Vibration and Harshness* (NVH) are shown in Figure 3. With this partitioning discipline-related metamodels, hereafter denoted sub-space metamodels, can be built, depending only on the set of significant variables for each discipline. This method has been presented in several previous publications, e.g. by [13], [14], [1] and [15].

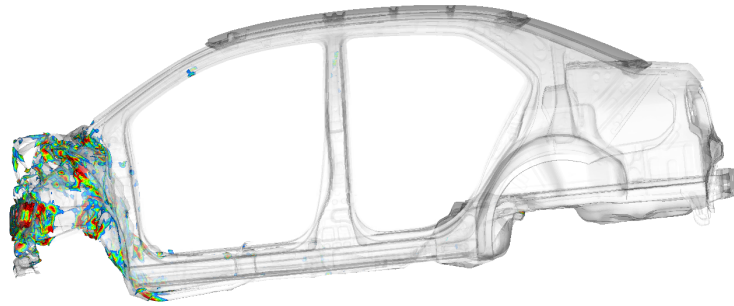


Figure 2: Front crash simulation of an automotive model. Each element is coloured according to its level of internal energy.^a

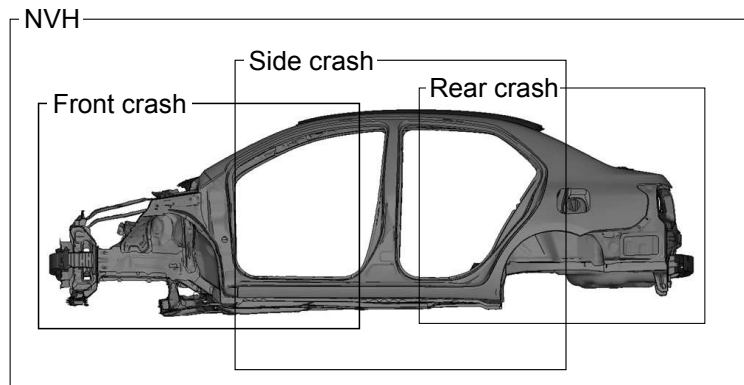


Figure 3: Conceptual partitioning of an automotive model into significant design variable sets related to each discipline

Here a mathematical formulation for introducing sub-space metamodels in metamodel assisted MDO is given. Unlike in previous work, all response functions are assumed to be defined in the full variable space of the optimisation problem in order to control insignificant variables. It will be shown that when sub-space metamodels are used within a trust region framework, this becomes necessary to account for possible deficient assumptions on partitioning.

^aThe model was developed by the National Crash Analysis Center (NCAC), The George Washington University, Washington, USA.

3.1. Formulation of sub-space metamodels

Consider solving the optimisation problem (1) using metamodels. The optimisation problem becomes

$$\begin{aligned} & \underset{\mathbf{x}}{\text{minimize}} && \tilde{f}_0(\mathbf{x}) \\ & \text{subject to} && \tilde{f}_j(\mathbf{x}) \leq 1, \quad j = 1, \dots, m \\ & && A_i \leq x_i \leq B_i, \quad i = 1, \dots, n \end{aligned} \quad (3)$$

where $\tilde{f}_0(\mathbf{x})$ is a metamodel of the objective function and $\tilde{f}_j(\mathbf{x})$ is a metamodel of the j -th constraint function. Given that the design variables in the optimisation problem can be categorised either as significant or insignificant for each related response. A projection can then be defined, for each response j , from the design variable space onto the space of the significant variables. This is denoted as

$$\left. \begin{aligned} \xi_j &= P_j^\xi \mathbf{x} \\ P_j^\xi &: \mathbb{R}^n \mapsto \mathbb{R}^{s_j} \end{aligned} \right\}, \quad j = 0, \dots, m \quad (4)$$

where n is the number of design variables in the optimisation problem and s_j is the number of significant variables for the response j . A projection onto the space of the insignificant variables is defined in the same manner as

$$\left. \begin{aligned} \psi_j &= P_j^\psi \mathbf{x} \\ P_j^\psi &: \mathbb{R}^n \mapsto \mathbb{R}^{n-s_j} \end{aligned} \right\}, \quad j = 0, \dots, m. \quad (5)$$

From here on the projections are described according to the following convention

$$\mathbf{x} = \begin{bmatrix} \xi_j \\ \psi_j \end{bmatrix}, \quad j = 0, \dots, m, \quad (6)$$

noting that the components of ξ_j and ψ_j are present in \mathbf{x} in arbitrary order. The responses in the optimisation problem can then be described as

$$f_j(\mathbf{x}) = f_j \left(\begin{bmatrix} \xi_j \\ \psi_j \end{bmatrix} \right), \quad j = 0, \dots, m \quad (7)$$

where the values of ψ_j can be chosen arbitrarily since they are deemed to be insignificant to the response. The metamodels of the responses may now be defined in the space of only the significant variables which allows a re-writing of the approximate optimisation problem according to

$$\begin{aligned} & \underset{\mathbf{x}}{\text{minimize}} && \tilde{f}_0(\xi_0) \\ & \text{subject to} && \tilde{f}_j(\xi_j) \leq 1, \quad j = 1, \dots, m \\ & && \xi_j = P_j^\xi \mathbf{x}, \quad j = 0, \dots, m \\ & && A_i \leq x_i \leq B_i, \quad i = 1, \dots, n \end{aligned} \quad (8)$$

where each approximated response is defined only in the space of variables that are significant to the response. The optimisation problem, however, is defined in the full design variable space. This has the benefit that as each metamodel is defined only in the space of the significant variables, the sampling of training points only needs to be carried out in that space while the values of the insignificant variables are kept constant.

If the number of significant variables is small compared to the number of design variables, the density of the training points will increase leading to a better quality metamodel as compared to what would have been achieved otherwise. Note that even though there is one projection per response, practicalities may require groups of responses to use the same projection, e.g. due to several responses being evaluated from the same simulation.

3.2. Sub-space metamodels in trust regions

In this section an approach to building sub-space metamodels within the MAM is proposed. A recovery mechanism for erroneous assumptions for sub-space partitioning is also suggested. Sub-space metamodels can be introduced in the MAM framework by re-writing the sequence of optimisation problems (2) as:

$$\begin{aligned}
 & \underset{\mathbf{x}}{\text{minimize}} && \tilde{f}_0^k(\xi_0) \\
 & \text{subject to} && \tilde{f}_j^k(\xi_j) \leq 1, \quad j = 1, \dots, m \\
 & && \xi_j = P_j^\xi \mathbf{x}, \quad j = 0, \dots, m \\
 & && \left. \begin{aligned} A_i^k &\leq x_i \leq B_i^k \\ A_i^k &\geq A_i \\ B_i^k &\leq B_i \end{aligned} \right\} \quad i = 1, \dots, n
 \end{aligned} \tag{9}$$

Note that the mid-range metamodels created in each iteration are here functions of the significant variables only. The significant variables for each discipline are identified by the designer. Such judgement may be based on, for instance, engineering experience or design variable ranking studies. In the previous work by [13], [14], [1] and [15], deficiencies in sub-space partitioning, i.e. by failing to identify a significant variable, can result in metamodelling errors that cannot be resolved by additional sampling. Regardless of how carefully the partitioning of variables is made, there is always a risk that significant variables will be incorrectly identified as insignificant. Therefore a recovery mechanism for such errors is needed. This can be implemented in the trust region strategy by making sure that the values of the insignificant variables for the individual response are updated at the end of each iteration according to the current best point as proposed in [2,3]. Let \mathbf{x}_{k-1}^* denote the solution vector to the previous iteration ($k-1$) for the optimisation problem (9). For each response this can be written in accordance to (7) as

$$\mathbf{x}_{k-1}^* = \begin{bmatrix} \xi_{k-1}^* \\ \psi_{k-1}^* \end{bmatrix}, \tag{10}$$

where ξ_{k-1}^* denotes the projection of the solution vector onto the space of the significant variables and ψ_{k-1}^* onto the space of insignificant variables. The values of ψ_{k-1}^* is then used as the constant values for the

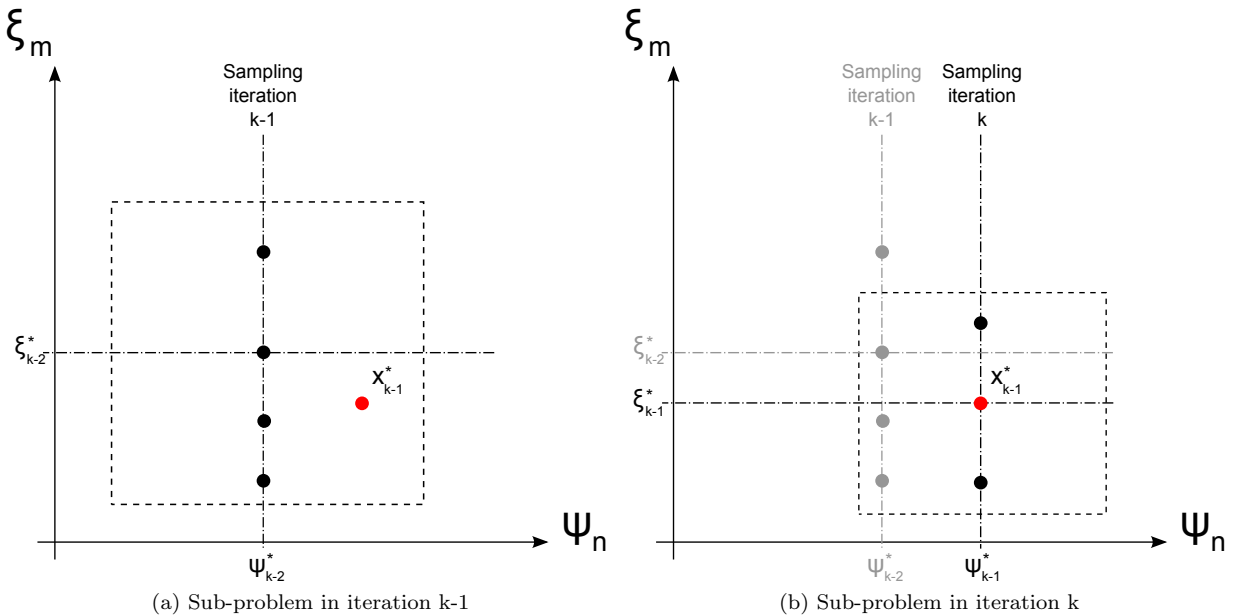


Figure 4: In the sampling for iteration k the values of the insignificant variables are kept constant at the values of the current best point, found in the previous iteration $k-1$.

insignificant variables during sampling in the current iteration, k , according to

$$\psi_k = \psi_{k-1}^*, \quad (11)$$

where ψ_k denotes the values of insignificant variables during sampling. Figure 4 demonstrates how the value of ψ_n changes from the previous iteration to the current for the two dimensional case. The change is due to updating the value according to the current best solution. As the metamodels for the new iteration are built using the sampling including this update, any changes in response values due to changes in insignificant variables from the previous iteration will be taken into account by the metamodels in the current iteration.

4. MDO of an aircraft wing subject to bird strike requirements

This section demonstrates a multidisciplinary optimisation of an aircraft wing structure subject to both stiffness and bird strike requirements. In order to account for all critical locations of bird impact, 10 separate bird strike simulations are considered. Advantage is taken of the local nature of the bird impact with the use of sub-space metamodels. This allows to perform the study to a much reduced computational cost than would otherwise be possible.

4.1. The wing structure

The considered wing is a 3 m long aluminium structure with a root chord of 830 mm and tip chord of 670 mm. It has two longitudinal spars and 11 ribs as shown in Figure 5. The material is precipitation-hardened aluminium (6061-T6) with properties outlined in Table 1.

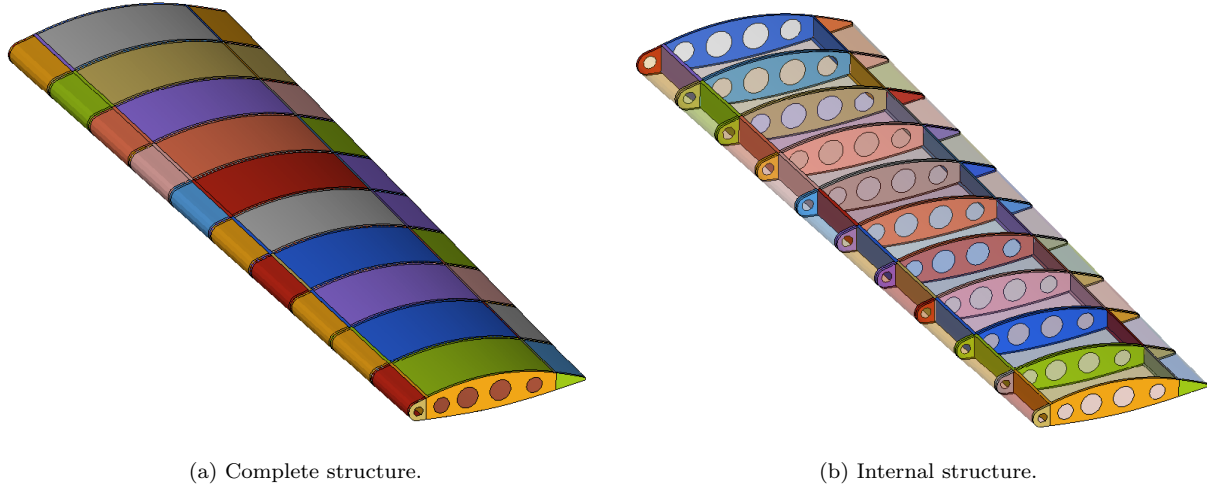


Figure 5: The wing model.

Table 1: Material characteristics for aluminium (6061-T6).

Property	Constant	Value	Unit
Material density	ρ	2.8	g/cm^3
Young's modulus	E	68.3	GPa
Poisson's ratio	ν	0.33	—
Yield strength	σ_y	241.1	MPa
Ultimate tensile strength	σ_u	279.0	MPa

4.2. Linear static model

The stiffness requirements are evaluated using a linear static finite element model. The loading is applied to a single point per rib, which is then distributed to the edges of the rib using one dimensional distributing elements as shown in Figure 6a. The wing is rigidly constrained at the fuselage end of the wing in degrees of freedom 1-3 of the nodes around the edges of the rib as shown in Figure 6b.

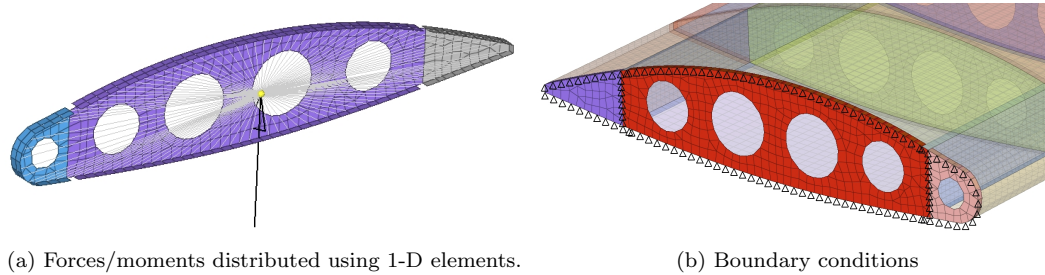


Figure 6: Details on load application and boundary conditions.

Two load cases, shown in Figure 7, are considered. In the first one the wing is bent upwards by applying forces at each of the previously discussed rib loading points. The displacement at the tip of the wing due to the loading is considered as a response. In the second case the wing is twisted by applying moments at the rib loading points. The twist of the wing at the tip, due to the loading, is used as a response. The analysis is carried out using Altair OptiStruct [16] with the assumption of infinitesimal strain theory and isotropic linear-elastic material model. Analytical gradients can be efficiently obtained using the adjoint method.

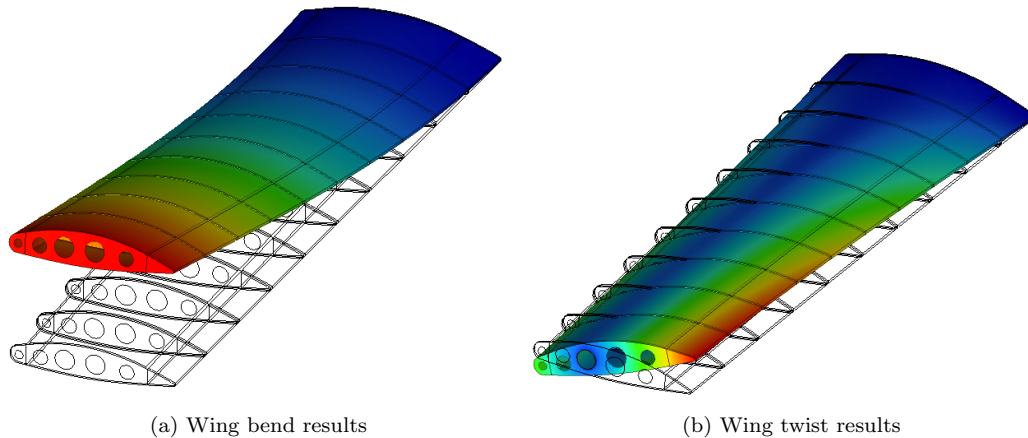


Figure 7: Deformation of the wing for the bend and twist cases.

4.3. Dynamic explicit model

Bird strikes are high speed impact events and are thus evaluated using an explicit time-stepping scheme using Altair RADIOSS [17]. The constitutive model is elasto-plastic with isotropic hardening and failure with parameters according to Table 2. The work-hardening part of the curve is defined using tabular data of plastic strain versus stress, and the failure criterion is defined as a constant rate decrease of stress from the point of maximum tensile failure strain, ϵ_u , until reaching zero stress at the point of maximum tensile failure damage, ϵ_m . The elements are deleted as they reach the tensile strain for element deletion, ϵ_d .

The bird strike requirement is for a 4lb, or 1.81kg, bird impacting the leading edge of the wing at a speed of 150m/s. The bird is modelled using smooth particle hydrodynamics (SPH) which is a meshless Lagrangian method based on interpolation theory. SPH is commonly used to model fluid structure interaction problems where the arbitrary Lagrangian Eulerian (ALE) formulation is expected to fail because of excessive mesh distortion. A bird exhibits fluid like behaviour at high impact speeds and can therefore be modelled realistically using the SPH formulation [18].

Table 2: Parameters of constitutive model for aluminium (6061-T6).

Property	Constant	Value	Unit
Material density	ρ	2.8	g/cm^3
Young's modulus	E	68.3	GPa
Max tensile failure strain	ϵ_u	0.08	—
Max tensile failure damage	ϵ_m	0.12	—
Tensile strain for element deletion	ϵ_d	0.13	—

The bird model, developed by Altair RADIOSS [17], has the shape of a cylinder with hemispherical ends. The radius R is 57 mm which leads to a total volume of 1939 cm^3 . The model contains 41544 cells weighing approximately 0.0437 g each, adding up to a total mass of 1.81 kg and an initial density of 0.935 g/cm^3 . The average distance between neighboring particles is 4.03 mm . The constitutive model is a polynomial equation of state (EOS), representing a hydrodynamic viscous fluid material defined as

$$P = C_1 \cdot \left(\frac{\rho}{\rho_0} - 1 \right) \quad (12)$$

where P is the pressure, $C_1 = 2.106\text{ GPa}$ a material constant (the bulk modulus), and ρ and ρ_0 represents the current and initial density respectively. The properties for the SPH model is summarised in Table 3.

Table 3: Parameters of constitutive model for SPH model.

Property	Constant	Value	Unit
Material density	ρ	0.935	g/cm^3
Bulk modulus	C_1	2.106	GPa
Particle mass	m_p	43.67	mg
Particle distance	h_p	4.03	mm
Number of particles	n_p	41544	—

As the impact location of the bird along the leading edge is arbitrary, several simulations need to be performed altering the impact location. To reduce the number of simulations needed, an assumption that the critical location for bird impact is in the centre of each wing section, between the ribs. This means that in total 10 simulations, with varying start point of the bird as shown in Figure 8a, are to be carried out to assess the requirements for bird strike.

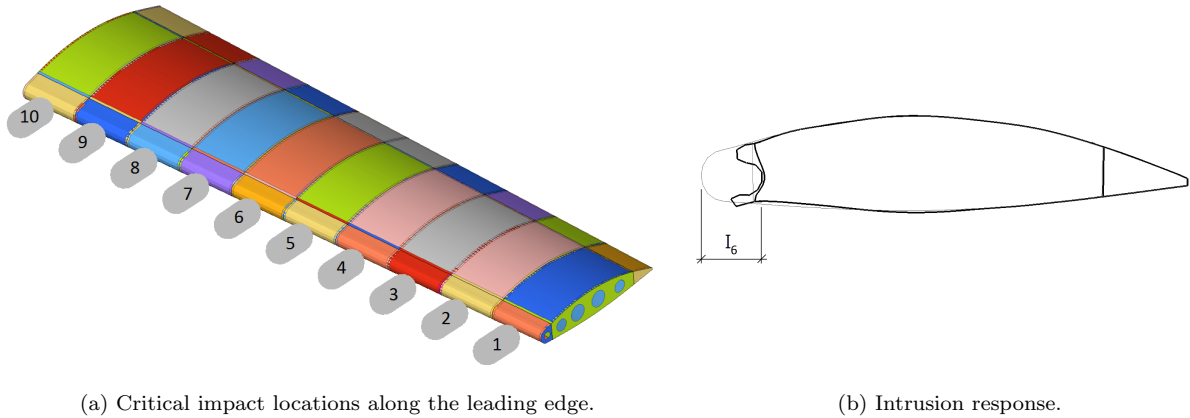


Figure 8: Impact location and response definition.

A bird strike simulation with start position 6 is shown in Figure 9.

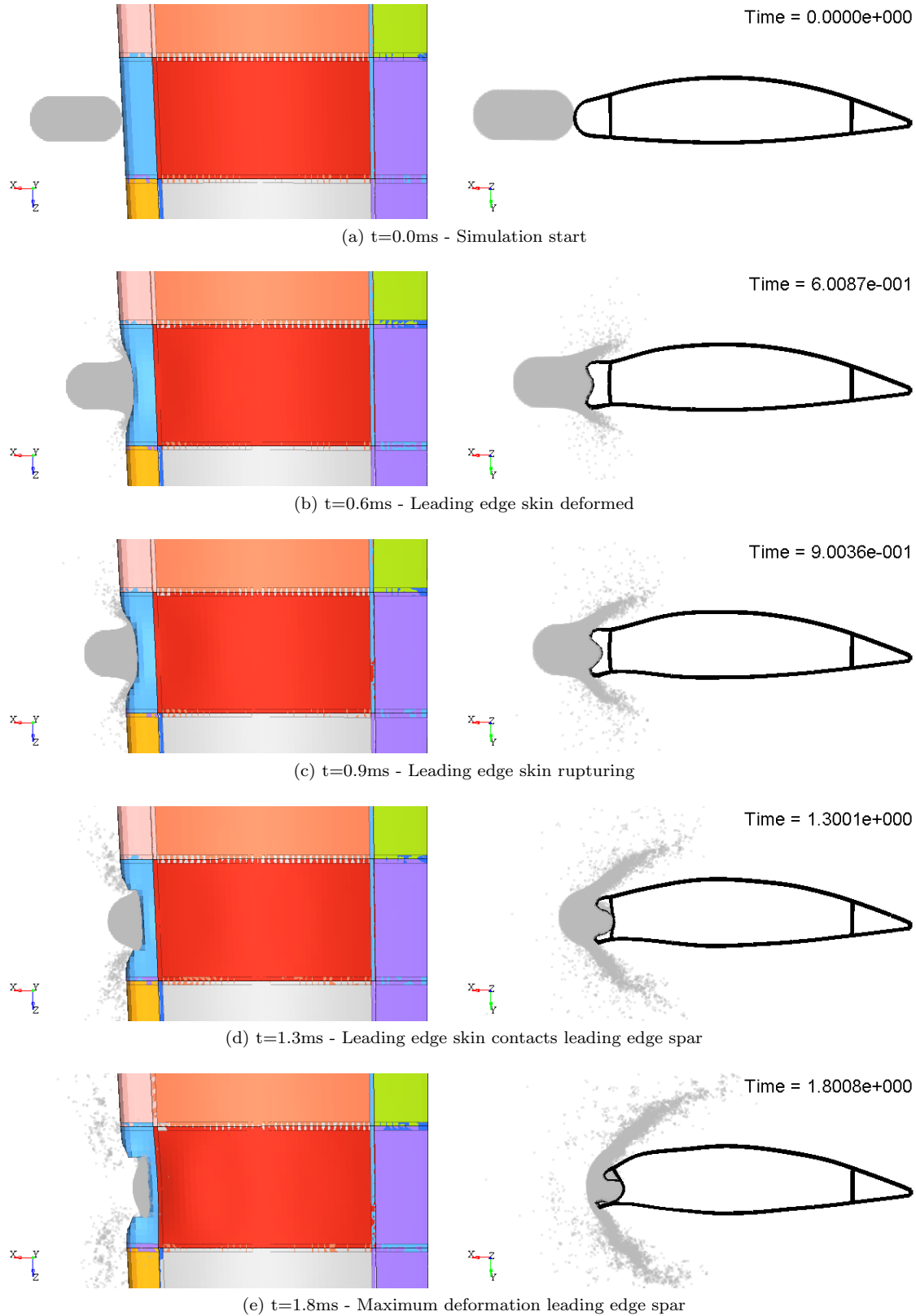


Figure 9: History of the bird strike simulation with starting position 6.

It shows that the bird impacts the leading edge skin which provides the initial energy absorption. The leading edge skin ruptures and makes contact with the leading edge spar which deforms as a consequence. The requirements for the impact is that the structural integrity of the wing is not to be compromised. This is interpreted such that the leading edge skin is allowed to fail, however the leading edge spar must remain intact. In this study the magnitude of intrusion into the wing, measured at the location of impact as shown in Figure 8b are used as constraints.

4.4. Optimisation procedure

The objective of the optimisation is to minimise the weight of the structure subject to meeting the previously discussed structural requirements. The design variables are the thicknesses of the 100 components. The starting thickness for all components are 3 mm with a lower bound of 2 mm and upper bound of 5 mm. Note that the leftmost rib is not designable as in this study it is constrained by boundary conditions.

The minimum number of points required by the MAM per iteration is set to the number of points needed for linear regression, $n + 1$, recalling that n is the number of design variables. It is set to this value regardless of how many points are needed by the chosen metamodel technique, in this case Kriging. It is useful to increase the number of points per iteration slightly in order to obtain better metamodels. The number of desired points per iteration is therefore chosen as $1.5n$. As the stiffness simulations have available gradients, gradient-enhanced metamodel building is used. This allows the number of points per iteration to be significantly reduced. Here the number of points required for simulations that have available gradients is chosen as $1.5n/\sqrt{n}$, resulting in 15 points per iteration. For the bird strike simulations no gradients are available which means that, for 100 design variables, the minimum number of points required is 101 while the desired number is 152. The total number of desired points for the 10 bird strike simulations would hence be 1520 points per iteration, a prohibitively large number.

In this problem sub-space metamodels can be used since the bird strike simulations have local design variable dependence. For each simulation, assumptions are made on which variables are significant to the response. For each impact location of the bird, eight design variables, shown in Figure 10 are assumed to have most of the influence on the response. Other variables may have a slight influence, and could have been considered, but for the price of an increase in computational cost. Instead, any influence from other variables will be taken care of by the recovery mechanism outlined in Section 3.2. This leads to a minimum number of 9 points and a desired number of points of 12 points per simulation and iteration. For the load case where the bird impacts the leading edge skin adjacent to the rigidly constrained rib, there are only 6 significant variables which leads to a minimum of 7 points and a desired number of 9 points. In total, a minimum of 78 and a desired number of 117 bird strike simulations per iteration.

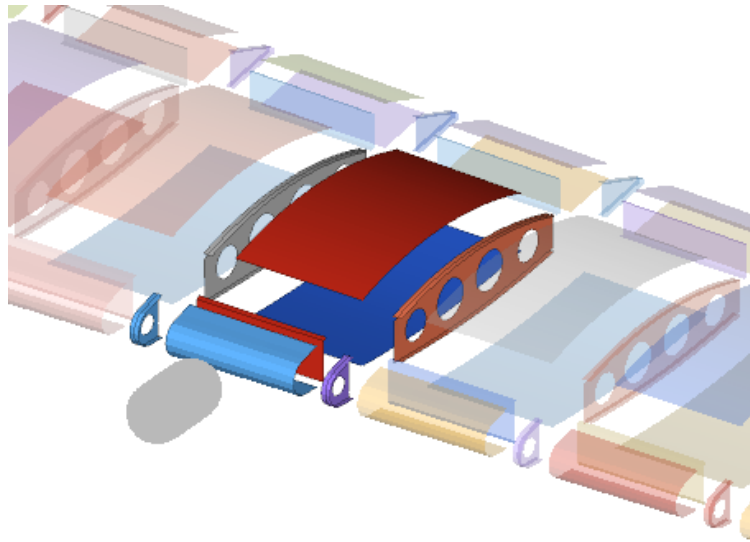


Figure 10: Assumed significant variables for bird at position 6.

4.5. Results

The history of the objective function and constraints during the optimisation are shown in Figure 11. The optimisation finished in 8 iterations, having evaluated 139 stiffness simulations and 1276 bird strike simulations in total for the 10 bird locations, less than would be required per iteration had sub-space metamodels not been used. The final mass is 4.7% less than the initial design and all previously violated constraint violations were reduced to less than 1%. The initial and final response values are shown in Table 4 and the final thickness distribution is shown in Figure 12. From the result it can be noted that none of the panels have gone to the upper thickness of 5 mm, but some to the lower one of 2 mm. Many of the ribs have a resulting thickness which is in the thinner part of the thickness range. This is most likely because of the very simplistic set of static requirement used for the optimisation. As can be expected, all leading edge skins have high thickness whilst leading edge ribs are thinner. This is most likely because the leading edge skin is more likely to rupture if the leading edge rib is less compliant.

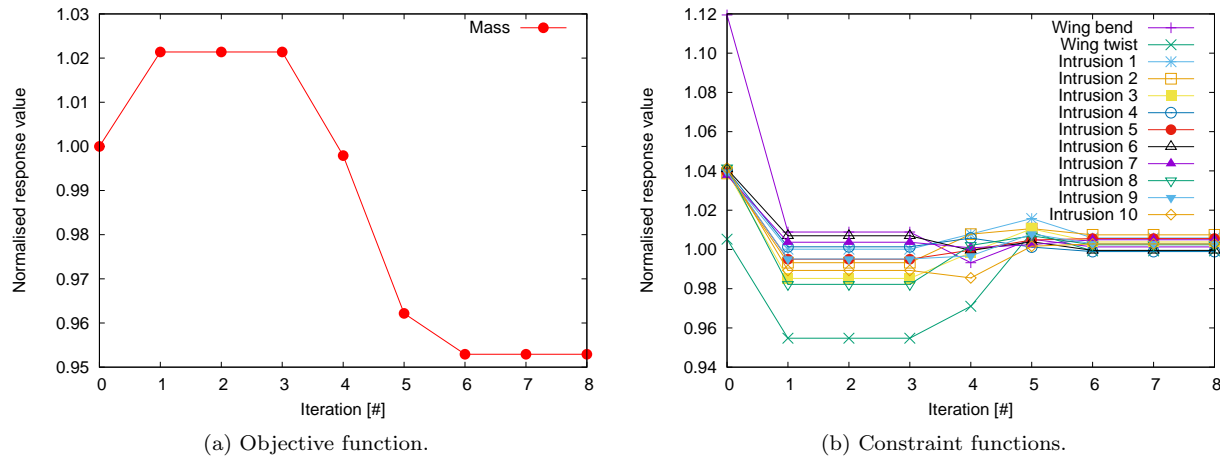


Figure 11: Optimisation history. Objective function is normalised to initial value and constraints are normalised to target.

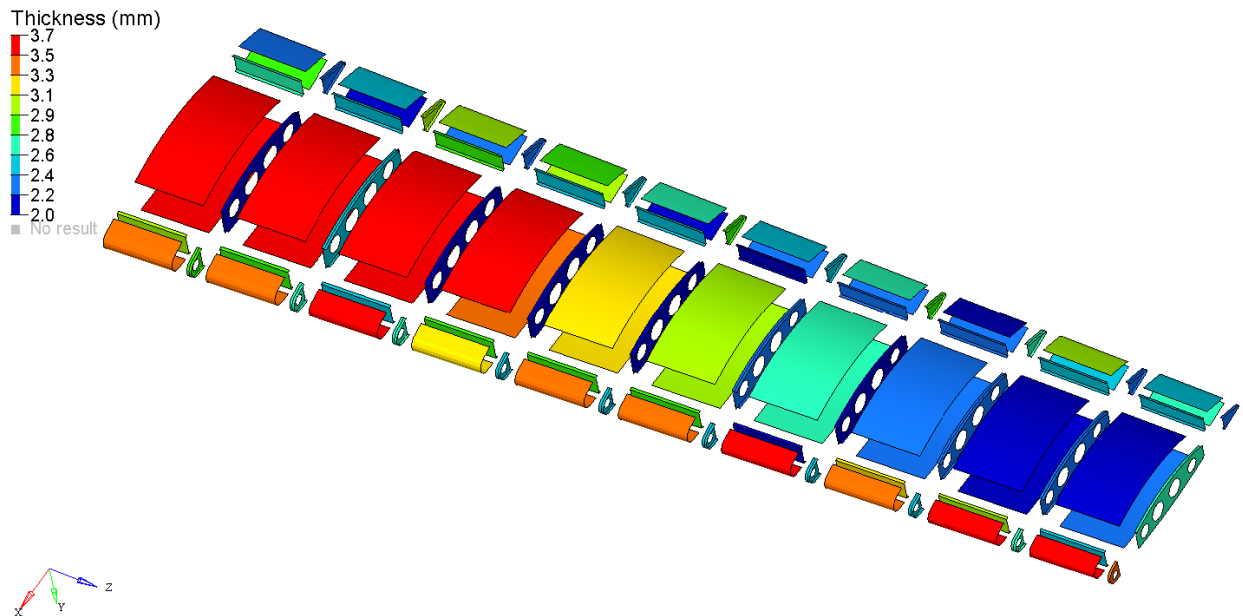


Figure 12: Final thickness for each of the considered components.

Table 4: Results of the optimisations. Objective function is normalised to initial value and constraints are normalised to target.

#	Response	Initial design	Final iteration
1	Mass		−4.7%
2	Wing bend	11.9%	0.1%
3	Wing twist	0.5%	0.0%
4	Intrusion 1	3.9%	0.6%
5	Intrusion 2	3.9%	0.7%
6	Intrusion 3	4.0%	0.4%
7	Intrusion 4	4.0%	0.0%
8	Intrusion 5	3.9%	0.6%
9	Intrusion 6	4.1%	0.0%
10	Intrusion 7	3.8%	0.5%
11	Intrusion 8	4.2%	0.2%
12	Intrusion 9	3.9%	0.3%
13	Intrusion 10	4.1%	0.3%

5. Conclusions

A multidisciplinary design optimisation of a wing structure was carried out. The considered load cases was static bending and twisting stiffness as well as bird strike requirement for impact at 10 locations. The computational cost of evaluation of the bird strike requirements is many times larger than the one of the static requirements. The optimisation was carried out using an approach previously proposed by the authors for solving MDO problems using metamodels built in individual sub-spaces of the design variable space. The approach uses existing knowledge of design variable dependence for each of the disciplines to decrease the number of required evaluations, and hence the related computational budget, in each iteration of a trust-region based optimisation procedure. The optimisation finished in 8 iterations having evaluated 139 stiffness simulations and 1276 bird strike simulations in total, less than would be required per iteration had sub-space metamodels not been used. The final result is a mass save of 4.7% and a reduction of all previously violated constraints to less than 1%.

Acknowledgments

The authors greatly acknowledges funding from European Union Seventh Framework Programme FP7-PEOPLE-2012-ITN under grant agreement 316394, Aerospace Multidisciplinarity Enabling DDesign Optimization (AMEDEO) Marie Curie Initial Training Network.

References

- ¹Ollar, J., Toropov, V., and Jones, R., “Mid-Range Approximations in Sub-Spaces for MDO Problems with Disparate Discipline Attributes,” *15th AIAA/ISSMO Multidisciplinary Analysis and Optimization Conference, Atlanta, GA, USA, July 16-20, 2014.*, 2014.
- ²Ollar, J., Toropov, V., and Jones, R., “Adaptive Sub-Space Approximations in Trust-Regions for Large Scale MDO problems,” *56th AIAA/ASCE/AHS/ASC Structures, Structural Dynamics, and Materials Conference, Kissimmee, FL, USA, January 5-9, 2015.*, 2015.
- ³Ollar, J., Toropov, V., and Jones, R., “Sub-space approximations for MDO problems with disparate disciplinary variable dependence,” *Submitted to Structural and Multidisciplinary Optimization*, 2016.
- ⁴Toropov, V., “Simulation approach to structural optimization,” *Structural optimization*, Vol. 1, No. 1, 1989, pp. 37–46.
- ⁵Toropov, V., *Multipoint approximation method in optimization problems with expensive function values. In: Computational systems analysis 1992: proceedings of the 4th International Symposium on Systems Analysis and Simulation*, No. v. 4, Elsevier, 1992.
- ⁶Toropov, V., Filatov, A., and Polynkin, A., “Multiparameter structural optimization using FEM and multipoint explicit approximations,” *Structural optimization*, Vol. 6, No. 1, 1993, pp. 7–14.

- ⁷van Keulen, F., Toropov, V., and Markine, V., “Recent refinements in the multi-point approximation method in conjunction with adaptive mesh refinement,” *ASME Design Engineering Technical Conferences and Computers in Engineering Conference*, 1996.
- ⁸Toropov, V., van Keulen, F., Markine, V., and de Boer, H., “Refinements in the multi-point approximation method to reduce the effects of noisy structural responses,” *6th Symposium on Multidisciplinary Analysis and Optimization*, 1996.
- ⁹Toropov, V., Markine, V., and Holden, C., “Use of mid-range approximations for optimization problems with functions of domain-dependent calculability,” *3rd ISSMO/UBCAD/UB/AIAA World Congress of Structural and Multidisciplinary Optimization, Buffalo, NY, USA, May 17-21, 1999.*, 1999.
- ¹⁰Korolev, Y., Toropov, V., and Shahpar, S., “Large-scale CFD Optimization based on the FFD Parametrization using the Multipoint Approximation Method in an HPC Environment,” *16th AIAA/ISSMO Multidisciplinary Analysis and Optimization Conference*, 2015.
- ¹¹Hickernell, F. J., Hong, H. S., Lécuyer, P., and Lemieux, C., “Extensible Lattice Sequences for Quasi-Monte Carlo Quadrature,” *SIAM J. Sci. Comput.*, Vol. 22, No. 3, March 2000, pp. 1117–1138.
- ¹²Mortished, C., Ollar, J., Jones, R., Benzie, P., Toropov, V., and Sienz, J., “Aircraft Wing Optimisation based on Computationally Efficient Gradient-Enhanced Kriging,” *57th AIAA/ASCE/AHS/ASC Structures, Structural Dynamics, and Materials Conference, Kissimmee, FL, USA, January 4-8, 2015.*, 2016.
- ¹³Sobieszcanski-Sobieski, J., Kodiyalam, S., and Yang, R., “Optimization of car body under constraints of noise, vibration, and harshness (NVH), and crash,” *Structural and Multidisciplinary Optimization*, Vol. 22, No. 4, 2001, pp. 295–306.
- ¹⁴Kodiyalam, S., Yang, R., Gu, L., and Tho, C.-H., “Multidisciplinary design optimization of a vehicle system in a scalable, high performance computing environment,” *Structural and Multidisciplinary Optimization*, Vol. 26, No. 3-4, 2004, pp. 256–263.
- ¹⁵Ryberg, A.-B., Bckryd, R., and Nilsson, L., “A metamodel-based multidisciplinary design optimization process for automotive structures,” *Engineering with Computers*, Vol. 31, No. 4, 2015, pp. 711–728.
- ¹⁶Altair Engineering, Inc., *OptiStruct 13.0 User’s Guide*, Altair Engineering, Inc., 2014.
- ¹⁷Altair Engineering, Inc., *RADIOSS 13.0 User’s Guide*, Altair Engineering, Inc., 2014.
- ¹⁸Heimbs, S., “Computational methods for bird strike simulations: A review,” *Computers & Structures*, Vol. 89, No. 2324, 2011, pp. 2093 – 2112.

Turbine Stator Well Geometry Benefits – Method Validation and Design Optimisation

Julien Pohl* and Harvey M. Thompson†

School of Mechanical Engineering, University of Leeds, Leeds, LS2 7JT, UK

Vincenzo Fico‡ and Gary A. Clayton‡

Thermo-Fluids Systems, Rolls-Royce plc., Derby, DE24 8BJ, UK

This paper summarises the two part work carried out during project 7 of work package 3 of the EU funded research project AMEDED. At first, the outcome of a practical application and extension of a numerical coupled FEA-CFD methodology is presented. Extensive use is made of FEA (solids) and CFD (fluid) modelling techniques to understand the thermo-mechanical behaviour of a turbine stator well cavity, due to the interaction of cooling air supply with the main annulus. In this investigation, two different geometries (baseline and a deflector plate design) with a specific amount of cooling air are modelled and the impact of the structural deflections on the heat transfer is investigated.

The second part focuses on a CFD-based automated optimisation of a turbine stator well (TSW) geometry with an included stationary deflector plate. Experiments as well as numerical simulations have shown that due to the deflector plate the cooling flow is fed more directly into the disc boundary layer, allowing more effective use of less cooling air, leading to improved engine efficiency. Therefore, the deflector plate geometry is embedded in an automated optimisation loop to further reduce the amount of cooling air. The optimisation strategy concentrates on a flexible design parameterisation of the cavity geometry with deflector plate and its implementation in an automatic 3D meshing system. The parameterised geometry is optimised using a metamodel-assisted approach based on regressing Kriging in order to identify the optimum position and orientation of the deflector plate inside the cavity.

Nomenclature

f	Objective function, [-]
g	Constraint, [-]
\dot{m}_{cool}	Cooling mass flow rate, [kg/s]
n	Number of design variables, [-]
r	Radius, [m]
Re_ϕ	Rotational Reynolds number, [-]
T_m	Metal temperature, [K]
v_θ	Tangential velocity, [m/s]
y^+	Normalised near wall spacing, [-]
\mathbf{x}	Design vector, [-]
β	Swirl fraction, [-]
ω	Rotational speed, [rad/s]
θ_m	Non-dimensional metal temperature, [-]

I. Introduction

Engine components are commonly exposed to air temperatures exceeding the thermal material limit in order to increase the overall engine performance and to maximise the engine specific fuel consumption.

*Marie Curie Fellow and PhD candidate.

†Professor in Computational Fluid Dynamics and academic supervisor.

‡Project partners and specialists in CFD and thermal analyses of secondary air systems.

To prevent the overheating of the materials and thus the reduction of the component life, an internal flow system must be designed to cool the critical engine parts and to protect them. As the coolant flow is bled from the compressor and not used for the combustion an important goal is to minimise the amount of coolant in order to optimise the overall engine performance.

During a typical flight cycle an aero-engine undergoes different operating conditions which cause varying temperatures, pressures, stresses and displacements to the engine components. From an engineering perspective, it is desirable to be able to accurately predict these behaviours in order to stay within the environmental and safety margins and to maximise component life. This also avoids costly experimental engine tests and increases the competitiveness of the aero-engine company in their market.

Predicting the metal temperatures is of paramount importance as they are a major factor in determining the component stresses and lives. In addition, as modern engines operate in ever harsher conditions due to efficiency requirements, the ability to predict thermal displacements becomes very relevant: on one hand, to prevent damage of components due to excessive rubbing, on the other hand, to understand how much air is flowing internally within the secondary air system for cooling and sealing purposes, not only in the design condition but throughout the engine life-span. In order to achieve this aero-engine manufacturers aim to use more and more accurate numerical techniques requiring multi-physics models, including thermo-mechanical finite elements and CFD models, which can be coupled in order to investigate small variations in temperatures and displacements.

This paper summarises the work carried out during project 7 of work package 3 of the EU funded research project AMEDEO (Aerospace Multidisciplinary Enabling DEsign Optimisation)¹ and shows a practical application and extension of the methodology developed during the five year research programme MAGPI (Main Annulus Gas Path Interaction).² Extensive use is made of FEA (solids) and CFD (fluid) modelling techniques to understand the thermo-mechanical behaviour of a turbine stator well cavity, due to the interaction of cooling air supply with the main annulus. Previous work based on the same rig showed difficulties in matching predictions to thermocouple measurements near the rim seal gap.³⁻⁶ In this paper, additional results from two previous studies^{7,8} are presented, where further use has been made of existing measurements of hot running seal clearances in the MAGPI rig. The structural deflections have been applied to two existing models in order to evaluate the impact in flow interactions and heat transfer in the TSW.

In addition to a baseline test case, a geometry with a stationary deflector plate is modelled and validated for one particular flow case. Experiments as well as numerical simulations have shown that due to the deflector plate the cooling flow is fed more directly into the disc boundary layer, allowing more effective use of less cooling air, leading to improved engine efficiency. Therefore, the deflector plate geometry is embedded in a CFD-based automated optimisation loop to further reduce the amount of cooling air. Full details of this process are summarised in the papers of Pohl et al.^{9,10} This work focuses on presenting further results of the same study.

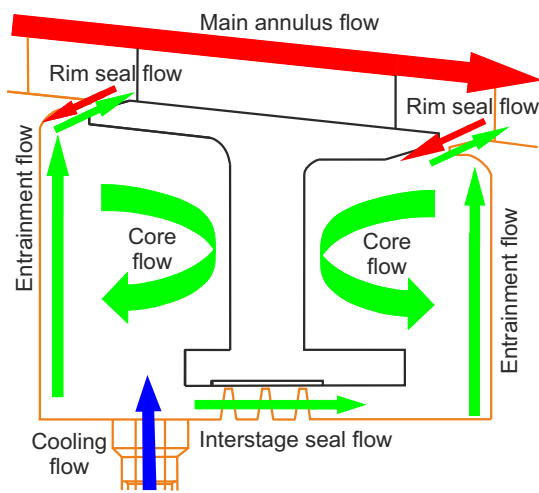


Figure 1. Typical TSW flow structure for the 'baseline geometry'

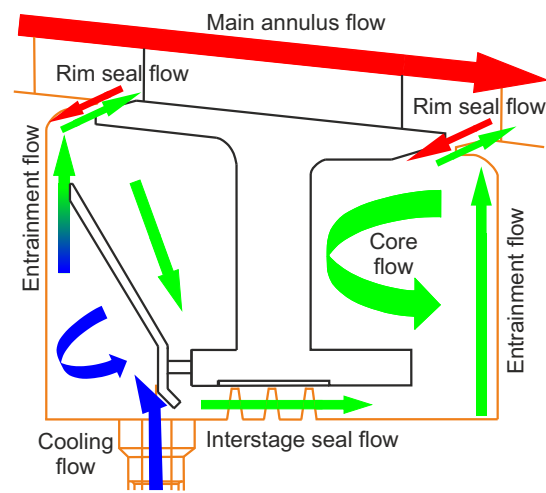


Figure 2. Typical TSW flow structure for the 'deflector geometry'

II. TSW Flow Theory

This section gives an overview of typical flow patterns in two different TSW designs. In Fig. 1, the flow field as it is present in the so called baseline design is shown.⁷ Figure 2 depicts the typical flow scenario in a TSW with an integrated stationary deflector plate,⁹ which is beneficial with respect to the upstream rotor disc cooling compared to a baseline geometry without a deflector plate. The orange and black geometry contour lines represent rotating and stationary parts, respectively.

For both cases, cooling air is introduced into the upstream cavity radially through a drive arm hole. Other than for the baseline geometry, where a traditional rotor-stator flow is formed,¹¹ the cooling air does not penetrate the cavity forming a core flow, but instead impinges the deflector plate and is turned towards the rotor disc, by forming a complex 3D vortex flow structure. The cooling air which reaches the upstream rotor disc is then entrained radially outwards by the rotating part of the turbine. The rim seal flow characterises the mixing zone between the hot gas coming from the main annulus and the cooling air. The interaction of these two flows strongly affects the temperatures inside the cavity. Three different flow scenarios in the two TSW designs can be distinguished depending on the amount of cooling air and the size of the interstage seal clearance:^{12, 13}

Net gas ingestion: If the amount of cooling air is small and/or the interstage seal clearance is large, the rim seal flow is dominated by hot gas entering the cavity.

Net gas egress: If the amount of cooling air is large and/or the interstage seal clearance is tight, the rim seal flow is dominated by cooling air leaving the cavity in the main annulus.

Local ingestion/egress: If the cavity flow is balanced locally hot gas enters the cavity but also cool air enters the main annulus. This phenomenon is driven by the rotor-stator interaction in the main gas path and the turbulent mixing in the rim region.

For both designs, the portion of air/gas mixture staying in the cavity then finds its way to the interstage seal clearance. In the deflector plate design this is guaranteed since the deflector plate is mounted to the stator foot by a few pins, spacers or bolts in order to allow air to pass between these parts, such that the air flow is driven by the presence of a pressure gradient from outer to inner radii between the stator wall and the deflector plate.

Interstage seals are used to reduce the flow of air from the upstream to the downstream stator well cavities. This seal flow is, as mentioned above, largely influenced by the clearance size and also the pressure drop across the seal, which is a function of the upstream and downstream conditions including the pressure drop over the stage in the main annulus. The flow structure in the downstream cavity can then again be described as a traditional rotor-stator flow, consisting of a disc entrainment flow, a core flow and a rim seal exchange flow.¹¹

III. Numerical Modeling and Methodology

This section gives a brief overview of the numerical modeling approach and the numerical methods used for the aerothermal coupling and the automated optimisation. At first details are given for the aerothermal coupling approach, which is used to predict the metal temperatures taking into account of the structural deflections. Then, in the second part, the numerical modeling and the parameterisation for the meta-model assisted optimisation process are briefly presented. For full details reference is made to the publications of Pohl et al.⁷⁻¹⁰

III.A. Aerothermal Coupling

The analysis models are based on the MAGPI two-stage turbine test rig.^{14, 15} Since the turbine was designed to suit the subsequent FEA and CFD analyses, with 39 nozzle guide vanes and 78 rotor blades for each stage, the analysis models could be set-up as sector models at 1/39th of the complete rotor-stator system keeping the accuracy and the computational costs within feasible limits.

The 3D FEA models, shown in Fig. 3 in grey, are 1/39th sectors containing the rotor blade rows and discs, the second stage stator vane and the discs, connecting drive arm and stator foot. The deflector geometry additionally contains the sector of the deflector and one scaled bolt.⁷ The models are set up to run thermally only. The boundary conditions in the regions of the TSW as well as in the rotor 1 blades and stator 2 vane are coupled to the CFD models. The remaining non-coupled boundary conditions are obtained from a matched model against test data. In order to evaluate the impact of the structural deflections on the conjugate heat transfer, the experimentally measured displacements are applied to the different models and run separately.

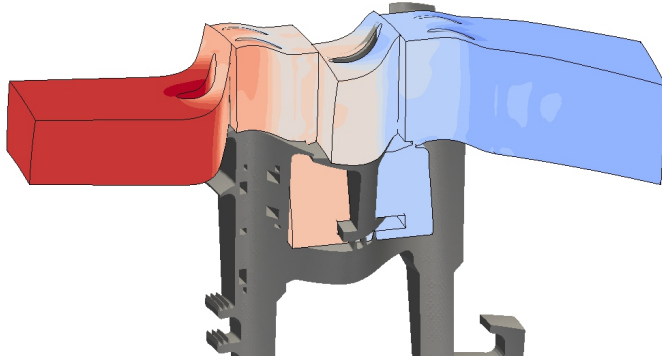


Figure 3. Extent of the 3D CFD sector geometry contoured by total temperature superimposed with the 3D SC03 sector model (grey)

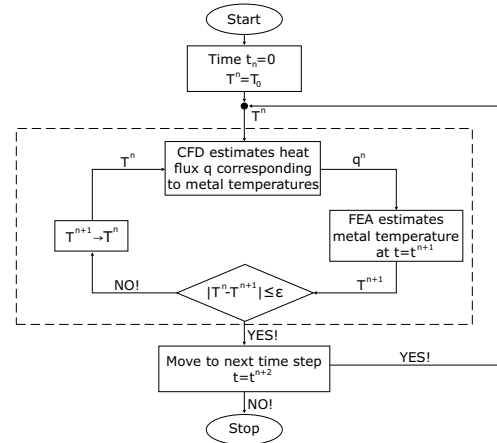


Figure 4. Schematic representation of the aerothermal coupling process

In order to perform the coupled thermal analyses, 3D CFD models are created fitting the extent of the 3D FEA. Therefore, four grids are generated to discretise the two relevant geometries. At first, each case is meshed using the cold running clearances. In a second step, the experimentally measured radial deflections obtained from the experiments are applied to both geometries and then meshed. The extent of the obtained 3D CFD sector model coloured by total temperature can be seen in Fig. 3, as it is superimposed to the FEA model.

The computational domain is meshed using the Rolls-Royce in-house automatic meshing tool PADRAM (Parametric Design and Rapid Meshing).¹⁶ For both designs, the main annulus and the baseline cavity, high fidelity, fully multi-block structured meshes are produced, whereas for the deflector plate cavity hybrid unstructured meshes are generated. Adequate mesh size and topology sensitivity studies were conducted as reported in previous works.^{7,17} Grids of around a million cells per vane, plus four million cells in the baseline cavity and five million cells for the deflector plate cavity are created. The connections at the rim between the main annulus and the cavities are achieved in a conformal way. Details on the modelling approaches and the mesh convergence for both geometries can be found in the studies of Dixon et al.³ and Pohl et al.,⁷ respectively.

The commercial code FLUENT is used, for which the RANS equations are solved using second order finite volume discretisation of the domain in double precision. The $k-\omega$ SST turbulence model proposed by Wilcox¹⁸ is used after having been employed successfully in re-ingestion and FEA-CFD coupled studies by Guijarro et al.¹⁹ and Dixon et al.³ $y^+ < 1$ values are achieved in order to accurately resolve the viscous sublayer and heat transfer. Each case is run in a steady-state condition where the communication between stationary and rotating reference frames is achieved by mixing planes. The convergence of the numerical simulations is primarily assessed by monitoring residuals of mass, energy, and momentum equations and secondarily by checking mass balance (smaller than 0.1 % discrepancy) and enthalpy balance (smaller than 3 % discrepancy) of the converged solution.

The results presented here are based on the thermal coupling between the in-house FEA solver SC03 and the commercially available CFD code FLUENT. Both codes communicate through a Rolls-Royce proprietary library. It is within this functionality that the user specifies one or more coupled walls, outlining a CFD domain, which may cover a part or the whole of the finite element model. A schematic illustration of the process is depicted in Fig. 4, whilst a more detailed description is given by Verdicchio et al. for any CFD code application.²⁰

III.B. Optimisation Strategy

The optimisation is conducted using the Rolls-Royce SOPHY system (SOFT, PADRAM, HYDRA).²¹ SOFT (Smart Optimisation For Turbomachinery)²² provides a library of different optimisation algorithms and communicates through python scripts with the other codes in order to execute them in batch mode, to evaluate the results of the simulation. In general, these computations are run in parallel on an HPC cluster in order to reduce the overall run time.

The geometry used in this work is also based on the MAGPI rig test facility as described above. In order to keep the computational requirements within the capability of available computer facilities, it was decided to reduce the size of the discretised domain to a minimum. As in the previous numerical study on the original deflector plate geometry,⁷ in this work a 1/39th sector model is chosen, which is a reasonable approximation due to the periodicity of the 78 blades and 39 vanes per stage. Furthermore,

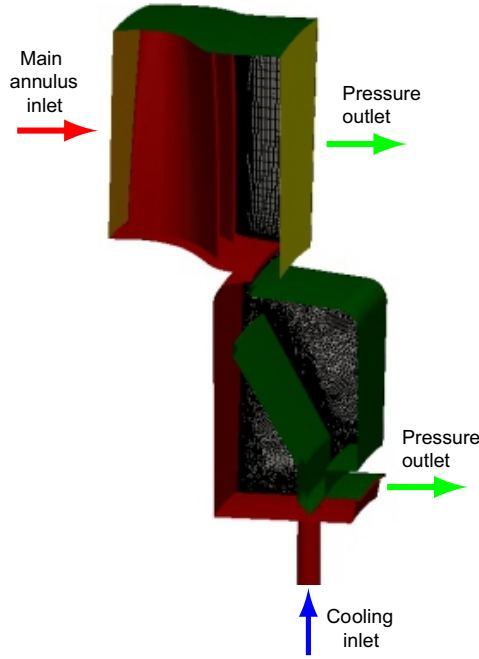


Figure 5. Extent of the 3D CFD sector model used during the design optimisation

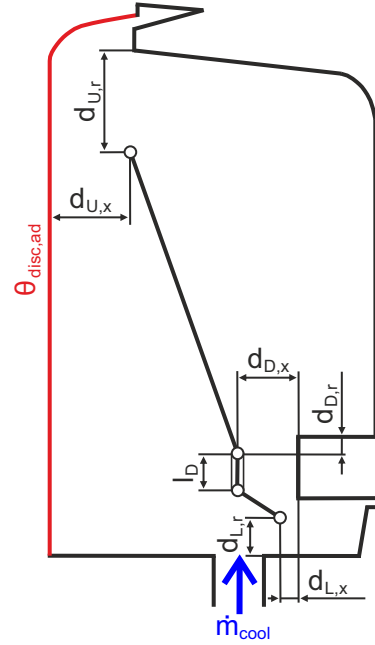


Figure 6. Parametric definition of the deflector plate inside the cavity

the two stage domain is reduced to only one rotor blade pair from the first stage and the upstream cavity including the deflector plate until the first fin of the interstage seal (see Fig. 5).

The mesh is generated as described in the previous section. At this stage the Rolls-Royce in-house CFD code HYDRA is used to solve the RANS equations using a second order finite volume discretisation of the domain in double precision. Following the recommendation of previous computational validation studies,^{4,8,10,19} the turbulence closure was done using the $k - \omega$ turbulence model with adaptive wall functions of Launder and Spalding²³ in the regions where the near wall resolution was large.

The cooling air inlet is defined as a mass flow inlet with a fixed temperature. The inlet for the main annulus is defined as a pressure inlet, where the total pressure is read across from the solution of the complete main annulus. The same approximations are taken for the outlets in the main annulus and the fin, where the static pressure distributions are taken from the full sector model run.

The walls are defined as adiabatic, to keep the computation within a reasonable time scale. During the early design phase of the MAGPI test rig, similar stand-alone adiabatic CFD simulations were carried out to get an idea of the impact on the disc temperature using different geometries and varying amounts of cooling air.¹⁷

The cavity geometry and the rotor geometry are not changed in this study. Only the shape and the position of the deflector plate are modified. The parameterisation of the deflector plate is done in 2D and is shown in Fig. 6. In total seven geometrical design parameters are defined:

- $d_{U,x}$ and $d_{U,r}$, which define the axial and radial degree of freedom of the upper point
- $d_{D,x}$, which defines the axial distance of the vertical bar to the stator foot
- $d_{D,r}$, which defines the radial degree of freedom of the point connecting the upper section to the vertical bar with respect to the outer radii of the stator foot
- l_D , which defines the length of curve vertical bar
- $d_{L,x}$ and $d_{L,r}$, which define the axial and radial degree of freedom of the lower point

In order to finally setup the automated optimisation loop, an objective function as well as the constraints have to be defined, both depicted in Fig. 6 by the blue arrow and the red contour line, respectively. The objective of this optimisation is to minimise the cooling air mass flow rate entering the cavity through the drive arm hole and defined as follows:

$$f(\mathbf{x}) = \dot{m}_{cool} \quad (1)$$

with \mathbf{x} being the design vector consisting of eight design parameters (seven geometrical and one for the cooling air mass flow rate). Also one constraint $g_j(\mathbf{x})$ is defined (see Fig. 6):

$$g_j(\mathbf{x}) = \theta_{disc,ad}^{max} - \theta_{disc,ad,j} \geq 0 \quad (2)$$

where $\theta_{disc,ad}^{max}$ is the non-dimensional maximum allowable area mean adiabatic wall temperature at the disc and $\theta_{disc,ad,j}$ the computed value for a particular design j . The maximum value is taken from the results of a numerical simulation of the baseline geometry without a deflector plate and an initial cooling mass flow rate of 55gs^{-1} , which is set to $100\% \dot{m}_{cool}$ in this study.

The actual optimisation is based on regressing Kriging and is described in detail in the papers of Pohl et al.^{8,9} The computation is conducted in parallel, where each CFD simulation is run on 24 cores.

IV. Results

In this section the results of the two studies are presented and discussed. At first, the impact of structural deflections on the metal temperature predictions is presented, which is followed by the results of the automated design optimisation.

IV.A. Impact of Structural Deflections on Metal Temperature Predictions

At first, the test case for the baseline geometry is evaluated which is followed by the evaluation of the test case with an included deflector plate. Both geometries are run at cold and hot running clearances in order to highlight the structural impact on the TSW heat transfer. The results of the aerothermal coupling for both designs with cold and hot clearances are shown in Figs. 7 and 8. On the left hand side the temperature predictions for the cold geometry are shown, in the middle the metal temperatures for the hot one. As the differences are hard to distinguish from these two separate representations, a difference plot for each flow case is illustrated on the right hand side of the same figure. The difference is taken by subtracting the cold from the hot solution.

Analysing the baseline case first (Fig. 7), it can be seen that the differences in temperature between the cold and hot geometry are locally significantly different. This is in particular the case in the upstream rim region at both the rotor and the stator. These differences propagate along the stator foot to lower radii. The remaining rotor parts are almost at an identical temperature regardless the choice of the seal clearance. This can be explained with local hot gas ingestion into the upstream cavity, which then penetrates the cavity along the stator once the interstage seal opens. As the amount of hot gas ingestion is only minor compared to the amount of coolant, the core flow is marginally affected and so is the rotor disc temperature.

As for the baseline design, the deflector geometry with cold and hot clearances is analysed using the coupled conjugate heat transfer method. The metal temperature contours for both seal clearances (cold on the left and hot in the middle) and the respective difference plot (right hand side) is represented in Fig. 8.

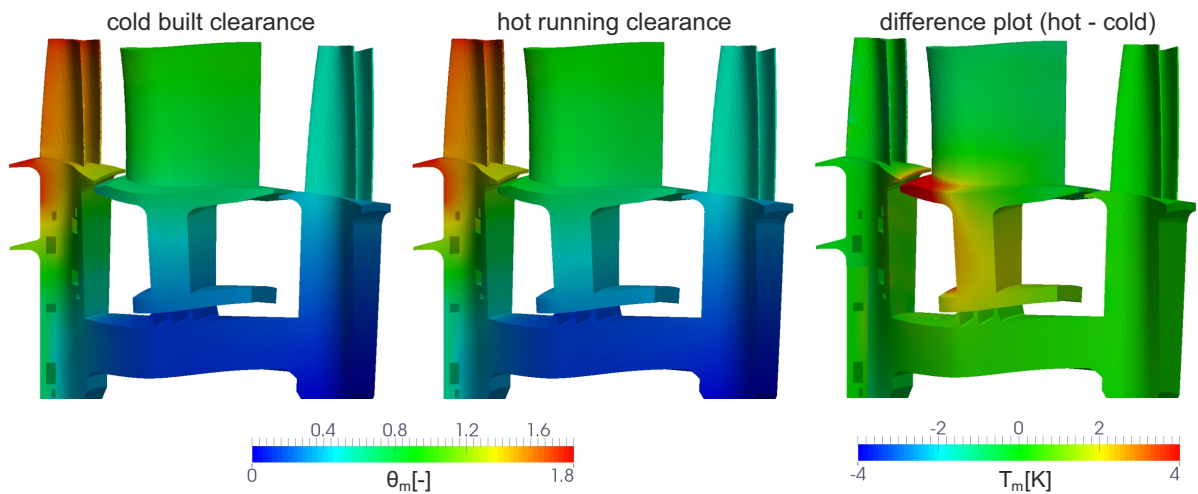


Figure 7. Metal temperature contours of the baseline design for the cold (left) and hot geometries (middle) including the respective temperature difference contours (right)

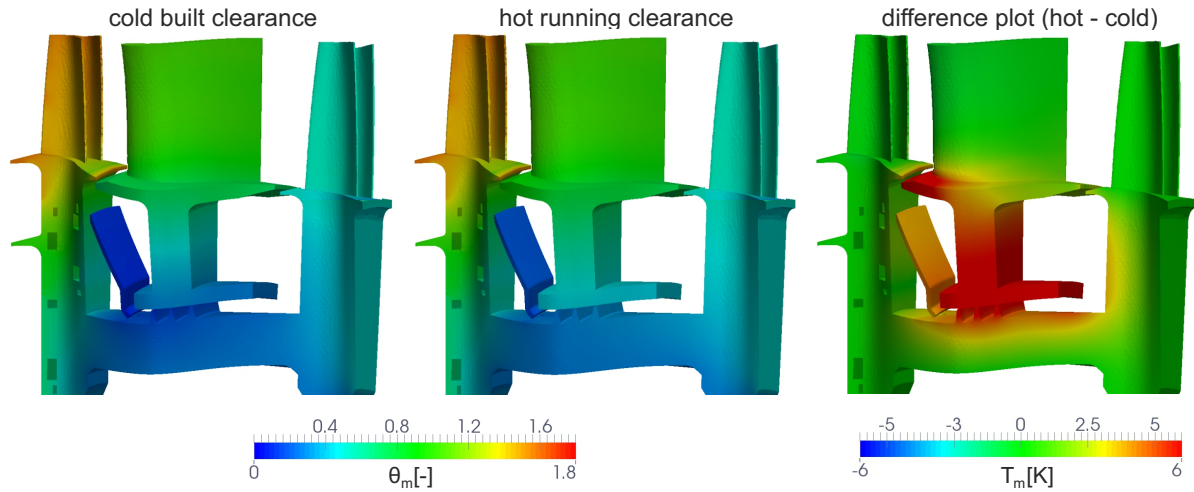


Figure 8. Metal temperature contours of the deflector plate design for the cold (left) and hot geometries (middle) including the respective temperature difference contours (right)

Compared to the baseline simulation, the impact of taking into account the structural deformations on the metal temperature predictions is more significant. The rim as well as the stator foot are significantly hotter when using the hot running clearance. Furthermore, the rotor rim is hotter as well as the interstage seal fins. However, the upstream rotor disc is only marginally affected. Again, these higher temperatures can be associated to the local hot gas ingestion, which is present when opening the interstage seal.

Both comparisons of these results against experimental test data showed that the predictions matched the experiments better¹⁰ due to the shift to higher values, which is related to the hot gas ingestion. This is particularly true along the stator. Slight improvements are also achieved at the rotor disc. However, the discrepancies at the rotor rim are still in an unacceptable range. An explanation for this mismatch is the lack of accuracy of steady-state CFD to predict the turbulent mixing in the rim region. Therefore, in future it is recommended to use unsteady CFD or higher order turbulence models such as LES rather than steady-state CFD in order to correctly predict the rotor rim temperatures.

IV.B. Optimisation Results

In this section, first steady-state adiabatic CFD analyses are carried out in order to evaluate the optimised TSW flow field with a reduced amount of cooling air and then the outcome of the optimisation is validated. Furthermore, this new flow field is compared against the flow field of the non-optimised design with the same amount of coolant. By doing this, the main advantages of the new design are highlighted.

In a second part, a back-to-back comparison of the metal temperatures of the optimised and non-optimised design with a reduced amount of cooling air is carried out. This is done to gain more confidence in the current optimisation methodology, where stand-alone CFD simulations are used to improve the metal component cooling. Furthermore, the comparison highlights the main differences between the optimised and non-optimised deflector design at a reduced coolant flow rate.

A comparison of the flow fields of the optimised deflector plate design (top) against the non-optimised (bottom) with respect to the position and shape based on the findings from the optimisation^{8,9} can be seen in Fig. 9: the upper tip of the deflector is moved close to the rotor disc, whereas the lower parts are moved close to the stator foot. The depicted mid-plane cuts are surface LIC (i.e. line integrated convolution) representations contoured by swirl fraction β ($= v_{\theta}/(\omega r)^{-1}$). Both simulations are run with a reduced cooling mass flow rate of $0.35 \dot{m}_{cool}$.

For the optimised deflector plate geometry, it can be seen that the cooling air enters the cavity swirled at disc speed ($\beta = 1$) and keeps its swirl as long as it does not impinge the deflector plate. This maintenance of swirl due to the position of the deflector close to the stator foot is beneficial for the cooling performance of the disc. Considering the non-optimised deflector, the cooling air loses all its swirl quickly after entering the cavity even before impinging the deflector.

Another interesting phenomenon can be seen at the lower tip of the deflector plate, where - for the optimised design - part of the highly swirled cooling air seems to move to the interstage seal straight away without cooling the disc. This ensures that the gap between the deflector lower tip and the rotor wall is sealed against hot gas coming from higher radii. This is not the case for the non-optimised geometry.

A comparison of mass flow rates passing the gap between the upper deflector plate tip and the rotor

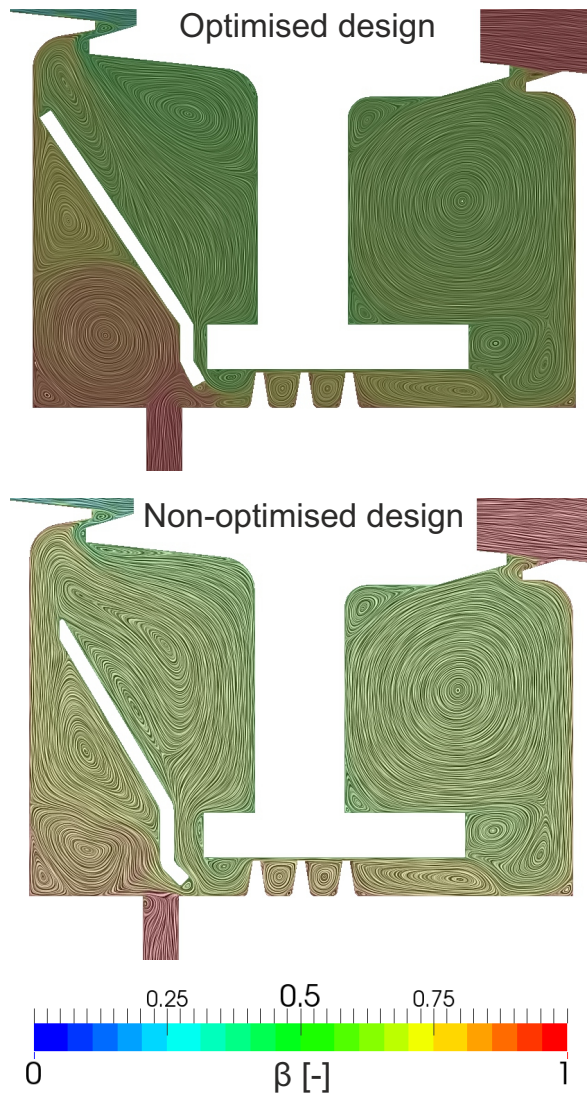


Figure 9. Surface LIC representation contoured by swirl fraction for the optimised (top) and non-optimised (bottom) deflector plate design with the minimised cooling mass flow rate

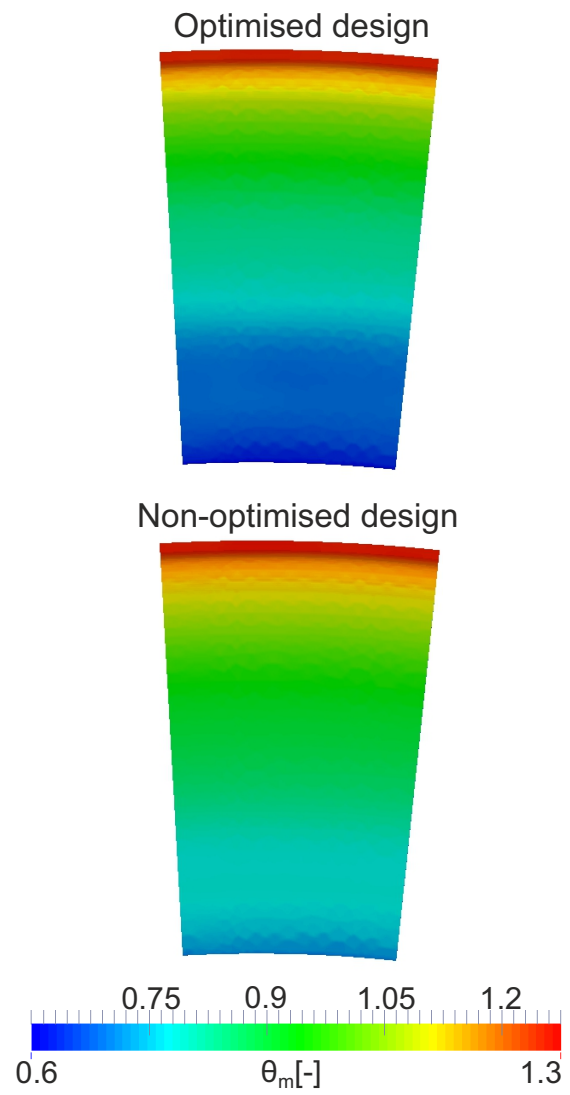


Figure 10. Comparison of the non-dimensional metal temperatures at the upstream rotor disc for the optimised (top) and non-optimised (bottom) deflector plate design with the minimised cooling mass flow rate

disc shows a significant difference in the two designs and supports the previous assumptions: for the optimised deflector plate a mass flow rate of around $0.28 \dot{m}_{cool}$ passes the gap whereas for the non-optimised design the mass flow rate is $0.76 \dot{m}_{cool}$. This indicates that, for the optimised design, a portion of cooling air is used to seal the gap at the lower tip from hot gas recirculation and in the non-optimised design a significant amount of hot gas is recirculated instead. This should also reflect in the rotor disc temperatures.

In Fig. 10, the rotor disc metal temperature contours obtained from the aerothermal coupling for both cases are depicted. On the top the contours for the optimised deflector plate design are depicted and on the bottom for the non-optimised design, both at a reduced coolant mass flow rate. From these two plots it can be seen that the optimised deflector design provides a better disc cooling, which one could already infer from the swirl contours.

Having said that, it can be concluded that the optimisation converged to a better deflector design, keeping the rotor disc cool while reducing the amount of cooling air. However, a large amount of hot gas enters the cavity, which inevitably results in a heatup of the metal of the stationary components. Also it is worth mentioning that the simulations are run with a constant interstage seal clearance only. The thermo-mechanical impact of the stator heating on the interstage seal clearance is not considered although this would need to be taken into consideration in any real engine design (as covered in the previous section).

V. Conclusion

In this paper two separate studies are presented. At first the impact of structural deflections on the heat transfer in TSWs is analysed using cold and hot interstage seal clearances, which were obtained from experiments. A fully automated FEA-CFD coupling capability was demonstrated and results from two different models were compared.

It was found that the use of hot running clearances results in an increase of stator metal temperatures inside the TSW, which are in better agreement with the experimental measurements. However, the discrepancies in the rotor rim region still persist in the predictions. It will be desirable to incorporate unsteadiness and higher order turbulence models in the CFD solution. Findings in previous works^{7,19} showed how the flow unsteadiness caused by the rotor-stator interaction modifies the rotor downstream wakes and therefore the turbulence mixing near the rim gap.

In the second part, an automated design optimisation using Kriging of a 3D sector model of a TSW test rig geometry with an inserted stationary deflector plate has been carried out. The geometry has been parameterised in such a way that flexibility of the design is ensured: different shapes and positions of the deflector plate inside the cavity have been generated automatically.

The outcome of the optimisation using adiabatic steady-state CFD has shown that the optimised design provides better rotor disc cooling than the non-optimised design. This outcome has been verified using the coupled FEA-CFD method to compare metal temperatures for the new design to those for the non-optimised design. These results were in agreement with the stand-alone CFD results.

For future work in this research area, some recommendations are given here. When applying this method to real engine running conditions, the thermo-mechanical movements are very important. Not only, is it likely that a variation in seal size affects the final flow solution, but also the very extreme positions of the deflector should be chosen very carefully in order to prevent rubbing and damage at the most critical running conditions.

Acknowledgements

The present investigations were supported by the European Commission within the AMEDEO Marie Curie initial training network (grant reference 316394) and the authors want also to thank the European Commission for its support within the Framework 6 Programme, Research Project MAGPI, AST5-CT-2006-030874 for the use of the test rig geometry.

A special mention must be made to Rolls-Royce staff Christopher Barnes, Shahrokh Shahpar and Ralf Schlaps for their support as well as Jeff Dixon for his technical advice.

References

- ¹AMEDEO, 2013. Aerospace Multidisciplinary Enabling Design Optimisation. Grant reference: 316394.
- ²MAGPI, 2006. Main Annulus Gas Path Interaction - Specific Targeted Research Project. Proposal Contract no.: 30874.
- ³Dixon, J. A., Guijarro-Valencia, A., Coren, D., Eastwood, D., and Long, C., 2014. "Main Annulus Gas Path Interactions - Turbine Stator Well Heat Transfer". *J Turbomach*, **136**, February, pp. 021010–1–16.
- ⁴Smith, P. E. J., Muggleston, J., Tham, K. M., Coren, D. D., and Long, C. A. "Conjugate Heat Transfer CFD Analysis in Turbine Disc Cavities". *ASME Turbo Expo GT2012-69597*.
- ⁵Andreini, A., DaSoghe, R., and Facchini, B., 2011. "Turbine Stator Well CFD Studies: Effects of Coolant Supply Geometry on Cavity Sealing Performance". *J Turbomach*, **133**, April, pp. 021008–1–11.
- ⁶Lück, H., Schäfer, M., and Schiffer, H.-P. "Simulation of Thermal Fluid-Structure Interactions in Blade-Disc Configuration of an Aircraft Turbine Model". *ASME Turbo Expo GT2014-26316*.
- ⁷Pohl, J., Fico, V., and Dixon, J. A., 2015. "Turbine Stator Well Cooling - Improved Geometry Benefits". In *ASME Turbo Expo 2015*, GT2015-42658.
- ⁸Pohl, J., Thompson, H. M., Guijarro Valencia, A., López Juste, G., Fico, V., and Clayton, G. A. "Structural Deflection's Impact in Turbine Stator Well Heat Transfer". *to appear in J Eng Gas Turb Pow.*
- ⁹Pohl, J., Thompson, H. M., Schlaps, R. C., Shahpar, S., Fico, V., and Clayton, G. A., 2016. "Innovative Turbine Stator Well Design Using Design Optimisation". In *16th ISROMAC & 1st ISIMET*.
- ¹⁰Pohl, J., Thompson, H. M., Schlaps, R. C., Shahpar, S., Fico, V., and Clayton, G. A. "Innovative Turbine Stator Well Design Using a Kriging Assisted Optimisation Method". *to appear in J Eng Gas Turb Pow.*
- ¹¹Daily, J. W., and Nece, R. E., 1960. "Chamber Dimension Effects on Induced Flow and Frictional Resistance of Enclosed Rotating Disks". *J Basic Eng-T ASME*, **82**, pp. 217–232.
- ¹²Phadke, U. P., and Owen, J. M., 1988. "Aerodynamic Aspects of the Sealing of Gas Turbine Rotor-Stator Systems - Part 1: The Behaviour of Simple Shrouded Rotating Disk Systems in Quiescent Environment". *Int J Heat Fluid Flow*, **9**, pp. 98–105.
- ¹³Phadke, U. P., and Owen, J. M., 1988. "Aerodynamic Aspects of the Sealing of Gas Turbine Rotor-Stator Systems - Part 2: The Behaviour of Simple Seals in Quasi-Axisymmetric External Flow". *Int J Heat Fluid Flow*, **9**, pp. 106–112.
- ¹⁴Eastwood, D., Coren, D. D., Long, C. A., Atkins, N. R., Childs, P. R. N., Scanlon, T. J., and Guijarro-Valencia, A., 2012. "Experimental Investigation of Turbine Stator Well Rim Seal, re-Ingestion and Interstage Seal Flows Using Gas Concentration Techniques and Displacement Measurements". *J Turbomach*, **134**, August, pp. 082501–1–9.

- ¹⁵Eastwood, D., 2014. "Investigation of Rim Seal Exchange and Coolant Re-Ingestion in Rotor Stator Cavities Using Concentration Techniques". PhD thesis, University of Sussex, Sussex, UK.
- ¹⁶Shahpar, S., and Lapworth, L., 2003. "PADRAM: Parametric Design and Rapid Meshing System for Turbomachinery Optimisation". *Power-Gen International*, **6**, pp. 579–590.
- ¹⁷Dixon, J. A., Guijarro-Valencia, A., Bauknecht, A., Coren, D., and Atkins, N., 2013. "Heat Transfer in Turbine Hub Cavities Adjacent to the Main Gas Path". *J Turbomach*, **135**, March, pp. 021025–1–14.
- ¹⁸Wilcox, D. C., 1998. *Turbulence Modeling for CFD*. DCW Industries.
- ¹⁹Guijarro-Valencia, A., Dixon, J. A., Soghe, R. D., Facchini, B., Smith, P. E. J., Muñoz, J., Eastwood, D., Long, C. A., Coren, D., and Atkins, N. R. "An Investigation Into Numerical Analysis Alternatives For Predicting Re-Ingestion in Turbine Disc Rim Cavities". *ASME Turbo Expo GT2012-68592*.
- ²⁰Verdicchio, J. A., 2001. "The Validation and Coupling of Computational Fluid Dynamics and Finite Element Codes for Solving Industrial Problems". PhD Thesis, University of Sussex, Sussex, UK, July.
- ²¹Shahpar, S., 2005. SOPHY: An Integrated CFD Based Automatic Design Optimisation System. Report No. ISABE-2005-1086.
- ²²Shahpar, S., 2002. "SOFT: A New Design And Optimisation Tool for Turbomachinery". In CIMNE 2002, K. G. et al., ed.
- ²³Launder, B. E., and Spalding, D. B., 1974. "The Numerical Computation of Flows". *J Comp Meth Appl Mech Eng*, **3**, pp. 269–289.

Development of a Process Workflow for Simulation of a Gas-Liquid Cyclone Separator with Uncertainty Quantification in an Open-Source Environment

Animesh Ranjan^{*}

Department of Mechanical Engineering, Technical University of Ingolstadt, Ingolstadt, Germany.

Swami S Venkat[†]

Department of Mechanical Engineering, RWTH Aachen, Aachen, Germany.

Romit Maulik[‡]

Department of Mechanical Engineering, Oklahoma State University, Stillwater, Oklahoma, USA.

Flaviu Bogdan[§]

Department of Civil Engineering, Bauhaus University, Weimar, Germany.

Cyclone separation is a technique to separate particulate matter or a given gaseous phase from a fluid jet using rotational effects and gravitational forces. They are employed in sawmills, oil refineries, cement industries and is also the fundamental principle of several everyday appliances such as vacuum cleaners. The categorical utilization of Cyclone separators has prompted a deeper understanding of an otherwise complex phenomena. With the advent of advanced CFD approaches and enhancement of computational resources, fluid flow in a cyclone separator can be understood beyond basic analytical methods such as Stokes' law. The paper discusses the intricacies of a 3D fluid flow simulation in a Gas Liquid Cylindrical Cyclone Separator (GLCC) using OPENFOAM. It also addresses the uncertainties in the boundary conditions, turbulence models and other flow parameters and seeks to achieve improved correlation between experiment and CFD simulation. An axisymmetric model is also developed and tested for correlation with experimental results. The overall results show reasonable agreement between experiment and simulation and could pave way for greater understanding of the physical phenomena in GLCC separator and numerical simulation or physical design optimization of the GLCC structure

Nomenclature

GLCC	=	Gas-Liquid Cyclone Separator
DoE	=	Design of Experiments
KE	=	Kinetic Energy
ALHS	=	Advanced Latin Hypercube Sampling
OF	=	Openfoam
CFD	=	Computational Fluid Dynamics

Communicating Author: animesh.ranjan@gmx.net

^{*}Research assistant

[†]Research assistant

[‡]PhD Candidate.

[§]Scientific Investigator.

I. Introduction

A Gas Liquid Cyclone Separator is employed widely in the Oil and Gas industries, especially in Oil refineries to facilitate phase separation. The mechanism causing separation of phases includes gravitational forces and rotational (centripetal and Coriolis) forces. The underlying mechanistic models cannot predict phase fraction at separation and pressure/velocity changes. In order to capture the complex flow behavior within a cyclone separator and facilitate design development and optimization, a CFD simulation needs to be carried out. An outline of the complex flow phenomena in a cyclone separator is shown in Figure 1. The wet and dry steam, illustrated here, flow through an inlet channel and assume a tangential velocity as they enter the separator domain. The high velocities of the two phases lead to centripetal forces and swirling flow which further leads to separation of the two fluids. Due to density differences and buoyancy forces, the dry steam separates and exits through the upper slot while wet steam is removed through the lower outlet. There might be, however, dry steam bubbles trapped in wet steam or water droplets carried through by the gaseous phase and they might exit along with the continuous phase at the respective outlet. This phenomenon is referred to as gas carry-under and liquid carry-over respectively. Such phenomena along with several others are beyond the scope of most mechanistic models [1]

The flow field within a Cyclone separator needs to be correctly captured using a CFD-simulation software. In this paper, the employed software is OPENFOAM. OPENFOAM is capable of simulating 2D and 3D single and multi-phase flow simulations. The various objectives of the study are:

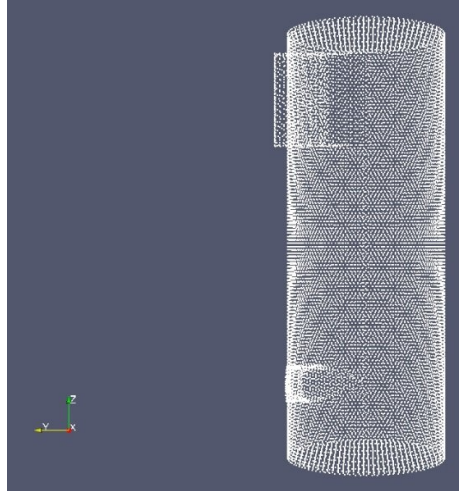


Figure 1: A geometrical representation of a Cyclone Separator

- Successfully simulating a 3D single-phase simulation
- Successfully generation of an axisymmetric model and subsequent 2D single phase simulation
- Stochastic study for estimation of best - fit OPENFOAM and ANSYS parameters to experimental data.

CFD equations comprise of the mass and momentum conservation equations. Problems involving thermal effects also include the energy equation, used either to estimate energy lost/gained by system or compute temperature in non-isothermal problems. It also accounts for coupling between velocity and temperature fields in the flow domain. Fluid flow behavior is largely associated with the momentum equation which includes a diffusive and a convective part. Reynolds number, a constant representing the degree of convection in the fluid, can be used to predict flow patterns in a given domain. At low Reynolds number, where the diffusive action of the fluid is dominant, the reduction of fluid kinetic energy is faster and fluid flow is laminar. On the other hand, turbulent flow occurring at high Reynolds number represents a more chaotic flow regime comprising of flow vortices, energy dissipation and varying scales of vortex generation. [2]

II. Numerical Simulation

A Gas Liquid Cylindrical Cyclone (GLCC) Separator, consists of an inlet and one or more outlets. The fundamental principle of a GLCC is generation of a swirl velocity, resulting in a centrifugal force leading to separation of liquid - gas interfaces through lower and upper openings respectively. Liquid carry-over and/or Gas carry - under might be prevalent in some cases but they are ignored in the current study. Since the study aims to compare the simulation results with OPENFOAM, Flotran with ANSYS CFX and experimental results, the geometrical characteristics used in Erdal et al will be reproduced here and the mesh/boundary conditions will be applied to the same geometry. The mesh characteristics, however, may vary depending on the ease of mesh generation and/or accuracy of results

The process flow developed by Erdal et al included the usage of ANSYS CFX as a single, multi - phase solver for liquid, gas - liquid mixture respectively. The meshing was presumably carried out using ANSYS mechanical which allowed for a generation of a uniform, hexahedral mesh. In order to replicate the process in OPENFOAM, the process - chain has to be briefly discussed since OPENFOAM has been used as a primary solver for the project but the pre - processing and post - processing tasks have been executed using third-party

standalone programs which allow importing, exporting OPENFOAM relevant data. Figure 2 shows the employed work - flow for the given project with Salome and Paraview being the asset programs.

Geometry creation and meshing operations have been carried out using Salome, an open-source tool with OPENFOAM solver-readable data export capability. Due to limitations of efficient meshing algorithms and limited handling of open source software, a perfect hexahedral mesh for complex geometries may not be entirely possible or could turn out to be a time or cost - intensive process. Instead, a tetrahedron mesh was generated and to account for accuracy of the model, the number of elements was significantly increased compared to the total number of hexahedral elements in Erdal et al.

In order to evaluate the 3D single phase model, a process - flow is required which sequentially considers and includes model complexity and can simultaneously be used to evaluate the accuracy of turbulence models in the current study. The model considered here is the RANS or (Reynolds Averaged Navier Stokes) turbulence models, namely, k-epsilon and k-omega SST models are evaluated. The process - flow for model evaluation is shown in fig 3. The laminar flow solution is useful to identify the complexity of the model and to confirm the need for a turbulence model. The laminar problem is followed by evaluation of the model with a series of turbulence models to arrive at the most optimum model for the given application. Although it has been mentioned by Erdal et al that the k-epsilon model could be used to evaluate the given problem statement, there is a need to re-consider the model assumptions and evaluate a certain number of existing turbulence models before further processing of the problem.

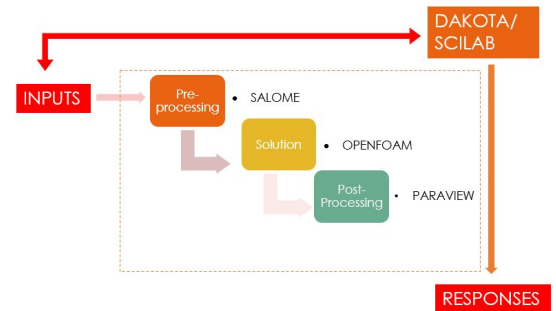


Figure 2: Illustration of Process - Workflow

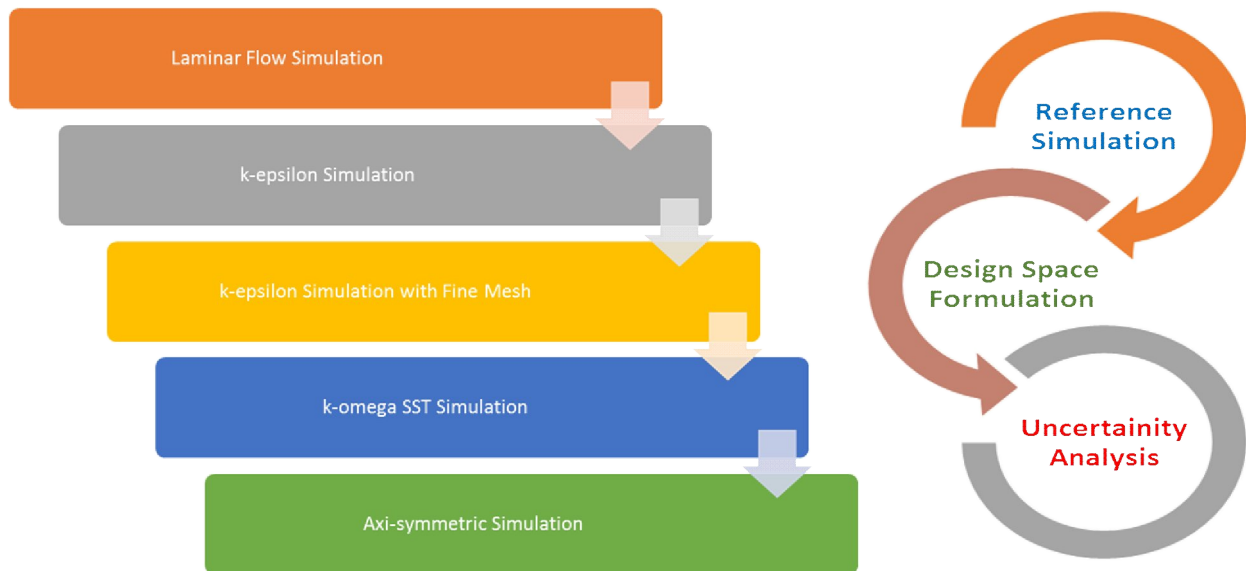


Figure 2: Sequential Solution of GLCC-Simulation

III. Sensitivity Study

The individual simulations using 2D, 3D numerical models with and without turbulence models have been evaluated with available experimental data and results from commercial software. 3D meshes with k-epsilon turbulence model have been shown to be the most accurate, of all iterations performed. However, there exists several parameters of the numerical solver along with the inlet velocity boundary condition, whose impact is not clearly understood. There also exist numerical parameters related to the turbulence model, whose reference values are based on empirical relations from literatures. The impact of such numerical parameters are also not clearly outlined. In the current section, an effort will be made to visualize the effect of introducing a response window to some of the aforementioned parameter sets on defined response entities, specific to the problem in hand. As a results, a sensitivity study will be performed to understand the influence of numerical parameters on the simulation results and identify the range of variation of the responses.

Parameter Name	Reference Value	Minimum Value	Maximum Value
Courant Number	5	5	50
Solver – Laplacian Gauss Range	0.33	0.1	0.5
Solver – Linear Gradient Scheme Range	0.33	0.1	0.5
Solver – Tolerance Value	1e-8	1e-7	1e-4
Inlet Velocity	-4.3	-5	-4
Turbulence Length Scale	7	3	10

Parameter Name	Reference Value	Minimum Value	Maximum Value
Turbulent viscosity constant	0.09	0.05	0.15
Shear rate generation multiplier	1.44	1	2
Dissipation rate multiplier	1.92	1.5	2.5
Schmidt Number - KE	1.0	0.5	1.5
Schmidt Number – Dissipation	1.3	1	2
Inlet Velocity	-4.3	-4	-5
Turbulence Length Scale	7	3	9

Table 1: List of Parameters used in the Sensitivity study : Solver parameters sensitivity & Turbulence parameters sensitivity.

The response evaluation was based on the Euler-difference norm formulation given by :

$$E(a, b) = \sqrt{(a_1 - b_1)^2 + (a_2 - b_2)^2 + (a_3 - b_3)^2 + \dots + (a_n - b_n)^2} \quad (1)$$

Here a_i represents simulation result values while b_i represents the experimental values.

IV. Results

The following figures 3 and 4 depict the comparison of the OPENFOAM results with experiment and CFX results, using the k-epsilon turbulence model with the finer mesh. Figure 3 shows a good correlation of velocity vectors with the CFX results and the figure 4 shows that OPENFOAM has a better agreement with the experiment in comparison to the CFX at both the probes.

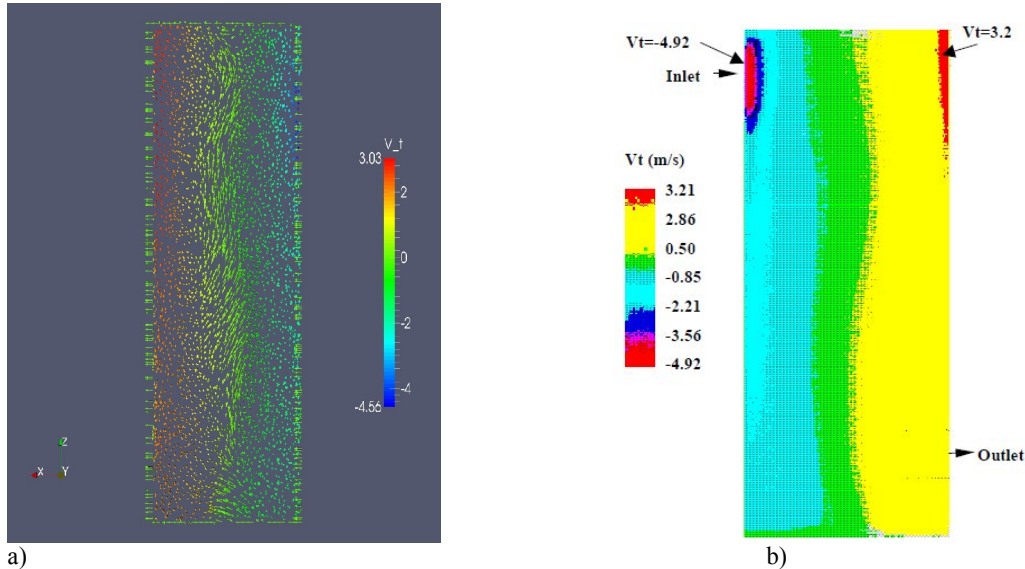
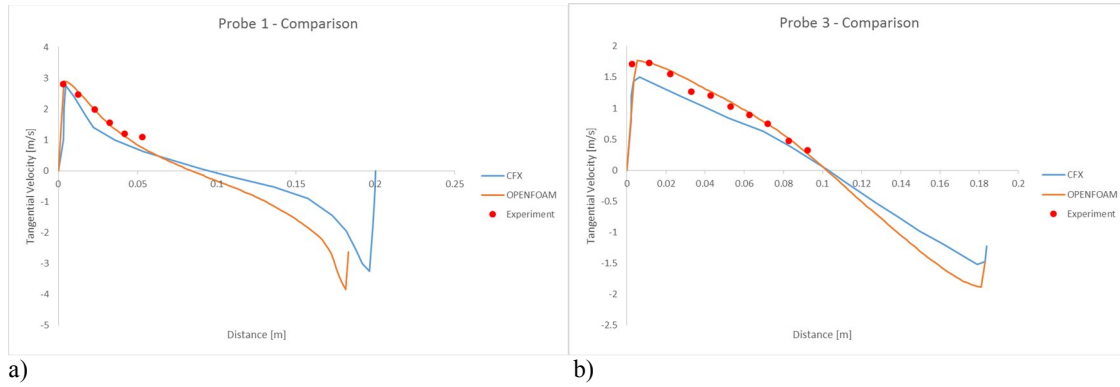
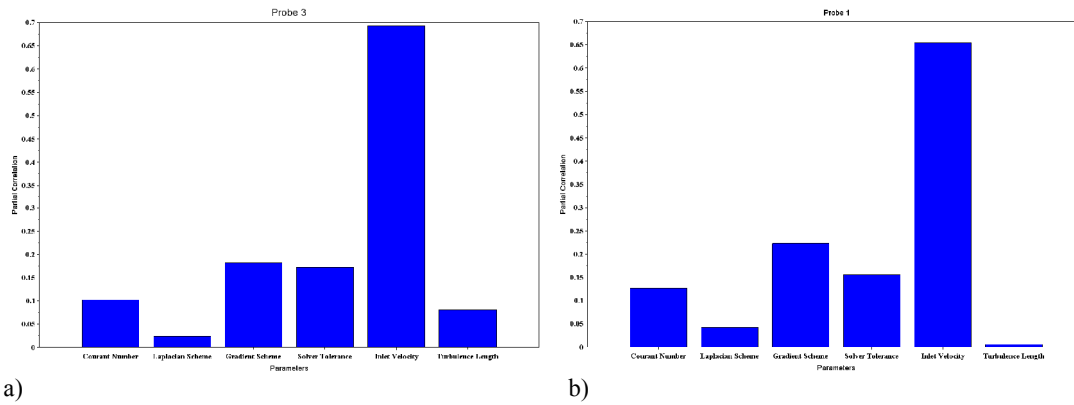


Figure 3: Contour plot of velocity vectors in a) OPENFOAM and b) ANSYS CFX

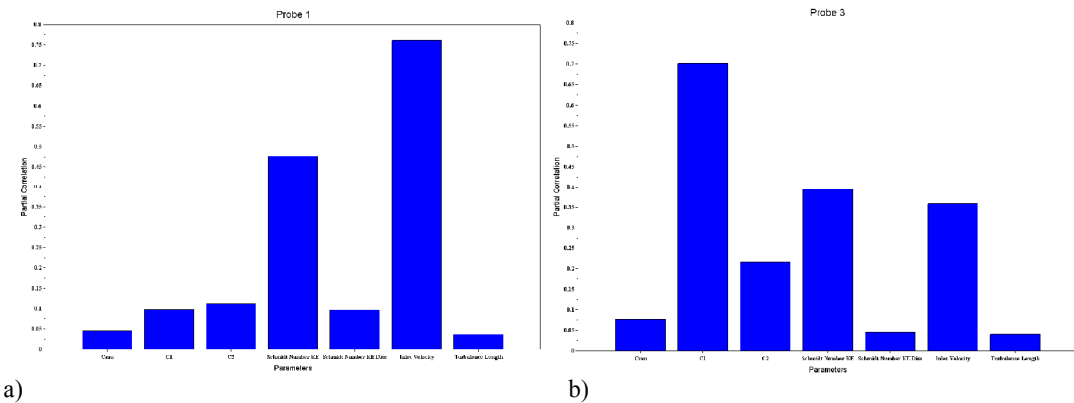


a) **Figure 4: Tangential velocity comparison between OPENFOAM, CFX and experiment at a) Probe 1 and b) Probe 3**

Figures 5 and 6 show the correlation factors of the input parameters with respect to the eulerian norm responses at the probe 1 and 3 for the two sensitivity studies (solver and turbulence characteristics) performed. The Tables 2 and 3 list the revaluation results of the sensitivity studies. In the case of turbulence characteristics, inlet velocity is the most important variable and other solver parameters have minimal effects on the solution. For the turbulence characteristics, inlet velocity, shear rate multiplier and Schmidt number KE are the most sensitive parameters.



a) **Figure 5: Correlation factors of input parameters with respect to the response for the sensitivity study of solver characteristics in a) Probe 1 and b) Probe 3**



a) **Figure 6: Correlation factors of input parameters with respect to the response for the sensitivity study of turbulence characteristics in a) Probe 1 and b) Probe 3**

Statistical Measure	Probe 1	Probe 3
Coefficient of Multiple Determination (R^2)	68.91%	58.13%
Multiple Correlation Coefficient (R)	82.40%	76.24%
Adjusted Coefficient of Multiple Determination	61.90%	52.48
Sensitive parameters	Inlet velocity, Gradient scheme	

Table 2: Revaluation results of sensitivity study to solver characteristics

Statistical Measure	Probe 1	Probe 3
Coefficient of Multiple Determination (R^2)	68.91%	58.13%
Multiple Correlation Coefficient (R)	82.40%	76.24%
Adjusted Coefficient of Multiple Determination	61.90%	52.48
Sensitive parameters	Inlet velocity, Gradient scheme	

Table 3: Revaluation results of sensitivity study to turbulence characteristics

V. Conclusions

An effort has been made to recreate a simulation basis carried out in a commercial software, ANSYS CFX with an open - source software, OPENFOAM and reproduce similar results. The project also highlights an evaluation procedure for numerical CFD problems and an advanced approach to arrive at reliable numerical simulation results. Integration of stochastic methods to design workspace is a significant leap in the process work-flow and highlights the effectiveness of Design of Experiments to arrive at improved design and simulation models. In the end, the dual objective of creating a simulation work-flow for GLCC model in an open-source environment along with development of a highly accurate numerical model was achieved in the stipulated time. Certain aspects that could not be covered during the course of the project are:

- Evaluation of the GLCC model with Reynolds' Stress Models
- Identification of suitable responses to DoE study.
- Further analysis of response variations to the furnished design space.

References

- [1] Separators, "Pipeline Ancillaries,"SpiraxSarco [Online]. Available:<http://www.spiraxsarco.com/Resources/Pages/SteamEngineering-Tutorials/pipeline-ancillaries.aspx/>.
- [2] Wilcox David C, Turbulence Modelling for CFD, DCW Industries, Library of Congress Cataloging in Publication Data, La Canada, 1994
- [3] George William K, "Lectures in Turbulence for the 21st Century", Chalmers University of Technology, Gothenburg.
- [4] Germano, M., Piomelli, U., Moin, P. and Cabot, W. H. (1991), "A dynamic sub-grid scale eddy viscosity model", Physics of Fluids, A(3): pp 1760-1765, 1991.
- [5] Kim, W and Menon, S. (1995), "A new dynamic one-equation subgrid-scale model for large eddy simulation", In 33rd Aerospace Sciences Meeting and Exhibit, Reno, NV, 1995.
- [6] Orszag, Steven A. (1970). "Analytical Theories of Turbulence". Journal of Fluid Mechanics (see, e.g., page 385) 41 (1970): 363386
- [7] M. ErdalFerhat, A. ShiraziSiamack, ShohamOvadia, Kouba Gene E., CFD Simulation of Single-Phase and Two-Phase Flow in Gas-Liquid Cylindrical Cyclone Separators, SPE Annual Technical Conference & Exhibition, Denver, U.S.A., 6-9 October, 1996.
- [8] J. H. Ferziger, M. Peric, Computational Methods for Fluid Dynamics, Springer, 3rd Ed., 2001.
- [9] H. Jasak, Error Analysis and Estimation for the Finite Volume Method with Applications to Fluid Flows, Ph.D. Thesis, Imperial College, London, 1996.

- [10] Bardina, J.E., Huang, P.G., Coakley, T.J. (1997), "Turbulence Modeling Validation, Testing, and Development", NASA Technical Memorandum 110446.
- [11] Launder, B. E., and Sharma, B. I. (1974), "Application of the Energy Dissipation Model of Turbulence to the Calculation of Flow Near a Spinning Disc", Letters in Heat and Mass Transfer, vol. 1, no. 2, pp. 131-138.
- [12] Menter, F. R. (1993), "Zonal Two Equation k - ω Turbulence Models for Aerodynamic Flows", AIAA Paper 93-2906.
- [13] Menter, F. R. (1994), "Two-Equation Eddy-Viscosity Turbulence Models for Engineering Applications", AIAA Journal, vol. 32, no 8. pp. 1598-1605.

Effect of Aspect Ratio and Boundary Conditions on the Eigenfrequency Optimization of Composite Panels using Lamination Parameters

Gokhan Serhat* and Ipek Basdogan†

Department of Mechanical Engineering, College of Engineering, Koc University, Istanbul, 34450, Turkey

Eigenfrequency optimization of laminated composite panels is a common engineering problem. This process mostly involves designing stiffness properties of the structure. Optimal results can differ significantly depending on the values of the model parameters and the metrics used for the optimization. Building the know-how on this matter is crucial for choosing the appropriate design methodologies as well as validation and justification of prospective results. In this paper, effects of aspect ratio and boundary conditions on eigenfrequency optimization of composite panels by altering stiffness properties are investigated. Lamination parameters are chosen as design variables which are used in the modeling of stiffness tensors. This technique enables representation of overall stiffness characteristics and provides a convex design space. Fundamental frequency and difference between fundamental and second natural frequencies are maximized as design objectives. Optimization studies incorporating different models and responses are performed. Optimal lamination parameters and response values are provided for each case and the effects of model parameters on the solutions are quantified. The results indicate that trends of the optima change for different aspect ratio ranges and boundary conditions. Moreover, convergence occurs beyond certain critical values of the model parameters which may cause an optimization study to be redundant.

I. Introduction

Advantageous properties of the composite laminates allowed their usage in the engineering structures to rise swiftly over the last decades¹. Complex nature of such structures resulted in the development of more advanced modeling and optimization tools. Optimization of laminated composite structures for mechanical and vibro-acoustic requirements often involves alteration of stiffness properties. The results can change significantly depending on the values of the model parameters and the performance metrics used for the optimization. Building the know-how on this matter is important for choosing the appropriate design methodologies as well as validation and justification of prospective results. Hence, it is essential to investigate and quantify the effect of models and the response types on the optimization results.

Vibrational characteristics of panel structures are strongly influenced by their stiffness properties. Hufenbach et al. showed that varying the fiber angles can alter dynamic properties of laminated composite panels and significantly change the sound fields resulting from panel vibrations². Tinnsten and Esping used plate thickness and fiber orientation angle as design variables to carry out an acoustic optimization study to minimize sound intensity levels due to vibrating plates³.

In vibro-acoustic design, one possible method is to reduce vibrations of the emitting structure by modifying its eigenfrequencies. Maximization of fundamental eigenfrequency can be used to avoid resonances occurring due to external excitation sources with the frequencies ranging from zero and up to the optimum fundamental eigenfrequency⁴. For example, Marburg and Hardtke improved the acoustic performance of a vehicle hat-shelf by increasing its fundamental frequency⁵. Narita and Robinson, obtained optimum laminate configurations yielding maximum fundamental frequencies for different boundary conditions and aspect ratios by following a layer-wise design approach⁶. Abdalla et al. also maximized the fundamental frequency of the laminated panels by using lamination parameters to model equivalent stiffness properties⁷. When the excitation frequencies lie in the range between two neighboring eigenfrequencies, maximization of the corresponding frequency gap is found to be more effective⁴. Honda et al. conducted a study to maximize the difference between fundamental and second natural frequencies by using lamination parameters as design variables⁸.

Communicating Author: ibasdogan@ku.edu.tr

* Ph.D. Candidate, Department of Mechanical Engineering, College of Engineering, Koc University.

† Associate Professor, Department of Mechanical Engineering, College of Engineering, Koc University.

In existing studies, effect of some model parameters on the optimal solutions was not covered in detail. For example, for panel aspect ratio, most of the studies used a few discrete values but the critical values where solutions converge to specific designs were not presented. Depending on the values of the model parameters and response types, the optimum design point might be pushed towards the boundary of the feasible domain. Being aware of such limiting cases is crucial in the assessment of the results. Furthermore, it might even eliminate the necessity for an optimization process by directly providing the user the optima for certain values of the model parameters.

In this paper, effects of aspect ratio and boundary conditions on eigenfrequency optimization of composite panels by altering stiffness properties are investigated. In the optimization process, lamination parameters are used as design variables which are used in the modeling of stiffness tensors. This technique provides a convex design space by eliminating the dependency of the optimum solutions on the assumptions made on initial laminate configuration. Fundamental frequency and the difference between fundamental and second natural frequencies are maximized as design objectives. Optimization studies are conducted varying panel aspect ratio and boundary conditions. Optimal laminate configurations are provided for multiple cases and effects of the model parameters on the optimal responses are quantified. The results indicate that convergence occurs beyond certain threshold values of the model parameters and optimization may be redundant. In Section II, the design problem including model details, stiffness formulation using lamination parameters and the performance metrics used in the optimization are explained. In Section III, effects of model parameters on optimal results are presented and discussed. Conclusions and directions for future studies are summarized in Section IV.

II. Design Problem

A. Panel Model

The plate model used in the analyses has nominal plate dimensions of 1000mm × 1000mm which are varied for the studies involving aspect ratio. The plate thickness is 10.0 mm. Simply-supported or clamped conditions are used as the boundary conditions. The plate material is graphite/epoxy composite with the properties given in Table 1^{6,9,10}.

Table 1. Material properties of uni-directional graphite/epoxy composite laminate

E_1 (GPa)	138
E_2 (GPa)	8.96
G_{12} (GPa)	7.1
ν_{12}	0.3
ρ (kg/m ³)	1.6
$\eta = 2\zeta$	0.008

B. Lamination Parameters

B.1. Formulation

Stiffness formulation for the laminated composites using lamination parameters was initially proposed by Tsai and Hahn¹¹. One advantage of this method is that it gives a compact representation of the laminate configuration by approximating the overall properties in terms of equivalent stiffness values. The laminate is parametrized by using certain number lamination parameters as design variables rather than the number of plies, their relative thicknesses and orientation angles. The second advantage of using this method is the convex design space which was demonstrated by Grenestedt¹².

The formulation of the constitutive relations for a laminated composite plate is carried out by using Classical Laminated Plate Theory (CLPT) which is based on Kirchhoff plate theory that disregards shear deformation. It yields accurate results for thin plates where other dimensions are assumed to be at least 10 times higher than the plate thickness¹³. From the vibro-acoustic point of view, this formulation provides accurate results for low frequencies where shear waves do not significantly contribute to sound transmission¹⁴. The following constitutive equation is obtained by using CLPT:

$$\begin{Bmatrix} N \\ M \end{Bmatrix} = \begin{bmatrix} A & B \\ B & D \end{bmatrix} \begin{Bmatrix} \varepsilon^0 \\ \kappa \end{Bmatrix} \quad (1)$$

where N and M are the vectors of force and moment resultants per unit depth respectively, ε^0 is the vector of mid-plane strains, and κ is the vector of plate curvatures. Stiffness tensors for the in-plane extension A , in-plane/bending coupling B and bending D can be formulated in terms of the lamination parameters and material

invariants. Normalized in-plane stiffness tensor of balanced and symmetric composite laminates can be modeled using only two lamination parameter variables as follows ¹⁵:

$$A^* = \frac{A}{t} = \begin{bmatrix} U_1 & U_4 & 0 \\ U_4 & U_1 & 0 \\ 0 & 0 & U_5 \end{bmatrix} + \begin{bmatrix} U_2 & 0 & 0 \\ 0 & -U_2 & 0 \\ 0 & 0 & 0 \end{bmatrix} V_1^* + \begin{bmatrix} U_3 & -U_3 & 0 \\ -U_3 & U_3 & 0 \\ 0 & 0 & -U_3 \end{bmatrix} V_3^* \quad (2)$$

In Eq. (3), t stands for the laminate thickness. V_i^* 's are the normalized lamination parameters: $V_1^* = \cos(2\theta)$, $V_3^* = \cos(4\theta)$ where θ is the layer angle. U_i 's are the material invariants which can be calculated through the formulae given in the equations from 3 to 12:

$$U_1 = \frac{1}{8}(3Q_{11} + 3Q_{22} + 2Q_{12} + 4Q_{66}) \quad (3)$$

$$U_2 = \frac{1}{2}(Q_{11} - Q_{22}) \quad (4)$$

$$U_3 = \frac{1}{8}(Q_{11} + Q_{22} - 2Q_{12} - 4Q_{66}) \quad (5)$$

$$U_4 = \frac{1}{8}(Q_{11} + Q_{22} + 6Q_{12} - 4Q_{66}) \quad (6)$$

$$U_5 = \frac{1}{8}(Q_{11} + Q_{22} - 2Q_{12} + 4Q_{66}) \quad (7)$$

$$Q_{11} = \frac{E_1}{(1 - \nu_{12}\nu_{21})} \quad (8)$$

$$Q_{22} = \frac{E_2}{(1 - \nu_{12}\nu_{21})} \quad (9)$$

$$Q_{12} = \frac{\nu_{12}E_2}{(1 - \nu_{12}\nu_{21})} \quad (10)$$

$$Q_{66} = G_{12} \quad (11)$$

$$\nu_{21} = \frac{E_2}{E_1} \nu_{12} \quad (12)$$

Coupling tensor B vanishes for symmetric laminates. In addition to symmetry, when the laminate is balanced consisting of a large number of homogenously distributed layers; its bending stiffness becomes equal to: $D = At^3/12$. This assumption is adopted in this study which makes D also to be a function of V_i^* and V_3^* having the same design space as A .

B.2. Miki's Lamination Diagram

Miki's Lamination Diagram is a graphical tool to visualize the feasible domain of the balanced and symmetric laminates ¹⁶. A sample diagram with exemplary points for 0° , $\pm 45^\circ$ and 90° laminates is depicted in Fig. 1. The

normalized lamination parameters: V_1^* and V_3^* are horizontal and vertical axes of the diagram, respectively. The feasible domain is shown by the shaded area. The bottom of the feasible domain is bounded the curve: $V_3^* = 2(V_1^*)^2 - 1$. The design points on this curve are obtainable by balanced symmetric laminates with one unique angle. The line: $V_3^* = 1$ bounds the feasible domain at the top. The points on this line can be achieved by using different volumetric fractions of 0° and 90° layers. All other feasible design points need to lie in the enclosed region. In the following sections, the normalized lamination parameters are denoted by V_i 's without the superscript $*$'s for clarity.

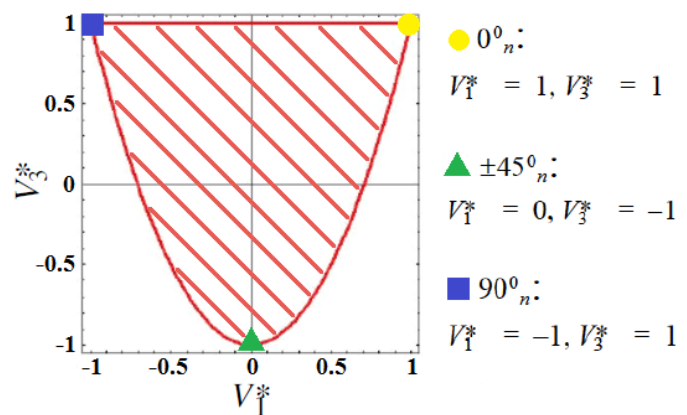


Figure 1. Miki's Lamination Diagram and feasible design domain.

C. Performance Metrics

In vibro-acoustic design, different responses can be used as the metrics to evaluate the design performance. In this study, fundamental natural frequency and the difference between fundamental and second natural frequencies are maximized as the objectives with the motivation of avoiding resonance due to external harmonic excitation.

III. Effect of Model Parameters on Optimal Results

Natural frequencies of a plate structure strongly depend on its dimensions. The plate aspect ratio (a/b) is an important quantity that designates dimensional characteristics where a is the plate length and b is the plate width. Boundary conditions also play a crucial role in the dynamic properties of the structure. For lower order frequencies, the difference between clamped and simply-supported conditions is even more significant¹⁷.

In this section, panel aspect ratio and boundary conditions are considered as the model parameters and their influence on the optimal designs is determined. Initially, the plate is chosen to be a square. Then, the aspect ratio is gradually increased by keeping the plate area constant. The analyses are conducted for both simply-supported and clamped boundary conditions to capture the combined effects. Analytical studies, as well as FE simulations, are performed to calculate the responses. Panel thickness is held constant for all cases.

A. Maximum Fundamental Frequency

In the literature, closed-form analytical formulae for the several responses are available for constant-stiffness laminates. For the simply-supported plate, the natural frequencies in (rad/s) are calculated analytically by using the equation given by Gurdal⁹ as:

$$\omega_{mn} = \sqrt{\left(\frac{\pi^4 t^2}{12\rho a^4}\right) \left(D_{11}^* m^4 + 2(D_{12}^* + 2D_{66}^*) m^2 n^2 \left(\frac{a}{b}\right)^2 + D_{22}^* \left(\frac{na}{b}\right)^4\right)} \quad (15)$$

where t is the laminate thickness, ρ is the laminate density, a is panel length (in the x-direction), b is panel width (in the y-direction), m is the number of half-waves in the x-direction and n is the number of half-waves in the y-direction. D_{ij}^* 's are the normalized bending stiffness terms defined as:

$$D_{ij}^* = \frac{12D_{ij}}{t^3} \quad (16)$$

In this optimization problem, the first natural frequency is maximized respecting the limiting values of lamination parameters V_1 and V_3 , dictated by the Miki's Lamination Diagram. A brute-force approach is used in the calculation of natural frequency response and its optimization since analytical computations are not computationally intensive. As an example, the response surface for the fundamental frequency of a (1000×1000×10.0 mm) square plate as a function of lamination parameters is illustrated in Fig. 2. One can observe the convex nature of the design space when modeled using lamination parameters, which results in a single optimum point located on the boundary of the Miki's Diagram.

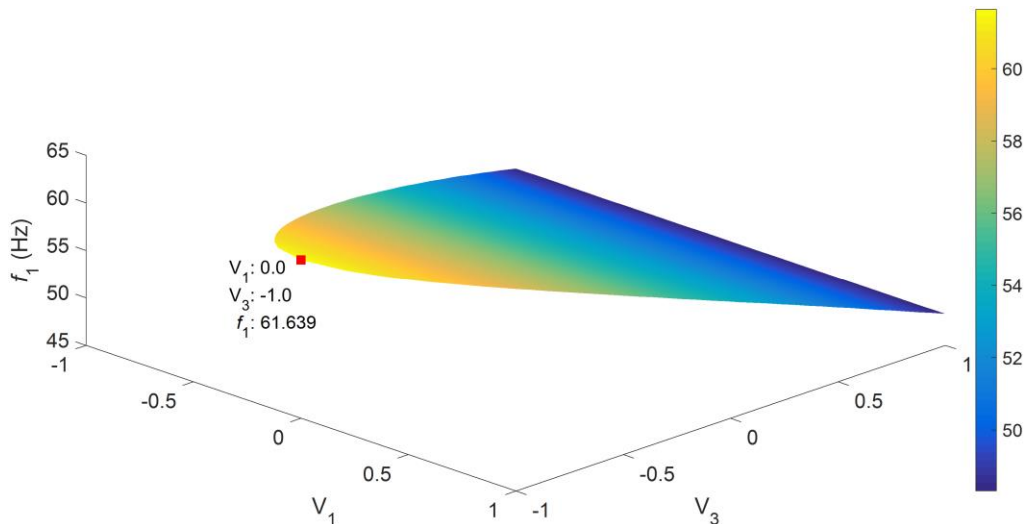


Figure 2. Fundamental natural frequency of a square simply-supported plate as a function of lamination parameters and the optimum point.

A.1. Simply-Supported Plate

In Figure 3, the maximum fundamental frequencies of the simply-supported plate at the corresponding optimum lamination parameter pairs: V_1 , V_3 are shown for different aspect ratios: AR . For the square plate, the lamination parameters ($V_1 = 0$, $V_3 = -1$) are found to provide the maximum fundamental frequency which is in accordance with Narita's results ⁶.

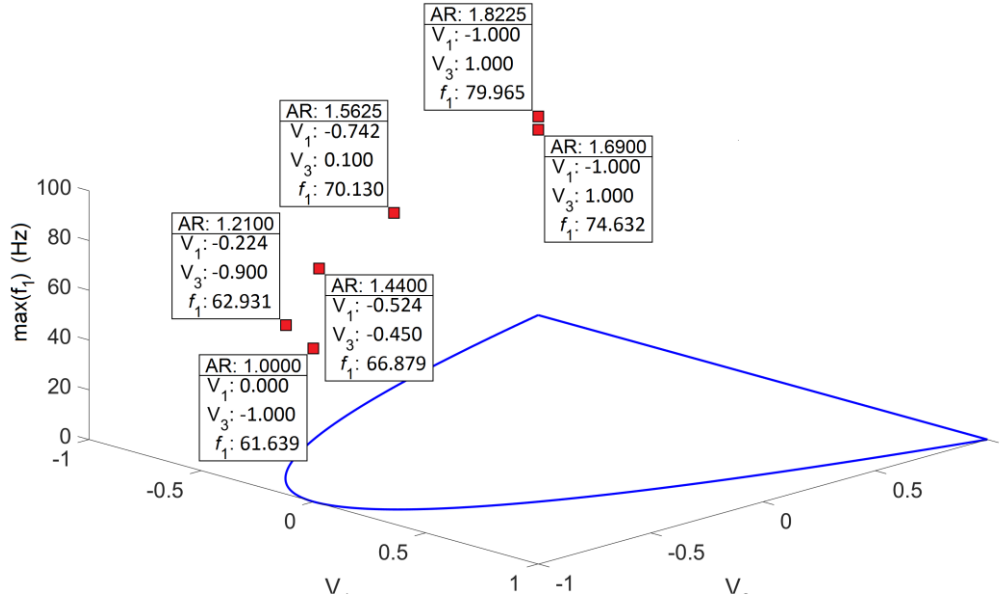


Figure 3. Maximum fundamental frequencies of the simply-supported plate at the corresponding optimum lamination parameter pairs for different aspect ratios.

For simply-supported plate boundary conditions, the optimum designs for the natural frequencies are found at the boundary of the Miki's Diagram for all aspect ratios. As explained in section (B.2), the points on the boundary can be obtained only single-angle laminate configurations. The angle for the laminate lay-up is determined as ⁹:

$$\theta = \frac{\cos^{-1}(V_1)}{2} \quad (17)$$

Using Eq. 17, the variation of the laminate angle at the maximum first natural frequency with respect to the aspect ratio is determined and presented in Fig. 4. Eq. The suitable configuration for the initial square plate with aspect ratio 1.0 is determined as $\pm 45^\circ$ laminate. The results indicate that, as the aspect ratio is increased, the values of the optimal angles also increase in an exponential rate. After the aspect ratio is bigger than the threshold value of (1.69), the optimum laminate configuration for the maximum fundamental frequency is obtained with 90° layers.

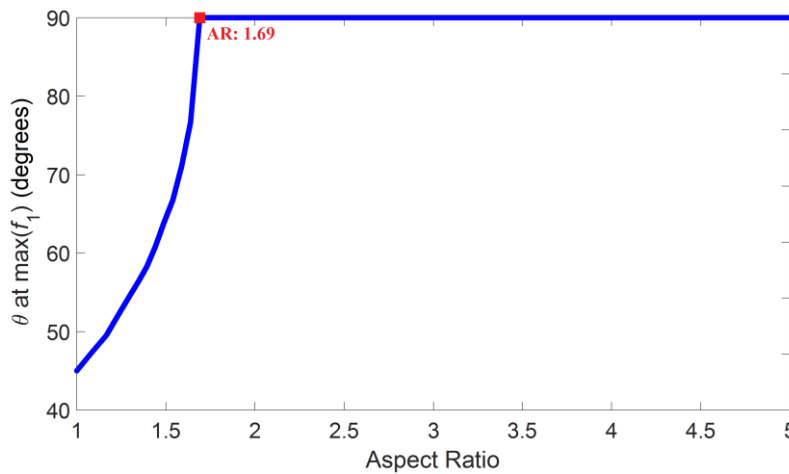


Figure 4. Fiber orientation angle θ at the maximum fundamental frequency of simply-supported plate vs. panel aspect ratio.

The maximum fundamental frequency is another quantity whose dependency on panel aspect ratio is analyzed. As shown in Fig. 5, a non-linear increase is observed in the maximum value of the fundamental frequency for the increasing values of the aspect ratio until the threshold value of 1.69. This point is coincident with the aspect ratio where optimal ply orientation angle for the maximum frequency becomes 90° . Beyond this value, the maximum frequency increases proportionally with the aspect ratio. This linear behavior results from modifying plate dimensions, but keeping the internal structure unchanged.

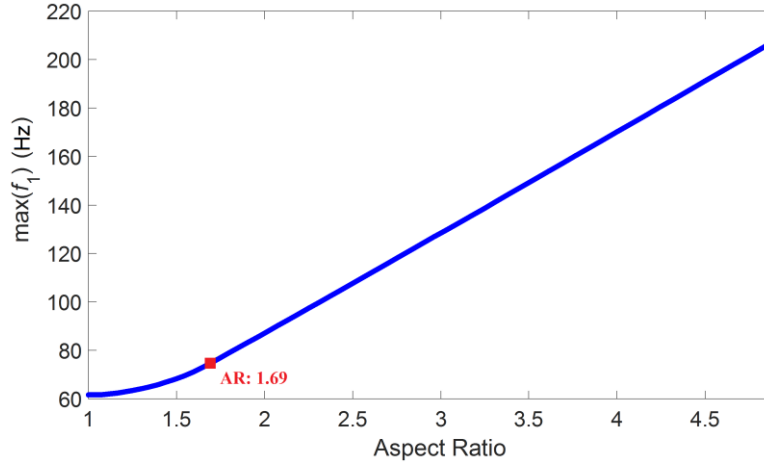


Figure 5. Maximum fundamental frequency of simply-supported plate vs. panel aspect ratio.

A.2. Clamped Plate

The responses for the clamped plate are calculated using commercial FEA software OptiStruct¹⁸. Unlike simply-supported plate, for clamped boundary conditions, the optimum points do not always lie on the boundary of the Miki's Diagram. In Fig. 6, the maximum 1st natural frequency over the lamination parameter variables is given. For the initial aspect ratio of 1.0, the optimum configuration has been found as ($V_1 = 0.0$, $V_3 = 1.0$). This configuration can only be obtained by 0° – 90° laminates with an equal volumetric percentage. As the aspect ratio is increased, the optimum design point rapidly converges to ($V_1 = -1.0$, $V_3 = 1.0$) which is, in fact, the same as the point of convergence for the simply-supported conditions. One should note that for clamped boundary conditions, the change in the maximum frequency is considerably smaller compared to the simply-supported plate. This is because kinematic stiffening effect resulting from the boundary conditions is significantly more dominant than the stiffening due to the fiber orientations.

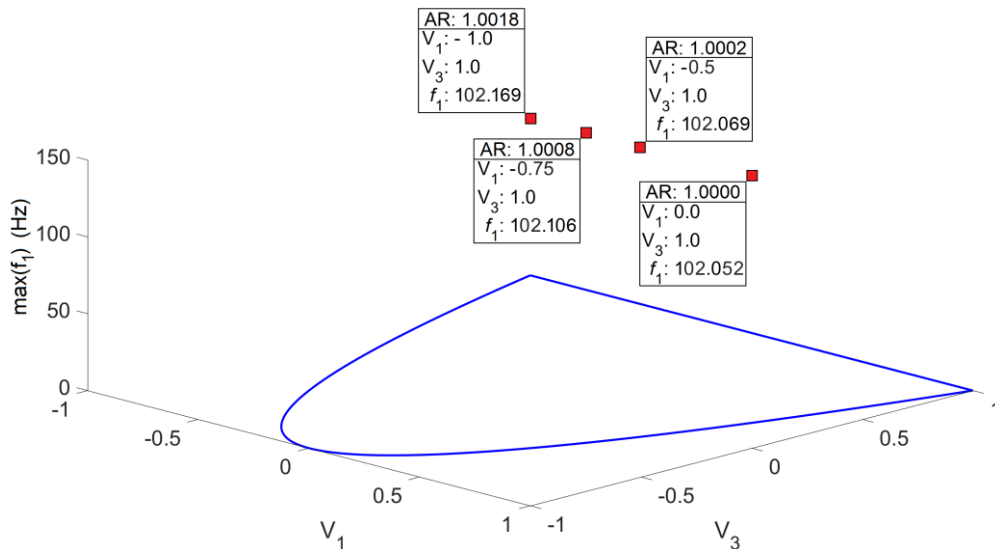


Figure 6. Maximum fundamental frequencies of the clamped plate at the corresponding optimum lamination parameter pairs for different aspect ratios.

B. Maximum Difference Between the 1st and 2nd Natural Frequencies

Figure 7 (a) shows the variation in the optimum lamination parameters for the maximum difference between fundamental and second natural frequencies for the simply-supported plate. The change in the solutions for

increasing aspect ratio is indicated by arrows. In this case, the solutions do not initially lie on the boundary of Miki's diagram. As aspect ratio is increased from 1.0 to 1.44, optimum design points gradually move from ($V_1 = 0.0$, $V_3 = 1.0$) to ($V_1 = 0.687$, $V_3 = 0.850$). After this point, a jump is detected and the optimum is suddenly found at ($V_1 = 0.559$, $V_3 = -0.375$). Starting from $AR = 1.5$ the solutions appear on the boundary. As the aspect ratio is increased the solution approaches towards upper right corner of the Miki's diagram until the point ($V_1 = 0.975$, $V_3 = 0.900$) and $AR = 1.96$. At this point, a kink occurs and the trend of the optima movement change its direction for increasing values of the aspect ratio. Finally, the solutions converge to ($V_1 = 0.418$, $V_3 = -0.650$) for $AR \geq 4.0$. In Fig. 7 (b), graph for the optimal solutions is given from top view, to demonstrate the points lying on the boundary more clearly.

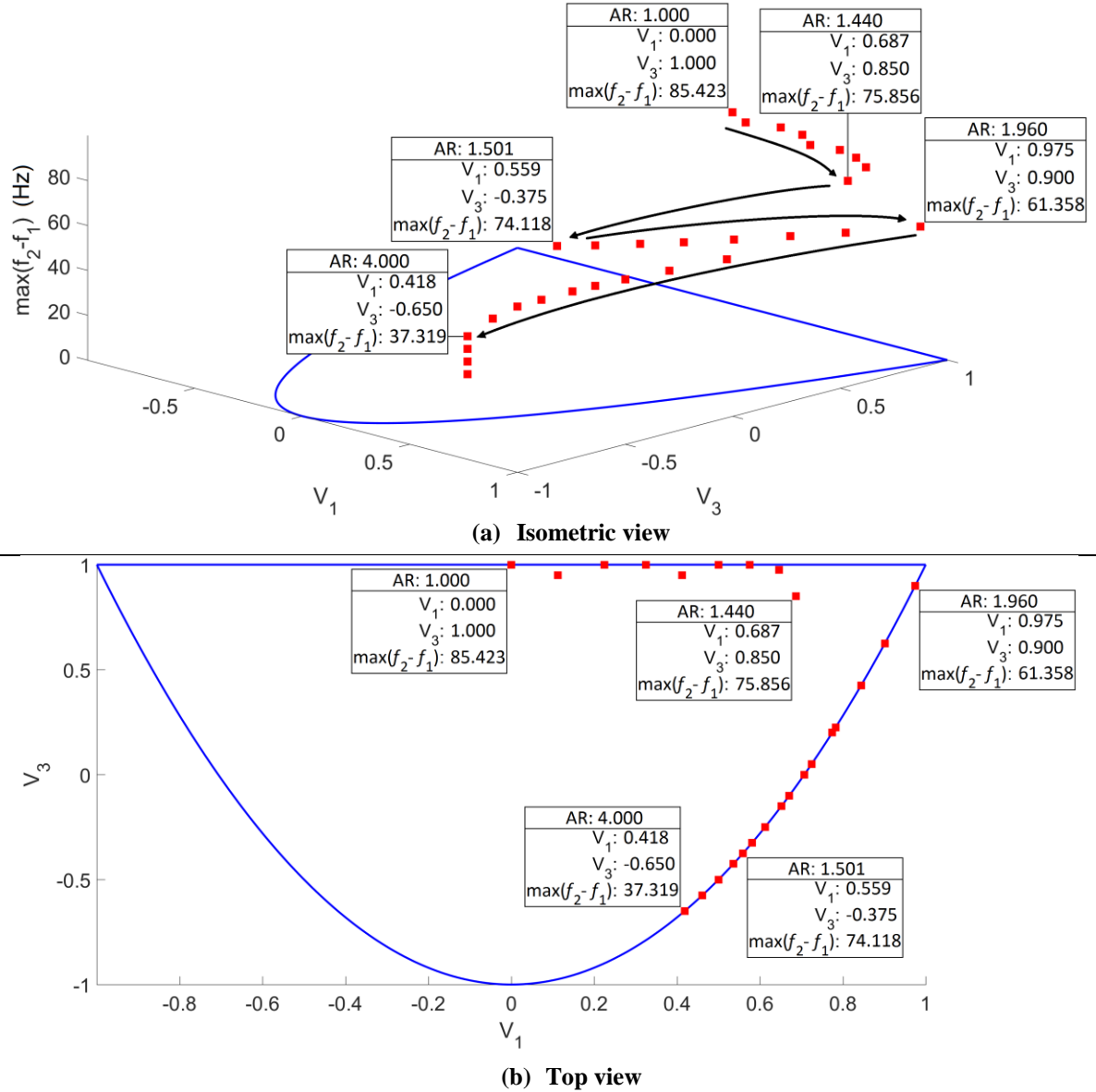


Figure 7. Maximum difference between the 1st and 2nd natural frequencies of the simply-supported plate at the corresponding optimum lamination parameter pairs for different aspect ratios.

For the portion of the design points lying on the boundary, the laminate angle can be calculated using Eq. 17 as before. Figures 8 and 9 show the maximum difference between fundamental and second natural frequencies and corresponding fiber orientation angle vs. panel aspect ratio, respectively. The graphs indicate that the maximum difference has always a decreasing trend with the increasing aspect ratio starting from 1.5. However, at $AR = 1.96$, an inflection point is detected where the second derivative becomes positive. The fiber angle for the maximum difference is found as 28° at the beginning. At $AR = 1.96$, the fiber angle reaches its minimum of 6.5° . When aspect ratio becomes more than 4, the optimum fiber angle converges approximately to 33° . For frequency

difference, the clamped plate is not considered, since the sensitivity is observable only with the unpractically small changes in the aspect ratio which is shown in the fundamental frequency calculations.

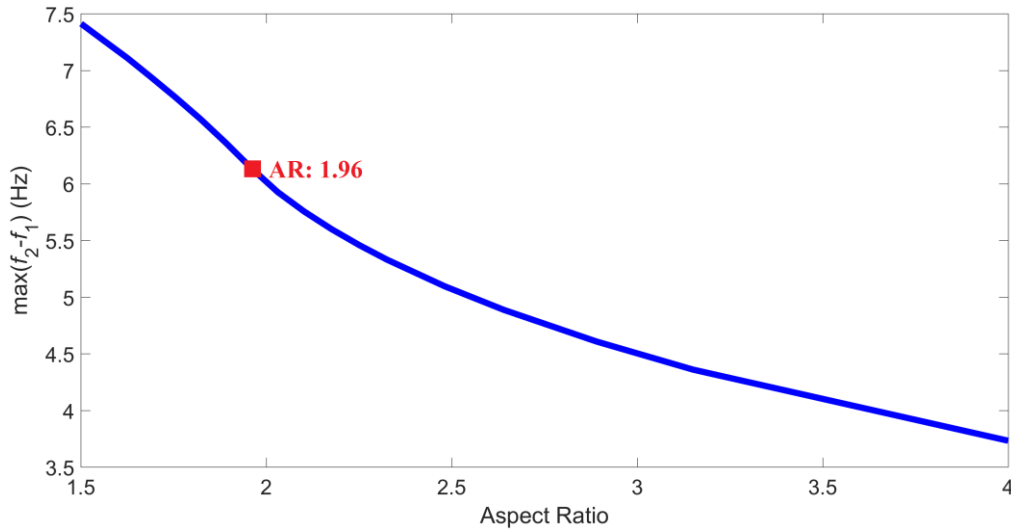


Figure 8. Maximum difference between the 1st and 2nd natural frequencies of the simply-supported plate vs. panel aspect ratio.

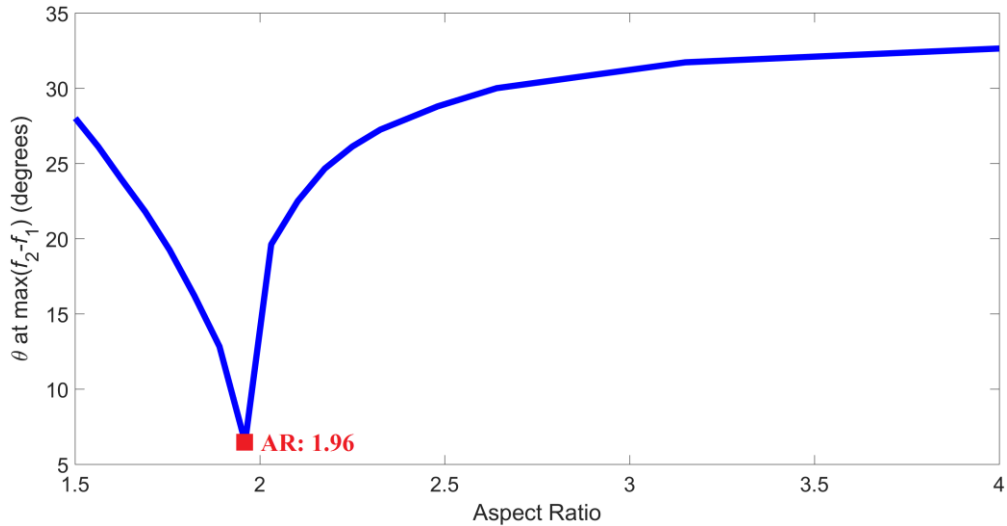


Figure 9. Fiber orientation angle θ at the maximum difference between the 1st and 2nd natural frequencies of the simply-supported plate vs. panel aspect ratio.

IV. Conclusions

In this study, effects of panel aspect ratio and boundary conditions on eigenfrequency optimization of composite panels are investigated. In the optimization process, lamination parameters are chosen as design variables which are used to calculate laminate stiffness tensors. Fundamental frequency and difference between fundamental and second natural frequencies are maximized as design objectives. It is shown that under thin plate assumptions, the maximum fundamental frequency of simply-supported plates always increases with the increasing aspect ratio. However, the increment is parabolic until aspect ratio becomes 1.69 and linear for larger values. In addition, maximization is redundant when the aspect ratio is 1.69 or higher, as the optimum laminate angle is always 90°. For clamped plates, optimum laminate angle for the maximum fundamental frequency quickly becomes 90° with a small increment in the aspect ratio. It is also observed that stiffening effect of the clamped boundary conditions is considerably more dominant over the stiffening due to the fiber orientations for thin plates. Maximum difference between fundamental and second natural frequencies of the simply-supported plates always decreases by the larger values of the aspect ratio. Optimal solutions for this case do not initially lie on the boundary of the Miki's diagram. These points require layers of multiple angles to be obtained. When the aspect ratio is 1.5 or higher the results are located on the boundary. For AR = 1.5, corresponding laminate orientation angle is around 28°. A critical point is detected at AR = 1.96 where the second derivative of the maximum frequency difference

vs. aspect ratio curve changes sign. This point is coincident with the dip of the optimal fiber angle vs. aspect ratio graph. For aspect ratios of 4.0 or larger, the optimal angle curve levels off at the fiber angle of approximately 33°.

The effect of panel curvature will be considered for future studies. Then, combined effects of the curvature, aspect ratio, and different boundary conditions can be investigated. In addition, solutions for several other vibro-acoustic responses such as equivalent radiated power can be calculated to compare with the optimal eigenfrequency designs obtained in this study.

Acknowledgments

The authors thank Marie Curie Initial Training Network “AMEDEO” for financial support of the work.

References

- ¹Kaufmann, M. “Cost/Weight Optimization of Aircraft Structures,” Licentiate Dissertation, School of Engineering Sciences, KTH, Stockholm, Sweden, 2008.
- ²Hufenbach, E.W., Kroll, L., Holste, C., Täger, O., and Barkanov, E. “Design of dynamically loaded fiber-reinforced structures with account of their vibro-acoustic behavior,” *Mechanics of Composite Materials*, Vol. 37, No. 2, 2001, pp. 235–248.
- ³Tinnsten, M., and Esping, B. “Optimization of acoustic response,” *Structural Optimization*, Vol. 18, 1999, pp. 36–47.
- ⁴Du, J., and Olhoff, N. “Topological design of freely vibrating continuum structures for maximum values of simple and multiple eigenfrequencies and frequency gaps,” *Structural Multidisciplinary Optimization*, Vol. 34, 2007, pp. 91–110.
- ⁵Marburg, S., and Hardtke, H.J. “Shape Optimization of a Vehicle Hat-Shelf Improving Acoustic Properties for Different Load Cases by Maximizing First Eigenfrequency,” *Computers and Structures*, Vol. 79, 99, 2001, pp. 1943–1957.
- ⁶Narita, Y., and Robinson, P. “Maximizing the fundamental frequency of laminated cylindrical panels using layerwise optimization,” *International Journal of Mechanical Sciences*, Vol. 48, 2006, pp. 1516–1524.
- ⁷Abdalla, M.M., Setoodeh, S., and Gurdal, Z. “Design of variable stiffness composite panels for maximum fundamental frequency using lamination parameters,” *Composite Structures*, Vol. 81, 2007, pp. 283–291.
- ⁸Honda, S., Narita, Y., and Katsuhiko, S. “Discrete Optimization for Vibration Design of Composite Plates by Using Lamination Parameters,” *Advanced Composite Materials*, Vol. 18, 2009, pp. 297–314.
- ⁹Gurdal, Z., Haftka, R.T., and Hajela, P. *Design and Optimization of Laminated Composite Materials*, 1st ed., John Wiley & Sons, New York, 1999.
- ¹⁰Chung, D.D.L. “Review: Materials for vibration damping,” *Journal of Materials Science*, Vol. 36, 2001, pp. 5733–5737.
- ¹¹Tsai, S.W., and Hahn, H.T. *Introduction of composite materials*, Technomic Publishing, Lancaster, PA, 1980.
- ¹²Grenestedt, J.L., and Gudmundson, P. “Layup optimization of composite material structures,” *Proceedings of IUTAM symposium on optimal design with advanced materials* edited by P. Pedersen, Vol. 1, Elsevier Science, Amsterdam, 1993, pp. 311–336.
- ¹³Kubiak, T. *Static and Dynamic Buckling of Thin-Walled Plate Structures*, Springer International Publishing, Switzerland, 2013.
- ¹⁴Yuan, C., Bergsma O., and Beukers A. “Sound Transmission Loss Prediction of the Composite Fuselage with Different Methods,” *Application of Composite Materials*, Vol. 19, 2012, pp. 865–883.
- ¹⁵Gurdal, Z., and Olmedo, R. “In-Plane Response of Laminates with Spatially Varying Fiber Orientations: Variable Stiffness Concept,” *AIAA Journal*, Vol. 31, No. 4, 1993, pp. 751–758.
- ¹⁶Miki, M. “Design of Laminated Fibrous Composites Plates with Required Flexural Stiffness,” *Recent Advances in Composites in the United States and Japan, ASTM STP 864*, J.R. Vinson and M. Taya, Eds., American Society for Testing and Materials, Philadelphia, 1985, pp. 387–400.
- ¹⁷Blevins, R.D. *Design Formulas for Dynamics, Acoustics and Vibration*, John Wiley & Sons, West Sussex, UK, 2016.
- ¹⁸OptiStruct, Altair Engineering Inc., v13.0, Troy, MI.

Experiments on Checkpointing Adjoint MPI Programs

A.Taftaf and L. Hascoët

INRIA, 2004 Route des Lucioles, Sophia-Antipolis, France, {Elaa.Teftef, Laurent.Hascoet}@inria.fr

Checkpointing is a classical strategy to reduce the peak memory consumption of the adjoint. Checkpointing is vital for long run-time codes, which is the case of most MPI parallel applications. However, for MPI codes this question has always been addressed by ad-hoc hand manipulations of the differentiated code, and with no formal assurance of correctness. In a previous work, we investigated the assumptions implicitly made during past experiments, to clarify and generalize them. On one hand we proposed an adaptation of checkpointing to the case of MPI parallel programs with point-to-point communications, so that the semantics of an adjoint program is preserved for any choice of the checkpointed part. On the other hand, we proposed an alternative adaptation of checkpointing, more efficient but that requires a number of restrictions on the choice of the checkpointed part. In this work we see checkpointing MPI parallel programs from a practical point of view. We propose an implementation of the adapted techniques inside the AMPI library. We discuss practical questions about the choice of technique to be applied within a checkpointed part and the choice of the checkpointed part itself. Finally, we validate our theoretical results on representative CFD codes.

I. Introduction

Checkpointing is a classical technique to mitigate the overhead of adjoint Algorithmic Differentiation (AD). In the context of source transformation AD with the Store-All approach, checkpointing¹ reduces the peak memory consumption of the adjoint, at the cost of duplicate runs of selected pieces of the code. Checkpointing is best described as a transformation applied with respect to a piece of the original code (a

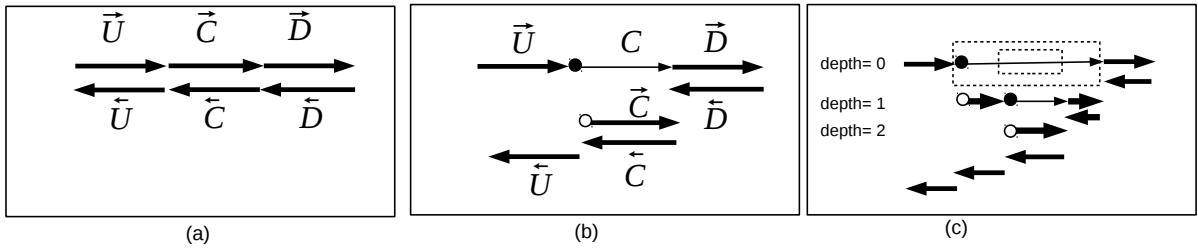


Figure 1. (a) A sequential adjoint program without checkpointing. The two thick arrows in the top represent the forward sweep, propagating the values in the same order as the original program, and the two thick arrows in the bottom represent the backward sweep, propagating the gradients in the reverse order of the computation of the original values. (b) The same adjoint program with checkpointing applied to the part of code C . The thin arrow reflects that the first execution of the checkpointed code C does not store the intermediate values in the stack. (c) Application of the checkpointing mechanism on two nested checkpointed parts. The checkpointed parts are represented by dashed rectangles.

“checkpointed part”). For instance figure 1 (a) and (b) illustrate checkpointing applied to the piece C of a code, consequently written as $U; C; D$. On the adjoint code of $U; C; D$ (see figure 1 (a)), checkpointing C means in the forward sweep **not** storing the intermediate values during the execution of C . As a consequence, the backward sweep can execute \vec{D} but lacks the intermediate values necessary to execute \vec{C} . To cope with that, the code after checkpointing (see figure 1 (b)) runs the checkpointed piece again, this time storing the intermediate values. The backward sweep can then resume, with \vec{C} then \vec{U} . In order to execute C twice (actually C and later \vec{C}), one must store (a sufficient part of) the memory state before C and restore it before \vec{C} . This storage is called a *snapshot*, which we represent on figures as a \bullet for taking a snapshot and as a \circ for restoring it. Taking a snapshot “ \bullet ” and restoring it “ \circ ” have the effect of resetting a part of the machine state after “ \circ ” to what it was immediately before “ \bullet ”.

Checkpointing is vital for long run-time codes, which is the case for most MPI parallel applications. However, for MPI codes this question has always been addressed by ad-hoc hand manipulations of the differentiated code, and with no formal assurance of correctness. In a previous work², we proposed an

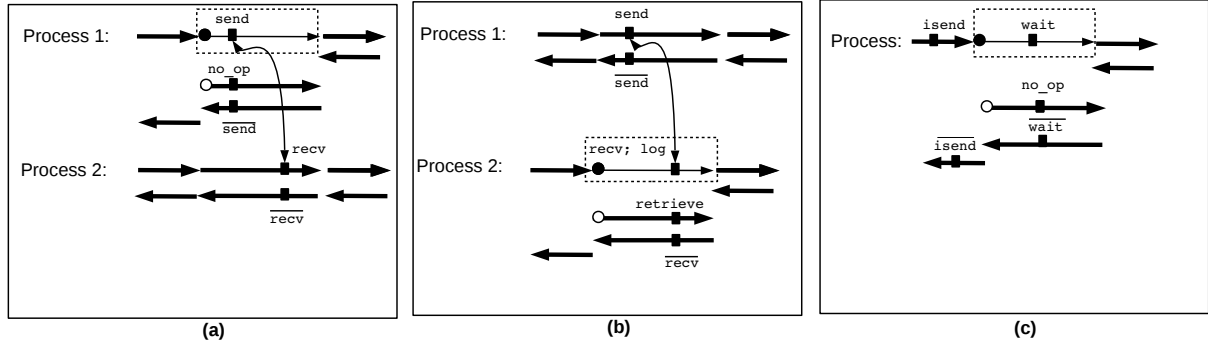


Figure 2. Three examples in which we apply checkpointing coupled with receive-logging. For clarity, we separated processes: process 1 on top and process 2 at the bottom. In (a), an adjoint program after checkpointing a piece of code containing only the *send* part of point-to-point communication. In (b), an adjoint program after checkpointing a piece of code containing only the *recv* part of point-to-point communication. In (c), an adjoint program after checkpointing a piece of code containing a *wait* without its corresponding non blocking routine *isend*.

adaptation of checkpointing to the case of MPI parallel programs with point-to-point communications, so that the semantics of an adjoint program is preserved for any choice of the checkpointed part. This adapted technique, called “receive-logging”, is sketched in figure 2. For simplicity, we omit the *mpi_* prefix from subroutine names and omit parameters that are not essential in our context. The receive-logging technique relies on logging every message at the time when it is received.

- During the first execution of the checkpointed part, every communication call is executed normally. However, every *receive* call (in fact its *wait* in the case of non-blocking communication) stores the value it receives into some location local to the process. Calls to *send* are not modified.
- During the duplicated execution of the checkpointed part, every *send* operation does nothing. Every *receive* operation, instead of calling any communication primitive, reads the previously received value from where it has been stored during the first execution. We say that these operations are “de-activated”.

Although this technique does not impose restrictions on the choice of the checkpointed part, message-logging makes it memory-costly. In the previous work,² we proposed a refinement to our general technique. It consists in duplicating the communications, “message-resending”, whenever it is possible. The principle is to identify *send-recv* pairs whose ends belong to the same checkpointed part, and to re-execute these communication pairs identically during the duplicated part, thus, performing the actual communication twice. Meanwhile, communications with one end not belonging to the checkpointed part are still treated by receive-logging. Figure 3 (b) shows the application of checkpointing coupled with receive-logging

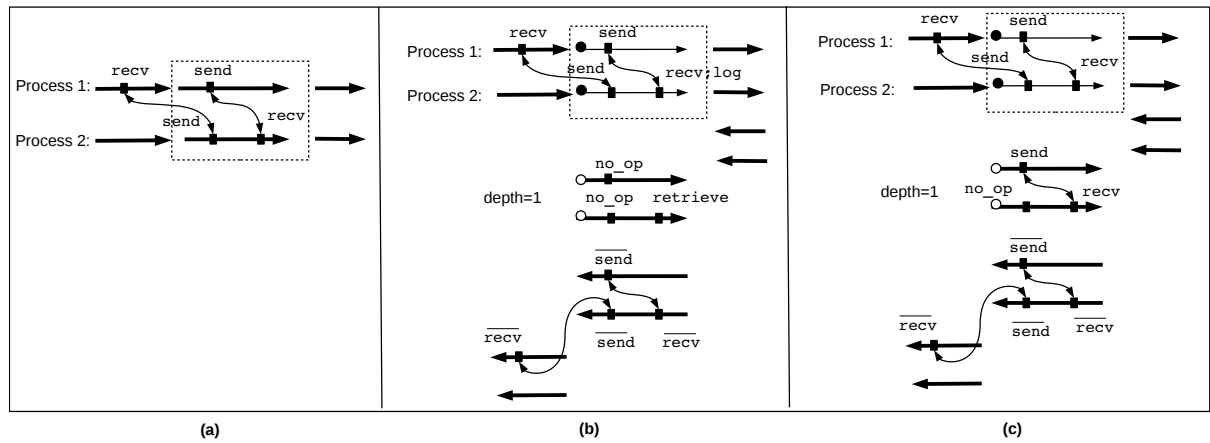


Figure 3. In (a), an MPI parallel program running in two processes. In (b), the adjoint corresponding to this program after checkpointing a piece of code by applying the receive-logging. In (c), the adjoint corresponding after checkpointing a piece of code by applying receive-logging coupled the with message-resending.

technique to some piece of code. In this piece of code, we select a *send-recv* pair and we apply the

Since the outer checkpointed part is right-tight, we chose to apply message re-sending to the `recv` of process 2 together with its `send`. As result of checkpointing, see figure 4 (b), the *receive* call of process 2 is activated when the depth of checkpointing is equal to 1. Since this *receive* will be de-activated during the depth just after, i.e. during depth=2, its received value has been logged during the current depth and retrieved during the depth just after.

In this paper, we see checkpointing MPI parallel programs from a practical point of view. In section II, we propose an implementation of receive-logging coupled with message-resending inside the AMPI library.³ In section III, we propose a further refinement to the receive-logging technique. In sections IV and V, we discuss practical questions about the choice of technique to be applied within a checkpointed part and the choice of the checkpointed part itself. Finally, in section VI, we validate our theoretical results on representative CFD codes.

II. Implementation Proposal

We propose an implementation of receive-logging coupled with message re-sending inside the AMPI library. This proposal allows for each end of communication to be activated during some depths of the checkpointed adjoint, i.e. we apply the message-resending to it, and de-activated during some others, i.e. we apply the receive-logging to it.

II.A. General view

The AMPI library is a library that wraps the calls to MPI subroutines in order to make the automatic generation of the adjoint possible in the case of MPI parallel programs. An interface for this library has already been developed in the operator overloading AD tool dco,⁴⁵ and under development in our AD tool Tapenade.⁶ This library provides two types of wrappers:

- The “forward wrappers”, called during the forward sweep of the adjoint code. Besides calling the MPI subroutines of the original MPI program, these wrappers store in memory the needed information to determine for every MPI subroutine, its corresponding adjoint, we call this “adjoint needed information”. For instance, the forward wrapper that corresponds to a `wait`, `FWD_AMPI_wait` calls `wait` and stores in memory the type of non blocking routine with whom the `wait` is paired.
- The “backward wrappers” called during the backward sweep of the adjoint code. These wrappers retrieve the information stored in the forward wrappers and use it to determine the adjoint. For instance, the backward wrapper that corresponds to a `wait`, `BWD_AMPI_wait` calls `irecv` when the original `wait` is paired with an `isend`.

A possible implementation of receive-logging coupled with message-resending inside the AMPI library will either add new wrappers to this library, or change the existing forward wrappers. Let us assume that the future implementation will rather change the existing forward wrappers. In this case, these wrappers will be called more than once during the checkpointed adjoint, i.e. these wrappers will be called every time the checkpointed part is duplicated. An important question to be asked, thus, when the adjoint needed information has to be saved? Is it better to save this information during the first execution of the checkpointed part or is it better to save this information each time the message-resending is applied, or is it better to save this information the last time the message-resending is applied?

Since this information is used only to determine the adjoint, we think that the third option is the best in terms of memory consumption. We notice, however, that if no message-resending is applied to the forward wrapper, then, we have to save this information during the first execution of the checkpointed part. Also, if the stack is the mechanism we use to save and retrieve the adjoint needed information, then, this information has to be retrieved and re-saved each time we do not apply the message-resending.

II.B. Interface proposal

It is quite difficult to detect statically if a checkpointed part is right-tight or if an mpi routine is orphan or not with respect to a given checkpointed part. This could be checked dynamically but it would require performing additional communications to the ones that already exist, i.e. each `send` has to tell its corresponding `recv` in which checkpointed part it belongs and vice versa. We believe that a possible implementation of receive-logging coupled with message-resending will require the help of the user to specify when applying the message-resending, for instance through an additional parameter to the `AMPI_send` and `AMPI_recv` subroutines. We call this parameter “resending”. To deal with the case of nested structure of checkpointed parts, the resending parameter may for instance, specify for each depth

of the nested structure, whether or not message-resending will be applied e.g. an array of booleans, in which the value 1 at index i reflects that message-resending will be applied at depth= i and the value 0 at index j reflects that message-resending will not be applied at depth= j , i.e. we will apply rather receive-logging.

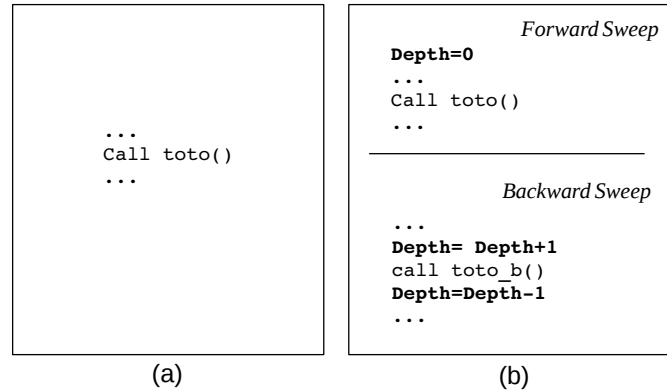


Figure 5. (a) a program that contains a call to a subroutine “toto”. (b) the adjoint program after checkpointing the call to “toto”. In the adjoint code we placed instructions that allow a dynamic detection of the depth

From the other side, we may detect dynamically the depth of each end of communication belonging to a nested structure of checkpointed parts. The main idea is to:

- create a new global variable, that we call “Depth”, and initiate it to zero at the beginning of the adjoint program.
- increment the variable Depth, before each forward sweep of a checkpointed part.
- decrement the variable Depth, after each backward sweep of a checkpointed part.

At run time, the depth of an end of communication is the value of Depth. The instructions that allow initiating, incrementing and decrementing Depth may be easily placed by an AD tool inside the adjoint program. For instance, our AD tool Tapenade checkpoints every call to a subroutine. This means that if we have a call to a subroutine “toto” in the original code, we will have a call to “toto” in the forward sweep of the adjoint code and a call to “toto.b” in the backward sweep of this code, in which “toto.b” contains the forward sweep and the backward sweep of the subroutine “toto”, see figure 5. To detect the depth of each end of communication that belongs to “toto” at run time, it suffices to increment Depth before the call to “toto.b” and decrement Depth after the call to “toto.b”, see figure 5.

Let us assume that Depth will be set as an MPI global variable. i.e. `MPI.Depth`. Figure 6 shows the various modifications we suggest for the wrappers `MPI_FWD_send` and `MPI_FWD_recv`. We see in figure 6 that we added resending as an additional parameter to our MPI wrappers. For each end of communication, we check if the message-resending is applied at the current depth through a call to a function called “isApplied”. This function takes the value of `MPI.Depth` and resending as inputs and returns true if the message-resending is applied at the value of `MPI.Depth` and false in the opposite case. We check also if the message-resending will ever be applied in the following depths, through a call to a function called “willEverBeApplied”. This function takes the values of `MPI.Depth` and resending as inputs and returns true if the message-resending will ever be applied in the following depths and false in the opposite case. The algorithm sketched in figure 6 may be summarized as:

- When message-resending is applied at the depth d , we call the `recv` and `send` subroutines. If message-resending is not applied at depth $d + 1$, then we log in addition the received value. If message-resending will never be applied after depth, then we have to save the adjoint needed information in both send and receive operations.
- When message-resending is not applied at depth, we retrieve the logged value in the receive side. If message-resending is applied at depth+1, then, it is better in terms of memory to free the logged value. As we already mentioned, if the stack is the mechanism we use to save and retrieve the adjoint needed information, then this information has to be retrieved and re-saved in both send and receive operations.

We note that in our implementation proposal, if the user decides to apply the message-resending to one static mpi call, then this decision will be applied to all the run-time mpi calls that match this static call.

```

AMPI_FWD_recv(V,resending)
{
  If (AMPI_Depth==0) || (isApplied(resending,AMPI_Depth)== true) then
    call MPI_recv(V)
    If (isApplied(resending, AMPI_Depth+1)==false) then
      log(V)
    endif
    If (willEverBeApplied(resending, AMPI_Depth)==false) then
      store the needed information for the adjoint
    Endif
  Else
    retrieve(V)
    If (isApplied(resending, AMPI_Depth+1)==true) then
      free(V)
    endif
    restore the needed information for the adjoint
    store the needed information for the adjoint
  }
}

AMPI_FWD_send(V,resending)
{
  If (Depth==0) || (isApplied(resending,AMPI_Depth)== true) then
    call MPI_send(V)
    If (willEverBeApplied(resending, AMPI_Depth)==false) then
      store the needed information for the adjoint
    Endif
  Else
    restore the needed information for the adjoint
    store the needed information for the adjoint
  }
}
    
```

Figure 6. the modifications we suggest for some AMPI wrappers

III. Further refinement: logging only the overwritten receives

We propose a further refinement to our receive-logging technique. This refinement consists in not logging every received value that is not used inside the checkpointed part, or, it is used but it is never modified since it has been received until the next use by the duplicated instance of the checkpointed part, e.g. see figure 7. Formally, given **Recv** the set of variables that hold the received values inside the checkpointed part, **Use** the set of variables that are read inside the checkpointed part and **Out** the set of variables that are modified inside the checkpointed part (only the variables that are modified by more than one *receive* operation are included in the **Out** set of variables) and in the sequel of the checkpointed part, we will log in memory the values of variables **OverwrittenRecvs** with:

$$\text{OverwrittenRecvs} = \text{Recv} \cap \text{Use} \cap \text{Out}$$

The values of **OverwrittenRecv** are called “**overwritten recvs**”. Clearly, this is a small refinement as in the real codes, the number of **overwritten recvs** is much more important than the number of **non-overwritten** ones.

IV. Choice of techniques to be applied

We saw previously various techniques to reduce the memory cost of the receive-logging technique. Some of them duplicate the call to mpi communications, which may add extra cost in terms of time execution and some of them propose not logging all the received values, but only those that are used and will be probably overwritten by the rest of the program. One important question to be asked, then, is for a given checkpointed piece, what is the best combination of techniques to be applied, i.e. what is the combination that allows a reduction of the peak memory consumption without consuming too much in terms of time execution?

In the case where the checkpointed part is not right-tight, we can only apply receive-logging to all the

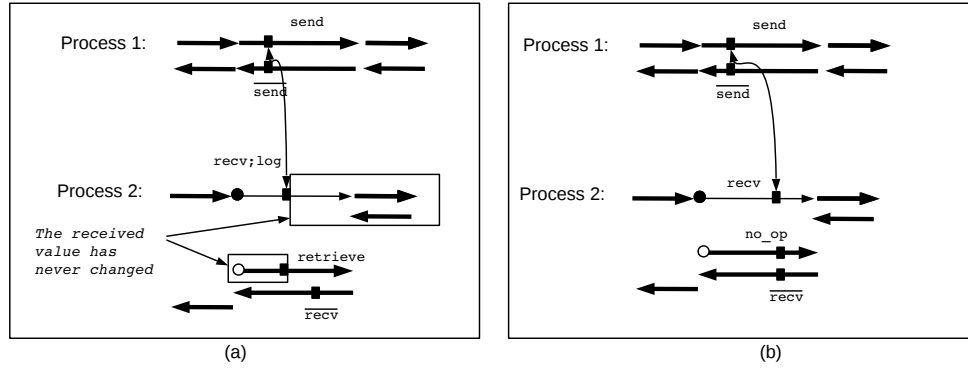


Figure 7. (a) An adjoint code after checkpointing a piece of code containing only the *receive* part of point-to-point communication. Checkpointing is applied together with the receive-logging technique, i.e. the *receive* call logs its received value during the first execution of the checkpointed part and retrieves it during the re-execution of the checkpointed part. In this example, the received value is never modified since it has been received until the next use by the duplicated instance of the checkpointed part, i.e. in the part of code surrounded by rectangles. (b) The same adjoint after refinement. In this code the received value is not saved anymore.

ends of communications inside this checkpointed part.

In the opposite case, i.e. the checkpointed part is right-tight:

- for all **orphan** ends of communications, we can only apply receive-logging.
- for the **non-orphan** ends of communications, we have the choice between applying the receive-logging and the message-resending techniques. When the **non-orphan** ends are **overwritten recvs**, then, it is more efficient in terms of memory to apply message-resending to these **overwritten recvs** together with their **sends**. Actually, applying receive-logging to these **recvs** will require extra storage. From the other hand, when the **non-orphan** ends are basically **non-overwritten recvs**, then, applying receive-logging to these **recvs** and their **sends** has the same cost in terms of memory as applying message-resending to these pairs **sends-recvs**. Thus, in this case we prefer applying receive-logging to these **recvs** and their **sends** as it requires less number of communications than in the case where message-resending is applied.

V. Choice of checkpointed part

So far, we have discussed the strategies to be applied to communication calls, given the placement of checkpointed portions. We note, however, that this placement is also some thing that can be chosen differently by the user, with the objective of improving the efficiency of the adjoint code. This issue is discussed by this section.

In real codes, the user may want to checkpoint some processes P independently from the others, either because checkpointing the other processes is not worth the effort, i.e. checkpointing the other processes does not reduce significantly the peak memory consumption, or checkpointing them will instead increase the peak memory consumption. In this case, is it more efficient in terms of memory to :

1. checkpoint only P , in which case we will have many **orphan** ends of communications which means applying the receive-logging to the majority of mpi calls inside the checkpointed part,
2. or, checkpoint the set of processes P together with the other processes with whom P communicate, in which case we will apply the message-resending to all the mpi calls inside the checkpointed part ?

As the receive-logging technique is in general memory costly, one may prefer the option 2. However, in real codes, the option 2 may sometimes not be the best choice. Actually, choosing the best checkpointed part depends on many factors such as: the cost of **overwritten recvs**, the cost of snapshot of other processes, etc.. It depends also on the needs of the end-user, i.e. efficiency in terms of time or memory? The diagram of figure 8 summarizes the various decisions to be made regarding an example case with 2 processes and 2 alternative checkpointing choices "A" and "B".

- In "A", only process 1 is checkpointed. In this case, we can only apply receive-logging.
- In "B", the two processes 0 and 1 are checkpointed. In this case, we will apply the message-resending.

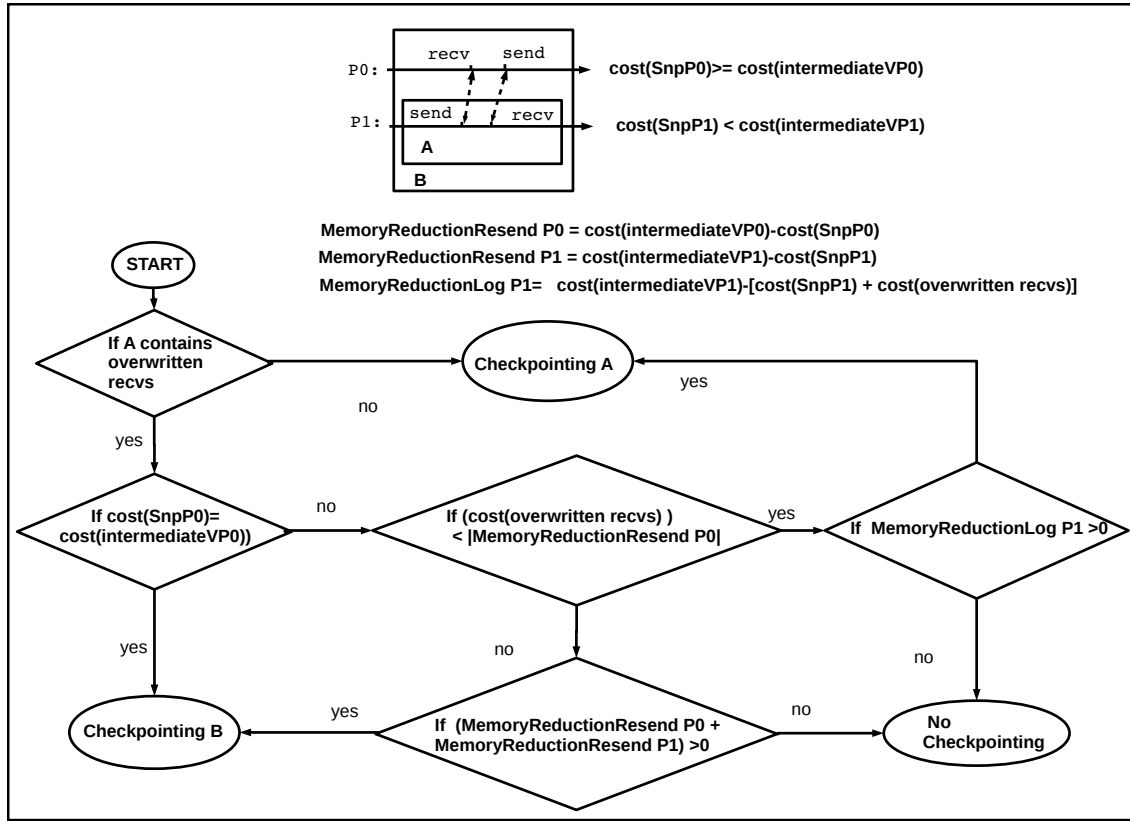


Figure 8. Top: a program run on two processes. In this program, we selected two different checkpointed parts. Down: a diagram that summarizes the best checkpointed part to be chosen in each case.

In diagram 8, we assume that the efficiency in terms of memory is our priority. We see, thus, that in some cases, e.g. when the memory cost of snapshot of process 0, $\text{cost}(\text{SnP0})$, is almost equal to the memory cost of logging the intermediate values of the same process, $\text{cost}(\text{intermediateVP0})$, checkpointing “B” is the most efficient in terms of memory. Since checkpointing “A” is always the most efficient in terms of number of communications, i.e. the receive-logging does not duplicate the communications, the choice of the best checkpointed part depends on the needs of the end-user.

From the other side, the diagram shows that in some other cases, e.g. when we have no **overwritten recvs**, checkpointing “A” is the most efficient not only in terms of number of communications, but also in terms of memory consumption.

VI. Experiments

To validate our theoretical works, we selected two representative CFD codes in which we performed various choices of checkpointed parts. Both codes resolve the wave equation by using an iterative loop that at each iterations resolves:

$$U(x, t + dt) = 2U(x, t) - U(x, t - dt) + [c * dt/dx]^2 * [U(x - dx, t) - 2U(x, t) + U(x + dx, t)]$$

In which U models the displacement of the wave and c is a fixed constant. To apply checkpointing, we used the checkpointing directives of Tapenade, i.e. we placed `$AD CHECKPOINT-START` and `$AD CHECKPOINT-END` around each checkpointed part. By default, the checkpointed code applies the message-resending technique, i.e. by default the resulting adjoint duplicates the calls to MPI communications. To apply the receive-logging, we de-activated by hand the duplication of MPI calls. In addition, for each **recv** call, we added the needed primitives that handle the storage of the received value during the first call of this **recv** and the recovery of this value when it is a duplicated instance of the **recv**.

VI.A. First experiment

The first test is run on 4 processes. Figure 9 shows the various communications performed by these processes at each iteration of the global loop. We see in this figure, that at the end of each iteration, the process 0 collects the computed values from the other processes. In this code, we selected two

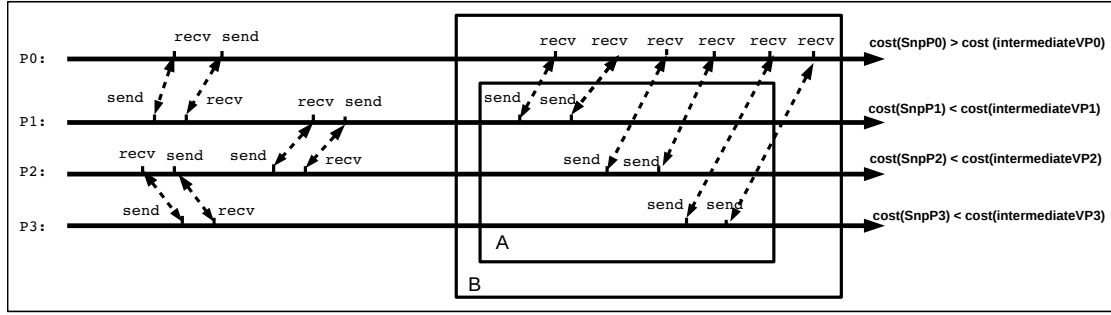


Figure 9. Representative code in which we selected two checkpointed parts

alternative checkpointed parts: “A”, in which we checkpoint the processes 1,2 and 3 and “B”, in which we checkpoint all the processes. We see in figure 9, that checkpointing the process 0 increases the peak memory consumption of this process, i.e. the memory cost of snapshot of process 0, $\text{cost}(\text{SnpP0})$, is greater than the memory cost of logging its intermediate values, $\text{cost}(\text{intermediateVP0})$. We applied the receive logging to all MPI calls of the part of code “A” and the message-resending to all the MPI calls of the part “B”.

The results of checkpointing “A” and “B” are shown in table 1. We see that the code resulting from checkpointing “A” is more efficient than the code resulting from checkpointing “B” not only in terms of number of communications, i.e. it performs less than 24000 communications, but also in terms of memory consumption, i.e. it consumes less than 1.3 MB. The efficiency in terms of number of communications was expected since the receive-logging de-activates the duplication of MPI communications and thus does not add extra communications to the adjoint code as it is the case of the message-resending. From the other side, the efficiency in terms of memory consumption can be explained by the fact that the checkpointed part “A” does not contain any **overwritten** **recvs**, i.e. it contains only **sends**, and thus does not require any extra storage. These results match the analysis of subsection V.

	without CKP	CKP “B”	CKP “A”
Memory cost of P0 (MB)	8	9.3	8
Memory cost of P1,2,3 (MB)	12.6	9.4	9.4
Total Memory cost (MB)	45.8	37.5	36.2
Number of communications	48000	72000	48000

Table 1. Results of the first experiment

VI.B. Second experiment

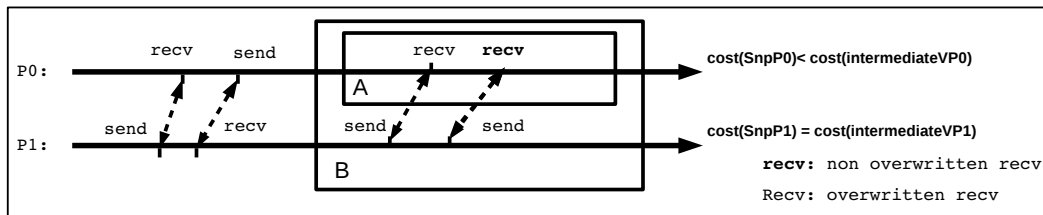


Figure 10. Representative code in which we selected two checkpointed parts

The second test is run on two processes. The communications performed by these two processes are shown in figure 10. In this test we study two alternative checkpointed parts as well. The first part “A” is run on only one process, i.e. process 0 and the second part “B” is run on the two processes. Here, checkpointing the process 1 does neither increase, nor decrease the peak memory consumption, i.e. the cost of snapshot of process 0 is almost equal to the cost of logging the intermediate values of process 0.

The results of checkpointing “A” and “B” are shown in the table 2. Unlike the first experiment, checkpointing “B” here is more efficient in terms of memory. In fact, the resulting adjoint consumes less than 41 KB than the adjoint resulting from checkpointing “A”. This can be explained by two facts: the first one is that “A” contains **overwritten** **recvs** and the second one is that checkpointing process P1

does not decrease the memory consumption. These results also match the analysis of subsection V. We notice here, that checkpointing “A” is always more efficient in terms of number of communications than checkpointing “B”. Clearly, the choice of the best checkpointed part depends here on the needs of the user.

	without CKP	CKP “B”	CKP “A”
Memory cost of P0 (MB)	15.58	12.36	12.39
Memory cost of P1 (MB)	12.45	12.42	12.43
Total Memory cost (MB)	28.03	24.78	24.82
Number of communications	16000	24000	16000

Table 2. Results of the second experiment

VII. Discussion And Further Work

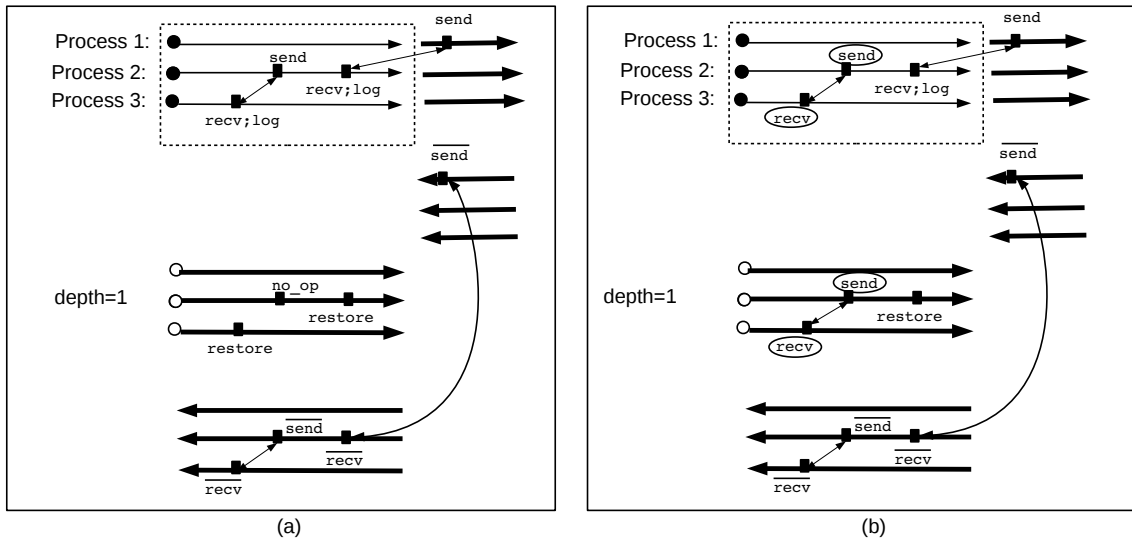


Figure 11. (a) The receive-logging applied to a parallel adjoint program. (b) Application of the message re-sending to a send-recv pair with respect to a non-right-tight checkpointed code

We considered the question of checkpointing in the case of MPI-parallel codes. Checkpointing is a memory/run-time trade-off which is essential for adjoint of large codes, in particular parallel codes. However, for MPI codes this question has always been addressed by ad-hoc hand manipulations of the differentiated code. In a previous work, we introduced, a general checkpointing technique that can be applied for any choice of the checkpointed part. This technique is based on logging the received messages, so that the duplicated communications need not take place. On the other hand, We proposed a refinement that reduces the memory consumption of this general technique by duplicating the communications whenever possible. In this work, we proposed an implementation of these techniques inside the AMPI library. We discussed practical questions about the choice of strategy to be applied within a checkpointed part and the choice of the checkpointed part itself. At the end, we validated our theoretical results on representative CFD codes.

There are a number of questions that should be studied further:

We imposed a number of restrictions on the checkpointed part in order to apply the message-re-sending. These are sufficient conditions, but it seems they are not completely necessary. Figure 11 shows a checkpointed code which is not right-tight. Still, the application of the message re-sending to a send-recv pair (whose ends are surrounded by circles) in this checkpointed part, does not introduce deadlocks in the resulting checkpointed code.

The implementation proposal we suggest in section II allows an application of receive-logging coupled with message-re-sending that may be considered as “semi-automatic”. Actually, this proposal requires the help of user to specify for each end of communication, the set of depths in which it will be activated, i.e. in which depths message-re-sending will be applied to this end. An interesting further research is, thus, how to automatically detect this information, for instance by detecting if a checkpointed part is

right-tight and also if an end of communication is orphan or not with respect to a given checkpointed part.

Acknowledgments

This research is supported by the project “About Flow”, funded by the European Commission under FP7-PEOPLE-2012-ITN-317006. See “<http://aboutflow.sems.qmul.ac.uk>”.

References

- ¹Dauvergne, B. and Hascoët, L. The Data-Flow Equations of Checkpointing in reverse Automatic Differentiation. *International Conference on Computational Science, ICCS 2006, Reading, UK*, 2006.
- ²Taftaf, A and Hascoët, L. On The Correct Application Of AD Checkpointing To Adjoint MPI-Parallel programs *European Congress on Computational Methods in Applied Sciences and Engineering*, 2016
- ³J. Utke, L. Hascoët, P. Heimbach, C. Hill, P. Hovland, U. Naumann, Toward Adjoinable MPI. *Proceedings of the 10th IEEE International Workshop on Parallel and Distributed Scientific and Engineering, PDSEC'09*, 2009.
- ⁴M. Schanen, U. Naumann L. Hascoët, J. Utke, Interpretative Adjoints for Numerical Simulation Codes using MPI. *International Conference on Computational Science, ICCS 2010*.
- ⁵M. Towara, M. Schanen, U. Naumann, MPI-Parallel Discrete Adjoint OpenFOAM. *International Conference on Computational Science, ICCS 2015*.
- ⁶Hascoët, L. and Pascual, V. The Tapenade Automatic Differentiation tool: Principles, Model, and Specification. *ACM Transactions On Mathematical Software*, 39,3, ”<http://dx.doi.org/10.1145/2450153.2450158>”, 2013.

Continuous Adjoint Method Using an Implicit, Block-Coupled Solver in OpenFOAM[®]

Christos K. Vezyris

Evangelos M. Papoutsis-Kiachagias

Kyriakos C. Giannakoglou

National Technical University of Athens, School of Mech. Eng.,

Parallel CFD & Optimization Unit, Athens, Greece

This paper is concerned with the continuous adjoint method for shape optimization. An implicit numerical solver, programmed in the OpenFOAM[®] extend project (foam-extend-3.1), for both the Navier–Stokes and the corresponding continuous adjoint equations, is developed and its use is demonstrated.

The implicit, block-coupled solver is based on the pseudo-compressibility approach. The block-coupled solver computes the solution to the governing equations simultaneously, leading to faster convergence and, among other, an implicit treatment of the numerically stiff Adjoint Transpose Convection (ATC) term.

Benchmark test cases originating from the 11th ASMO International Conference on Numerical Optimization Methods for Engineering Design, are used. First, the U-bend channel proposed by the VKI is optimized for minimal total pressure losses between the inlet and outlet. The second problem is concerned with the minimization of the drag force exerted on the side mirror of the DrivAer vehicle model developed by the TU Munich, in its fastback configuration. Finally, the acoustic signature on the side window of the DrivAer vehicle, approximately quantified by the integral over a near-window volume of the squared turbulent viscosity modeled by the Spalart–Allmaras turbulence model, is minimized.

I. Introduction

In this work, the adjoint method, which is the most efficient way (in either its continuous or discrete variant) to compute the gradient of the objective function w.r.t. a set of design variables³, is used. Here, the continuous adjoint method is considered for shape optimization problems. The incompressible Navier–Stokes equations alongside with the Spalart–Allmaras turbulence model¹⁰ PDE are considered as the state equations. The continuous adjoint method⁵ suggests that the adjoint PDEs are firstly derived and then discretized.

Several CFD packages, among which OpenFOAM[®], use the SIMPLE algorithm to numerically solve the momentum and continuity equations. A Poisson type equation is derived, from the continuity equation, for the pressure computation².

Solving the incompressible fluid flow equations in a segregated manner allows for lower memory usage. In contrast, block-coupled solvers simultaneously solve the complete set of the Navier–Stokes equations leading to lower total computation time. In such solvers, rank two tensors are used as matrix coefficients instead of scalar quantities (being the case for segregated solvers), leading to increased memory requirements.

One way to couple the system of incompressible fluid Navier–Stokes equations is by considering the pseudo-compressibility approach. This approach relies upon adding a pseudo-time derivative of the pressure, multiplied with $1/\beta$, to the continuity equation, where β is a user defined scalar quantity.

In this paper, first the formulation of the flow solver, based on the pseudo-compressibility approach, is presented, followed by the derivation of the continuous adjoint formulation. Finally, the programmed software is used to run two cases and optimization results are presented. For the optimization of the U-bend channel, the shape of the solid walls can be changed in order to reduce the total pressure losses between the inlet and outlet. For the DrivAer case, the side mirror shape should be redesigned in order to reduce firstly the drag force exerted on the car model geometry and secondly, the noise perceived by the driver. The latter is computed according to a surrogate aero-acoustic model that makes the differentiation of the turbulence model necessary while developing the adjoint method.

II. Development of an Implicit Block Coupled solver in OpenFOAM[®]

In incompressible fluid flows, a way to overcome the numerical decoupling between the continuity and momentum equations is the pseudo-compressibility approach¹. The continuity equation is augmented by a pseudo-time

derivative of the pressure, multiplied by a coefficient ($1/\beta$). By doing so, the system of equations governing the incompressible flow becomes hyperbolic. Thus, numerical schemes developed primarily for compressible flows, are used⁸.

After the addition of the pseudo-time derivatives, the mean-flow PDEs, read

$$R_p = \frac{1}{\beta} \frac{\partial p}{\partial t} + \frac{\partial v_j}{\partial x_j} = 0 \quad (1)$$

$$R_{v_i} = \frac{\partial v_i}{\partial t} + v_j \frac{\partial v_i}{\partial x_j} + \frac{\partial p}{\partial x_i} - \frac{\partial}{\partial x_j} \left[(v + v_t) \left(\frac{\partial v_i}{\partial x_j} + \frac{\partial v_j}{\partial x_i} \right) \right] = 0 \quad (2)$$

where p and v_i , $i = 1, 2, 3$ are the static pressure divided by the density and velocity, respectively, β is the artificial compressibility coefficient and x_i , $i = 1, 2, 3$ the Cartesian coordinates, v and v_t are the bulk and turbulent viscosity, respectively. Based on the Spalart–Allmaras turbulence model¹⁰, the viscosity coefficient is given by $v_t = \tilde{v} f_{v_1}$, where \tilde{v} (acting as an additional state variable) results from the solution of the corresponding state equation,

$$R_{\tilde{v}} = \frac{\partial \tilde{v}}{\partial t} + \frac{\partial (v_i \tilde{v})}{\partial x_i} - \frac{\partial}{\partial x_i} \left[\left(v + \frac{\tilde{v}}{\sigma} \right) \frac{\partial \tilde{v}}{\partial x_i} \right] - \frac{c_{b2}}{\sigma} \left(\frac{\partial \tilde{v}}{\partial x_i} \right)^2 - \tilde{v} P(\tilde{v}) + \tilde{v} D(\tilde{v}) = 0 \quad (3)$$

The production $P(\tilde{v})$ and destruction $D(\tilde{v})$ terms are given by

$$P(\tilde{v}) = c_{b1} \tilde{S}, \quad D(\tilde{v}) = c_{w1} f_w(\tilde{S}) \frac{\tilde{v}}{\Delta^2} \quad (4)$$

where the definition of the remaining terms f_{v_1} , f_w , \tilde{S} , and constant values c_{b1} , c_{b2} , c_{w1} and σ can be found in the paper¹⁰ introducing the model. Δ stands for the distance from the nearest wall.

For the discretization of the inviscid fluxes, the approximate Riemann solver proposed by Roe⁹ is used. In the Roe flux scheme, a Jacobian matrix based on averaged face-sharing neighboring cells must be computed. Thus, the inviscid numerical flux crossing the interface between two adjacent control volumes centered at P and Q reads,

$$\Phi_n^{PQ} = \frac{1}{2} \left(f_{nk}^P + f_{nk}^Q \right) n_k^{PQ} - \frac{1}{2} \left| \bar{A}_{nmk}^{PQ} n_k \right| (U_m^R - U_m^L) \quad (5)$$

where n_k^{PQ} are the components of the unit vector normal to the interface between the control volumes P and Q , pointing to cell Q , the Jacobian A is computed based on the Roe-averaged flow variables, \vec{U}^R and \vec{U}^L are the flow variables ($\vec{U} = (p, v_i)$) on the right- and left-hand sides of the control volumes interface, obtained by extrapolating \vec{U}^Q and \vec{U}^P , respectively.

The pseudo-compressibility approach has been implemented in foam-extend-3.1 using the existing block matrix infrastructure. It should be mentioned that foam-extend-3.1 uses cell-centered, finite-volume discretization schemes with the ability to support arbitrary convex polyhedral meshes. For the discretization of the diffusion terms, the standard OpenFOAM[®] approach is used (*fvm::laplacian()*). Contributions of the inviscid fluxes are accounted for without using existing OpenFOAM[®] operators. Instead these contributions are manually distributed, on the left/right-hand side matrices. Each element of the diagonal and off-diagonal left-hand-side matrices (*diag, l, u* in OpenFOAM[®]) is a rank-two tensor (*tensor3*) for 2D simulations (*tensor4* for 3D). After the discretization of the primal equations, based on the implemented Roe scheme given in Eq. (5) (for the inviscid part), the system for a control volume P reads

$$A_P \vec{U}_P + \sum_i^{neighbors} C_i \vec{U}_i = \vec{b}_P \quad (6)$$

where,

$$A_P = \begin{bmatrix} a_{pp} & a_{pv_x} & a_{pv_y} & a_{pv_z} \\ a_{v_x p} & a_{v_x v_x} & 0 & 0 \\ a_{v_y p} & 0 & a_{v_y v_y} & 0 \\ a_{v_z p} & 0 & 0 & a_{v_z v_z} \end{bmatrix}_P, \quad C_i = \begin{bmatrix} c_{pp} & c_{pv_x} & c_{pv_y} & c_{pv_z} \\ c_{v_x p} & c_{v_x v_x} & 0 & 0 \\ c_{v_y p} & 0 & c_{v_y v_y} & 0 \\ c_{v_z p} & 0 & 0 & c_{v_z v_z} \end{bmatrix} \quad \text{and} \quad \vec{U} = \begin{bmatrix} p \\ v_x \\ v_y \\ v_z \end{bmatrix}$$

It should be mentioned that during the discretization, contributions resulted from the second neighbors of a control volume P are treated explicitly (i.e. included in \vec{b}_P).

III. The Continuous Adjoint Method

In the current work, three different objective functions F_i are considered. The first one refers to the volume averaged total pressure losses between the inlet and outlet (which is a typical target in internal aerodynamics). The second one corresponds to the drag force (in external aerodynamics) exerted on a body, while the third one refers to the acoustic noise perceived by the driver of a car. The latter is measured by the integral over a predefined volume of the squared turbulent viscosity of the Spalart–Allmaras model. These objective functions are

$$F_1 = - \int_{S_{I,O}} \left(p + \frac{1}{2} v_k^2 \right) v_i n_i dS \quad (7)$$

$$F_2 = \int_{S_w} \left[p n_i - (v + v_t) \left(\frac{\partial v_i}{\partial x_j} + \frac{\partial v_j}{\partial x_i} \right) n_j \right] r_i dS \quad (8)$$

$$F_3 = \int_{\Omega} v_t^2 d\Omega \quad (9)$$

where n_i is the outward normal unit vector, r_i are the components of a unit vector aligned with the farfield velocity, S_I , S_O and S_w stand for the inlet, outlet and solid wall boundaries, respectively.

In the continuous adjoint method, the augmented objective function F_{aug} is defined as the sum of the objective function F and the field (Ω) integral of the residual of the state equations $\vec{R}_{\vec{U}} = 0$, $\vec{U} = (p, v_i, \tilde{v})$ multiplied by the adjoint fields $\vec{\Psi} = (q, u_i, \tilde{v}_a)$, $F_{aug} = F + \int_{\Omega} \vec{\Psi} \vec{R}_{\vec{U}} d\Omega$. Its variation w.r.t. the design variable array, b_n ($n = 1 \dots, N$), after applying the Leibniz theorem, becomes^{6,7},

$$\frac{\delta F_{aug}}{\delta b_n} = \frac{\delta F_i}{\delta b_n} + \int_{\Omega} q \frac{\partial R_p}{\partial b_n} d\Omega + \int_{\Omega} u_i \frac{\partial R_{v_i}}{\partial b_n} d\Omega + \int_{\Omega} \tilde{v}_a \frac{\partial R_{\tilde{v}}}{\partial b_n} d\Omega + \int_S (q R_p + u_i R_{v_i} + \tilde{v}_a R_{\tilde{v}}) \frac{\delta x_k}{\delta b_n} n_k dS \quad (10)$$

The adjoint field equations and their boundary conditions are derived by eliminating field integrals depending on $\frac{\partial p}{\partial b_n}$, $\frac{\partial v_i}{\partial b_n}$, $\frac{\partial \tilde{v}}{\partial b_n}$. The field adjoint to the mean-flow and turbulence equations are given by

$$R_q = \frac{\partial q}{\partial t} + \frac{\partial u_j}{\partial x_j} = 0 \quad (11a)$$

$$R_{u_i} = \frac{\partial u_i}{\partial t} - v_j \left(\frac{\partial u_i}{\partial x_j} + \frac{\partial u_j}{\partial x_i} \right) - \frac{\partial}{\partial x_j} \left[(v + v_t) \left(\frac{\partial u_i}{\partial x_j} + \frac{\partial u_j}{\partial x_i} \right) \right] - \beta \frac{\partial q}{\partial x_i} - \tilde{v} \frac{\partial \tilde{v}_a}{\partial x_i} - \frac{\partial}{\partial x_i} \left(e_{jli} e_{jmq} \frac{C_S}{S} \frac{\partial v_q}{\partial x_m} \tilde{v} \tilde{v}_a \right) = 0 \quad (11b)$$

$$R_{\tilde{v}_a} = \frac{\partial \tilde{v}_a}{\partial t} - v_j \frac{\partial \tilde{v}_a}{\partial x_j} - \frac{\partial}{\partial x_j} \left[\left(v + \frac{\tilde{v}}{\sigma} \right) \frac{\partial \tilde{v}_a}{\partial x_j} \right] + \frac{1}{\sigma} \frac{\partial \tilde{v}_a}{\partial x_j} \frac{\partial \tilde{v}}{\partial x_j} + 2 \frac{c_{b2}}{\sigma} \frac{\partial}{\partial x_j} \left(\tilde{v}_a \frac{\partial \tilde{v}}{\partial x_j} \right) + \tilde{v}_a \tilde{v} C_{\tilde{v}}(\tilde{v}, \tilde{v}) + \frac{\partial v_t}{\partial \tilde{v}} \frac{\partial u_i}{\partial x_j} \left(\frac{\partial v_i}{\partial x_j} + \frac{\partial v_j}{\partial x_i} \right) + (-P + D) \tilde{v}_a = 0 \quad (11c)$$

where e_{ijk} is the permutation symbol. Terms C_S , S and $C_{\tilde{v}}$ can be found in a previously published work⁷ by the same group, which was though based on a segregated scheme.

The adjoint inviscid numerical fluxes are computed with a nonconservative scheme which, for the interface of two adjacent control volumes with barycenters P and Q , reads

$$\Phi_n^{adj,PQ} = -\frac{1}{2} A_{mnk}^P (\Psi_n^P + \Psi_n^Q) n_k - \frac{1}{2} \left| \bar{A}_{mnk}^{PQ} n_k \right| (\Psi_n^R - \Psi_n^L) \quad (12)$$

$$\Phi_n^{adj,QP} = \frac{1}{2} A_{mnk}^Q (\Psi_n^P + \Psi_n^Q) n_k + \frac{1}{2} \left| \bar{A}_{mnk}^{PQ} n_k \right| (\Psi_n^R - \Psi_n^L) \quad (13)$$

where similar notation as in Eq. (5) holds, with $\vec{\Psi} = (q, u_i)$.

The discretized set of the adjoint field equations, for a finite volume P with cell-centered storage, reads

$$A_P \vec{\Psi}_P + \sum_i^{neighbors} C_i \vec{\Psi}_i = \vec{b}_P \quad (14)$$

where,

$$A_P = \begin{bmatrix} a_{qq} & a_{qu_x} & a_{qu_y} & a_{qu_z} \\ a_{u_x q} & a_{u_x u_x} & a_{u_x u_y} & a_{u_x u_z} \\ a_{u_y q} & a_{u_y u_x} & a_{u_y u_y} & a_{u_y u_z} \\ a_{u_z q} & a_{u_z u_x} & a_{u_z u_y} & a_{u_z u_z} \end{bmatrix}_P, C_i = \begin{bmatrix} c_{qq} & c_{qu_x} & c_{qu_y} & c_{qu_z} \\ c_{u_x q} & c_{u_x u_x} & c_{u_x u_y} & c_{u_x u_z} \\ c_{u_y q} & c_{u_y u_x} & c_{u_y u_y} & c_{u_y u_z} \\ c_{u_z q} & c_{u_z u_x} & c_{u_z u_y} & c_{u_z u_z} \end{bmatrix}$$

As it could be noticed, the coefficients (both diagonal and off-diagonal) of the left-hand-side matrix, for the adjoint system of equations, are full, rank two tensors (*tensor3* or *tensor4* for 2D, 3D simulations respectively in OpenFOAM[®] terminology). These off-diagonal terms incorporate the contribution of the Adjoint Transpose Convection ($-v_x \frac{\partial u_x}{\partial x} - v_y \frac{\partial u_y}{\partial x} - v_z \frac{\partial u_z}{\partial x}$ for the 3D, x-adjoint momentum equation). With the developed implicit, block-coupled solver these contributions are cast in the left-hand side matrix instead of being treated as source terms. The implicit treatment of the stiff ATC terms, in some cases, ensures convergence.

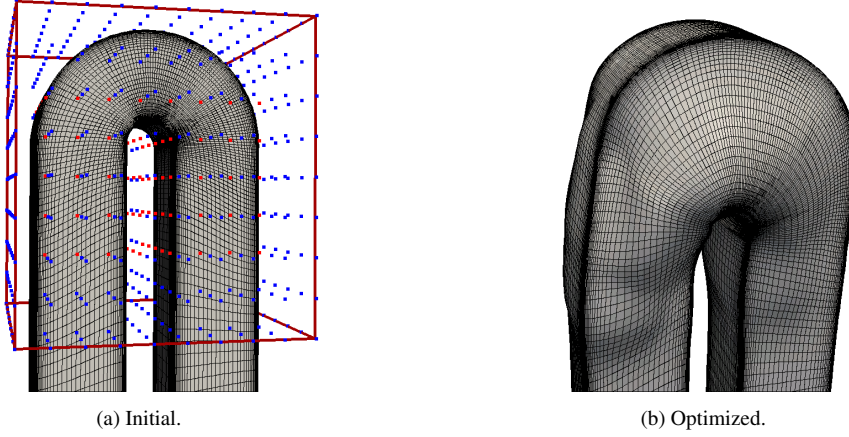


Figure 1: U-Bend geometry. The volumetric B-Splines control points which are allowed to move are colored red whereas all blue points remain still.

After having computed the adjoint fields using the pseudo-compressibility approach, by numerically satisfying the adjoint equations and their boundary conditions, the variation of F_{aug} becomes independent of variations in the state variables, leading to the expressions of the sensitivity derivatives in terms of \vec{U} and $\vec{\Psi}$ in conjunction with variations in geometrical quantities. The sensitivity derivatives of any of the three objective functions this paper deals with, are given by

$$\begin{aligned} \frac{\delta F_{aug}}{\delta b_n} = & A_{F_1} - \int_{S_W} (\mathbf{v} + \mathbf{v}_t) \left(\frac{\partial u_i}{\partial x_j} + \frac{\partial u_j}{\partial x_i} \right) n_j \frac{\partial v_i}{\partial x_k} \frac{\delta x_k}{\delta b_n} dS - \int_{S_W} (\mathbf{v} + \mathbf{v}_t) \frac{\partial \tilde{v}_a}{\partial x_j} n_j \frac{\partial \tilde{v}}{\partial x_k} \frac{\delta x_k}{\delta b_n} dS \\ & + \int_{\Omega} \tilde{v}_a \tilde{v} C_d(\tilde{v}, \tilde{v}) \frac{\partial \Delta}{\partial b_n} d\Omega \end{aligned} \quad (15)$$

where, depending on the objective function used,

$$A_{F_1} = 0 \quad (16)$$

$$\begin{aligned} A_{F_2} = & \int_{S_W} \left[-(\mathbf{v} + \mathbf{v}_t) \frac{\partial}{\partial x_k} \left(\frac{\partial v_i}{\partial x_j} + \frac{\partial u_j}{\partial x_i} \right) + \frac{\partial p}{\partial x_k} \delta_j^i \right] n_j r_i \frac{\delta x_k}{\delta b_n} dS \\ & + \int_{S_W} \left[-(\mathbf{v} + \mathbf{v}_t) \left(\frac{\partial v_i}{\partial x_j} + \frac{\partial u_j}{\partial x_i} \right) + p \delta_i^j \right] r_i \frac{\delta}{\delta b_n} (n_j dS) \end{aligned} \quad (17)$$

$$A_{F_3} = 0 \quad (18)$$

The distance field variation $\frac{\partial \Delta}{\partial b_n}$ is treated by introducing the eikonal equation and developing its adjoint as in a previous work⁷.

IV. Results

The test cases selected, for demonstration purposes, are the U-bend geometry by VKI and the DrivAer vehicle by TU Munich, both provided as benchmark test cases by the 11th ASMO UK/ISSMO/NOED2016 International Conference on Numerical Optimization Methods for Engineering Design. The three objective functions used are given in Eq. (7)-(9).

It is chosen not to run the U-bend channel with the predefined flow conditions¹¹; a laminar flow with the Reynolds number set to ~ 500 is considered. Despite the altered flow conditions, the imposed geometrical constraints¹¹ are taken into consideration during the optimization process. Specifically, with the hydraulic diameter being $D_h = 0.075\text{m}$, the arc curves and the inlet/outlet legs of the channel, up to $2D_h$, are allowed to change. Additionally, because of structural limitations, the overall displacement of the optimized geometry inner and outer curve need to remain inside the box shown in figure 1a.

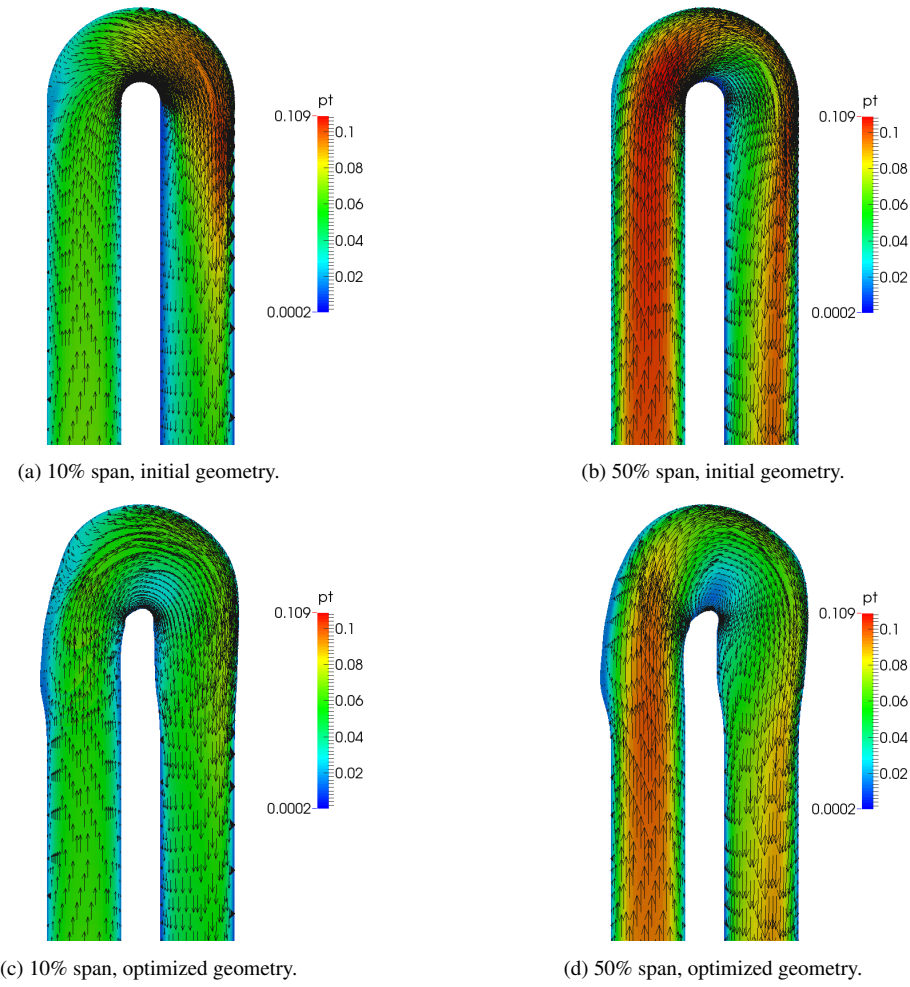


Figure 2: The computed total pressure and velocity vectors for the U-bend.

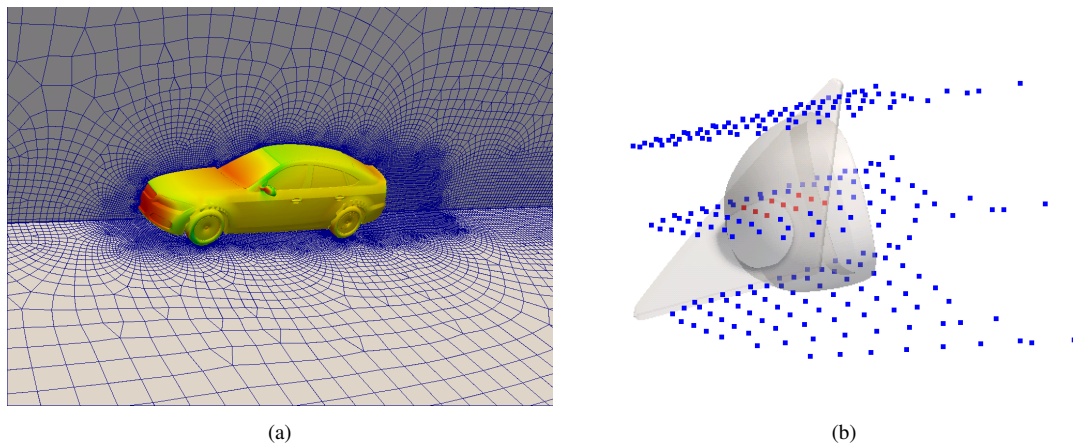


Figure 3: DrivAer test case: (a) Computational mesh and computed pressure over the car surface, (b) Control points of volumetric B-Splines.

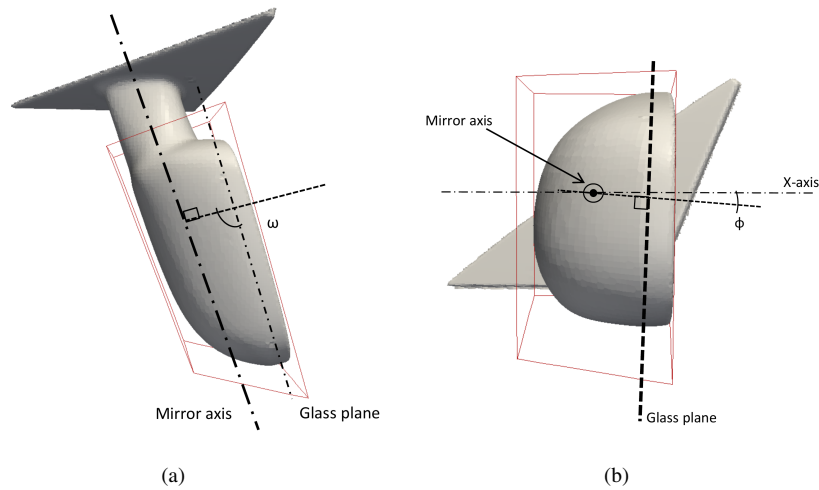


Figure 4: Control box of the DrivAer mirror. Images are taken from the conference manual⁴.

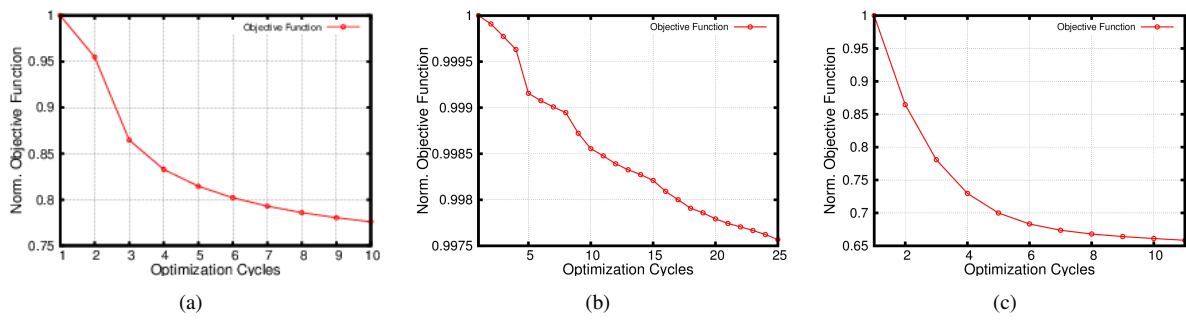


Figure 5: Optimization cycles (a) Total pressure losses, (b) Drag minimization, (c) Noise reduction. A steepest descent algorithm is employed.

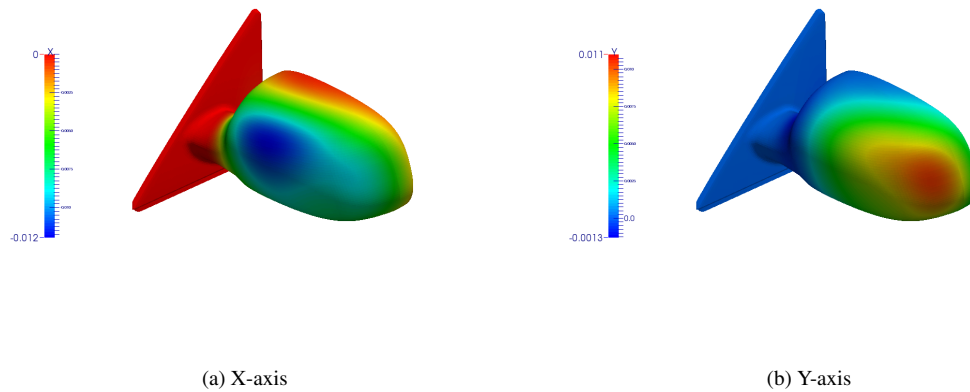


Figure 6: Drag force reduction objective function: Cumulative displacement along the two axes.

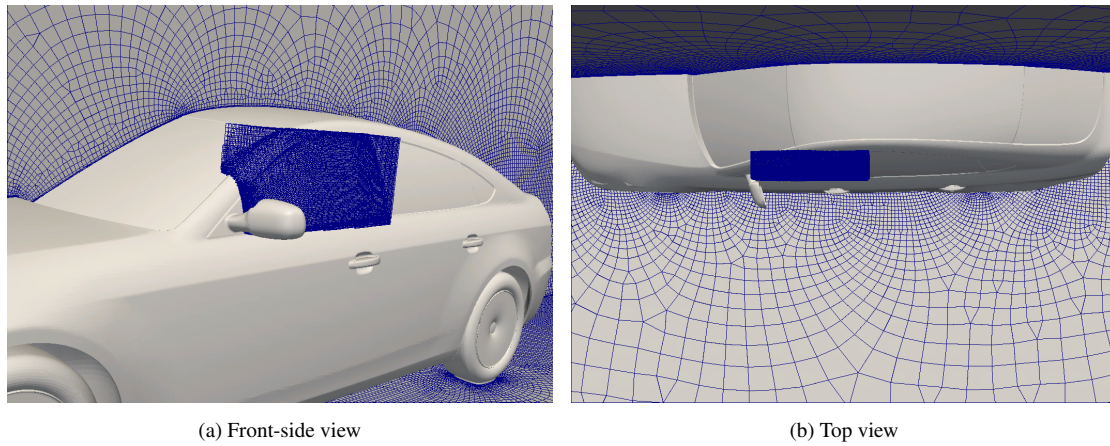


Figure 7: Control volume used for the turbulent dissipation integration when the noise reduction optimization case is considered.

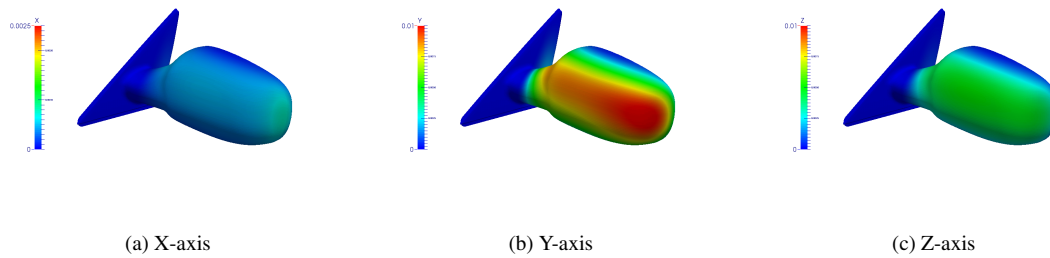


Figure 8: Cumulative displacement along the three axes in the optimization targeting noise reduction, given by (9).

The computational mesh of the U-bend counts for approximately 650×10^3 cells. Volumetric B-splines are used for the surface parameterization, with 600 design parameters, namely the displacements of the control points along the three axes. Initially, approximately 800 control points are created, however it is selected that the outer 1, 2, 2 rows of control points along the X-, Y-, Z-direction, respectively, remain frozen. This ensures that the geometrical constraints of the optimization case are met. The control box (which contains the control points) is plotted on the initial geometry, shown in figure 1a, while the optimized geometry is presented in figure 1b. Figure 2 shows the calculated total pressure and velocity vectors, at 10% and 50% span of the duct, before and after the optimization process. In figure 5a, the optimization cycles are illustrated, where it can be observed that a drop of approximately 23% is achieved. By means of the developed solver the optimization process is concluded $2 \times$ faster than the SIMPLE-based continuous adjoint optimization solver.

The computational mesh for the DrivAer vehicle is composed of approximately 5.3×10^6 polyhedral elements and is illustrated in figure 3a. The optimization is subjected to certain geometrical constraints.⁴ Specifically, let the glass mirror define a planar plane, as shown in figures 4a, 4b. Then, this plane (including both mesh faces and body/mirror casing surfaces) should only move as a rigid body in the outward direction. Furthermore, angles ω and ϕ , as illustrated in figures 4a, 4b, must be kept fixed. The displacement of the surfaces must be confined in the box shown in figures 4a, 4b and performed only in the outward direction.

For the parameterization of the mirror surface, volumetric B-Splines are used. In figure 3b, the control points of the parameterization are illustrated, with red color being the active ones (those are allowed to move along the X- and Y-axis). In total, 18 design parameters are used.

For the objective function of Eq. (8), the optimization process results in an overall objective function drop of approximately 0.25%. Figure 5b depicts the optimization cycles. The optimization process manually terminated when the proposed geometry stopped meeting the constraints. As it can be observed in figures 6a and 6b, the cumulative normal displacement of the surface along both directions is quantitatively similar.

The objective function, given in Eq. (9), is monitored in the control volume shown in figure 7a and 7b. The optimization process for this case resulted in 35% noise reduction. Moreover, the final configuration of the mirror produces a 0.22% drop of the drag force exerted on the car. The optimization progress is illustrated in figure 5c. Figure 8 gives the cumulative displacement along all axes. It can be observed that the predominant direction of displacement is along the Y-axis.

V. Conclusions

In this paper, the development of a new block-coupled solver for incompressible fluid flows in OpenFOAM[®] is presented. The solver is based on the pseudo-compressibility approach, by which the problem of decoupling between the momentum and continuity equations is overcome. The same solver is also used for the continuous adjoint equations, for which an implicit treatment of the stiff ATC term is introduced. The simultaneous solution of the flow variables, for both the primal and adjoint equations, promise lower computational time.

For demonstration purposes, two test cases are selected, both provided by 11th ASMO International Conference. The new solver achieves a 2× computational time improvement compared to the default OpenFOAM[®] segregated solver (based on the SIMPLE algorithm). This gain in time comes from the lower number of iterations, compared to its segregated counterpart, needed by the block-coupled solver to reach convergence.

Acknowledgements

This research was funded from the People Programme (ITN Marie Curie Actions) of the European Union's 7th Framework Programme (FP7/2007-2013) under REA grant agreement 317006 (AboutFLOW project). The first author was an AboutFLOW Early Stage Researcher.

References

- ¹A. J. Chorin. A numerical method for solving incompressible viscous flow problems. *Journal of Computational Physics*, 135(2):118 – 125, 1997.
- ²M. Darwish, I. Sraj, and F. Moukalled. A coupled finite volume solver for the solution of incompressible flows on unstructured grids. *Journal of Computational Physics*, 228(1):180 – 201, 2009.
- ³A. Jameson. Aerodynamic design via control theory. *Journal of Scientific Computing*, 3:233–260, 1988.
- ⁴Christos Kapellos, Michael Hartmann, Carsten Othmer, and Jens-Dominik Mueller. *NOED2016 Optimisation benchmark, Testcase 4 DrivAer, Version 1.0*, January 2015. <http://www.aboutflow.sems.qmul.ac.uk/content/events/munich2016/benchmark/testcase4/>.
- ⁵D. Papadimitriou and K. Giannakoglou. Aerodynamic shape optimization using first and second order adjoint and direct approaches. *Archives of Comp. Meth. in Eng.*, 15(4):447–488, 2008.
- ⁶D.I. Papadimitriou and K.C. Giannakoglou. A continuous adjoint method with objective function derivatives based on boundary integrals for inviscid and viscous flows. *Computers & Fluids*, 36(2):325–341, 2007.
- ⁷E.M. Papoutsis-Kiachagias and K.C. Giannakoglou. Continuous adjoint methods for turbulent flows, applied to shape and topology optimization: Industrial applications. *Archives of Computational Methods in Engineering*, 23(2):255–299, June 2016.
- ⁸M. M. Rahman and T. Siikonen. An artificial compressibility method for viscous incompressible and low Mach number flows. *International Journal for Numerical Methods in Engineering*, 75(11):1320–1340, 2008.
- ⁹P.L. Roe. Approximate Riemann solvers, parameter vectors, and difference schemes. *Journal of Computational Physics*, 43(2):357 – 372, 1981.
- ¹⁰P. R. Spalart and S. R. Allmaras. A one-equation turbulence model for aerodynamic flows. *La Recherche Aéronautique*, 43(1):5 – 21, 1994.
- ¹¹T. Verstraete. *NOED2016 Optimisation benchmark, Testcase 1 the VKI U-Bend*, March 2016. <http://www.aboutflow.sems.qmul.ac.uk/content/events/munich2016/benchmark/testcase1/>.

